A MICROSTRUCTURAL STUDY OF HEAT AFFECTED ZONE MICROFISSURING OF ELECTRON BEAM WELDS IN CAST ALLOY 718

by

Xiao Huang

A Dissertation

Submitted to the Faculty of Graduate Studies

in partial fulfilment of the

requirements for the degree of

Doctor of Philosophy

Metallurgical Science Laboratories

Department of Mechanical and Industrial Engineering

University of Manitoba

Winnipeg, Manitoba

A MICROSTRUCTURAL STUDY OF HEAT AFFECTED ZONE MICROFISSURING OF ELECTRON BEAM WELDS IN CAST ALLOY 718

BY

XIAO HUANG

A Thesis submitted to the Faculty of Graduate Studies of the University of Manitoba in partial fulfillment of the requirements for the degree of

DOCTOR OF PHILOSOPHY

Dedicated to

Mrs. and Mr. Prins

Without their help and encouragement, this would be impossible

ABSTRACT

Heat-Affected Zone(HAZ) microfissuring occurs during electron beam welding of cast Alloy 718. In order to understand this phenomenon and find a solution, a series of investigations have been carried out to examine the microstructure of the base material in various heat treated conditions (homogenized, solution treated and aged) and the microstructure of HAZ and fusion zone and to evaluate the weldability of Alloy 718 heat treated to different conditions. The microstructures were examined using Scanning Electron Microscopy (SEM), Transmission Electron Microscopy (TEM), Secondary Ion Mass Spectrometry (SIMS), Electron Back-Scatter Diffraction (EBSD) technique and optical image analyzer. The weldability was evaluated by measuring crack length around the HAZ and the sum of individual crack lengths on each weldment section (Total Crack Length) was used to represent the material's weldability in this study.

The microstructure of cast Alloy 718 was observed to consist of A_2B Laves phase, δ-Ni_3Nb phase, M(C,N) carbonitrides and MN nitrides, with occasional presence of γ" and γ' in the interdendritic areas. The nature of grain boundaries in the cast alloy was examined using EBSD technique and it was found that 93% of the grain boundaries were of the random type. It was found that on increasing the homogenization temperature from 1037 to 1163°C, the amount of δ-Ni_3Nb and Laves phases decreased and that of M(C,N) carbonitrides remained constant. Solution heat treatment at 927°C enhances the precipitation of both inter- and intragranular δ-Ni_3Nb phase. Ageing heat treatment increases the material's hardness through the precipitation of γ"+γ'.

The grain boundary segregation after homogenization heat treatments, at temperatures ranging from 950 to 1140°C, followed by either air cooling or water quenching, was analyzed using SIMS. Boron segregation was observed, the extent of which decreased initially (from 950 to 1066°C) and then increased (from 1066 to 1240°C) when air cooling was used. In the case of water quenching, the boron segregation decreased continuously with an increase in homogenization temperature (from 950 to 1163°C). The occurrence of both equilibrium and non-equilibrium segregation could account for the segregation of boron. Segregation of carbon, sulphur and phosphorus was also examined using SIMS. However, none of these elements was found to be present at grain boundaries.

The examination of HAZ and fusion zone microstructures revealed that the majority of the precipitates in EB fusion are MC-type carbides, with small amounts of Laves phase and $M_{23}C_6$. In HAZ, constitutional liquations of both Laves phase and M(C,N) occurred and resulted in resolidified Laves phase and M(C,N).

The Total Crack Length (TCL) after homogenization heat treatment decreased initially (from 1037 to 1066°C) and then increased (from 1066 to 1163°C). No correlation between the amount of secondary phases and the TCL was observed. However, the variation in TCL with homogenization temperatures had a similar trend as that of the variation in boron segregation with temperature after air cooling.

This suggests that boron segregation plays an important role in controlling the HAZ microfissuring. A mechanism to explain the effect of boron on HAZ microfissuring has been proposed. The solution heat treatment reduced the TCL as compared to the homogenization treatment, while ageing treatment caused an increase in the value of TCL.

ACKNOWLEDGEMENTS

The author wishes to express her sincerest thanks to the following people for their help and guidance: Drs. M.C. Chaturvedi, N.L. Richards, J. Cahoon, Messrs. J. Van Dorp, D. Mardis and L. Oree. Among whom, I would specially thank my supervisor Dr. M. C. Chaturvedi, for giving me the opportunity to work on this interesting project and the financial support.

Thanks are due to Pat, Norman, Irene and Klaus for giving me a second family at this new country. It has been my great pleasure to have Norman as my co-supervisor. Not only has he given me countless advice in my project, he has also taught me the way of doing scientific research. He is like my father and my best friend.

I must also acknowledge my gratitude to my best friends, Liwen, Archana, Fariba, Sterling, Lincoln and Zhang for their precious friendship and constant support throughout all these years.

I would express my greatest appreciation to my colleagues at Bristol Aerospace Ltd., specially to J. Davies for conducting the electron beam welding trial. Thanks are also due to N. Goel for his continuous support and encouragement.

Special recognition must be given to Drs. J. Jackman and J. Bowker at CANMET, K. Aust at University of Toronto and G. Palumbo at Ontario Hydro for their help in conducting various experiments and many valuable discussions.

Last, I would say I am very grateful to my parents, my sister and Ken for the love, understanding and patience they have been given to me, which make my life meaningful.

TABLE OF CONTENTS

LIST OF FIGURES

LIST OF TABLES

LIST OF SYMBOLS

C_o	Average or bulk solute (impurity) concentration
C_b	Solute grain boundary concentration
C_{bo}	Solute grain boundary saturation concentration
$C_b(t)$	Grain boundary concentration at time t
C_v	Vacancy concentration
C_S	Instantaneous solid composition forming at any fraction of solid f_s (wt%)
C_S	Solute concentration (at%)
C_{mass}	Solid solubility
C_{VS}	Vacancy-solute complex concentration
C_g	Segregating atom concentration in the unsegregated regions
E_A	Activated energies for diffusion of impurities
E_b	Binding energy between segregant and interface
E_f	Free energy of adsorption at the grain boundary (= $-E_b$)
E_f	Vacancy formation energy
E_b	Vacancy-solute binding energy
$E_{VS}^{\ b}$	Vacancy-solute binding energy
E_{VS}	Vacancy-solute binding energy
$E_{VS}^{\ B}$	Vacancy-solute binding energy
E_{el}	Elastic strain energy
$E_V^{\ f}$	Vacancy formation energy
E_S	Interfacial energy of removed atom

E_{ss}	Di-solute formation energy
E_v	Vacancy formation energy
E_{vv}	Di-vacancy formation energy
E_{vs}^{A}	Average activation energy for diffusion of complexes and impurities in the matrix
E_{vf}	Vacancy formation energy
S_v	Vacancy formation excess entropy
A	Correction factor = 20
b	Width of the crack at the interface and equal to one Burger's Vector
2c	Particle thickness
d	Thickness of the boundary layer through which the solute must diffuse
d	Slip band length
d	Grain Size
D	Solute bulk diffusion coefficient
D	Diffusivity of solute in the liquid
D_{vs}	Complex diffusion coefficient
D_b	Grain boundary diffusion coefficients
D_m	Volume diffusion coefficients
R	Growth rate
D/R	Characteristic distance
G	Shear modulus
I	Welding beam current

l	Crack length
k	Boltzman's constant
k	Distribution coefficient
k_E	Effective distribution coefficient
K	Mass constant
K	Geometry factor
N	Avogadro's number
P	Beam power
r_o	Matrix atom radius
r_i	Impurity atom radius
R	Solidification speed
R'	Growth speed of crystal
S	Welding speed
t_c	Critical time
t	Time
T_i	Starting temperature
T_m	Alloy's melting point (average of liquidus and solidus)
V	Beam accelerating potential
$\underline{X}$	Ratio of diffusivity to growth velocity
X_L	Mole fraction of solute in the liquid
X_S	Mole fraction of solute in the solid
Z	Co-ordination number (= 12 for FCC)

β	Enrichment factor = C_b/C_g
γ	Effective fracture surface energy and $=2\gamma_{SL}-\gamma_{GB}$,
γ_{SL}	Solid/liquid interfacial energy
γ_{SV}	Solid/vapour free surface energy
γ_{ML}	Base metal liquid surface energy
γ_{SM}	Surface energy between solid weld metal and the base metal
γ_c	Free surface energy of the secondary phase
γ_{SS}	Grain boundary energy
γ_a	Applied stress
ν	Poisson's ratios
σ	Stress
μ	Shear modulus
σ_E	Local shear stress
θ	Cooling rate
θ	Dihedral angle
ϕ	Wetting angle
ν	Welding speed
Φ	Position of the interface relative to the heat source
Ω	Atomic volume
δ	Grain boundary width

CHAPTER ONE

INTRODUCTION

Alloy 718 is a γ"-precipitation-hardened Ni-Fe-Cr base alloy which was developed for aerospace applications in the early 1960's. It has high strength at elevated temperatures (540-560°C), good corrosion resistance and freedom from strain-age cracking. However, the presence of Nb in this alloy makes it susceptible to intergranular and interdendritic cracking in the heat-affected-zones (HAZ) in welded regions. The alloy was originally utilized in the wrought form and most of the research work reported in the literature was conducted on the alloy welded in the wrought condition. Microfissuring in this condition can be controlled efficiently through reducing the grain size. Recently, an increasing number of components of cast alloy 718 are being widely used in industry in large components such as compressors and turbine frames in aircraft engines which reduces machining and welding operations. Compared to wrought alloy 718, more severe microfissuring has been observed in the cast alloy 718 generally due to the coarse grain size, presence of a lower melting point Laves phase and heavy dendritic segregation.

Several studies have been carried out in the past on cast alloy 718. The metallurgical factors which govern the HAZ microfissuring can be summarized as: 1) chemical composition, 2) heat treatment condition, 3) presence of low melting point phases which cause constitutional liquation during the welding cycle and 4) grain boundary precipitates and segregation affected by the composition of the alloy and the pre-welding heat treatment given to it. The practical approaches which can be used to improve the

material's weldability are: 1) optimizing heat treatment condition and 2) varying welding parameters. In the present investigation, the effect the heat treatment (including homogenization, solutioning, ageing and overageing) on the microstructure and its influence on the weldability of the material have been studied. The HAZ microfissuring has been discussed in terms of the volume fraction of secondary phases, grain boundary precipitates and segregation and hardness of the material.

Segregation of trace elements to grain boundaries has dramatic effects on an alloy's metallurgical properties, such as temper embrittlement, intergranular stress corrosion cracking and intergranular hydrogen embrittlement. The HAZ microfissuring also appears to be associated with the elemental segregation at grain boundaries. It was also observed that the enrichment of impurities at grain boundaries can be induced by either equilibrium segregation or non-equilibrium segregation. Another objective of this study was to further understand the occurrence of both these types of segregation during homogenization treatment and the relationship between the elemental segregation and HAZ microfissuring.

CHAPTER TWO

LITERATURE REVIEW

A great deal of research has been conducted on various physical, metallurgical and welding aspects of wrought Alloy 718, but information on these aspects on cast 718 are lacking. Therefore, the literature review of the background characteristics is mostly based on information on wrought alloys. The review first deals, very briefly, with the physical metallurgy of Alloy 718 and then with various factors that influence the weldability and heat affected zone cracking of Alloy 718.

2.1 Physical Metallurgy of Alloy 718

2.1.1 Introduction

Alloy 718 is a Ni-Fe based superalloy developed by H.L Eiselstein in the early 1960's [1]. Initially the alloy was used by General Electric as a turbine material in an aircraft jet engine and the alloy's most important properties at that time were its resistance to creep and stress rupture. As new applications were unveiled in various industries, Alloy 718 gained wider acceptance because of its elevated temperature properties, fabricability and cost effectiveness. Beyond the original (and still the largest) application in aircraft engines, it is currently being used as a generic alloy in nuclear and cryogenic structures and where environmental cracking resistance is required. Applications vary from rotating and static components in engines to high-strength bolts and fasteners, components for sour-gas wells and pipelines, nuclear reactor and space vehicles, marine shafts and even high temperature tools for extrusion and shearing. As a result, Alloy 718 is the most

widely used superalloy, accounting for nearly 35% of all superalloy production [2].

The chemical composition range of the alloy is given in Table 2-1. Although originally designed as a wrought alloy, it has been cast into large structural components by conventional casting techniques and micro-casting technique which results in finer grains (ASTM #3-5) [3]. Additionally, the alloy can be successfully atomized and made into products by powder metallurgy. The microstructure and properties are controlled by the hot-working schedule and variation in alloy composition. Wrought Alloy 718 can be processed in three different ways to obtain the properties listed in Table 2-1 [4].

Table 2-1 Composition range of alloy 718 (wt%)

Ni	Cr	Fe	Nb	Mo	Al	Ti
50.0 ~ 55.0	17.00 ~ 21.00	Bal.	4.75 ~ 5.50	2.80 ~ 3.30	0.2 ~ 0.80	0.65 ~ 1.15
Mn	Si	B	C	S	Mg	
0.35 max	0.35 max	0.006 max	0.08 max	0.015 max	Residual	

Table 2-2 Alloy 718 Processing Options

Processes	Grain size (ASTM #)	UTS @ R.T. Min.(N/mm^2)	UTS @ 649°C Min.(N/mm^2)
Standard*: 1st Forge 1066-1093°C 2nd Forge 1037-1066°C	4	1275	1000
High Strength*#: 1st Forge 1037-1066°C 2nd Forge 1010-1037°C	8	1343	1068
Direct Age+# 1st Forge 996-1024°C 2nd Forge 968-996°C	10	1447	1171

*sol at 968°C/2hrs, W.Q., age at 718°C/8hrs, F.C.at 38°C/hr to 621°C and hold for 8hrs.

+age at 718°C/8hrs F.C. 38°C/hr to 621°C, age at 621°C/8hrs.

+#limited to simple shapes.

2.1.2 Alloy Phases present in Alloy 718

The primary strengthening phases in Alloy 718 are DO_2-ordered γ" phase and an $L1_2$-ordered γ' phase, both of which are coherent with the face centred cubic γ matrix. Alloy 718 also has a large number of phases which either have a characteristic morphology or form in a specific temperature range such that their tentative identification can be made

if the thermal history of the alloy is known. The phases normally found are discrete MC carbide particles, a round, island-like and lamellar Laves phase (AB_2), a needle/plate-like δ-phase (Ni_3Nb), disk-shaped γ" (Ni_3Nb, Al) and spheroid γ' ($Ni_3(Al, Nb)$) [5]. The MC phase forms upon solidification and remains stable to about 1250°C on heating. The Laves phase forms upon solidification in high niobium interdendritic regions and is stable up to about 1175°C. The δ-phase precipitates within the temperature range of 843 to 982°C during heat treatment or upon solidification in high niobium areas. It is stable up to 1010°C in wrought alloy, and up to 1121°C in cast Alloy 718. The γ" forms during continuous cooling or during heat treatment at 712 to 899°C and precipitates are smaller when formed at lower temperatures. The γ' phase forms upon cooling after solidification or when heat treatment is conducted in the 637 to 718°C temperature range, and it constitutes about one-quarter of the total amount of precipitate formed in alloy 718 [6]. Other phases such as M_6C carbides, MN nitrides, M_3B_2 boride, HCP-η, σ and μ phases have been also observed in alloy 718 [7], and carbides, nitrides and borides dissolve at temperatures between 1225 and 1290°C. The structure and characteristics of individual constituents are described next.

Gamma Matrix(γ):

The matrix of Alloy 718 is a FCC nickel-iron-base austenitic phase called gamma(γ) that usually contains a high amount of elements such as Co, Cr, Mo and Nb for solid solution hardening of the matrix and enhancing other properties such as corrosion and oxidation resistances.

Laves(A_2B) Phase:

Laves phase possesses one of the three related crystal structures of $MgCu_2$, $MgZn_2$ and $MgNi_2$-type and have a general formula AB_2. These phases have been named after Laves [8]. $MgCu_2$ is cubic with 24 atoms per unit cell, whereas $MgZn_2$ and $MgNi_2$ are hexagonal with 12 and 24 atoms per unit cell respectively. The atomic arrangements in these three structures are summarized in Table 2-3.

Table 2-3 Structure of Laves Phase [10]

Structure	Arrangement	
	A-atom-layers	B-atom-tetrahedra
$MgCu_2$	XYZXYZ (along [111])	joined point to point
$MgZn_2$	XYXY (along [001])	joined point to point and base to base alternately
$MgNi_2$	XYXZXYXZ (along [001])	Mixture of the above two arrangements

One of the main factors contributing to the existence of the Laves phase is of geometrical origin (size factor); i.e. space filling in a convenient way. Goldschmidt radii of the pure elements are not important in dictating which of the three structures will form; it is only necessary that the A atoms be larger than the B atoms and that they be able to contract or expand to achieve the ideal ratio of 1.225. The electronic factor has been used to predict which of the three crystal structures will form in binary systems [8]. It is impossible to classify these types of compounds in terms of their electron/atom ratios.

In Alloy 718 Laves phase has a C14 crystal structure with a_o=0.47nm and c_o=0.76nm. Analysis by Energy Dispersive Spectrometry (EDS) yielded a composition consistent with the formula $(Ni_{0.5}Cr_{0.25}Fe_{0.25})_2$(NbMoSi) [9]. It may form either during the solidification process or during annealing at 1038°C.

MC Carbides:

MC carbides as mentioned earlier usually form during solidification, they occur as discrete particles distributed interdendritically both in inter- and intragranular positions. The MC carbide forms independently or on the substrate of MC nitrides, has a FCC structure and little or no orientation relationship with the alloy matrix. MC carbides if dissolved in subsequent heat treatment are a major source of carbon for the alloy. The preferred order of formation of MC carbides in superalloys is HfC, TaC, NbC, and TiC in order of decreasing stability. M atoms can substitute for each other, such as (Ti, Nb)C.

γ" Phase:

γ" is DO_{22}-ordered Ni_3Nb phase (Fig.2.1 [11]) that precipitates in Fe-Ni-base alloys containing Nb. Alloy 718 is the outstanding example of an alloy in which γ" formation has been commercially exploited and used as a primary precipitation hardening phase. The γ" phase is disk shaped and its volume fraction in Alloy 718 is substantially in excess of that of γ'. The most significant feature of γ" is probably the ease with which it forms at moderate temperatures after prior solutioning by heat treatment or joining

processes. Because of this behaviour, Alloy 718 can be aged after welding to produce a fully strengthened microstructure with exceptional ductility.

A lack of notch ductility in alloy 718 has been associated with a γ" precipitation-free-zone (PFZ). However, the γ" PFZ can be eliminated and ductility restored by appropriate heat treatment. Alloys hardened with γ" phase achieve high tensile strengths and very good rupture properties at lower temperatures, but the conversion of γ" to γ' or δ above 677°C causes a sharp reduction in strength. Work on long time exposure has shown that the γ" is stable for 10,000 hrs at 600°C, with very little particle coarsening. However, at higher temperatures and for times in excess of 3,000 hrs, the γ" decomposes to form either γ' (650-850°C) or δ (750-1000°C) [12,13]. A chemical composition difference between δ and γ" has been observed and estimated to be as follows [5]:

δ: $[Ni_{0.73}Fe_{0.01}Cr_{0.01}]_3[Nb_{0.18}Ti_{0.05}Al_{0.02}]$

γ": $[Ni_{0.53}Cr_{0.21}Fe_{0.01}]_3[Nb_{0.13}Ti_{0.06}Al_{0.04}Mo_{0.01}]$

By chemical extraction studies, the amount of precipitate in the fully heat treated condition has been found to be about 19 wt% [11]. The coherency strain associated with BCT γ" particles is considerably greater than that for γ'. The γ" precipitates form as discs with $\{100\}_\gamma//(001)_\gamma$ and $<100>_\gamma//[001]_\gamma$ orientation relationship [11]. The precipitate particles have an average diameter of 600Å and thickness of 50-90Å, and tend to remain coherent during coarsening. The data on coarsening of γ" during thermal exposure is shown in Table 2-4.

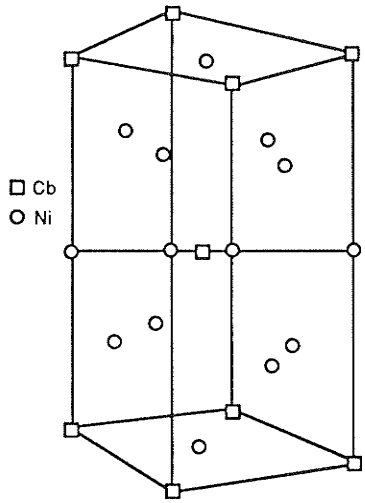

Fig.2.1 Unit cells illustrating ordering of the strengthening precipitate BCT γ'' (DO_{22}), one unit cell [11].

γ' Phase :

γ' is an ordered ($L1_2$) intermetallic A_3B compound with FCC crystal structure. Its shape has been found to be related to its mismatch with the matrix. γ' occurs as spheres at 0-0.2% lattice mismatch, becomes cubic with increasing mismatch around 0.5-1.0%, and finally becomes platelet when mismatch exceeds 1.25% [14]. It is crystallographically related to the γ matrix by the orientation relationship $\{100\}_{\gamma'}//(100)_{\gamma}$ and $<100>_{\gamma'}//[100]_{\gamma}$ [11]. In the γ'-type A_3B, relatively electronegative elements, such as Ni, Co or Fe comprise the A, and more electronegative elements such as Al, Ti, Ta and Nb comprise B. Alloying elements affect the mismatch of γ' with the matrix γ phase,

and the antiphase domain boundary (APB) energy, morphology and stability of γ' phase. The strengthening effect of γ' is related to its particle size, APB energy and stacking fault energy, strength, coherency strains, volume fraction, diffusivity in γ, and possibly, γ'-γ modulus mismatch [12].

Table 2-4 Coarsening of γ" during thermal exposure

Heat treatment	Diameter of disc γ" (Å)	Diameter of spherics γ' (Å)	Amount of γ"+γ'(wt%)
Fully heat treated	600	250	19
FHT+1200°F/100hrs	725	300	n/a
FHT+1400°F/100hrs	3000	600	n/a
FHT+1550°F/16hr	3500	750	n/a
FHT+1600°F/16hr	5500	n/a	9%

δ-Ni_3Nb (Doa-ordered)

The most stable Ni_3Nb precipitate is the orthorhombic δ phase which nucleates at grain boundaries and grows into plates lying on the matrix {111} planes [13]. δ also forms at other interfaces such as twin boundaries, inclusions and Laves phases [9]. Intragranular δ has been also observed and it nucleates in association with stacking faults within γ" particles [15]. In the region where δ precipitates do not find a suitable habit plane variant

parallel to the grain boundary, their growth is often found to be associated with a migration of the grain boundaries thus creating a serrated grain boundary structure [15,16]. The serrations arise from the cellular precipitation of Ni_3Nb following the To-Turnbull mechanism [17] and are angular in nature. The crystallographic orientation relationship between the austenite γ and the equilibrium δ phase has been observed to be [15]: $\{111\}_\gamma // (010)_\delta$; $<1\underline{1}0>_\gamma // [100]_\delta$. The lattice parameters of this orthorhombic δ are a=0.5141nm, b=0.4231nm and c=0.4534nm [15].

The time-temperature-precipitation curves of grain boundary δ-Ni_3Nb are shown in Fig.2.2 [18]. It should be noted that a lower solution temperature enhances Ni_3Nb precipitation upon direct ageing. The differences in the defect density and Nb supersaturation from one solution temperature to another may be responsible for delaying the growth of Ni_3Nb precipitates with increasing solutioning temperature during direct aging.

The δ phase is a very effective barrier to static recrystallization. It tends to precipitate heavily in worked grains at temperatures at or below 990°C and resist grain boundary migration even if it is in a spheroidal form [19]. When the temperature rises well above 990°C, δ particles go into solution and rapid grain growth occurs. Increasing δ Ni_3Nb plate size, associated with increasing grain size, decreases the stress-rupture ductility of Alloy 718.

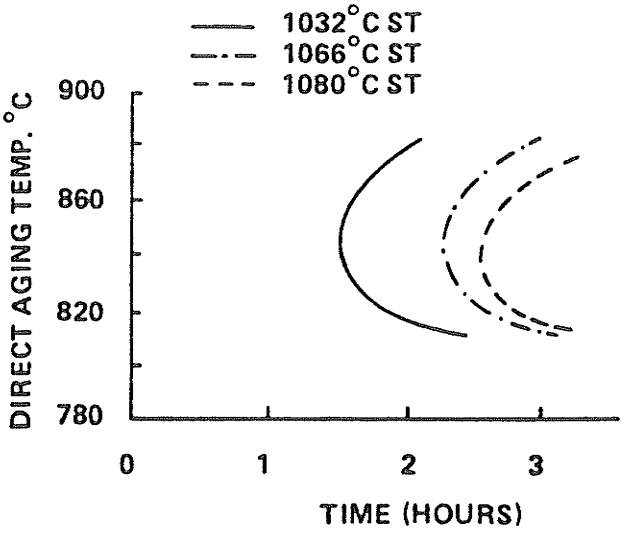

Fig.2.2 Inconel 718 grain boundary Ni_3Nb time-temperature-precipitation (TTP) curves for samples solution treated at 1032°C, 1066°C and 1080°C [18].

M_3B_2-type boride:

Interganular M_3B_2-type borides (6μm-9μm) have been observed in direct-aged wrought Alloy 718 [5]. The borides exhibit strong partitioning of both Nb and Mo, while Ti and Cr partition approximately equally between M_3B_2 and the matrix. Borides also contain Al, Fe, Ni, however, these elements are present in small concentrations relative to the γ matrix. Two types of M_3B_2 borides were reported in the weld and HAZ areas of wrought Alloy 718 [20], one rich in Mo and one without Mo.

M_6C carbides:

M_6C has been observed to precipitate on grain boundaries in hot rolled Alloy 718 bar and inhibit grain growth during solution treatment at 1010°C [21]. It has a FCC structure with a lattice parameter of about 1.1nm which is similar to that of $M_{23}C_6$. The M_6C carbides may appear as blocky particles or take the Widmanstatten morphology [22]. The M position in M_6C can be replaced by other elements as $(Ni,Co,Cr)_4(Mo,W)_2C$.

2.1.3 Strengthening Mechanisms in Superalloys

Alloy 718 is primarily strengthened by coherent ordered γ" through the following factors [25]:

1) Coherency strain

2) Existence of order in γ"

3) Differences in elastic moduli between γ" and matrix

4) Difference in Stacking Fault Energy (SFE) of particle and matrix

γ' also contributes to the strength of Alloy 718 by the factors 2 through 4 listed above [6]. The existence of alloying elements, such Mo and Nb, also provides additional strength to the alloy. The general strengthening mechanisms in superalloys hardened by γ" and/or γ' are summarized in the following table. The coherency and order strengthening mechanisms have been thoroughly examined [23, 24 and 25].

Table 2-5 Strengthening Mechanisms of Superalloys

	γ'(4%)+γ"(15%) (in 718) [11]	γ"(Co-Ni-Cr) [23]	γ'alloy [24]
underage	Coherent (γ"+γ')	Ordered and Coherent	Ordered
aged (peak)	Coherent (γ"+γ') and Coherent γ'+γ"		Ordered (principal) Ordered

2.1.4 Influence of alloying elements

Iron and Chromium

An increase in Fe content of Alloy 718 can improve the alloy's forgeability and lower the cost. However, the addition of Fe has to be controlled to maintain the stability of the austenite structure and the alloy's corrosion and oxidation resistance. Besides its solid-solution strengthening effect, Cr provides an additional benefit to nickel-iron alloys by improving oxidation and corrosion resistance.

Aluminum and Titanium

The presence of Al provides secondary precipitation hardening by forming γ' Ni_3Al and retards the formation of hexagonal η-Ni_3Ti phase. The addition of Ti forms γ'-$Ni_3(Al,Ti)$ and MC type carbides [25]. Increasing Al/Ti and Al+Ti/Nb ratios produces a finer γ" particle size with a more uniform distribution. A higher Ti/Al ratio with more Nb to

provide the same Al+Ti/Nb ratios has been reported to stabilize γ" and at the same time produce more γ' [26].

Niobium and Molybdenum

Historically, the addition of Nb has been used to improve cracking resistance during welding and subsequent heat treatment in the Ni and Ni-Fe alloys. The Nb and Mo are involved in the formation of γ", δ, carbides, carbo-nitrides and Laves phase. These phases can affect ductility and can be involved in heat affected-zone liquation in the base metal grain boundaries. The tendency to form Laves phase is reduced by increased Ni and reduced Fe contents. Nb and Mo also act as solid-solution strengthening elements in superalloys.

Sulphur, Phosphorous and Boron

S, P and B exert the same effect in superalloys as they do in other alloy systems. S and P can cause embrittlement of material by segregating to austenite grain boundaries or by forming low melting eutectics at the grain boundaries. Small additions of boron can improve hot ductility and rupture life [22]. S,P and B cause fusion zone cracking problems in weldments if present in sufficient amounts (i.e. S greater than 0.008wt%, P greater than 0.025wt%, and B greater than 0.010wt%). B causes increased weld HAZ cracking sensitivity if present much above 0.003wt%. The effect of these tramp elements on weldability of alloys is discussed in a separate section.

Carbon

C containing superalloys have superior creep properties due to the presence of a network of uniformly distributed discrete carbide particles along the grain boundaries which inhibits grain boundary sliding and migration [22]. As the carbon level in Alloy 718 is lowered, the amount of Ni_3Nb increases and NbC decreases [27]. Reducing the carbon content to or below 0.01% has no significant deleterious effect on any tensile properties at room temperature or at 649°C. It has been also reported that reduced carbon content had an adverse effect on stress rupture properties of Alloy 718 [28]. However, this adverse effect can be compensated by the addition of Mg.

Magnesium

Mg improves the stress rupture life by reacting with impurities such as O, N and S, and alleviating their harmful effects [25]. It also gives rise to finely dispersed intragranular particles of sulphide [22]. If present in excessive amounts (>0.030wt%), fusion-zone cracking may occur.

Si

Si has been identified to increase the alloy's sensitivity to weld fusion zone cracking. It also appears to control the kinetics of Laves phase formation in this alloy. Increasing the Si content results in a greater volume fraction and apparent increased stability of Laves phase in the microstructure.

2.2 WELDING AND WELDING DEFECTS

2.2.1 Fusion Welding and Electron Beam Welding

Fusion welding is a process where two edges or surfaces to be joined are heated to above the melting point, and if necessary, molten filler metal added to fill the joint gap. Fusion welding can be classified into different varieties; e.g., gas tungsten arc welding (GTAW), submerged arc welding (SAW), gas metal arc welding (GMAW), shielded metal arc welding (SMAW), resistance welding (RW) and electron beam (EB) welding.

Electron beam welding is a process wherein the fusion is produced by the heat obtained from a concentrated beam composed primarily of high velocity electrons impinging upon the surface to be joined [29]. Electron beam welding usually takes place in an evacuated chamber in which the beam is generated by thermionic emission and focused onto the work piece. Welding in a chamber imposes several limitations but provides one of the outstanding advantages of the process - the potential for a pure and inert environment in which the metal may be welded without atmospheric contamination. Another outstanding feature of EBW is its ability to make exceedingly narrow, deeply penetrating welds. The weld width, for example, in a butt joint weld in 0.5" thick plate may be as little as 0.06". This is attributed to the unique penetration mechanism of the electron beam. Conventional arc and gas heating sources melt little more than the surface, and further depth of penetration comes solely by conduction of heat in all directions from this molten surface spot. Hence, the fusion zone is at least as wide as it is deep. In addition to this, EBW also produces a narrow heat affected zone and smaller grain size both in fusion

zone and HAZ.

The heart of the EBW process is the electron gun where electrons are emitted from a cathode with speed and direction imparted to these electrons by their attraction to the anode. Usually the electrons are generated from a heated filament and a precisely shaped cathode surrounding the filament electrostatically shapes the electrons into a converging beam. The electron accelerating anode is incorporated into the electron gun as illustrated in Fig.2.3 [29], making the beam completely independent of the workpiece.

The converging beam of electrons, accelerated to speeds in the range of 48,000 to 190,000 kilometres per second, passes through a small hole in the centre of the anode and continues toward the workpiece. After the beam leaves the anode, the mutual repulsion of electrons causes the beam to diverge as it travels. To counteract this effect, an electromagnetic lens system is used to reconverge the beam and thereby control the size of the beam focal spot at the workpiece. The beam convergence and divergence are gradual, so the useable length of the beam (depth of focus) for most welding applications could be several centimetres.

Heat input for welding is controlled by four basic parameters, the number of electrons per second impinging on the workpiece (beam current), the speed of electrons (accelerating voltage), the diameter of the electron beam at the surface of or within the workpiece (beam spot size), and the speed with which the workpiece or electron gun is

being translated (welding speed). A fundamental characteristic of an electron beam which can help to define its welding capability is the electron beam's power density at the workpiece. This factor is dependent upon the basic gun parameters of beam power (current x voltage) and beam spot size. The energy input, a widely used expression, can be expressed as

$$Energy\ input = \frac{Joules}{inch} = \frac{60VI}{S} = \frac{60P}{S} \qquad <1>$$

where V is beam accelerating potential in volts, I is the beam current in amperes, P is the beam power in watts and S is the welding speed in inches per minute.

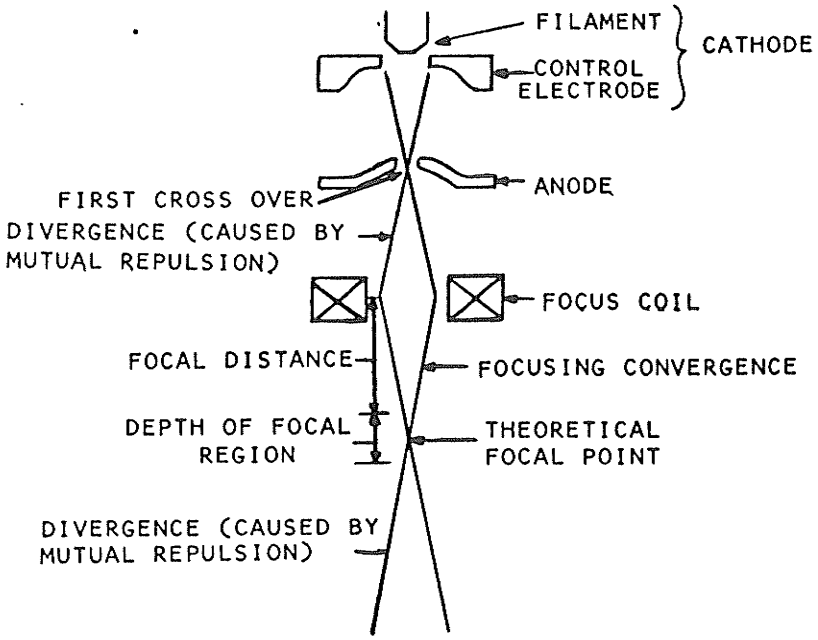

Fig.2.3 Structure of electron beam welder [29].

Changes in individual welding parameters will affect the penetration and bead geometry as follows:

1. Accelerating Potential- As the accelerating potential is increased, the penetration of the weld bead will also increase. For long gun-to-work distances, or when narrow parallel-sided welds are desired, the accelerating potential should be increased so as to attain maximum beam density

2. Beam Current - As the beam current is increased, penetration of the weld bead will also increase.

3. Weld Speed - As the weld speed is increased, the weld bead will become narrower and the penetration will start to decrease

4. Focus - Sharp focus will produce a narrow parallel-sided weld bead geometry, since the effective beam density is at its maximum. Defocusing the beam either by over-focusing or by underfocusing will increase the effective beam diameter thereby causing the beam density to be reduced, which, in turn, will produce a shallow or more V-shaped weld bead. Generally, EB welds in nickel-base alloys equal or exceed the strength of welds made by the GTAW process. With precipitation-hardenable alloys that are prone to fissuring or strain-age cracking, the EB process may result in more pronounced fissuring than would occur with GTAW or GMAW.

2.2.2 Welding Metallurgy and Welding Residual Stress

In fusion welding, the heat-affected zone is subject to a full weld thermal cycle and the solidified weld metal is exposed to the cooling part of the cycle. Heating and cooling

rates are usually high, and the heated metal is subject to plastic tensile/compression strain during cooling. Therefore, the metallurgical effects of the weld thermal cycle are complex and may in some instances result in an unfavourable change in the properties of the weldment.

2.2.2.1 Characteristics of Weld Solidification

Irrespective of the type of fusion welding process considered, the base metal is locally heated to its melting point and this has certain repercussions concerning the microstructural changes of the base metal at places nearest to the fusion line between the melted and unmelted metal. The microstructural changes include grain growth, precipitate dissolution and eutectic melting. An epitaxial solidification occurs which is a heterogeneous process and is illustrated in Fig.2.4 [30]. By this nucleation mechanism, a solid embryo of the weld metal forms at the melted-back surface of the base metal. The shape of the embryo depends on the various surface energies of the system, and the wetting angle φ is thus given by

$$\cos\varphi = \frac{\gamma_{ML} - \gamma_{SM}}{\gamma_{SL}} \qquad <2>$$

where γ_{ML} is the base metal liquid surface energy, γ_{SL} is the solidified weld metal-liquid surface energy and γ_{SM} is the surface energy between the solid weld metal and the base metal.

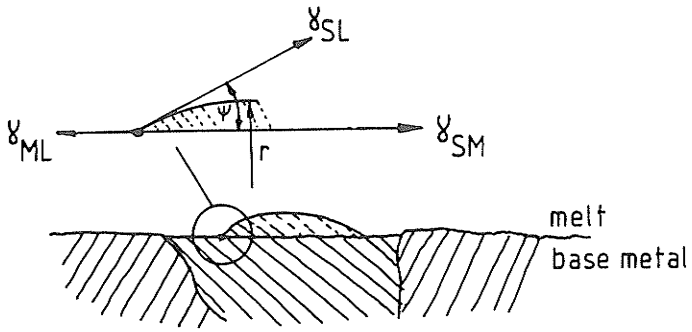

Fig.2.4 Heterogenous nucleation of a hemispherical cap of solid nucleus at the fusion boundary [30].

Since initial solidification of the weld metal occurs epitaxially and the weld metal is usually very similar in composition to the base metal, the following approximations are valid

$$\gamma_{SM} \approx 0, \quad \gamma_{ML} \approx \gamma_{SL} \qquad <3>$$

Therefore, the wetting angle φ is equal to zero. There is a negligible barrier to solidification of the weld metal (i.e. *no* undercooling of the melt is needed) and solidification occurs uniformly over the whole grain of the base metal.

Weld metal solidification and ingot casting are different from each other in total free energy of the solidification process as illustrated in Fig.2.5 [30]. As the weld metal continues to solidify the grains that have a $<100>$ axis (in FCC) approximately parallel to the steepest temperature gradient in the liquid quickly outgrow those grains with a less favourable orientation.

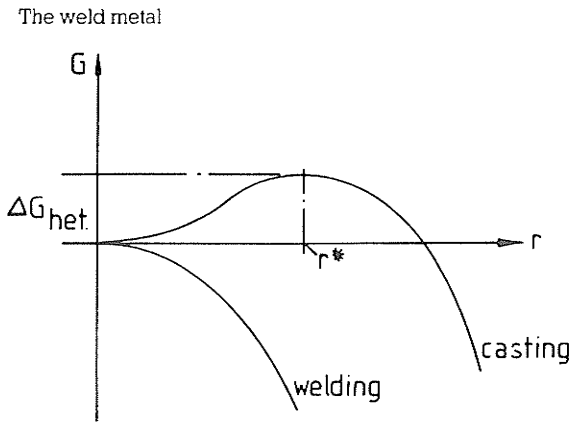

Fig.2.5 The different free energy driving forces for casting and welding solidification. Both are heterogeneous processes, but epitaxial solidification in welding reduces the nucleation barrier to virtually zero [30].

Consider the solidification of alloy X_o in the binary system shown in Fig.2.6 [30]. In the solidification processes, three limiting cases are generally considered:

1. Solidification occurs under complete equilibrium conditions

2. Solidification is not an equilibrium process and no diffusion occurs in the solid, but perfect mixing occurs in the liquid

3. Solidification is not an equilibrium process; no diffusion occurs in the solid and mixing in the liquid is not perfect but occurs by diffusional processes only.

The rapid rates of cooling of fusion welds imply that weld solidification cannot occur under equilibrium conditions so condition 1 can be ruled out. To begin, a good first

approximation is the assumption that negligible diffusion in the solid phase occurs. In the initial stages of solidification, good mixing of the liquid seems likely due to the turbulence of the melt. However, as the heat source moves away and solidification is completed it seems that convectional mixing gives way to diffusional mixing. On this basis it may be conjectured that weld solidification lies somewhere between situation 2 and 3, or more accurately, progressing from 2 to 3.

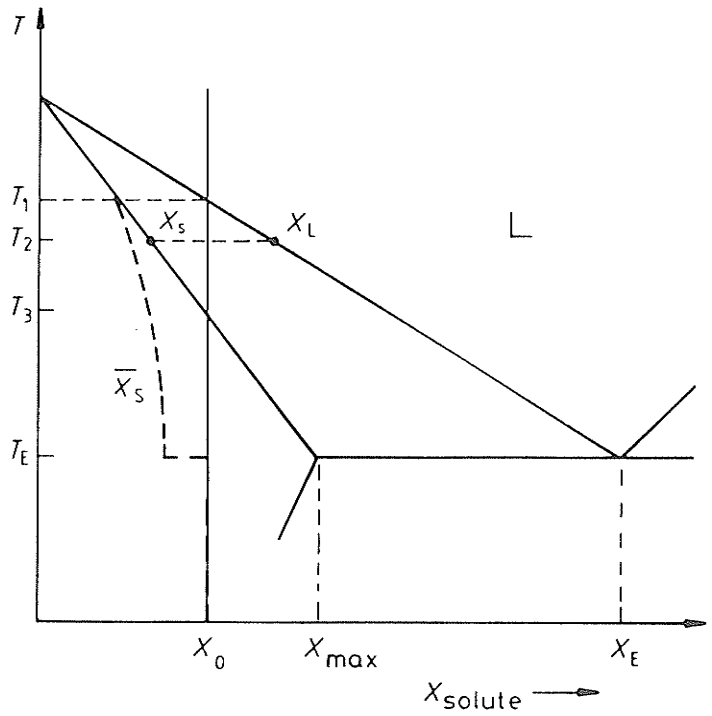

Fig.2.6 The non-equilibrium solidification of an alloy X_o in a sample binary system [30].

NO DIFFUSION IN SOLID: PERFECT MIXING IN LIQUID

Consider a cylindrical volume element of the growing crystal as shown in Fig.2.7 [30].

An alloy of composition X_o has a liquidus temperature of T_1 . Since solidification of the alloy occurs over a finite temperature range (T_1 to T_3), partitioning of solute elements has to take place. A partitioning coefficient, k, can be expressed as:

$$k=\frac{X_S}{X_L} \qquad <4>$$

where X_S and X_L are the mole fraction of solute in the solid and liquid which co-exist with one another at a given temperature. Assume that $k<1$, so the initial solid is purer than the liquid from which it forms. This implies that solute has to be rejected into the liquid, raising its concentration in the liquid to above X_o. As the solidification continues, the liquid becomes progressively richer in solute and solidification occurs at progressively lower temperatures. Since there is perfect mixing of the melt due to turbulence, 'local equilibrium' continues to exist at the solid-liquid interface. However, since there is no diffusion in the solid, the separate layers of solid retain their original compositions so that the mean composition of the solid is continuously lower than the solidus composition given by the phase diagram, i.e. the true solidus is defined by $\underline{X}_S$ in Fig.2.7. On the other hand, the liquid becomes progressively richer in solute and will attain the eutectic composition at the temperature T_E. The corresponding composition profiles for progressive volume element are shown in Fig.2.7b and Fig.2.7c.

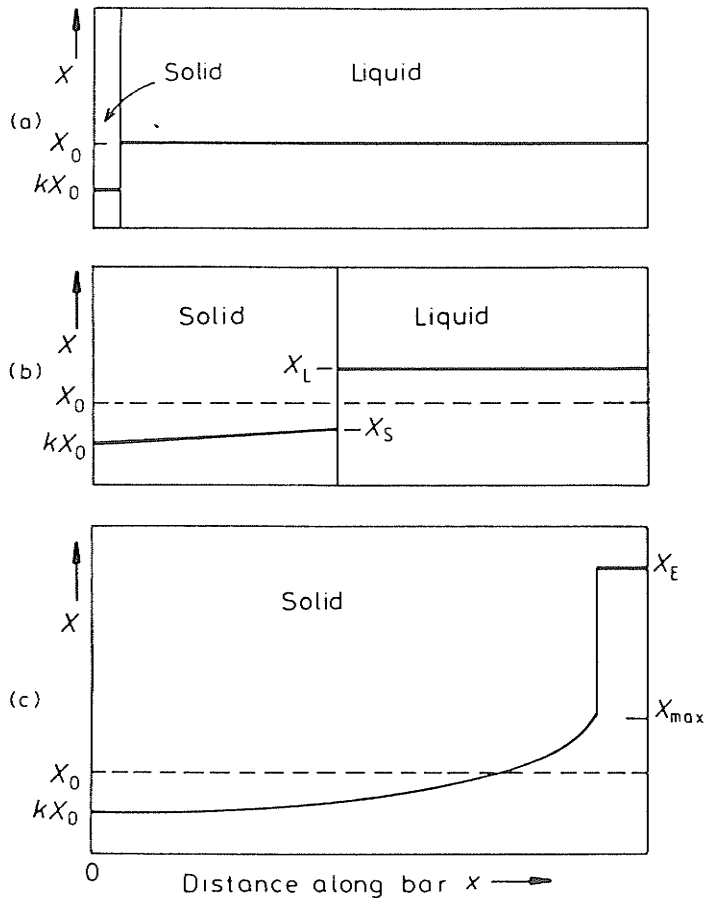

Fig.2.7 Composition profile in a solidifying cylindrical bar under the condition of perfect mixing in the liquid and no diffusion in the solid [30].

NO DIFFUSION IN SOLID: DIFFUSIONAL MIXING IN LIQUID

If there is no stirring or convection in the melt, the solute rejected into the liquid during solidification can only be transported away from the solid-liquid interface by diffusion. There will be a build up of solute ahead of the growing crystal, with a corresponding rapid increase in alloy content. During steady-state growth, the concentration profile in

the melt is such that the rate at which solute diffuses down the concentration gradient away from the interface is balanced by the rate at which solute is rejected from the solidifying liquid. The following equation describes this situation

$$-\frac{dX_L}{dx}D=R'(X_L-X_S) \qquad <5>$$

where D is the diffusivity of the solute in the melt, dx_L/dx refers to the concentration gradient into the liquid and R' is the growth speed of the crystal.

It should be noted that dissipation of latent heat of solidification need not be considered in this equation because the rate of heat conduction is several orders of magnitude faster than solute diffusion and it is therefore not significant in alloy solidification. The concentration profile of the liquid ahead of the interface shown in Fig.2.8 [30], is given by

$$X_L=X_o(1-\frac{1-k}{k}\exp[-\frac{x}{D/R'}]) \qquad <6>$$

This equation indicates that X_L increases exponentially from X_o/k at $\underline{x}=0$ (the interface) to X_o at some distance from the interface. The distance $\underline{x}$ describes the ratio of diffusivity to growth velocity

$$\underline{x}=\frac{D}{R'} \qquad <7>$$

Savage [31] has estimated $\underline{x}$ for various welding processes assuming an average solute diffusion coefficient of 5×10^{-5} cm^2/sec. The typical values of R' are given in Table 2-6.

The values of $\underline{x}$ are the predicted widths of the solute pile-up in front of the moving interface under steady-state solidification.

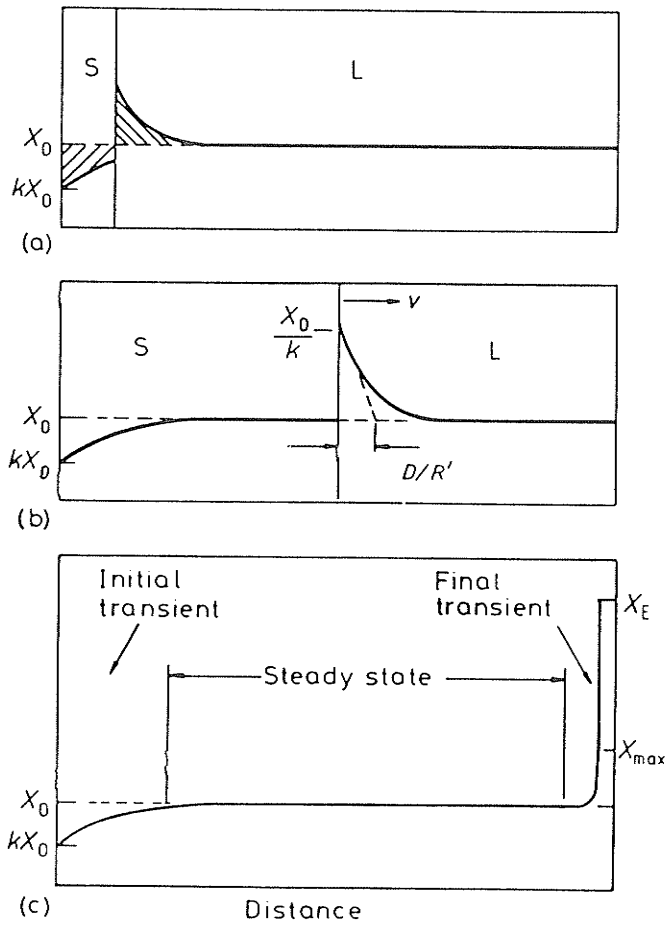

Fig.2.8 Composition profile of a solidifying bar when mixing in the liquid is controlled by diffusion [30].

Table 2-6 Extent of Diffusion Controlled Concentration Gradient in Welding Processes

Processes	R' (cm/sec)	$\underline{x}$ (cm)
Electroslag	10^{-3}	0.25
Manual Metal Arc	0.2	10^{-3}
Electron Beam	5	5×10^{-5}

In the final stages of solidification, the "bow-wave" of solute is compressed into a comparatively small volume of liquid and the solute composition is thus expected to rise rapidly. This suggests that the last stages of weld solidification are associated with the highest level of segregation, and that the segregation effect is likely to be greatest for those patterns of converging crystal growth that are typical of high-speed welding.

CELLULAR AND DENDRITIC SOLIDIFICATION IN WELDS

Consider steady-state solidification at a planar interface (Fig.2.9 [30]) in which both the concentration profile and the temperature gradient are a function of distance from the interface, x. Referring to the equilibrium diagram in Fig.2.7, if the solute concentration of the alloy increases, its solidification temperature, T_E, decreases, at least up to the eutectic composition. So the temperature gradient T_E in Fig.2.9 refers to the solidification temperatures corresponding to the enriched liquid ahead of the interface, X_L. However, the actual temperature gradient in the melt is determined by the position of the heat source relative to the interfaces and, as stated above, this varies as solidification

progresses to the weld centre line. A temperature gradient, T_L, is given in Fig.2.9 where T_L= Dt/dx in the liquid. If the temperature of the melt is below the solidification temperature of the enriched liquid, this part of the melt would be supercooled. In other words, this liquid (shaded region) remains liquid in spite of the fact that its temperature is below the equilibrium solidification temperature. Since supercooling arises from compositional or constitutional effects, this phenomenon is known as constitutional supercooling.

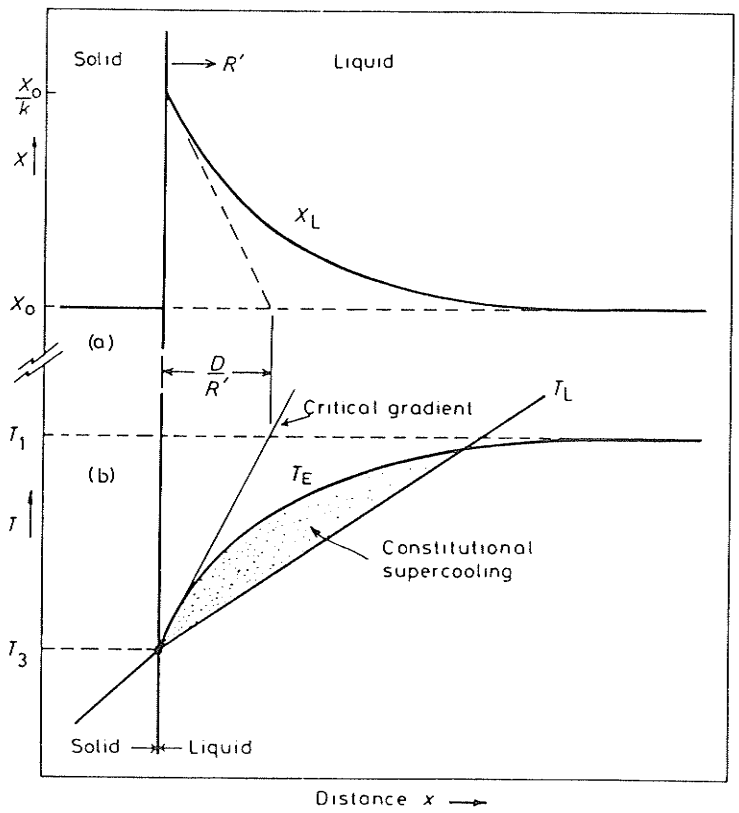

Fig.2.9 Constitutional Supercooling as a dependent of the temperature gradient in the melt, T_L [30].

Consider an initially planar interface growing under conditions of constitutional supercooling as in Fig.2.10 [30] where a small nodule has moved ahead of the interface. Despite the fact that the tip of the nodule is hotter than the planar interface, it may still be stable since its temperature remains below the liquidus temperature. Thus, only if the actual temperature in the liquid is higher than T_E will the nodule melt again.

Under steady-state growth, the critical growth is given by the ratio of the equilibrium solidification range of the alloy (T_1- T_3) and D/R', so that a stable planar interface can develop when

$$T_L > \frac{T_1 - T_3}{D/R'} \qquad <8>$$

The condition for constitutional supercooling to occur is given by Eq. <9>

$$\frac{T_L}{R'} < \frac{T_1 - T_3}{D} \qquad <9>$$

where R'=νcosΘ, ν=welding speed, and Θ=position of the interface relative to the heat source so that,

$$\frac{T_L}{\nu\cos\theta} < \frac{T_1 - T_3}{D} \qquad <10>$$

On the basis of this relationship, it can be stated that a planar front during solidification is difficult to maintain in alloys with a large solidification temperature range when welding speeds are high, or when the growth front tends to follow behind the heat source

(when $\Theta \to 0°$). Thus, in weld solidification, where T_L is initially high and Θ is relatively high, epitaxial growth from the base metal is likely to occur initially by the development of a planar growth front. As T_L and Θ decrease, constitutional supercooling is expected to occur resulting in a transition from planar to cellular growth. It was found that in most metals the cellular spacing (S) is related to the crystal growth rate, R', and the temperature gradient, T_L, as follows:

$$S=\frac{1}{R'T_L}, \quad S=\frac{1}{v\cos\theta T_L} \qquad <11>$$

Cell spacing affects the degree of segregation at the cell or dendritic boundaries, finer spacing giving less segregation. In determining the degree of segregation, the following are the important factors:

1. density and spacing of cell boundaries;
2. the segregation or partition coefficient, k, of the solute;
3. the total amount of solute present.

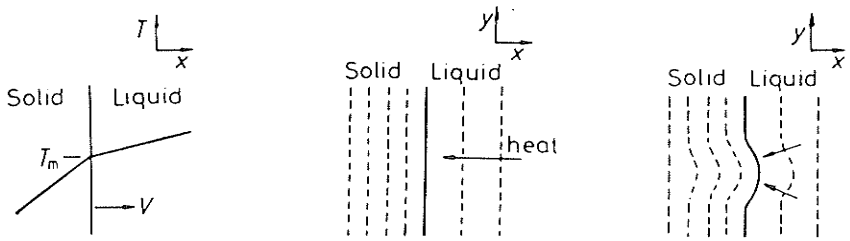

Fig.2.10 A solid protrusion that grows ahead of the planar interface when the liquid ahead of the interface is constitutionally supercooled [30].

Cellular microstructures are only stable for a certain range of T_L and Θ. As the temperature gradient or Θ reduces, the walls of the primary cells become unstable and develop secondary arms and at a later stage tertiary arms; i.e. a dendritic structure is developed as shown in Fig.2.11 [30]. It has been observed that dendrite arm spacings decrease with increasing cooling rate since higher cooling rates allow less time for lateral diffusion of the rejected solute and thus require smaller arm spacings to avoid constitutional supercooling.

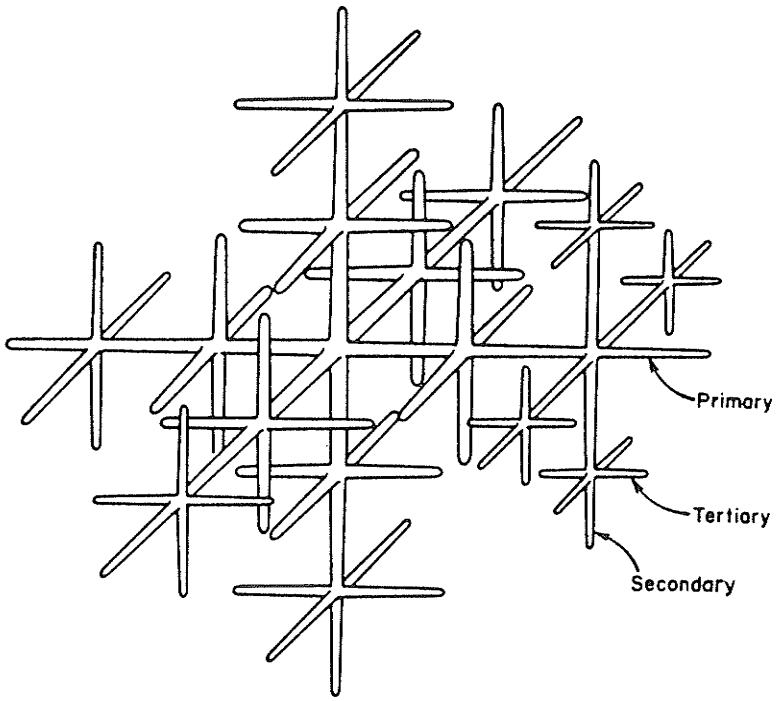

Fig.2.11 A fully developed dendrite. The primary, secondary and tertiary arms all correspond to <100> growth directions in cubic metals [30].

Various contributions of temperature gradient, alloying, crystal growth rate, etc. on the solidification microstructures developed in welds are illustrated schematically in Fig.2.12 [30].

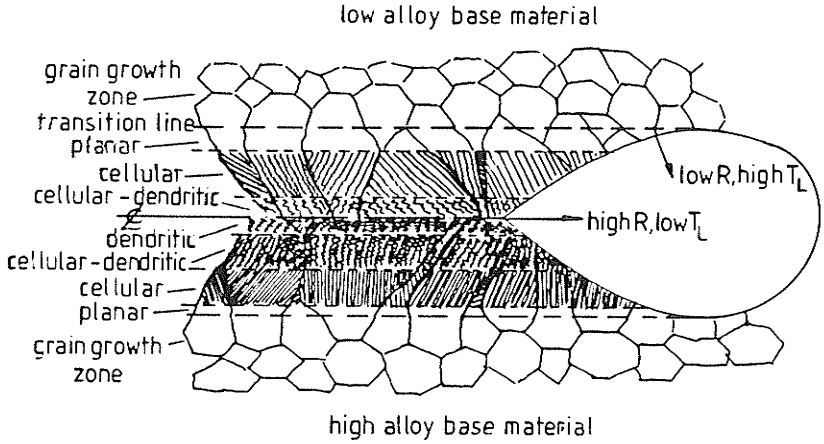

Fig.2.12 Schematic illustration of the various types of growth products developed during the solidification of weld metal as a function of alloy composition, crystal growth rate and temperature gradient in the melt [30].

2.2.2.2 Welding Residual Stress

Stresses and strains generated by changes in temperature during welding will be discussed in this section. Certain areas of material in the vicinity of the weld experience a different extent of expansion and contraction compared with other areas around it as seen in Fig.2.13 [30]. As the temperature increases, the initial expansion of the section is restrained by material further away from the heat source which generates compressive

stresses in the area as shown schematically in Fig.2.14 [30]. The corresponding stress-strain relationship is also shown in this figure. The elastic portion of the stress-strain curve is non-linear because the variation of Youngs modulus, E, with the temperature distribution. At some critical temperature (point 2), the flow stress in this area is exceeded and further heating results in a decline in stress as the metal becomes softer. The flow stress will continue to decline until it approaches zero/near the melting temperature where considerable plastic strain may occur. At the peak temperature reached by the section, the net strain is represented by the vector $1 \rightarrow 4$. On cooling, the reverse occurs; i.e. a tensile stress will be generated in the area adjacent to the fusion zone. Depending on the rigidity of the structure, the residual tensile stress may exceed the yield stress of the metal.

The main experimental techniques used to measure the residual stresses in welds are: 1) Mechanical, e.g., hole drilling,or saw cuts, 2) Moiré Pattern, 3) X-ray and 4) Ultrasonic.

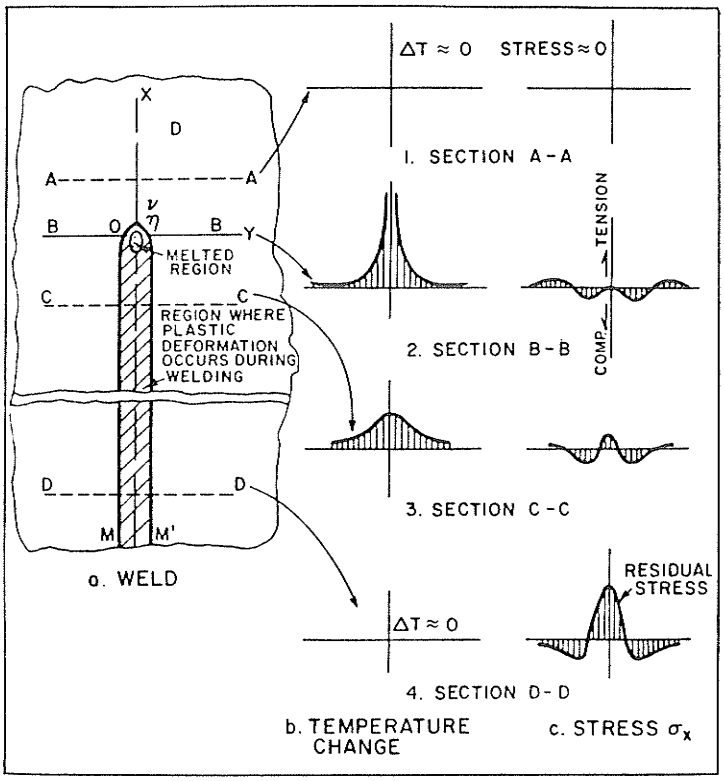

Fig.2.13 Schematic representation of changes of temperature and stresses during welding [30].

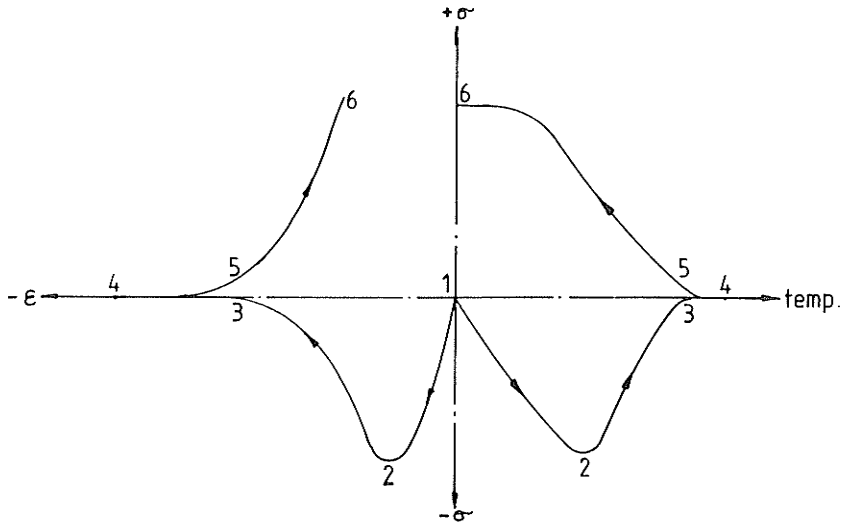

Fig.2.14 Schematic illustration of the variations in stress-temperature and stress-strain during a weld thermal cycle. Point 6 refers to the final residual stress and strain after the element has cooled to ambient temperature [30].

2.2.3 Welding Imperfections

Weld defects that occur during welding are generally categorized into:

1. solidification cracking (weld deposit).
2. liquation cracking, HAZ burning or hot tearing (fusion zone).
3. postweld heat treat cracking (weld deposit and HAZ).
4. cold cracking or hydrogen cracking (HAZ).
5. hydrogen attack (weld deposit).
6. gas porosity (weld deposit).
7. lamellar tearing (HAZ).

In the following sections, the first three types of defects will be discussed due to their relevance to this study.

2.2.3.1 Solidification Cracking

Solidification cracking may occur during cooling of the weld and these cracks occur predominantly at the weld centre line or between columnar grains. Cracking is typically observed to occur at temperatures about 200 $\sim$ 300°C below the solidus. The susceptibility of weld metal to solidification cracking appears to depend on three main factors:

1. the coarseness of the solidification microstructure;
2. the amount and species of segregation;
3. the geometry of the joint.

The type of solidification microstructure produced (equiaxed, cellular or dendritic) is controlled by welding process variables such as speed, amount of heat input, etc. Segregation cannot be avoided in solidification of an alloy weld. The amount of segregation depends on the partitioning coefficient, k. The value of k depends upon the alloying elements present in the material. Any alloying constituent which broadens the freezing temperature range of the alloy is likely to have a low value of k. Some approximate values of k for alloying elements in iron, are given in Table 2-7. According to this table, the elements most likely to segregate in steel are, in decreasing order, S, O, B, P, C, Ti, N and H.

Table 2-7 Partitioning Coefficients of Elements in Steel [30]

Element	Al	B	C	Cr	Cu	H	Mn	Ni	N
k	0.92	.05	.13	.95	.56	.32	.84	.80	.28
Element	O	P	Si	S	Ti	W	V	Co	Mo
k	.02	.13	.66	.02	.14	.95	.90	.90	.80

Slow solidifying welds with a coarse microstructure tend to promote centre line segregation resulting in hot cracking. The causes of solidification cracking are, in general, well understood. The partition and rejection of alloying elements at columnar grain boundaries and ahead of the advancing solid-liquid interface cause marked segregation. The segregants form low melting phases or eutectics with the metal to

produce highly wetting films at grain boundaries. These films weaken the structure to the extent that cracks form at the boundaries under the influence of the tensile residual stresses that occur during cooling.

Impurities or alloying elements most likely to cause solidification cracking have the following characteristics:

1. They have low partition coefficient, k.
2. They readily form secondary phase with the metal.
3. The secondary phases they form have low melting points or form eutectics with the base metal.
4. They cause a low wetting angle between the liquid and the solid metal and thus enable the liquid to spread along the grain boundaries.

The criterion as to whether cracks nucleate within the secondary phase or at the secondary phase-matrix interface is decided by their relative fracture strengths (unless the phase is still liquid). Assuming that brittle fracture occurs, the fracture strength of the secondary phase is given by

$$\sigma_f^c=(\frac{2E\gamma_c}{\pi c})^{1/2} \qquad <12>$$

where γ_c is the free surface energy of the secondary phase. The fracture strength of the secondary phase-matrix interface is given by Eq. <13>

$$\sigma_f^i = \frac{2\gamma_a}{\bar{b}} \qquad <13>$$

where b is the width of the crack at the interface and is approximately equal to one Burger's vector of matrix dislocations. γ_a is defined as the work of adhesion of the interface and is equal to

$$\gamma_a = \gamma_m + \gamma_c - \gamma_{c/m} \qquad <14>$$

where γ_m and $\gamma_{c/m}$ refer to the matrix and interfacial surface energies.

2.2.3.2 Liquation Cracking

The causes of liquation cracking are associated with grain boundary segregation aggravated by melting grain boundaries near the fusion line [30]. High residual stresses that occur as the weld cools tend to rupture these impurity-weakened boundaries. The origin of segregation in liquation cracking is quite different from that of solidification cracking. Melting of grain boundaries at the fusion line occurs at temperatures between the solidus and liquidus boundaries. Since melting nucleates preferentially at high energy crystal defects, such as surfaces and boundaries, there is a gradual increase in melted boundary width up to the melt zone. Impurities of low solubility in the matrix or from melted inclusions near the fusion line tend to diffuse to the melted boundaries.

Liquation cracking is dependent on the amount and type of impurities in the base metal, the volume fraction and density of inclusions, and the degree of restraint. The latter is

in turn dependent on the strength and thickness of the plates being welded. Another factor of importance concerns the dwell time at high temperatures. High energy welding processes thus increase the susceptibility to this problem.

2.2.3.3 Post Weld Heat Treatment Cracking

Several precipitation-hardened alloys suffer from severe heat affected-zone and weld metal cracking during post-weld heat treatment (PWHT). The cracks which occur during PWHT are intergranular and range in size from microscopic to several centimetres in length. Cracking has been found to occur only in restrained structures [32]. The cracks exhibit little plastic deformation and propagate very much like brittle intergranular cracks. The HAZ is known to be particular susceptible, although cracks may run far into the base metal. The phenomenon is commonly called 'strain-age cracking' (SAC), though there seems to be no clear evidence that this is associated with strain ageing. The failure mode in SAC is very similar to that in creep fracture and this has led investigators to conclude that these two phenomena are closely related. Therefore the SAC is considered to occur as a result of insufficient creep ductility. In the process of creep, the strain accommodation between grains, and particularly at grain corners, is normally accomplished by a combination of grain boundary sliding, vacancy diffusion and dislocation climb as shown in Fig.2.15 [30]. The total diffusional creep rate is given by:

$$\dot{\bar{\epsilon}} = \frac{2\sigma_a \Omega}{kTd^2} . D_m \left(1 + \frac{2\delta}{d} . \frac{D_b}{D_m}\right) \qquad <15>$$

where σ_a is the applied stress, Ω is the atomic volume, k is Boltzmann's constant, D_b and D_m are the grain boundary and volume diffusion coefficients, δ is the grain boundary width and d is the grain size.

Since the average applied stress, σ_a, is likely to be well below the strength of the hardened grains, it is assumed that creep deformation is mainly restricted to the grain boundaries. Experimental studies of the complete process of intergranular creep fracture have revealed three sequential but overlapping stages [33]:

1. nucleation of cavities on grain facets and triple junctions;
2. growth of these individual cavities to form cracks of one grain facet in length;
3. interlinkage of these single facet cracks to form cracks several grain diameters long which then rapidly lead to failure.

It has been concluded that the important factors that govern the PWHT cracking are:

1. The development of large grain size in the HAZ during welding tends to increase segregation, increase the likely number of ledges per grain boundary for cracking initiation, and reduce time-to fracture.

2. Reheating tends to encourage precipitation such as carbides in superalloys on grain boundaries leading to lower grain boundary strength.

3. The joint geometry and weld heat input determine the amount of relaxation strain

during reheating.

4. The presence of impurities on grain boundaries can reduce grain boundary cohesive strengths.

5. The presence of grain boundary particle, may be detrimental or beneficial depending upon such factors as their size, interfacial energy, etc.

6. γ' precipitation combined with denudation of grain boundary precipitation which reduces grain boundary strength.

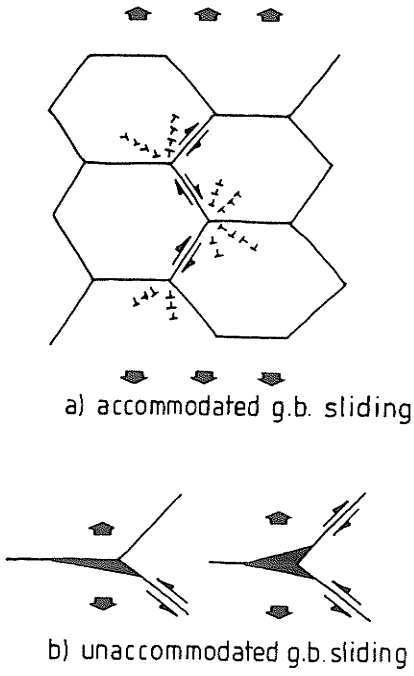

Fig.2.15 The accommodation of grain boundary sliding by vacancy diffusion along the grain boundary (a), cracks initiate when the grains are hardened and the accommodation is hindered (b) [30].

For materials that are susceptible to PWHT, the standard solution is to apply a stress relieving treatment to the welded components prior to the precipitation-hardening treatment. The temperature of stress relief varies with the alloy [34]. For every high hardening alloy, it is necessary to re-solution treat the material after welding. The condition of the material prior to welding also has an effect on the susceptibility of the material to post-weld heat treatment cracking.

2.2.4 Measurement of Cracking Sensitivity

The are numerous methods used to measure cracking sensitivities of different alloys and heats of the same alloy. These methods can be divided into five basic types [35]:

Production Welds: When components being welded have relatively little sensitivity, the most practical test is to do actual production welding. If welds crack, the component is then potentially scrapped.

Mockups: In many cases the critical features of an expensive component can be duplicated in a less expensive mockup. In this case the mockup can be used to develop welding parameters and can also be used to assess cracking sensitivity if it is made from the same heat of alloy as the production component.

Weld Restraint Cracking Tests: A large variety of weld-restraint cracking tests are available [36]. In general, these tests consist of a method of using a constraining structure that develops stress simulating the weldment. "Crack" or "no crack" is most often the criterion for evaluation.

Variable-Strain Weld Tests: There are several tests where the strain developed during

welding is completely controlled and varied in incremental amounts as required. The most notable of these tests is the Varestraint test developed by Savage and Lundin [37]. The test utilizes a plate-type specimen supported as cantilever beam. A bead-on-plate weld is made along the length, and as the arc passes a predetermined point, the plate is bent to conform to the curvature of the top surface of a removable die block. Blocks of different radii are used to develop different levels of augmented strain. Using this method, the augmented strain required to initiate cracking can be determined as well as the tendency for crack propagation to occur with increased strain.

Nonwelding Test: This is a technique to predict weld-cracking sensitivity or weldability that does not include an actual welding operation. The most usable and best explored method is the Gleeble test introduced by Nippes and Savage [38]. In this test, specimens are heated through simulated welding thermal cycles and tensile tested at various points within the thermal cycle. Strength and ductility results are used to infer weld-cracking behaviour. This method is also frequently used to examine the metallurgical changes in an alloy during thermal cycling, which is described in the next section.

2.2.5 Hot Ductility Test

As the material experiences a thermal cycle, its microstructure,and consequently the properties will be altered. The most effective way to study these is using the Gleeble test. The equipment consists of a time-temperature control device constructed to permit duplication of heating and cooling cycles experienced by regions adjacent to an arc weld. A 0.25 in-diameter specimen is held in the jaws of a high-speed tensile testing machine.

At selected points in the simulated weld thermal cycle, tensile tests are performed and the tensile strength and ductility of the alloy are measured as a function of test temperature. Typical hot ductility curves obtained on heating and on cooling are shown in Fig.2.16 [35]. The zero-ductility temperature is defined as that temperature on heating where the ductility drops to zero. Similarly, the zero-strength temperature is defined as that temperature on heating where the strength drops to zero.

HAZ cracks appear to occur during cooling, and fusion zone (FZ) cracking must occur during cooling because if cracks formed on heating, they would be healed by the molten metal. Due to these reasons, tensile testing is usually conducted on cooling.

Different criteria have been used by different investigators for interpreting hot ductility curves. These are:

1) minimum arbitrary ductility;
2) recovery rate of ductility, which represents the material's crack-resistance, i.e. the quicker the recovery, the more the alloy is resistant to cracking;
3) recovery rate of ultimate strength;
4) zero-ductility region (ZDR);
5) zero-ductility dip in middle-temperature range.

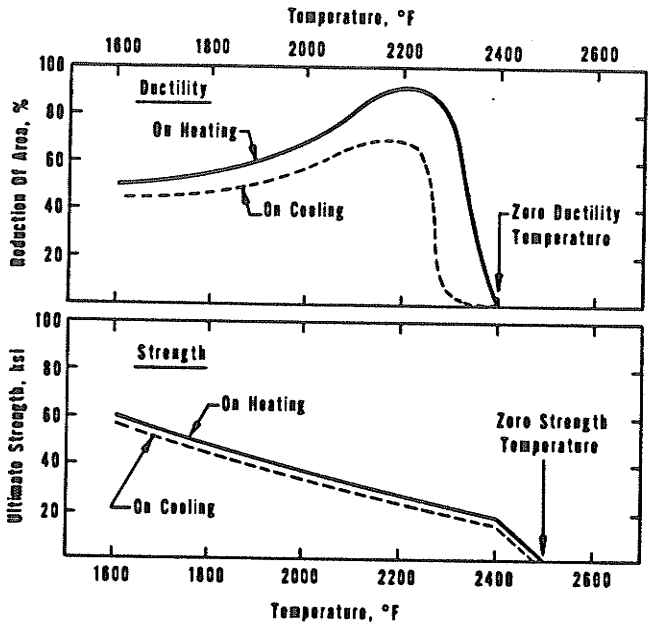

Fig. 2.16 Typical hot-ductility curves for Inconel 600 [35].

Testing parameters can have a significant effect on hot ductility response and thus on evaluation of cracking sensitivity. Variations in peak temperature, cooling rate and strain rate can be particularly important. The effect of peak temperature is illustrated in Fig.2.17 [35], where a three-dimensional representation is made of a weld heat affected zone in Hastelloy X. It is seen that the peak temperature depends on distance from the weld interface, decreasing as distance from the weld interface increases. For example, the point at 0.35 mm from the weld interface reaches a peak temperature of 1200°C and shows no loss in ductility on heating or cooling. The point at 0.25 mm from the weld interface reaches a peak temperature of 1230°C. At this point, ductility drops to zero but

reverses immediately upon cooling. At 0.15 mm from the weld interface when the peak temperature is 1260°C, ductility drops to zero on heating at 1230°C and does not return until a significant amount of cooling below 1260°C occurs. Closer to the weld interface, and consequently at higher peak temperature, the ZDR becomes larger and shows a zero-ductility plateau as illustrated. The peak temperature of testing consequently has a significant effect on the value of the ZDR. Larger ZDRs are obtained from higher peak temperature.

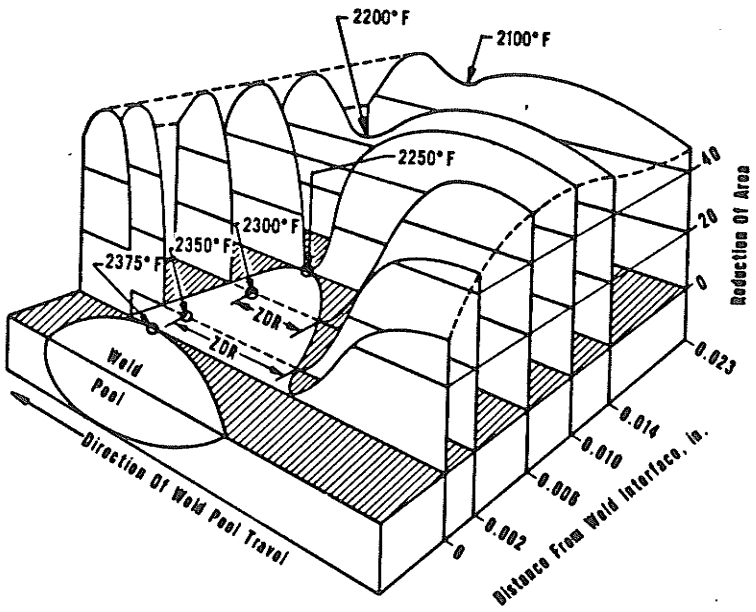

Fig.2.17 Three-dimensional representation of the effect of peak temperature on ductility response [35].

The Gleeble test can be also used to freeze the microstructure from various temperatures during heating or cooling cycles by simply quenching the specimens. The microstructure, including phase transformations, dissolution and the amount of liquid and its distribution can be examined by this method.

2.3 Mechanism(s) of HAZ Cracking and Microstructure of Weldment

2.3.1 Introduction

With alloys being pushed to their limit of strength and endurance, factors such as microcracking in weldments become more important. During welding, many of the grain boundaries in the HAZ rupture either during heating or cooling. Although alloy 718 was developed to be highly resistant to strain-age cracking during post weld heat treatment, it is susceptible to both liquation cracking in the weld HAZ [40,41] and, under conditions of high restraint, solidification cracking in the weld fusion zone [42]. HAZ liquation cracking results from the liquation induced by the thermal cycle and the inability of this liquid film to accommodate thermally-induced stresses during weld cooling. In the wrought alloy, the liquation is attributed to the constitutional liquation of MC carbides, while in cast alloy 718, this liquid film originates primarily from the constitutional liquation of a Nb-rich Laves phase in the interdendritic area [40,41]. Fusion zone solidification cracking occurs during the final stages of weld solidification due to the inability of the nearly-solidified weld metal to accommodate solidification shrinkage stresses [43]. In this section, the mechanism of HAZ cracking will be discussed in detail while FZ solidification cracking will be discussed only briefly.

2.3.2 Heat-Affected Zone Cracking - General

HAZ cracking susceptibility is a problem which plagues many of the highly alloyed nickel-base alloys. Fusion zone cracking is also encountered in these materials but is usually prevented by the selection of appropriate weld filler materials and by avoiding high constraint during welding. HAZ cracking is more insidious since the phenomenon is often related to the composition of the material and its microstructure, both of which have been optimized to achieve desirable base metal properties. Therefore, approaches which can be used to improve the weldability are limited. In general, the HAZ cracking is restricted to grain boundaries adjacent to the fusion line and appears to result from localized melting along these boundaries at temperatures slightly below the bulk solidus temperature.

Several mechanisms have been proposed to explain the HAZ hot cracking phenomenon. One mechanism involves the segregation of minor elements or impurities to the grain boundary leading to a localized composition with a lower melting point [44]. If the impurity is present in the matrix in supersaturated solution and sufficient time at the heat treatment temperature is given, it will segregate to the grain boundary. This segregation is driven by a chemical potential gradient toward the grain boundary. If there is insufficient time for the elements to diffuse to the boundary, a moving boundary may sweep up the impurity through a 'grain boundary sweeping' mechanism. Alternatively, a 'constitutional liquation' mechanism has also been advanced to explain HAZ cracking in several nickel-base alloys [45] and maraging steels [46]. Fundamentally, this involves

the melting of compounds in a region of the HAZ which is rapidly heated to near solidus temperatures. The rapid heating rates are such that complete dissolution of these compounds does not occur instantaneously above their solvus temperatures. The remaining compounds undergo a eutectic-type liquation reaction with the surrounding matrix at some higher critical temperature. This mechanism is discussed first in the following section.

2.3.3 Constitutional Liquation

The subject of heat-affected zone cracking in weldments has been investigated by many researchers. These investigations revealed that hot cracking is invariably associated with microsegregation that is generally present in the HAZ. The phenomenon termed "Constitutional Liquation", a mechanism that can adequately explain the observed microsegregation pattern in the weld HAZ, was first hypothesised by Savage [46,47] in 1959. In 1967, Pepe and Savage published their theory based on detailed experimentation on 18Ni maraging steel [46]. This theory has gained wide acceptance since then and has been used to develop a HAZ microfissuring mechanism. It was suggested that both mechanical and metallurgical factors must be present to cause hot cracking. During welding thermal cycle stresses are generated in the fusion zone and HAZ. The steep temperature gradients and rapid thermal cycles associated with the welding process make complex stress patterns unavoidable in these regions. Therefore, the prevention of hot cracking must be achieved by control of the contributing metallurgical factors. Since, as stated earlier, hot cracking is invariably associated with solute segregation in the weld

HAZ, the theory of constitutional liquation established the mechanism causing microsegregation. For simplicity, a hypothetical binary alloy system (Fig.2.18) is assumed for discussion purposes [46].

2.3.3.1 Equilibrium behaviour corresponding to an infinitely slow rate of heating

Fig.2.18 shows that at temperature T_1, the alloy with composition C_0 consists of a high melting intermetallic compound, A_xB_y, distributed as a secondary phase precipitate in the matrix α-phase. As the temperature increases at an infinitely slow rate, the solubility of B in the α-matrix increases until at temperature T_2 the last remaining A_xB_y should disappear converting the alloy to a homogeneous single phase solid solution of composition C_0. Continued heating at an infinitely slow rate from T_2 to just below T_5 would cause no further changes to occur other than those associated with normal grain growth and equilibrium grain-boundary segregation. At T_5, the solidus for the alloy, melting begins resulting in the formation of liquid of composition corresponding to point "C".

2.3.3.2 Nonequilibrium behaviour corresponding to an extremely rapid rate of heating

The disappearance of the second phase A_xB_y requires first the dissociation of the intermetallic compound A_xB_y, and subsequently the accommodation of the excess of atom "B" released as additional solute to the matrix. Since both steps are thermally activated

processes, the rate of disappearance of the second phase occurs at a finite rate which may be limited by either or both of the above steps in the overall process. Therefore, as the rate of heating is increased, a "critical heating rate" will be encountered above which the dissolution of the second phase A_xB_y will be incomplete during the interval required to raise the temperature to the solidus.

Assuming that the precipitates A_xB_y are spherical, Fig.2.19 shows the changes expected in the vicinity of the precipitate during heating to temperatures of T_3, T_e and T_4, respectively. During heating to temperature T_3, A_xB_y will begin to dissolve and shrink from its original size (represented by the dashed circle of Fig.2.19a to a smaller size (solid circle). The "B" atoms thus released should diffuse into the adjacent α-matrix. However, Fig.2.18 shows that the intermetallic compound A_xB_y must be in contact with α phase of composition "M" at the A_xB_y phase interface and decrease toward the original matrix composition (represented by point "O") at the interior of the α phase. The area of the double cross-hatched region of Fig.2.19a must be equal to the single-cross-hatched region if a material balance is to be maintained.

The slope of the concentration gradient produced in this way should depend upon the following factors:

1. The heating rate: the faster the heating rate, the steeper the gradient.
2. The diffusivity of solute: the slower the diffusivity of the solute atom, the steeper the gradient.

3. The relative ease with which the solute atoms are accommodated by each successive single phase region in the diffusion couple.

Fig.2.19 shows the additional changes which occur during heating from a temperature T_3 to the temperature T_e, the eutectic temperature. The dashed line represents the solute distribution present at temperature T_3 and the solid line represents the modified solute distribution at T_e. At T_e, the composition corresponding to point "e" permits formation of liquid at the interface of the intermetallic compound A_xB_y and the matrix. Further heating to T_4 would allow additional time for dissociation of A_xB_y and the expected distribution of solute atoms upon reaching temperature T_4 is shown in Fig.2.19c by a solid line.

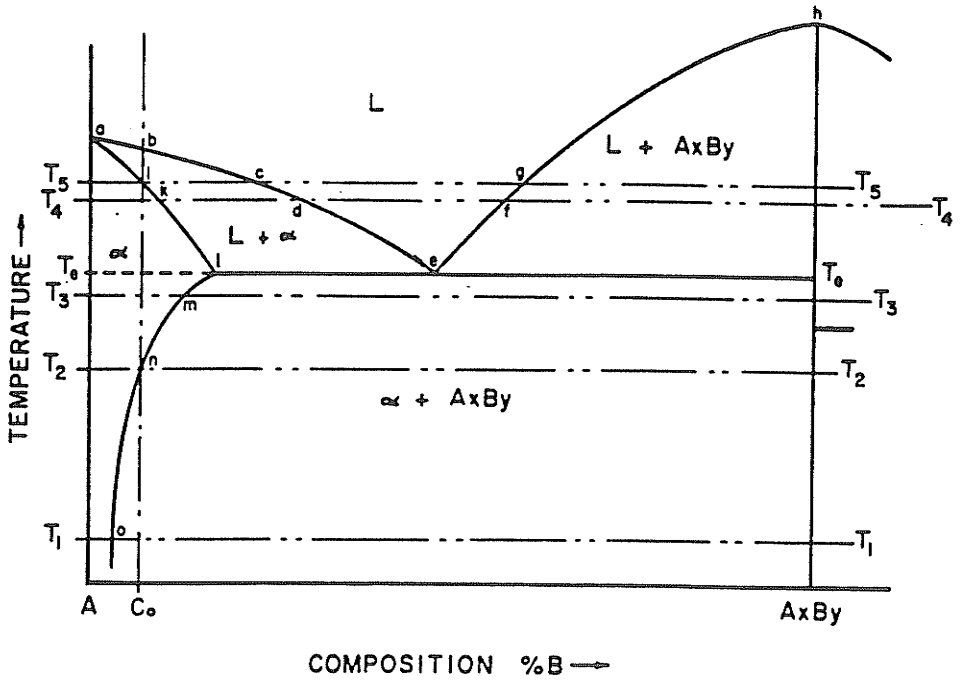

Fig.2.18 Schematic diagram of a portion of a hypothetical constitutional diagram for an alloy system exhibiting the behaviour necessary for constitutional liquation [46].

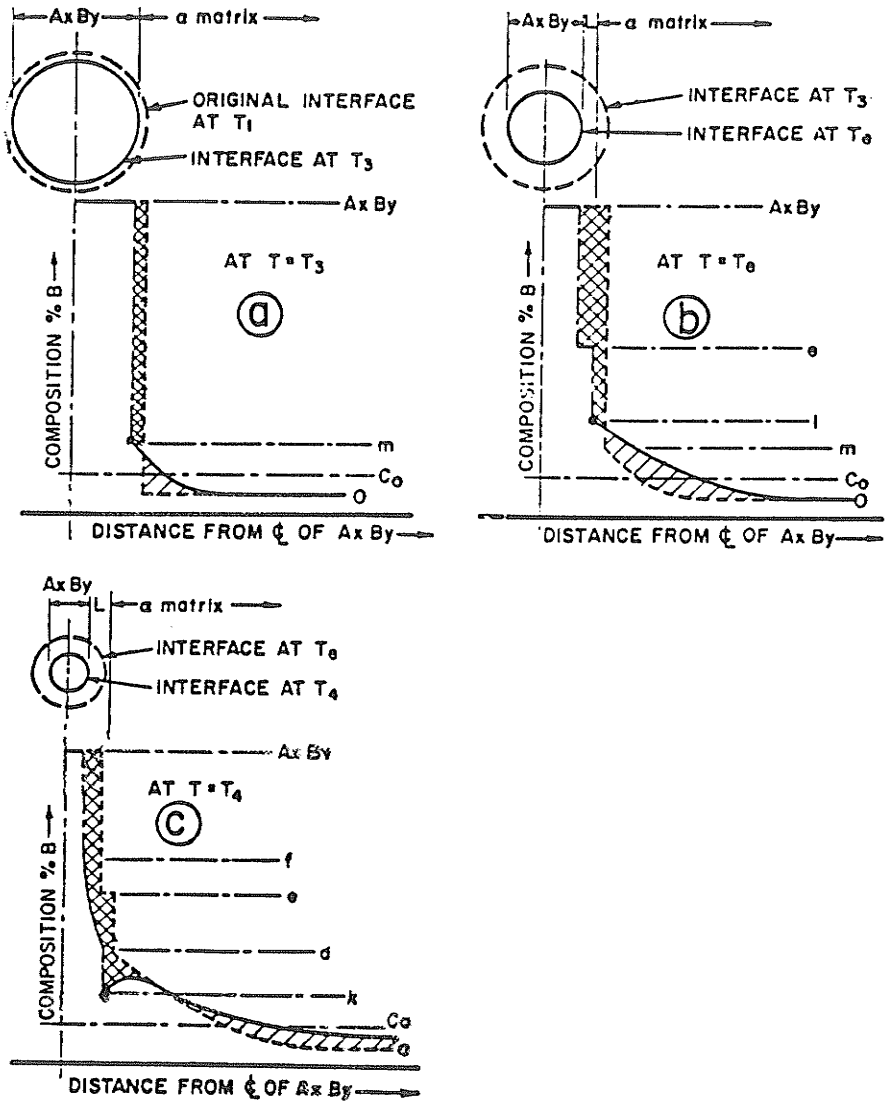

Fig.2.19 Schematic representation of the concentration gradients at various temperatures during formation of constitutional liquation.

It should be noted that each particle of A_xB_y remaining undissolved upon reaching T_4 under these conditions should be completely surrounded by a liquid film of variable composition ranging from "f" at the A_xB_y interface to "d" at the interface with the α-matrix. Thus, localized melting should be possible with rapid heating rates at temperatures significantly below the equilibrium solidus, T_5. This phenomenon, which in theory could occur at any temperature above T_e, is termed **constitutional liquation** as defined earlier.

Fig.2.20 [46] summarizes the changes in solute distribution that occur in a specimen which exhibits constitutional liquation if heated rapidly to T_4 and then held isothermally. Fig.2.20a represents the expected solute distribution after holding for a time t, just sufficient to complete the dissolution of the last remaining A_xB_y phase. Additional time at T_4 would permit further homogenization of the material. During the time interval t_1 to t_2, sufficient solute should have diffused into the α-matrix to decrease the width of the liquid phase to that shown by the solid line in Fig.2.20b. Eventually, nearly complete homogenization will occur, permitting the liquid phase to dissipate completely. Theoretically, an infinite time at temperature T_4 would produce a homogeneous structure of composition C_0. Fig.2.20c shows the concentration gradient that would probably be present at some time greater than that necessary to dissipate the liquid phase but less than that necessary to permit complete homogenization. Thus, according to theory, the liquid films produced by constitutional liquation should experience gradual modification in composition once the A_xB_y particles completely dissolve and should ultimately disappear

completely if the material is isothermally heated for a sufficiently long time at any temperature below the equilibrium solidus.

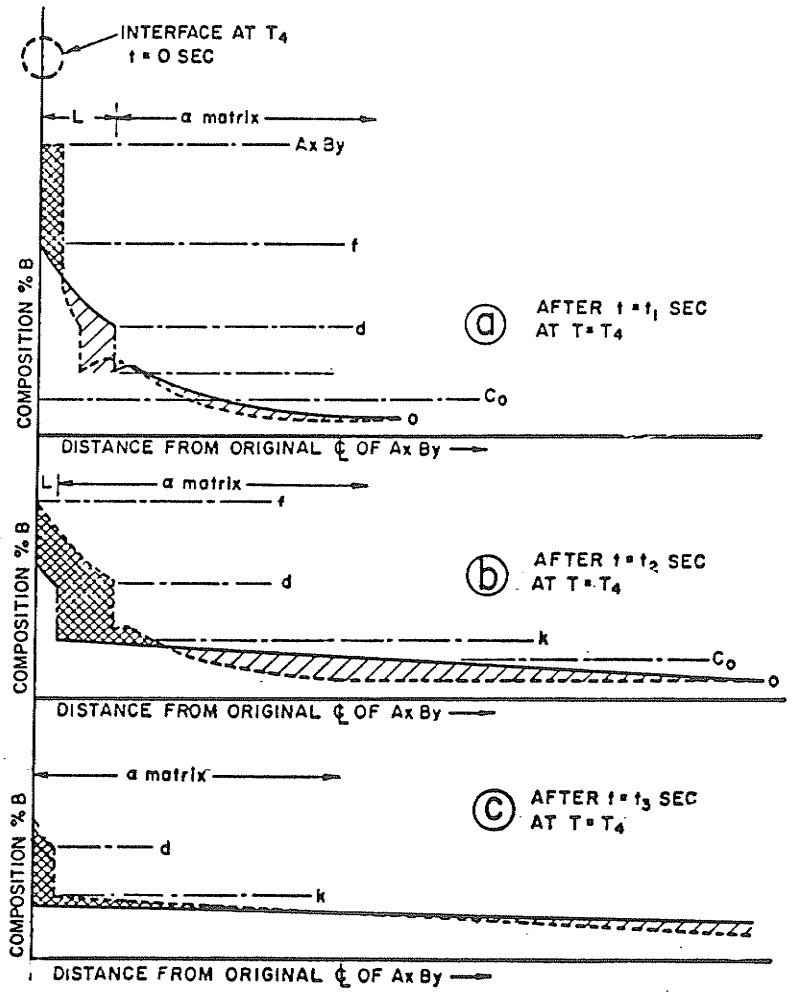

Fig.2.20 Schematic representation of the effect of holding a specimen exhibiting constitutional liquation at temperature below the equilibrium solidus [46].

In practice, the heating rates of welding processes range from approximately 200°C/sec for a typical fusion weld to over 55,000°C/sec for a resistance spot weld, and the average cooling rates range from 2-55°C/sec for a typical fusion weld to 17,000°C/sec for a spot weld. Therefore, when the above discussed models representing two extremes of cooling rate are applied to an actual situation, a certain discrepancy should be anticipated.

2.3.4 Generalized theory of super-solidus cracking in welds

In the early 1960's, Borland [43,48] proposed a theory to explain solidification liquation cracking which would prove useful to examine the HAZ cracking problem. He suggested that for cracking to occur it is not a sufficient condition that a wide freezing range exist. Not only should the alloy pass through a liquid-solid stage, but the liquid should also be present over a relatively wide temperature interval in a form that will allow high stress to be built up between grains. A liquid phase covering almost all of the grain faces during freezing will allow the development of high stresses on the narrow bridges joining adjacent grains whereas the liquid confined to grain edges and corners will prevent these high stresses from being built up.

The interphase and grain boundary energy is related to the dihedral angle θ by

$$\frac{\gamma_{SL}}{\gamma_{SS}} = \frac{1}{2\cos\frac{\theta}{2}} = \tau \qquad <16>$$

where γ_{SS} is the grain boundary energy, and γ_{SL} is the surface energy of liquid and solid. The ratio of γ_{SL}/γ_{SS} is of particular importance, and for convenience is designated as τ.

The dihedral angle is zero for $\tau=0.5$ and all the values below. The relationship between the dihedral angle and τ for $\tau \geq 0.5$ is shown below:

$\theta=0°$ $1/2\cos(\theta/2)=0.5$ liquid forms as film on G.B.

$\theta=60°$ $1/2\cos(\theta/2)=0.57$ liquid forms at grain edges

$\theta>90°$ $1/2\cos(\theta/2)=0.7>0.5$ liquid forms on grain corners

It has been suggested that in alloy systems where extensive solid solutions occur, when the liquid is of substantially similar composition to that of the previously frozen solid, 'wetting' of the grain faces and edges will be almost completed ($\tau \geq 0.5$) [43,48]. When τ is ≤ 0.5, the liquid is able to penetrate between existing grain boundaries and in doing so destroys the cohesion between adjacent grains. During the freezing process, τ increases and for most alloys reaches a value greater than 0.5 before solidification is complete. As τ increases above 0.5, the liquid progressively occupies less of the grain faces and at $\tau=0.57$ ($\theta=60°$) it can exist only as a continuous network along the grain edges. For $\tau \geq 0.57$, the liquid phase will collect at the grain corners and will extend less along the grain boundary edges as τ increases.

An increasing value of τ with cooling below the critical temperature competes with the increasing thermal strains and fissuring could be prevented only if the stresses imposed on the bridges between the growing dendrites do not exceed a critical value. The stress is a function of the grain boundary area that is joined and not separated by a liquid phase. The distribution and quantity of liquid is influenced by the grain size and shape,

and the effect of temperature (cooling rate) on the slope of liquidus and solidus curves. These slopes in turn determine the composition of the liquid in contact with the growing crystals and it is the composition of the liquid that largely determines the value of τ.

A liquid phase covering almost all the grain faces during freezing will allow the development of high stresses on the narrow bridges joining adjacent grains which could give rise to fissuring. Conversely, a liquid confined mainly to grain edges and corners will allow large areas of the grain faces to unite, thereby forming strong bonds which are able to withstand the weld cooling strains without cracking.

It is not certain if the factors affecting crack propagation are the same as those affecting crack initiation. It is possible that the extent of the Critical Solidification Range (C.S.R.) below the crack initiation temperature assumes a more important role in crack propagation than the dihedral angle.

2.3.5 Effect of Alloying Elements on the weldability

A great deal of research was carried out by Pease [49] in 1957 on the HAZ microfissuring problem in wrought nickel-base superalloys. Table 2-8, compiled by Pease, summarizes the effects of alloying and tramp elements on the weldability of nickel-base superalloys. It shows Nb to be beneficial to weldability (presumably because it does not cause strain age cracking). It also shows that boron (up to 300ppm) and other tramp elements such as sulphur are harmful.

Table 2-8 Effects of Alloying Elements on the Weldability[49]

Beneficial	No effect	Variable	Harmful
Nb	Mn	Al	Pb
Mg	Cu	Ti	S
	Cr	C	P
	Fe	Mo	Zr
	Co	Si	B

HAZ cracking susceptibility reportedly increases with the amount of eutectic present up to a point where the phenomenon of eutectic heating begins. Additions of C and Si were observed to increase the amount of eutectic-type constituent, melt/solidification temperature range and susceptibility to hot cracking (FZ cracking). Nb free alloys were observed by Cieslak to have a very low tendency toward solidification hot cracking [50]. Cieslak has also developed an empirical formula to estimate the mean crack length (MCL):

$$MCL(in) = 0.008 + 0.235(Cwt\%) + 0.013(Si) + 0.004(Nb) + 0.068(Nb)(C) + 0.011(Nb)(Si)$$

A systematic investigation was conducted by Kelly [51] on the effects of various elements on weldability of cast Alloy 718. The statistical results are shown in Table 2.9 and 2.10 [51].

Table 2.9 Heat Treatments Used on Alloy 718 Prior to Testing for Weldability [51]

Heat Treatment Code	Conditions (Temperature/Hold Time)
A. Short time Homogenization below Laves/γ eutectic temperature	1093°C/1hr
B. Medium time Homogenization below Laves/γ eutectic temperature	1093°C/10hrs
C. HIP around Laves/γ eutectic temperature + short time homogenization below Laves/eutectic temperature	1163°C HIP + 1093°C/1hr
D. Homogenization around Laves/γ eutectic temperature and slow heat to above the eutectic temperature	1163°C/1hr, ramp to 1177°C/3hr

Table 2.10 Effect of Elements on the Weldability of Cast Alloy 718 [51]

	C	Si	S	P	Cb	B	Fe	Mo	Hf	Zr	H.T.
Heat treatment A											
Total crack length				++[b]	--[a]	+2[d]		--			
Number of cracks											
Average crack length	--	--		++		+3[e]			++	+1[c]	
Heat treatment B											
Total crack length		--	-2	++	-1	+3	+3	--		++	
Number of cracks	++	--	--		-1	++	++				
Average crack length	-2		--			+3		+1	--	+1	
Heat treatment C											
Total crack length	--			++		+3	++	+1			
Number of cracks	++							+2		--	
Average crack length	-1	++		++	++		++	--	++		
Heat treatment D vs. heat treatment A											*[f]
Total crack length					++	++	++	--		-2	++
Number of cracks		-3		++						--	++
Average crack length				--	+2	+2	++	-2	++	+3	+3

(a) -- Low range reduces weldability
(b) ++ High range reduces weldability
(c) 1 = 90% confidence level
(d) 2 = 95% confidence level
(e) 3 = 99% confidence level
(f) * = Positive represents heat treatment D

Boron

It was found that boron has a statistically significant effect on the weldability of Alloy 718 as determined by the measurement of both total and average crack length. It appears that as long as Fe is present in the alloy B has a detrimental effect. The reason for this may be due to the fact that Fe promotes the formation of Laves phase. The presence of B should be more harmful in cast 718 than in wrought 718. The wrought form of alloy 718 can be thermomechanically homogenized to prevent any appreciable Laves phase formation in the HAZ of weldments, whereas such treatment is not viable in the cast alloy.

Silicon

Si showed a detrimental effect on weldability of cast Alloy 718 at low levels. The explanation given was at low Si levels, the carbide morphology changes from blocky to script which is more likely to be a site of fracture initiation. Therefore, the low Si level would cause more angular carbides and show reduced weldability. A high Si content did not appear to be harmful to weldability which was explained by the fact that a high Fe content of the alloy promotes the formation of Laves-phase with Si present. However, an increased HAZ cracking in wrought 718 that contains large amounts of both Si and Mn has been observed by other investigators [52].

Niobium:

Nb appears to have a positive effect on weldability when the alloy is heat treated to A and B, and a negative effect when treated according to C and D (as shown in Table 2.9 and 2.10). It was also found that the liquid Laves phase immediately wetted the grain boundary in the boron-containing heat, but melted in situ in the non-boron containing heat. Therefore, it would seem that B, by affecting the grain boundary wettability of Laves eutectic liquid that is always available, is the cause of the microcracking in cast Alloy 718 and not the Nb which only forms low melting phases that provide a liquid film for boron-affected grain boundaries.

Phosphorous:

The effect of P on weldability is less clearly understood in cast alloy 718 and further

investigations need to be carried out.

Carbon:

C shows no influence on weldability when its concentration is between 10 ppm and 0.1%. However, research work conducted by Thompson showed that increasing the carbon content from 0.02 to 0.06 wt% caused a modest increase in HAZ cracking [53,54].

Hafnium and Zirconium:

The effects of Hf and Zr are variable according to Kelly's investigations [51], but in general, it does seem to be necessary to add either element to Alloy 718 for improved weldability.

Molybdenum:

Mo reduces the weldability if present in high amounts after high temperature exposure, as opposed to the effect of Nb as reported in Table 2.9 and 2.10. As the Mo content of the alloy is increased, the Mo content in the Laves phase will increase due to partitioning of Mo and this would raise the Laves phase eutectic temperature.

Magnesium and Manganese

A reduction in microfissuring has been reported when the Mg, Mn and Si levels were kept above certain levels [55]. However, no explanation has been provided by the author.

Sulphur and Potency Factor:

Sulphur had long been suspected of contributing to HAZ cracking in nickel alloys [53,56]. Canonico [57] used Borland's relative potency factor [48] to show that, theoretically, sulphur should be much more potent than other elements in promoting HAZ microcracking. According to Canonico, the potency factor is given by:

$$Potency\ Factor=[M_L\frac{(1-K)}{K}] \qquad <17>$$

where M_L is liquidus slope in the phase diagram and K is the equilibrium distribution coefficient.

In carbon and alloy steel, the potency factor decreases in the following order: S→B→P→C→As→Nb→Sn→Zr→Ta. Quantitative values of potency factor for various tramp elements are also given in Table 2-11 [48].

Table 2-11 Potency Factors of Various Elements

Element	Relative Potency Factor
S	244,00
B	22,700
P	6,430
C	300

In Alloy 718 an increase in HAZ cracking was observed by Thompson [53,54] when the amount of S increased from 0.0008 to 0.009 wt%. S has been also found to be free of any detrimental effect within a lower limit beyond which weldability drops as the S content increases [51]. Since S is a surface active element, it is possible that a minimum amount is required to allow for proper coherency (wetting) of the matrix to carbides, nitrides, etc. However, above a certain S concentration value sulphide films begin to form and weldability will be reduced.

2.3.6 Effect of heat treatment on the weldability

The inherent microfissuring susceptibility of a metal has been shown to be a function of many metallurgical variables, including heat-to-heat chemistry difference, process condition (cast, wrought or forged), grain size and heat treatment. At present, no single mechanism or combination of mechanisms has been put forth to explain how these metallurgical variables interact and affect a material's microfissuring susceptibility. There is, however, a growing understanding of individual aspects of the microfissuring mechanism. This section will focus on the effect of heat treatment.

It has been generally observed in various nickel base alloys, both in wrought and cast conditions, that solution annealing reduces microfissuring susceptibility [52,58-62] while age hardening increases it and the cracking susceptibility becomes more sensitive as the solution temperature prior to ageing is increased. In cast Alloy 718, the effect of heat treatment on HAZ microfissuring (evaluated by total crack length) is summarized in

Table 2-12 [53]. The effect of heat treatment on the formation of secondary phases has been examined, since it has a direct effect on the HAZ, and is shown in Table 2-13 [54,63].

It has been found that in cast Alloy 718 the volume fraction of liquating phases (NbC and Laves) and the resultant volume fraction of liquid have direct consequences on the magnitude of HAZ liquation cracking if the process history and chemistry are the same except for the minor elements [54]. Numerous theories have been proposed to explain these phenomena and are summarized accordingly in the following sections.

Table 2-12 Effect of Heat Treatment on Total Crack Length

Heat Treatment Condition	TCL (mm)
As Cast	20
As Cast + 1700°F/1hr	15
As Cast + 2000°F/1hr + 1700°F/1hr	19.5
As Cast + 2000°F/1hr	21.5
As Cast + 1200°F/1hr	24
As Cast + 2000°F/1hr + 1200°F/1hr	25.5

Table 2-13 Effect of Heat Treatment on

Amount of Secondary Phases in Cast 718 (Vol.%)

Heat treatment	Carbides	Laves	Carbide+Laves
As-cast	0.55±0.20	1.56±0.318	1.91
1093°C/1h+650°C/1h	0.40±0.21	0.54±0.18	0.74
1093°C/1h+927°C/1h	0.38±0.13	0.51±0.23	0.89

2.3.6.1 Effect of Solution Treatment

It was suggested by Vincent [61] that in wrought Alloy 718 δ-Ni_3Nb precipitation during solution heat treatment increased microfissuring resistance. Duvall and Owczarski [60] found that microfissuring was initiated by the constitutional liquation of Nb-rich M(C,N) particles in wrought Alloy 718. Intergranular liquid produced by this reaction was found in both the solution annealed and age hardened conditions.

Extensive studies on wrought Alloy 718 by Thompson et al [62] showed that a larger reduction in microfissuring after the solution treatment was observed in a larger grain size material that had received a longer homogenization treatment than that observed in smaller grain size material. He suggested that the change in microfissuring susceptibility during solution annealing was not due to the δ-Ni_3Nb precipitation process. But no reasonable explanation was given for this phenomenon. The investigation of grain boundary chemistry in Alloy 718 in the solution treated condition showed that they were

not enriched in solute atoms by the solution treatment [64].

2.3.6.2 Effect of ageing

The relationship between hardness and microfissuring of specimens aged for various lengths of time is shown in Fig.2.21 [62]. The increase in microfissuring occurred prior to appreciable hardening. Furthermore, the hardness continued to increase while the microfissuring showed no change. Based on this observation, Thompson [62] concluded that neither matrix hardness nor $\gamma'+\gamma''$ precipitation influences the change in microfissuring due to age hardening. The dissolution of NbC and Laves phase and subsequent Nb and C segregation during the 650°C heat treatment was related to the observed increase in TCL after ageing [53]. Significant Nb and C segregation was found to occur at 650°C as revealed by Auger spectroscopy.

2.3.6.3 Effect of homogenization heat treatment

It has been shown that the lower temperature homogenization at 1093°C as compared to that at 1163°C results in improved weldability. Kelly [51] suggested the temperature of 1163°C is at or above the Laves-phase liquation temperature and Laves phase may liquate during heat treatment and therefore wet the grain boundaries. However, no evidence was given. The increasing microfissuring after 1163°C heat treatment was attributed to sulphur segregation which was observed to be present as a monolayer by Auger spectroscopy analysis [53].

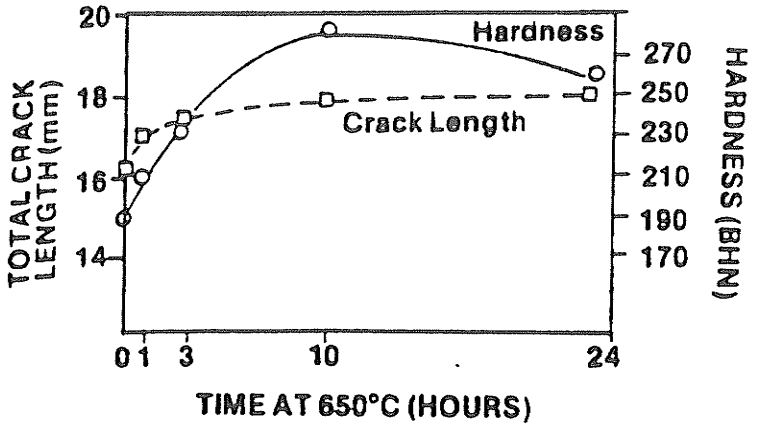

Fig.2.21 A comparison of the change in the microfissuring susceptibility with the change in hardness during age hardening [62].

Valdez and Steinman [65] found that in wrought Alloy 718 liquation cracking increased after heat treatment at 1066°C and the grain boundaries of the material were denuded of γ'' after subsequent ageing treatments suggesting that precipitation and/or segregation could occur on grain boundaries during high temperature solutioning.

2.3.6.4 Effect of Elemental Segregation at Grain Boundary

Other metallurgical changes caused by heat treatment besides phase changes are grain growth, atomic diffusion and elemental segregation. The sulphur segregation data for a number of binary nickel alloys [67] correlated with the microfissuring behaviour after various heat treatments is given in Fig.2.22 [62]. This suggests that heat treatment alters the intergranular chemistry by elemental segregation in such a way that microfissuring susceptibility can either be increased or reduced.

2.3.6.5 Gleeble Studies

The Gleeble technique has been used to simulate the welding cycle under controlled heating and cooling rates and weldability can be compared without using an actual welding process. As stated earlier, specimens can be quenched from various temperatures to freeze the microstructures for examination at room temperature. Gleeble analysis of a wrought Alloy 718 sample heat treated for 1 hour at 1093°C plus 1 hour at 650°C showed grain boundary liquid that had persistent wettability over a wide temperature range. The liquid film in a sample heat treated for 1 hour at 1093°C plus 1 hour at 927°C tended to unwet and form noncontinuous puddles upon cooling through the same temperature range. The 1093°C+650°C sample had an intergranular liquid that remained wetted to the grain boundaries at lower temperatures than the 1093°C+927°C sample. This observation suggests that prior heat treatment has an effect on the extent of hot cracking by changing the intergranular liquid distribution [63].

Another investigation on wrought Alloy 718 revealed that the presence of δ-Ni_3Nb in the initial microstructure resulted in a delayed grain boundary liquation and instantaneous grain boundary liquation in its absence [68] when Gleeble tests were done in the same temperature range (1200°C and 1215°C). In the solution treated wrought Alloy 718, the delay in carbide liquation may be due to Nb enrichment in the vicinity of the carbides following the dissolution of δ-Ni_3Nb which can potentially delay the onset of carbide dissolution. The delayed grain boundary liquation could also be explained on the basis of constitutional liquation of NbC particles if such particles were assumed to precipitate

during heating from the Nb-rich areas produced by δ dissolution. The instantaneous liquation of grain boundaries in the homogenized and aged conditions was related to both constitutional liquation and solute segregation. The segregation processes could include both equilibrium segregation of Nb during the homogenization step and non-equilibrium segregation of Nb by the dissolution of carbides along the grain boundaries during the heating cycle.

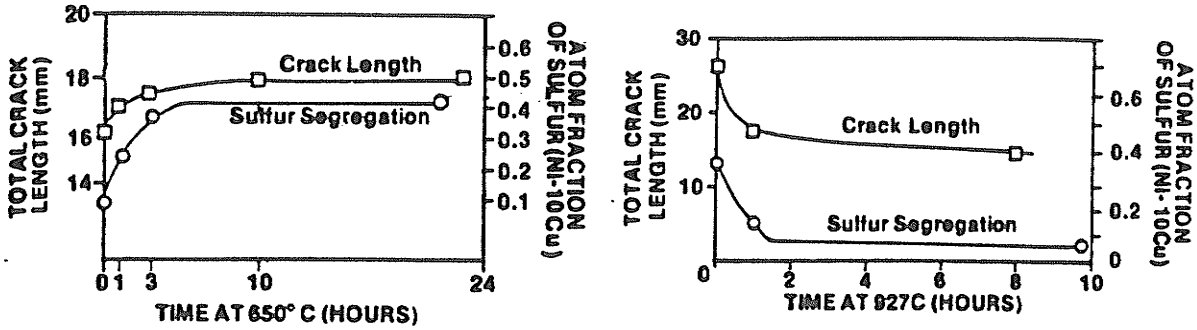

Fig.2.22 Correlation between the change in the microfissuring susceptibility and the rate of grain boundary sulphur segregation during age hardening. (a) for grain size 60 μm at temperature 655°C and (b) for grain size 200 μm at temperature 927°C [62].

2.3.7 Effect of Grain Size on Weldability

The first work reporting on the effect of grain size was carried out by Morrison et al [69]. They observed that when the grain size was larger than ASTM#2 specimens with larger grain size showed a greater tendency to microfissure than those with smaller grain sizes. However, they did not find any correlation between grain size variance and microfissuring when the grain size was less than ASTM#2. Extensive and systematic work has been conducted by Thompson [70]. He used a heat treatment at 1165°C for

various times to achieve different grain sizes in wrought Alloy 718 without causing a dissolution of the carbides or minimizing the intergranular segregation. An argon or water quench was used after the heat treatment. It was found that the relationship between HAZ grain size and microfissuring is linear; i.e. a 0.4% increase in microfissuring per micron increase in grain size.

The effect of grain size on microfissuring could be related to both the liquid distribution and grain boundary sliding. A large grain size would lead to a thicker liquid layer than a small grain size if the same volume of liquid is present in both cases. A large volume fraction of intergranular liquid could increase the range of temperature and the duration of time during which liquid wets the grain boundary faces under nonequilibrium freezing conditions. This would lead to increased microfissuring susceptibility. A large grain size would also cause a longer interface sliding length which would lead to a larger stress concentration, larger strains at grain boundary triple points, and increased crack initiation due to grain boundary sliding. Thus, a large grain size would be detrimental to the material's weldability.

A study by Williams and Singer [71] on Cu/Sn alloy considered the effect of grain boundary sliding on cracking in the presence of an intergranular liquid. They hypothesized that grain boundary sliding produces stress concentrations that aided crack propagation and that grain boundary sliding and the associated stress concentration is maximum on the maximum shear axis. They also suggested that grain boundary sliding

is a primary deformation mode when intergranular liquid is present. Work has also been reported that shows grain boundary sliding would be an effective mechanism for initiation of microfissures at grain boundary triple points [72]. Once these microfissures initiate, they could easily propagate through the intergranular liquid. No difference in the weldability of various grain size specimens (ASTM0-6) of cast alloy Rene 220C containing 60-100 ppm boron was detected by the spot varestraint test [66].

2.3.8 Effect of Welding Parameters on the HAZ Cracking

Few references exist in the literature on the effect of welding parameters on the weldability of cast alloys. Recent research by Richards et al [74] using bead on plate EB welding showed that travel speed was the most significant factor in influencing HAZ cracking behaviour by modifying the thermal gradient(s) and subsequently the state of stress in the HAZ. Twenty four welding trials were conducted by varying travel speed, voltage, current and working distance. The cracking tendency was evaluated by a cracking index (C.I.), which is given by:

$$C.I. = \frac{\sum (l_1 + l_2 + l_3 + etc.)}{area\ of\ HAZ} \qquad <18>$$

where L_1, L_2 and L_3 are individual micro-crack lengths. The C.I. then gave an assessment of the length of crack per unit area, which is a standard quantitative metallographic parameter. The cracking index C.I. was analyzed using step-wide multiple regression of the welding parameters resulting in the following equation:

$$C.I. = A \pm f_1 x_1 \pm f_2 x_2 \pm f_3 x_3 \pm etc. \qquad <19>$$

where A is a constant, f_1, f_2, and f_3 are numerical values and x_1, x_2, and x_3 are welding parameters.

The statistical analysis gave the following equation at 95% confidence level, with correlation coefficient of 0.42 and F value equal to 5.98:

C.I. = 0.095 + 0.0068 speed

The only parameter correlating with cracking index at the 95% confidence level was speed; i.e. reducing speed from 152cm/min to 51 cm/min would reduce the cracking index by 0.68 cm/cm_2.

Similar research has been carried out on wrought Incoloy 903 and the following equation has been developed [75]:

$$C.I. = 0.000394Sp - 0.0034mA - 0.0027kV + 0.013(P/W_{mid}) + 0.00016WD \qquad <20>$$

Confidence levels in this equation were as follows: for welding speed (Sp, mm/min) and welding current (Ma), greater than 99%, for depth of penetration/middle weld width (P/W_{wid}), 93%, for voltage (kV), 91%, and for working distance (WD, mm), 86%.

The form of both equations thus show a trend that cracking can be reduced over the range of beam parameters studied by reducing travel speed and increasing current and voltage (in the case of the wrought alloy). For a given heat input level this would

necessitate reducing the accelerating voltage since

$$Heat\ Input = \frac{Voltage\ x\ Current\ x\ 60}{speed} \qquad <21>$$

The low correlation of cracking index with the welding parameters in cast Alloy 718 relative to wrought Incoloy 903 is attributed to the inhomogeneity of the cast microstructure [74]. However, the general trend is that reducing speed and increasing current (wrought alloy) leads to reduced cracking for a given heat of alloy. Welding at reduced travel speeds and higher current has been shown to reduce thermal gradients in plasma arc welding. Higher temperature gradients will occur at higher speeds leading to an increased likelihood of cracking due to greater temperature differentials and higher stresses within the weld areas. Boucher and co-workers [76] have related the cracking behaviour to the maximum width to weld height ratio (L/H) measured on transverse sections. Total crack length was found to increase as L/H increased with cracking being eliminated at $L/H > 1.6$. Higher welding speeds were found to influence the cracking behaviour by decreasing L/H ratio ($L/H < 1.6$ promotes cracking). Thus, by affecting the weld morphology, through thickness stresses are increased which result in an increased likelihood of cracking.

2.3.9 Microstructure of Alloy 718 Weldment

2.3.9.2 Fusion Zone

The fusion zone microstructure of Alloy 718 has not been studied extensively and will be described in the discussion part of this dissertation, incorporating the results of this study.

2.3.9.3 HAZ

Fine Ni_3Nb precipitates that were originally present in the heat treated matrix were observed to redissolve during the weld thermal cycle [78]. Complete liquation of the original Laves phase and additional melting into the surrounding matrix was seen to occur in HAZ [77]. This Nb-rich liquid solidified initially as γ and finally as a eutectic comprised of Laves phase and γ. Nb-rich carbides were also observed in the resolidified region. Based on the coarseness of these particles, it has been suggested that they were matrix carbides which did not completely decompose in the liquid rather than being the products of resolidification [79].

2.3.9.4 Back Filling

A partial healing of HAZ cracking by the flow of liquid metal from the weld pool into the newly formed crack has been observed [80]. The pre-requisites for backfilling of cracks include:

(1) As the crack forms and propagates, it must maintain an interface with the molten weld pool long enough for backfilling to occur.

(2) The crack surfaces must remain uncontaminated by oxides or other compounds for the liquid metal to wet the newly formed surfaces and be drawn into the crack by capillary action.

(3) The viscosity of the liquid metal at the interface between the weld pool and the crack must be low enough to permit capillary action to backfill the crack.

(4) The effective solidification temperature of the liquid metal involved in backfilling must be less than the instantaneous temperature at the interface between the crack and the weld pool.

2.4 Grain Boundary Elemental Segregation

2.4.1 Introduction

HAZ cracking is often intergranular or interdendritic in form. The tendency of a given alloy to exhibit HAZ cracking can be influenced by several factors, including welding parameters (preheat, heat input, travel speed, heat source, etc.), environment, geometry and mechanical constraint in the work piece.

Physical and metallurgical properties that influence HAZ cracking include yield strength, ductility, thermal conductivity and thermal expansion. Among the most troublesome and least understood of the metallurgical factors however, is the harmful influence of certain trace elements or impurities [81,83]. The mechanism(s) by which these harmful impurities promote intergranular and interdendritic failure during welding is neither well documented nor well understood. In certain cases, poor weldability has been traced

directly to the formation of impurity rich grain boundary films (secondary phases) which may be brittle or possess lower melting temperatures than the matrix [81]. However, such films are not always present and in some cases it is evident that the offending impurities segregate strongly to the interfaces along which cracking occurs without formation of secondary phase films [84,85].

The distinction between segregation and formation of secondary phase films is significant with regards to understanding and controlling the weld cracking phenomenon. Secondary phase films are bulk phases and can form only when the local impurity content is above the solubility limit. Segregation layers, on the other hand, may be only a few atoms thick and still contain impurity concentration several orders of magnitude above the bulk impurity concentration of the alloy. Strong impurity segregation to grain boundaries can occur even when the overall impurity concentration is well below the solubility limit. This means that no new interfaces are formed as a result of segregation, however, the properties of the interfaces to which segregation occurs may be changed greatly. This consequently affects the material's weldability and other metallurgical properties/processes which have been summarized by Hondros et al [86] and are given in Fig.2.23.

The phenomena can be classified into two broad categories. The first one involves bonding or cohesion in which the adsorption of impurity affects either the mechanical strength of the alloy or the strength of adhesion between a metal and a non-metal. For

the second one, the segregant species may involve some kinetic based phenomenon such as precipitate growth or surface oxidation.

Elemental segregation can be induced during different thermal and chemical processes such as casting, hot forming, heat treatment, welding and surface chemical treatment (plating, anodizing, etc.). It is a diffusion-controlled process and can be categorized into two types, namely equilibrium and non-equilibrium segregation. A detailed review of equilibrium segregation and non-equilibrium segregation theory is given in the next section since it will be used to explain the results obtained in this investigation.

2.4.2 Equilibrium Segregation

2.4.2.1 Theory of Equilibrium Segregation

Equilibrium segregation is described as the movement of solute atoms from the bulk alloy to loosely packed sites such as grain boundaries, free surfaces, phase boundaries and stacking faults to reduce the grain boundary free energy. The earliest calculation of segregation was made in 1948 by Cottrell [87] who defined the segregation concentration as

$$C=C_o\exp[\frac{E_b}{RT}] \qquad <22>$$

where C_o is the average concentration, E_b is the binding energy between the segregant and the interface and R and T have the usual meaning. This simple treatment could be applied to any interface.

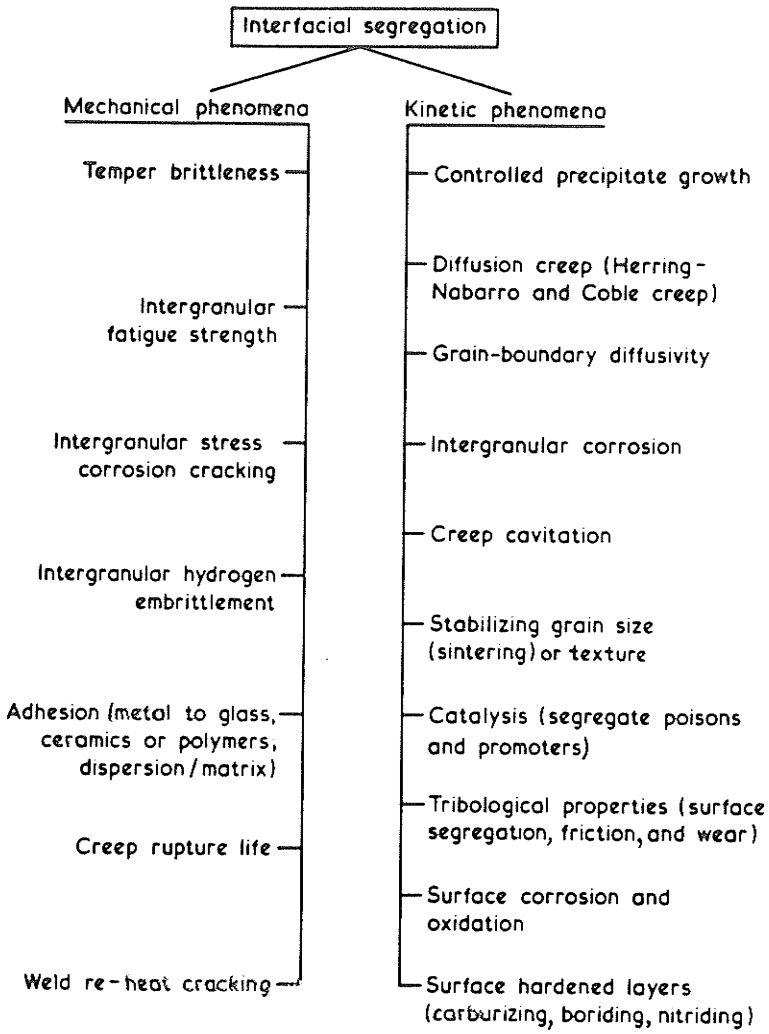

Fig.2.23 Effect of interfacial segregation on material properties [86].

In 1957, Mclean [88] proposed a rather more accurate expression based on adsorption theory with the following assumptions:

(1) A single layer segregation and single adsorbate.

(2) No site-to-site interaction.

(3) Only one element segregating to the interface and that this interface has a fixed number of identical sites at which the segregating element will be preferentially located.

(4) The filling of any particular site does not alter the probability of the filling of any other.

Mclean calculated the equilibrium concentration of the solute at a grain boundary in the following way. Suppose that there are N undistorted lattice sites with P solute atoms distributed among them, and n distorted interface sites with p solute atoms distributed among them. If the molar distortion energy of a solute atom in one of the N initially undistorted sites is E, and in one of the n initially distorted sites is e, then the free energy due to the solute atoms is

$$G=pe+PE-RT\ln\omega \qquad <23>$$

where RTlnω is the configurational entropy caused by the solute atoms and is equal to

$$\ln\omega=\ln(n)!N!-\ln(n-p)!p!(N-P)!P! \qquad <24>$$

The minimum in G occurs when

$$\frac{p}{n-p}=\frac{P}{N-P}\exp[\frac{E-e}{RT}] \qquad <25>$$

This equation may be re-expressed as

$$\frac{C_b}{1-C_b}=\frac{C_g}{1-C_g}\exp[\frac{E_f}{RT}], \quad C_b=\frac{C_g\exp[\frac{E_b}{RT}]}{1+C_g\exp[\frac{E_b}{RT}]} \qquad <26>$$

where C_b is the solute grain boundary concentration and C_g is the bulk solute concentration. E_f is the free energy of adsorption at the grain boundary and E_b is the binding energy of solute with the grain boundary which is equal to the negative value of E_f. Eq.<26> shows that the segregation rises as the solute content rises or as the temperature falls and because of the constraint of the fixed number of adsorption sites, the segregation eventually reaches a saturation value C_{bo}, which generally seems to be about one monolayer [89]. The definition of monolayer is that one monolayer contains a^{-2} segregant atoms per unit area where a^3 is the atomic volume of the segregant.

2.4.2.2 KINETICS OF SEGREGATION TO INTERFACES

Practically, the time available at a temperature is much less than that required for full segregation, and therefore it is important to know the time dependence of segregation. This dependence was first evaluated by Mclean [88]. By considering the flow of solute atoms from two infinite half crystals separated by a grain boundary, he applied Fick's law and matched the flow of solute atoms out of the crystals to the rate of accumulation at the boundary. Assuming a constant ratio between the grain boundary concentration and the concentration at the face of the grains adjacent to the boundary, Mclean derived an expression for the segregation kinetics given by:

$$\frac{C_b(t)-C_b(0)}{C_b(\infty)-C_b(0)}=1-\exp[\frac{FDt}{\beta^2 f^2}]erfc[\frac{FDt}{\beta^2 f^2}]^{\frac{1}{2}} \qquad <27>$$

where F=4 for grain boundary segregation, $C_b(t)$ is the grain boundary concentration at time t, D is the solute bulk diffusion coefficient, and ß is the ratio of the solute in the grain boundary to that in the adjacent atom layer of the bulk (also called the distribution coefficient) which is assumed to be constant and independent of the actual values of C_b and C_g. f is related to the atom sizes b and a of the solute and matrix respectively by $f=a^3b^{-2}$. f can also be interpreted as the width of the boundary and is approximated to be 2.5×10^{-10}m [90].

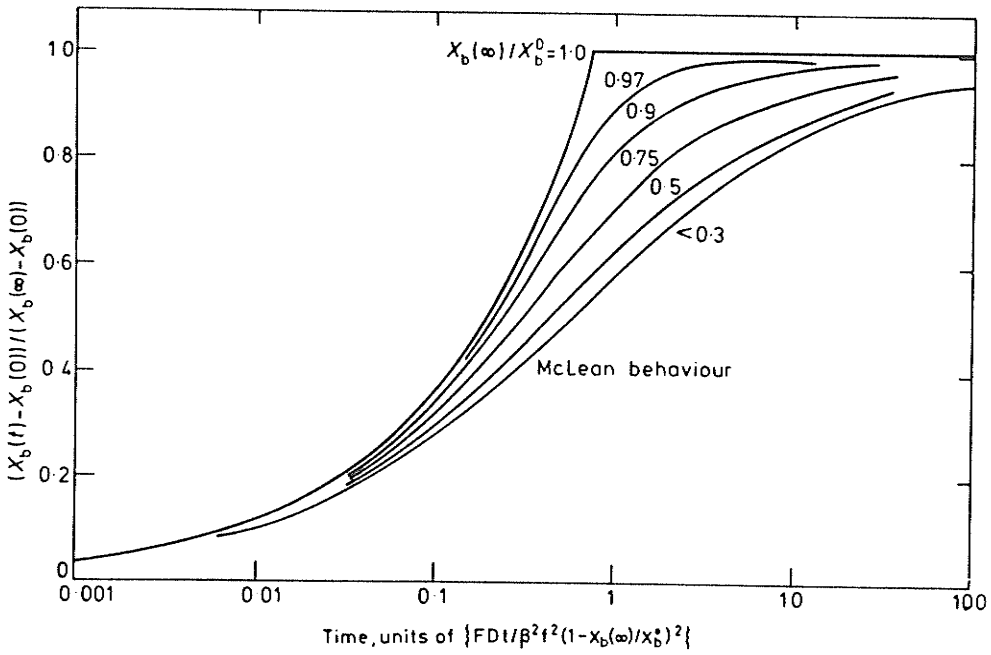

Fig.2.24 The kinetics of segregation in binary systems for varying degrees of saturation in the final equilibrium level [91].

The concentration variation with time is shown in Fig.2.24 (note that time is expressed in terms of the normalized unit $4Dt/\beta^2d^2$ where d is the thickness of the grain boundary). For short times, Eq. <27> can be simplified into:

$$\frac{C_b(t)-C_b(0)}{C_b(\infty)-C_b(0)}=\frac{2}{\beta}\frac{b^2}{a^3}\left[\frac{FDt}{\pi}\right]^{\frac{1}{2}} \qquad <28>$$

Eq. <27> and <28> are in fact limiting extremes of a general problem. In practice, β (enrichment ratio) is only constant for dilute systems with low segregation level. The values of β for various alloy systems are given in Fig.2.25 [91]. A more complex model of the kinetics of segregation in ternary systems has been advanced by Tyson [92] using Mclean's approach and incorporates Guttmann's theory [93] to define the grain boundary concentration.

Two useful times determined are those required for the segregation to build up to 50% and 90% of the final equilibrium level. They are:

$t_{50}=0.591\beta^2d^2/4D$ and $t_{90}=30.8\beta^2d^2/4D=52t_{50}$

If desegregation occurs, the quantity of adsorbate left in the grain boundary under desegregation conditions, (where the solute diffusion away from the grain boundary is not limited by low solubility), is given as:

$$\frac{C_b(t)-C_b(\infty)}{C_b(0)-C_b(\infty)}=erf\left(\frac{d}{4\sqrt{Dt}}\right) \qquad <29>$$

The 50% and 90% of desegregation obtained were:

$t_{50}^{d}=0.275d^2/D$

$t_{90}^{d}=7.91d^2/D=28.8t_{50}^{d}$

The desegregation for $\beta=30$ is shown by the desegregation curve in Fig.2.24 and it is seen that the desegregation is much faster than segregation (by a factor of β^2). This factor arises from the fact that in segregation at t_{50}, the solute atoms typically have to travel a distance of βd, whereas in desegregation they have only to move a distance approximately equal to β. There is very little direct evidence to show that segregation kinetics do in fact follow Mclean's analysis exactly but all observations made so far are compatible with his prediction [94,95].

Equilibrium segregation during quench and subsequent ageing was treated separately by Faulkner [90] and summed to give the final segregation parameter as following:

(1)Equilibrium Segregation During Quench

To quantify the amount of segregation during the quench, an effective time t in Eq. <27> must be evaluated and used. The major variable on which t depends is the cooling rate θ. An effective temperature which is representative of the complete cooling range must also be evaluated from the cooling history information. This temperature is related to the starting temperature (solution treatment), T_i, and t in the following expression:

$$T=T_i\exp(-\frac{t}{\tau}) \qquad <30>$$

where τ is given by $\tau=1000/\theta$.

This involves the assumption that cooling rates will commonly be in the range of 0-100°C/s, the temperature can therefore be estimated to be T_ix0.26. Using this assumption with Eq. <30>, an equivalent time at T_i is calculated to be $200/\theta$.

Another approach is to determine an equivalent time using

$t=RkT_i^2/\theta E_A$

where E_A is the activation energy for diffusion of impurities and R is a constant determined by empirical means to be 0.01.

(2)Equilibrium Segregation During Ageing

Equilibrium segregation during the ageing part of the heat treatment is simply calculated using β and D equal to the ageing or tempering temperature and the time equal to the ageing time. These variables are used directly in Eq. <27> to obtain a value of $C_b(t)$, the concentration in the monolayer on the boundary after an ageing time t.

(3)Combined Equilibrium Segregation in quench and age heat treatment

The contributions to equilibrium segregation from quenching $C_b(t)_q$ and from ageing $C_b(t)_{AGE}$ are summed up to give the total equilibrium contribution to C_b.

2.4.2.3 Prediction of The Free Energy of Segregation to Grain Boundary

The value of E_b was originally estimated by Mclean [88] from the elastic strain energy E_{el} of the solute in the lattice, all of which is assumed to be released on segregation. For

a solute atom of radius r_1 in a site of radius r_0, the elastic energy associated with one mole of solute is given as:

$$E_{el}=\frac{24\pi NKGr_0r_1(r_1-r_0)^2}{3Kr_1+4Gr_0} \qquad <31>$$

where K is the solute bulk modulus, G is the solvent or matrix modulus and N is Avogadro's number [96]. Values estimated by this approach are generally correct within a factor of two. A much more accurate treatment has been provided by Seah and Hondros [97] as follows:

$$\Delta G_b=\Delta G_1+\Delta G_{sol} \qquad <32>$$

where ΔG_1 and ΔG_{sol} are from solid solubility equation

$$C_b^{\,o}=\exp(\frac{\Delta G_{SOL}}{RT}) \qquad <33>$$

and the enrichment ratio equation

$$\beta_b=\frac{\exp(\frac{-\Delta G_1}{kT})}{C_b^{\,0}} \qquad <34>$$

Fig.2.25 shows a compilation of measurements of grain boundary enrichment ratio, β_b, (estimated by the grain boundary energy and surface analysis approaches) in relation to the solubilities of the segregation at the measurement temperature. It is clear that in the dilute limit ($\sim$ 0.01%), Eq.<34> provides the theoretical description of the experimental data of Fig 2.25. Seah and Hondros concluded that whilst ΔG_{sol} ranges from

zero to -80 kJ/mol, ΔG_i has a mean value of -10 Kj/mol with a standard deviation of only 6 Kj/mol. Thus, $\Delta G_b = \Delta G_{sol} - 10 \pm 6$ Kj/mol.

2.4.3 Non-Equilibrium Segregation

2.4.3.1 History

In contrast to the above discussed equilibrium segregation, various phenomena exist in which the apparent levels of segregation built up may extend to distances of as much as several micrometers across grain boundaries [98] and this effect is sensitive to the rate of cooling. The earliest observation of the effect of this type of segregation was announced by Westbrook and his collaborators when an unusual grain boundary hardening was observed in lead [99]. Further investigation was undertaken to study this phenomenon in zone-refined lead bicrystals with and without solute additions (Sn, Ag, Au, and In) [100]. It was observed from their investigation that:

1) The grain boundary hardening can be detected over a region of some tens of micrometer wide, as seen in Fig.2.26 [100], and can reach a maximum hardness value which can be as much as 40% higher than the bulk hardness.
2) No systematic variation in hardness of the grain interiors occurs with an increase in solute concentration (segregation) at the grain boundaries.
3) The relative effect of the solute addition on the grain boundary hardening varies inversely with the solid solubility (or the distribution coefficient, K) of the solute in lead.
4) The effect of grain boundary hardening increases with an increase in solute

concentration

5) Very low energy interfaces, such as coherent twin boundaries, show no hardness effect. Low-energy interfaces such as incoherent twin boundaries and certain large-angle grain boundaries (e.g. coincidence site boundaries) display less excess boundary hardening than most large-angle grain boundaries (random type). Lower energy interfaces are expected to have higher atomic fit in the boundary and therefore, less segregation of solute occurs in these boundaries.

6) The grain boundary hardness effect is also temperature dependent. It decreases and eventually disappears as the temperature is increased.

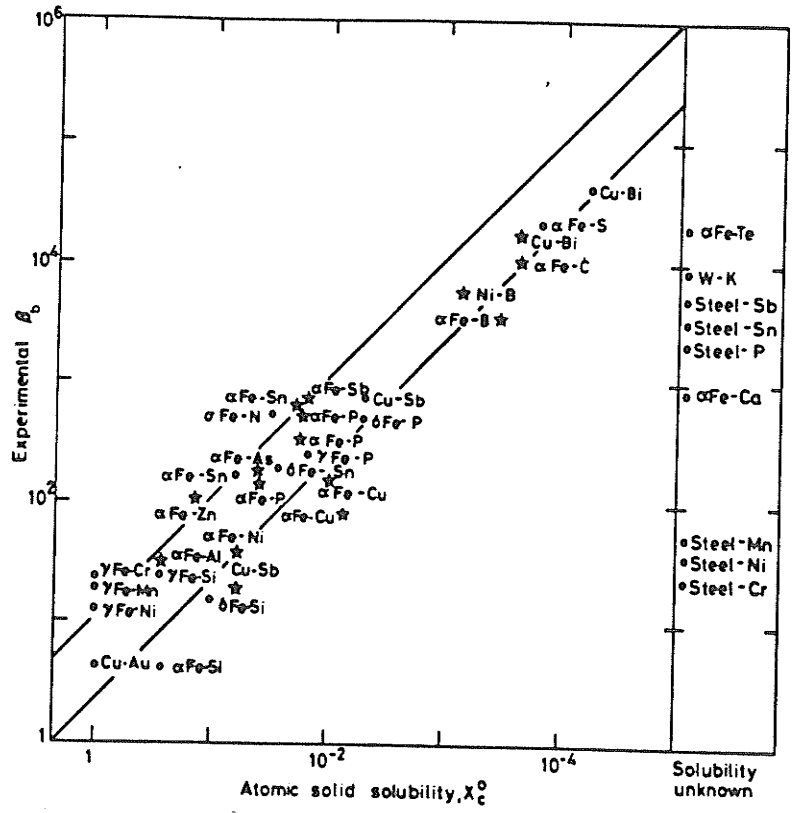

Fig.2.25 Correlation of measured grain-boundary enrichment ratios with the atomic solid solubility [91].

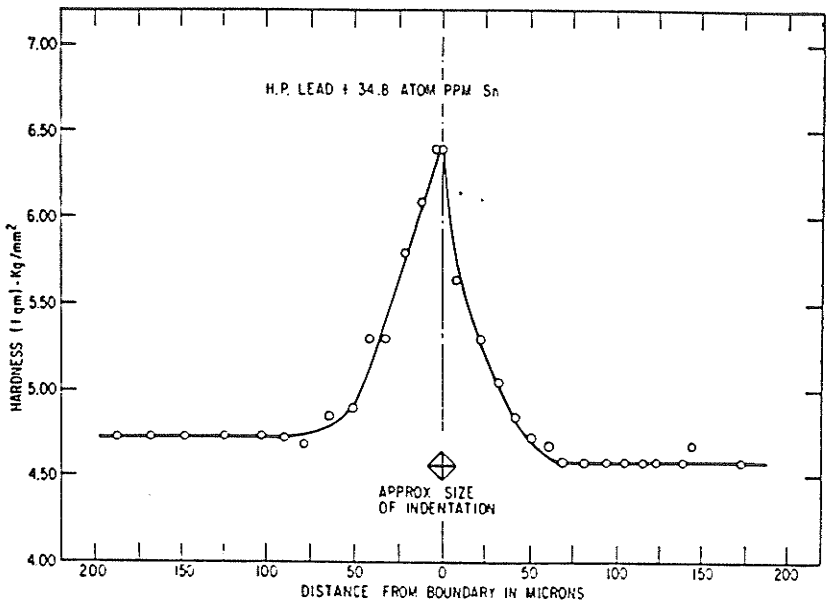

Fig.2.26 Hardness-distance profile near a grain boundary in a Pb-Sn sample [100].

The segregation theory that existed at that time could not explain the observed phenomena during the early stages of this study. It was suggested that the hardening is produced not directly by the substitutional solute, but by a mechanism which is facilitated by the abnormal generation and/or motion of some other type of defect in the vicinity of the boundary region, and which also requires the presence of solute atoms.

A solute clustering mechanism for grain boundary hardening based on a solute-vacancy interaction was proposed by Aust and coworkers in 1968 [101]. According to this mechanism, excess quenched-in vacancies tend to annihilate at grain boundary sinks. Those systems with a positive solute-vacancy binding energy (i.e. $K < 1$) can produce a

vacancy-coupled uphill diffusion of solute atoms toward the boundary [101,102]. Systems with K>1 will not lead to enrichment of solute by clustering near the grain boundary. Aust [101] developed the relationship between vacancy-solute binding energy (E_{vs}) and distribution coefficient (K) for various solvent-solute systems. This mechanism was later further developed by Anthony et al [103] and named as 'non-equilibrium segregation' [103-105].

2.4.3.2 Formation of Vacancy-Solute Pairs and Their Concentration

For a system containing vacancy-solute pairs in equilibrium with free solute atoms and free vacancies, the reaction is given by

$$VS \rightleftharpoons V + S$$

VACANCY-SOLUTE PAIR ==== FREE VACANCY + FREE SOLUTE

(COMPLEX)

$$C_{VS} \leftrightarrows (C_V^* - C_{VS}) + (C_s - C_{VS}) \qquad <35>$$

where C_{vs} is the concentration of the vacancy solute complex, C_V^* is the vacancy concentration and C_s is the solute (impurity) concentration. The mass relationship for this reaction has been developed by Howard and Lidiard [106] to be as follows:

$$\frac{C_{VS}}{[C_V^* - C_{VS}][C_S - C_{VS}]} = K \qquad <36>$$

where K=mass constant. When $C_s >> C_{vs}$, Eq. <36> can be simplified to,

$$C_{VS}=\frac{KC_SC_{V_*}}{1+KC_S} \qquad <37>$$

where the mass constant K is given for either substitutional or interstitial solid solution by

$K=Z\exp[E_{vs}/kT]$.

In this expression Z is a factor that accounts for the total entropy change upon forming a complex and E_{vs} is the binding energy between a vacancy and solute atom. For $E_{vs}>>kT$, the mass action constant will be very large and the degree of association between vacancies and solute atoms will be very strong.

When the temperature of a sample is abruptly changed to a different temperature, the concentration of vacancies will attempt to adjust to the new equilibrium value and is given by

$$C^*_V=\exp(\frac{S_V}{k})\exp(-\frac{E_V}{kT})=A\exp(-\frac{E_V}{kT}) \qquad <38>$$

where E_v and S_v are the energy and excess entropy of vacancy formation respectively.

The above equation gives the equilibrium fraction of lattice occupied by single vacancies in a pure metal. A modified expression was later proposed by Doig and Flewitt [107] for a binary FCC substitutional alloy containing a small concentration of solute atoms ($C_s<0.1$):

$$C_V^* = C_V[1 - ZC_S + ZC_S \exp[\frac{E_{VS}}{kT}]] \qquad <39>$$

where Z is the co-ordination number and has a value of 12 for a FCC lattice.

The rate at which the new equilibrium is approached is dependent on the temperature-time path followed, the impurities present, and the concentration and potency of various types of vacancy sinks. Available types of vacancy sinks include surfaces, grain boundaries, twin boundaries, stacking faults, dislocation sites and nucleated secondary defects such as vacancy loops, clusters or pores. Free surfaces are normally rather potent sinks for vacancies. Random grain boundaries can be also strong vacancy sinks whereas twins and low angle coincidence boundaries are less effective sinks. During a quench and subsequent hold at temperature, vacancy gradients will develop adjacent to vacancy sinks as the vacancies attempt to achieve a new equilibrium concentration. When E_{vs} is positive and $>>kT$, the vacancy flux will produce a coupled non-equilibrium segregation flow of solute atoms [108]. This non-equilibrium flow of solute atoms is thermodynamically driven by the decrease in free energy associated with the annihilation of excess vacancies at vacancy sinks.

In contrast, quench induced solute depletion near an interface can occur when E_{vs} is weakly positive and the solute diffusivity D_i is larger than the solvent diffusivity. This causes the solute to diffuse substitutionally [104,105]. Being the most mobile atoms in

the solution, solute will be disproportionately represented in the reverse atom flow caused by a vacancy flow. Thus, as vacancies migrate to vacancy sinks, solute atoms will be selectively ejected from regions near the grain boundaries or free surfaces into the interior of the grain by the escaping vacancies.

The relationship between K, E_{vs}/k and the mode of segregation has been studied in binary close-packed substitutional solid solution [104,105] and can be summarized as follows:

If $K<1$ and $E<<kT$, solute depletion zone occurs around vacancy sinks

If $K<1$ and $E>>kT$, solute-enriched zone occurs around vacancy sinks

If $K>>1$, there is minimal tendency for segregation to occur

Williams et al [109] calculated the boron-vacancy complex concentration in type 316 stainless steel by using the following equation

$$C_{VS}=\alpha Z[C_S][C_V]\exp(-\frac{E_V}{kT})\exp(\frac{E_{VS}}{kT}) \qquad <40>$$

Data used for this calculation is given in Table 2-14. The results suggest that

1) At 900°C there are few vacancies (~4ppm) and the fraction of boron in complexes is negligible.

2) At 1350°C the vacancy concentration is ~180ppm and a small but significant fraction (~7%) of the boron is in boron-vacancy complexes.

Boron concentration C_s	90ppm(atomic)
Vacancy formation energy E_v	1.4 eV
Vacancy motion energy E_m	1.3 eV
Boron-vacancy binding energy E_{vs}	0.5 eV
Z	12
α [110]	4
Vacancy diffusion D_v	0.5exp(-2.7/kT)
Boron diffusion D_I	$2x10^{-3}$exp(-0.91/kT)
Complex diffusion D_{VI}	0.5exp(-0.91/kT)

2.4.3.3 Vacancy-Impurity Atom Complex Binding Energy (E_{vs})

The value of E_{vs} was either taken to be the value tabulated in Table 2.14 or was calculated using elasticity theory. Based on a concept proposed by Cottrell [111], the following formula describes the binding energy of a vacancy with a foreign atom which has a misfit, ϵ, with the matrix lattice site.

$$E_{VS}=8\pi\mu r_0^3\epsilon^2 \qquad <41>$$

where μ is the shear modulus of the matrix, r_o is the matrix atom radius, r_i is the impurity atom radius and $\epsilon=\pm (r_i-r_0)/r_0$.

Chapman and Faulkner [112] calculated the boron-vacancy binding energy based on this elasticity theory. The complex can be modelled by removing an impurity atom from a di-impurity atom complex, and then allowing the resulting vacancy to equilibrate. The formation energy of the vacancy-impurity atom complex can be then approximated by the following expression:

$$E_{VS}^{f}=E_{SS}-E_{S}+4\pi r_{VF}^{2}S+\frac{8}{3}\pi G r_{VO}(r_{VF}-r_{VO})^{2} \qquad <42>$$

where $E_{SS}=2E_s+0.78$ Ev$=8\pi r_{vF}^{2}+0.78$ Ev (di-solute formation energy), E_s is the interfacial energy of a removed boron atom, r_{vo} is the initial vacancy radius before distortion = 0.88x10-10 m, r_{vF} is the final vacancy radius after distortion = $0.53x10^{-10}$m, S is the surface energy of iron = 1.9J/m^2 and G is shear Modulus = $5x10^{10}$N/m^2.

Substituting these values into Eq. <42>, the formation energy can be expressed as:

E_{vs}^{f} = E_s + 0.78 Ev + 0.4 Ev + 0.28 Ev = E_s + 1.48 Ev

The binding energy of the vacancy-impurity atom complex is then given by the difference between the formation energies

$$E_{IV}=E_{I}+E_{V}-E_{IV_f} \qquad <43>$$

where E_s is the impurity atom formation energy = E_s + 0.45 Ev and E_v is the vacancy formation energy = 1.6 eV.

Substituting E_{IV}, E_I and E_v in Eq. <43> gives

E_{IV}^{b} = E_s + 0.45 + 1.6 -1.48 - E_s = 0.57 eV

which is very close to the value of 0.5eV Williams postulated in his studies [109]. Values

calculated for other systems by this approach are given in Table 2-15. The available experimental data are also included for comparison.

2.4.3.4 Magnitude of Non-Equilibrium Segregation

The magnitude of non-equilibrium segregation has been calculated on the assumption that only diffusion of solute-vacancy complexes occurs [113,114]. In this calculation it is also assumed that the concentration at vacancy sinks changes only during cooling from temperature T_i to $T_{0.5Tm}$, where T_i is the heat treatment temperature and $T_{0.5Tm}$ is half of the melting temperature, since very little diffusion will occur below $T_{0.5Tm}$. The magnitude of the segregation is given by:

$$\frac{C_b}{C_g}=\exp\left(\frac{E_b-E_V^f}{kT_i}-\frac{E_b-E_V^f}{T_{0.5Tm}}\right)\frac{E_b}{E_V^f} \qquad <44>$$

where E_V^f is the free energy of vacancy formation.

The value of E_b calculated from Eq. <44> for different cooling ranges between T_i and $T_{0.5Tm}$ is shown in Fig.2.27 [114].

Karlsson used the finite difference method and Fick's coupled diffusion equation to calculate the non-equilibrium segregation profile in stainless steel containing 206ppm (atomic concentration) boron [115]. The results are shown in Fig.2.28 [115].

Table 2-15 Binding Energies of Impurities in Various Alloy Systems

Element	Interstitial No.	E_{IV}^{b}(eV) (Experiment)	E_{IV}^{b}(eV) (Theory)
Ni matrix			
Si	0	0.73	0.195
Ti	0	-	0.404
Mo	0	-	0.27
α-iron matrix			
Mo	0	-	0.308
Si	0	-	0.202
B	0	-	0.477
P	0	-	0.364
γ-iron matrix			
Mo	0	0.05	0.254
Si	0	0.35	0.277
B	2	-	0.498
Ti	0	0.10	0.443

*Interstitial number = 2 (octahedral site in FCC) 0(substitutional)

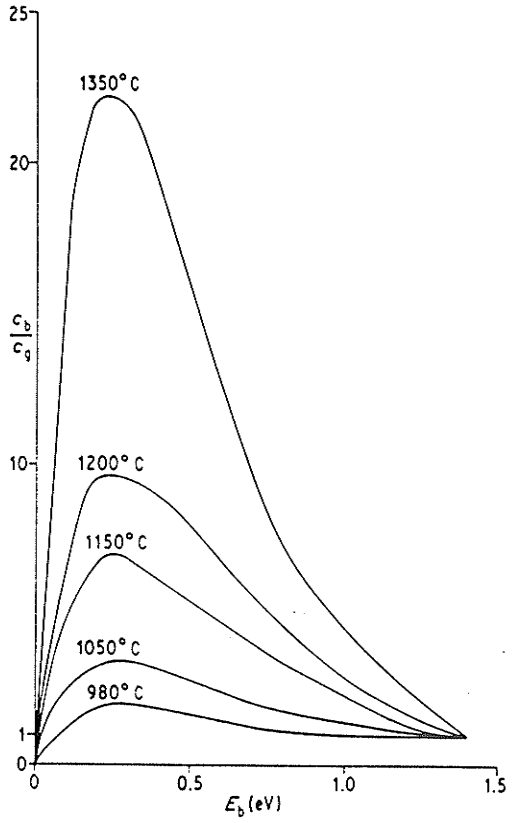

Fig.2.27 Effect of vacancy-impurity binding energy E_b on the non-equilibrium segregation magnitude C_b/C_g on cooling to 750°C from different solution treatment temperatures [114].

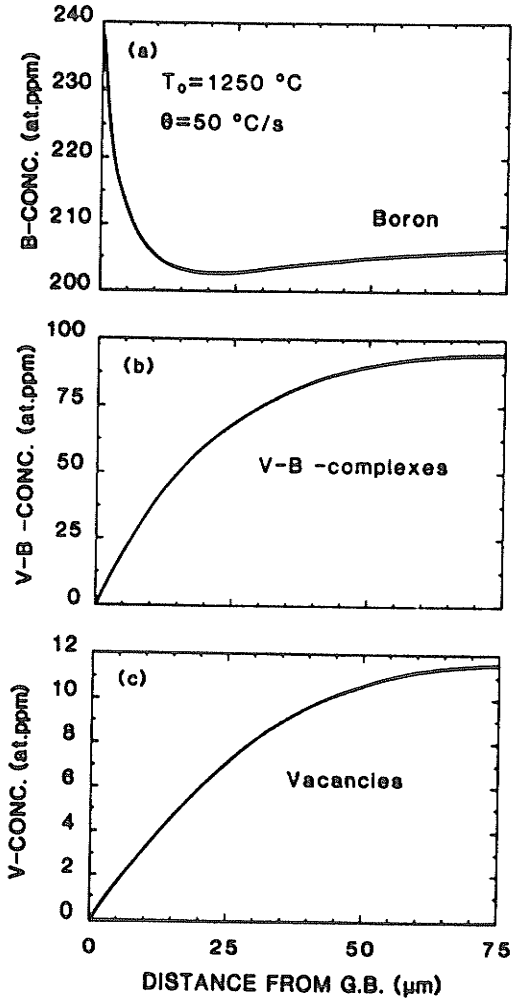

Fig.2.28 Simulated concentration profiles for austenite with 206 at. ppm boron, cooling rate 50°C/s from 1250°C. (a) free boron atoms plus vacancy-boron complexes, (b) vacancy-boron complexes and (c) free vacancies [115].

2.4.3.5 Kinetics of Non-Equilibrium Segregation

On cooling from T_i to $T_{0.5Tm}$, the effective time spent at temperature T_i can be calculated for any cooling rate, θ, or heat treatment cycle. An effective time, t_θ, as a function of cooling rate θ is given by [114],

$$t_\theta = \frac{RkT_i^2}{\theta E^A_{VS-S}} \qquad <45>$$

where E^A_{VS-S} is the average activation energy for diffusion of solute-vacancy complexes and impurities in the matrix, and R is the gas constant. If an isothermal step occurs in the heat treatment at a temperature T_A for a time of t_A, then the effective time spent at temperature T_i is

$$t_\theta = t_A \exp[-\frac{E^A_{VS-S}}{kT_iT_A}](T_i - T_A) \qquad <46>$$

During non-equilibrium segregation two distinct processes occur, namely, segregation and de-segregation. First, impurities are drawn from the grains to the boundaries by the motion of solute-vacancy complexes. The ratio of the resulting impurity concentration on the grain boundaries, C_b, relative to the concentration in the matrix, C_g, can never exceed the predicted value as shown in Eq. <44>. Thus, any accumulation of impurities must occur near the grain boundaries in a zone extending a distance proportional to the amount of segregation taking place.

The theoretical concentration profile, quantified for different times, is shown in Fig.2.29

[114]. By applying Fick's second law for semi-infinite solids, it was quantified to be,

$$\frac{C_x - C_g}{C_b - C_g} = erfc \frac{x}{2\sqrt{D_{VS} t_\theta}} \qquad <47>$$

where D_{sv} is the complex diffusion coefficient and C_x is the concentration of impurity at a distance x from the grain boundary. It is assumed that D_{VS} is given by the product of the frequency factor for vacancy diffusion and the exponential term containing the activation energy for diffusion of the impurity atom in the matrix. The extent of segregation when this process occurs can be given approximately by the following:

$$X_V = \sqrt{D_V t_\theta} \qquad <48>$$

However, when t_θ exceeds a critical time, t_c, back diffusion will dominate (or the desegregation of the impurity down the concentration gradient towards the centre of the grain). The rate-determining step in this process is the diffusion coefficient of impurity atoms, D_S. The critical time after which desegregation begins, t_c, is governed by the relative diffusion rates of the solute-vacancy complexes towards the grain boundary and the diffusion rates of impurities away from the grain boundary and is given by,

$$t_c = \frac{\delta d^2 \ln(D_V/D_I)}{4(D_V - D_O)} \qquad <49>$$

or in another form [116]:

$$t_c = \frac{d^2(\ln D_{VS}^{\ 0} - Q_{VS}/kT - \ln D_S)}{\delta[D_{VS}^{\ 0}\exp(-Q_{VS}/kT) - D_S]} \qquad <50>$$

where δ is a numerical factor, d is the grain size, $D_{vs}^{\ 0}$ is the frequency factor and Q_{vs} is the activation energy for the diffusion of solute-vacancy complexes.

The theoretical composition profiles during desegregation are shown in Fig.2.30 [114]. The situation can be described by the thin film solution of the diffusion equation. Thus the concentration of impurity, C_x, at a distance, x, from the grain boundary after time t_θ (where $t_\theta > t_c$) is given by

$$\frac{C_x - C_g}{C_b - C_g} = \left(\frac{D_{VS}t_c}{D_S t_\theta}\right)^{1/2} \exp\left(\frac{-x^2}{4D_S t_\theta}\right) \qquad <51>$$

The extent of desegregation when this process occurs can be given by:

$x_S = (D_S t_\theta)^{1/2}$

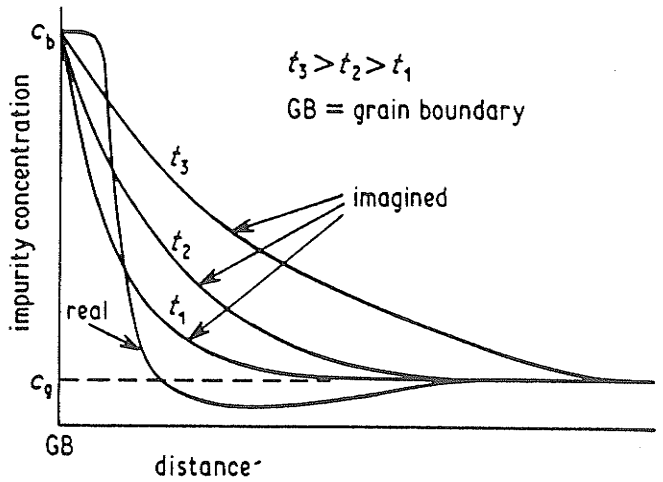

Fig.2.29 Imaged segregation concentration profile [114].

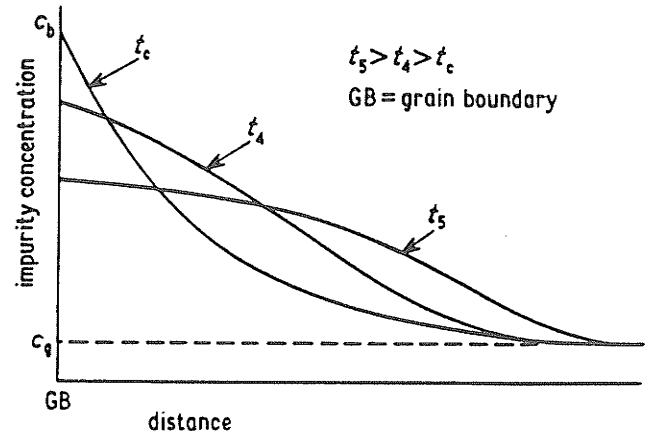

Fig.2.30 Imaged desegregation concentration profile [114].

2.4.3.6 Grain Boundary Segregation During Isothermal Holding

Three types of variation in the intensity of boron segregation with isothermal holding time have been observed in Fe-30%Ni alloy and steel [117] as shown in Fig.2.31. The first two of these involve the appearance of a segregation peak, after which there was either complete or partial disappearance of segregation. The first was found to be associated with the back diffusion of boron into the depleted zone. The second involved a conversion of temporary segregation into grain boundary precipitates and occurred at intermediate temperatures. The third type was observed at the low temperature where precipitation occurred prior to the appearance of the segregation peak. It was noted that the segregation attained its maximum value more quickly at higher temperatures, but was eventually more intense at lower temperatures. This is expected since the rate of boron back diffusion increases with temperature (as it is a thermally activated process and the temperature difference is greater when a material is held at a lower temperature). The

appearance of such peaks on segregation-holding time curves is another unique characteristic of non-equilibrium segregation. It indicates that part of the segregation is unstable and is dynamic in nature [117].

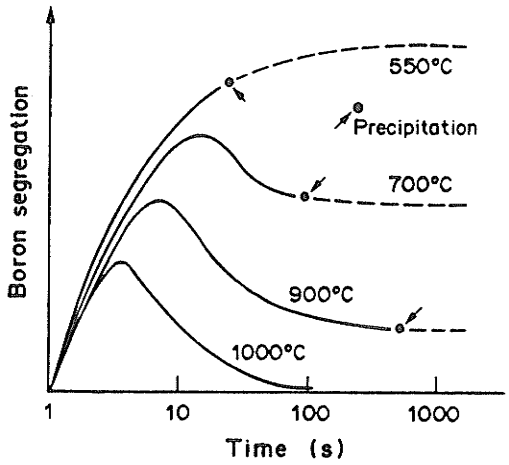

Fig.2.31 Schematic representation of the dependence of boron segregation on temperature and hold time in steel [117].

The isothermal kinetics of non-equilibrium segregation was developed for both segregation and desegregation processes [118]. Based on the following equation:

$$C_v(T)=C_g(E_b/E^f)\exp[\frac{E_b-E^f}{kT_o}-\frac{E_b-E^f}{kT}] \qquad <52>$$

An isothermal kinetic relationship has been derived and is given by:

$$\frac{C_b(t)-C_b(T)}{C_b(T_i)-C_b(T)}=1-\exp\left(\frac{4Dt}{\left(\frac{C_b(T_i)}{C_g}\right)^2 d^2}\right)erfc\left[\frac{2(Dt)^{1/2}}{\frac{C_b(T_i)}{C_g}d}\right] \qquad <53>$$

This equation describes the non-equilibrium segregation concentration $C_b(t)$ of solute atoms at the grain boundary as a function of holding time t ($<t_c$) at temperature T_i when cooling from temperature T. The parameter d is the width of the concentration layer of solute atoms. When $t>t_c$, the desegregation concentration can be calculated using Eq. <54>,

$$C_b(t)=C_g+\frac{1}{2}(C_b(t_c)-C_g)erf\left[\frac{x+d/2}{\sqrt{4D_S(t-t_c)}}\right]-erf\left[\frac{x-d/2}{\sqrt{4D_S(t-t_c)}}\right] \qquad <54>$$

where t is the isothermal holding time at T_i, $t_c = t_c(T_i)$, D_S is the diffusion coefficient of solute atoms in the matrix, and x is the distance from the centre of the grain boundary. A concentration profile near the grain boundary at various holding times is shown in Fig.2.32 [118].

2.4.3.7 Non-Equilibrium Segregation During Continuous Cooling and The Occurrence of Segregation Depleted Zone

During continuous cooling from various temperatures, it was found that the degree of segregation of boron at grain boundaries in steel and in a Fe-30%Ni alloy decreased with increasing temperature when a rapid cooling rate was used [119,120]. The segregation was not sensitive to the cooling rate and did not lead to a boron depleted zone next to the

boundaries. It is suggested to be a Mclean type of segregation [119,120]. However, when an intermediate cooling rate was used, the severity of boron segregation first decreased with temperature and then increased. This trend was found to be a representative of the sum of both equilibrium and non-equilibrium segregation [119]. Non-equilibrium segregation is strongly dependent on the cooling rate and the degree of segregation is highest at intermediate cooling rates when the time is just sufficient to allow vacancy-solute atom pairs to diffuse to the grain boundary but not to let the deposited solute atoms diffuse away from the boundary zone.

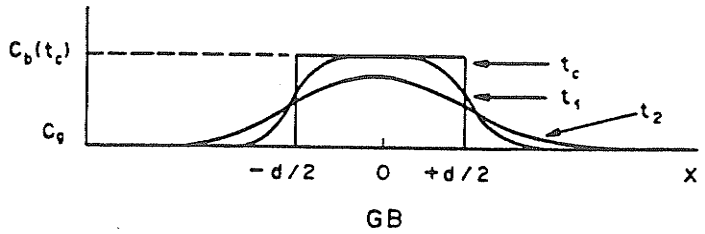

Fig.2.32 The concentration profiles near the grain boundaries as the holding times are equal to the critical time t_c, t_1, t_2 ($t_c < t_1 < t_2$) at T_{i+1} [118].

The results from He and other investigators [121] indicate that boron segregation during cooling is the result of the diffusion of solute-vacancy complexes through the boron depleted zone adjacent to the two sides of the boundary. The boron distribution remains homogeneous (and unchanged) in regions far away from the grain boundary. From this observation, it has been concluded that the degree of segregation is independent of the grain size as long as the grain diameter is more than double the width of the boron

depleted zone. The boron depleted zone in carbon steel was found to be around $5 \sim 30 \mu m$.

A method for calculating the non-equilibrium segregation during continuous cooling has been deduced by Xu et al [118,122] using an effective time $t_e(T)$. A cooling curve for a sample can be replaced by the stepped curve, each step of which is formed by horizontal and vertical segments to calculate the effective time:

$$t_e(T) = \sum_{i=1}^{n} t_i \exp[-E^A_{VS-S}(T-T_i)/kTT_i] \qquad <55>$$

where a value of 0.91 Ev is used for E^A_{VS-S}, t_i and T_i are isothermal holding time and temperature respectively at the i step of the stepped curve. The effect of diffusion of solute atoms (or solute-vacancy complexes) during continuous cooling is the same as that of the sample held at a constant temperature (T) for a length of time equal to the effective time for continuous cooling at the same temperature. The concentration can be calculated by substituting the obtained value $t_e(T)$ for t in Eq. <53>. The calculated value suggests that when $t_e < t_c$ and the solute dissolution temperature is constant, the lower the cooling rate, the greater the segregation of solute atoms to the grain boundaries.

2.4.3.8 Effect of Grain Boundary Orientation and Grain Size on Grain Boundary Segregation

Differences in the relative intensities of B segregation on different grain boundaries were

observed during a study of boron segregation in 316L stainless steel [123] using the SIMS technique. It is well known that during equilibrium segregation a significant variation in concentration can result due to the variation in grain boundary structure [124,125]. For non-equilibrium segregation, the important factor is the ability of the boundary to act as a vacancy sink. Experiments have shown that most grain boundaries, with the exception of special boundaries like coherent twins, can operate as highly efficient vacancy sinks [126,127]. Therefore, the amount of non-equilibrium segregation should be almost the same at the majority of boundaries whereas special boundaries, such as coherent twins, should be devoid of or have fewer segregated solute atoms. Karlsson's studies support this view [123,128]. His studies also suggest that high intensity at non-special boundaries could be caused by a comparatively larger boundary area being exposed at these boundaries and not by any real variation in the amount of boron segregation. In accordance with Faulkner's model [114], it was also predicted that a large grain size leads to a higher intensity of segregation and the enrichment of boron segregation on grain boundaries increases with increasing grain size [115]. However, Williams et al observed a slightly lower level of segregation in coarse grained material [109]. This aspect needs to be further investigated.

2.4.3.9 Techniques for Detection of Grain Boundary Segregation

Several techniques can be used to directly detect elemental segregation at grain boundaries. They include PTA (Particle Track Autoradiography), SIMS (Secondary Ion Mass Spectroscopy), TEM/EDS, Auger, AP (Atomic Probe), IAP (Imaging Atomic

Probe) and FIM (Field Ion Microscopy). A few examples of observations of boron segregation to the grain boundaries are given below

(1) Williams [109] first observed non-equilibrium segregation of boron in type 316 stainless steel, Fig.2.33, solution treated at 1350°C for 0.5 hour, furnace cooled to temperature T_i in the range of $900 < T_i < 1350$°C, held for 0.5 hour and cooled at 50°C/sec to room temperature [109].

(2) Karlsson employed SIMS to observe boron distribution in boron-containing steel (40ppm), Fig.2.34, after cooling from 1250°C at 31°C/sec [123].

(3) The most successful up-to-date quantitative detection of grain boundary segregation of boron was performed by Karlsson and Norden [128-131] by combining TEM/FIM/AP/IAP as shown in Fig.2.35 [128].

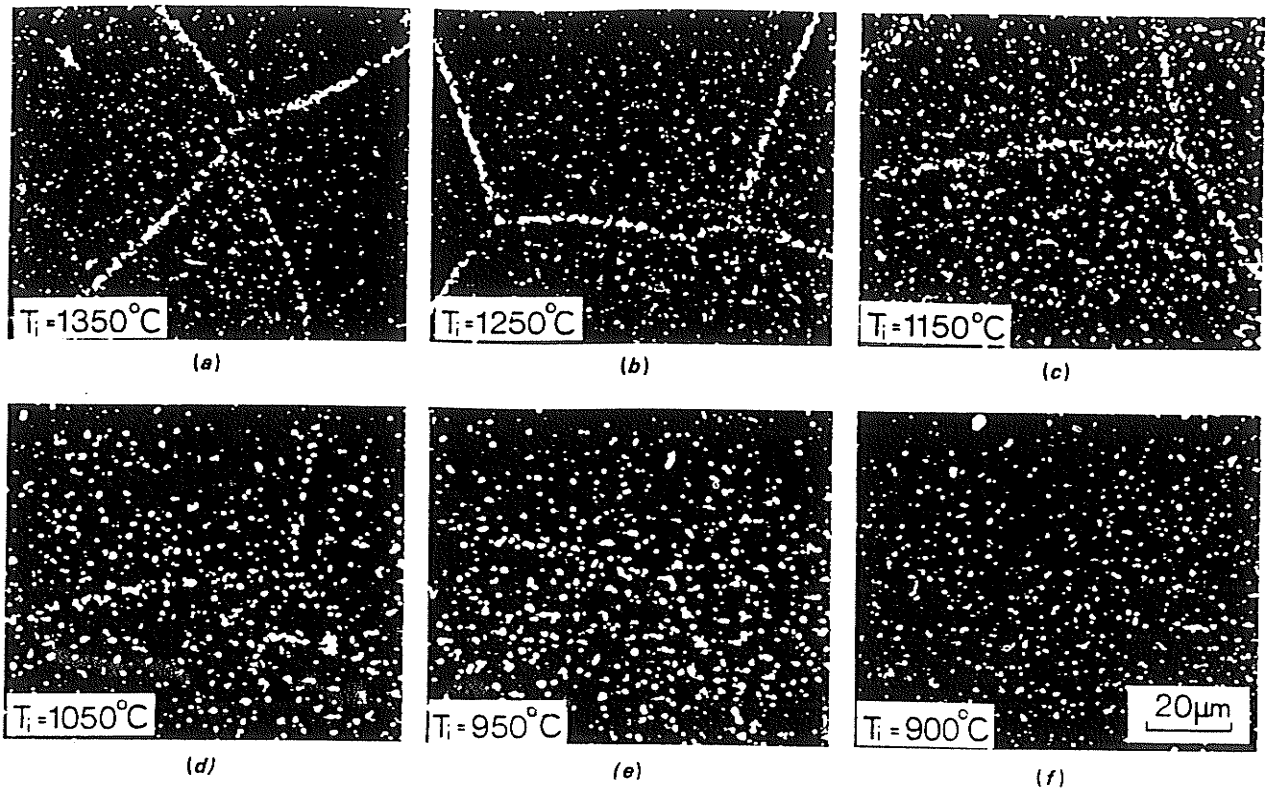

Fig.2.33 Optical autoradiographs of Type 316 steel specimens solution-treated at 1350°C for 0.5 h, furnace-cooled to temperature T_i in range of $900 < T_i < 1350$°C, held 0.5 h, and cooled at 50°C/s to room temperature [109].

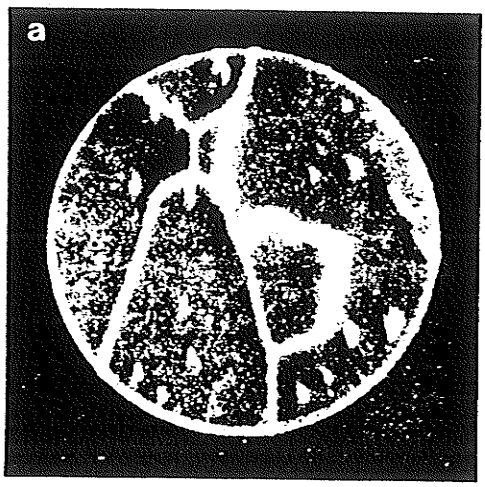

Fig.2.34 Ion micrograph showing the distribution of B ($^{11}B^{16}O_2^-$) in the "high B" steel after cooling from 1250°C at 31°C/s [123].

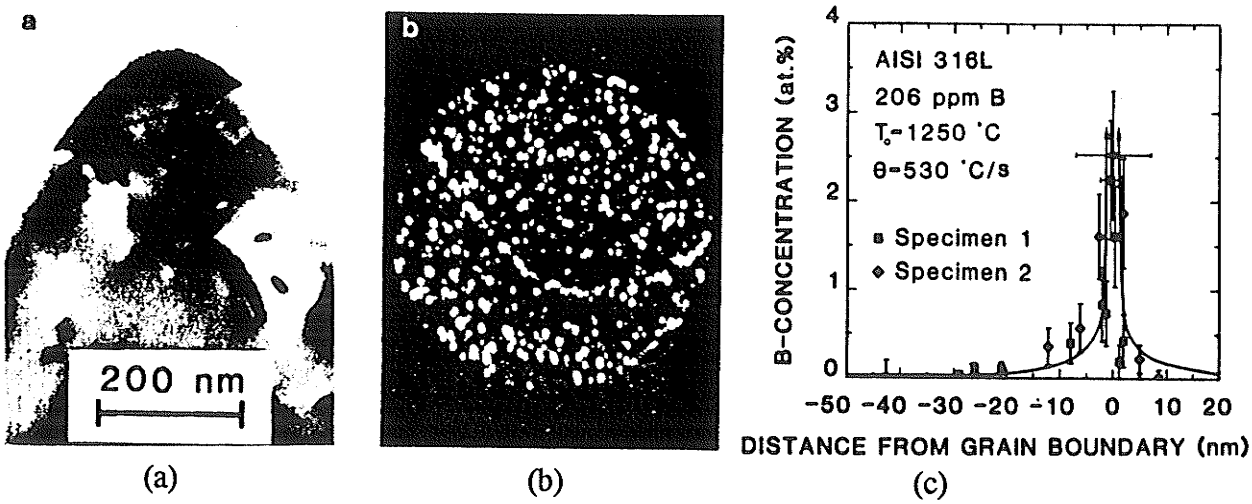

(a) (b) (c)

Fig.2.35 TEM micrographs, FIM micrographs and boron concentration profile for high boron steel. (a) TEM micrographs of specimens containing grain boundaries, (b) Corresponding FIM micrographs of the boundaries and (c) AP concentration profile for B. Each data point represents one AP point analysis. The full lines show the profiles as derived from TEM/FIM/AP/IAP data [128].

2.4.3.10 Summary of Observations on Non-Equilibrium Segregation

(1) Non-equilibrium segregation will occur if the vacancy-impurity binding energy is greater than 0.2eV [114].

(2) A sufficient condition for non-equilibrium segregation to occur is that the solute-vacancy complexes should be more mobile than the free solute atoms. In the opposite case, depletion occurs at the boundary.

(3) The solute or impurity concentration has a maximum at the boundary and extends to a few μm. Farther away, there is a solute depleted zone and the concentration is unaffected in the grain beyond that region.

(4) The maximum impurity enrichment at the grain boundary will occur at some intermediate cooling rate. Higher mobilities of solute increase this cooling rate as do higher starting temperatures and smaller grain size.

(5) The enrichment factor is increased with increasing: i) the difference in mobility of solute-vacancy complexes and free solute atoms, ii) the mobility of solute or solute-vacancy complexes, iii) the grain size, iv) the binding energy of solute-vacancy complexes, v) the starting temperature, and vi) a decrease in the mobility of vacancies.

(6) The cooling rate giving the maximum enrichment factor decreases with decreasing starting temperature.

(7) The differences between equilibrium and non-equilibrium segregation are: i) equilibrium segregation is confined to within a few atomic layers at the boundary and the amount of segregation increases with decreasing temperature; ii) non-

equilibrium segregation gives a broader (often several hundred atom wide layers [128]), smooth concentration profile with the maximum at the boundary and with the amount of segregation increasing with increasing starting temperature. Non-equilibrium segregation is also strongly dependent on the cooling rate, the amount of segregation being highest at some intermediate cooling rate [109,114 and 128].

2.5 Boron and It's Behaviour in Iron and Nickel Alloys

2.5.1 Significance of Boron Addition

Boron is the most effective agent for improving hardenability in steel since a few ppm of boron can result in very significant effects on hardenability [132]. The increase in hardenability has been explained as a result of a reduction in the free energy of the austenite grain boundaries due to segregation of boron atoms, thereby retarding the transformation of austenite. This is achieved by decreasing the number of active nucleation sites [133], and the rate of diffusion of carbon at or near the austenite grain boundaries. Some interaction of boron with carbon is responsible for the effect of boron on hardenability which is indicated by the well-known observation that the efficiency of boron decreases as the carbon content increases [134]. The main effect of boron in stainless steels and superalloys is to improve the creep rupture life of these alloys by inhibiting grain boundary cavitation during creep. Boron is thought to reside in the grain boundaries filling open spaces present there. This strengthens the region by slowing down grain boundary diffusional processes which contribute to creep deformation [132]. This effect can also be related to the influence of boron on the size and spatial distribution of

borocarbides formed during heat treatment prior to creep or during early stages of the creep process. Boron has been also reported to stabilize the fine γ' in superalloys and prevent the formation of denuded zones around grain boundaries [135]. It has been also reported that the mechanical properties of boron containing alloys are less vulnerable to environmental degradation by grain boundary attack in the intermediate temperature regime, where type II hot corrosion occurs [136]. However, the presence of boron, in some cases, also leads to problems of brittleness which is attributed to crack initiation by fine intergranular borocarbides [137].

2.5.2 Solubility of Boron in Iron and Nickel Alloys

The maximum boron solubilities in Goldschmidt's low carbon alloys 20Cr-25Ni, 18Cr-15Ni and 20Cr-25Ni (+Nb,Mn,Si) are 58ppm, 95ppm and 158ppm(wt) respectively [138]. The precipitating phase has been identified in all cases as borides, $(Fe,Cr)_2B$, which form a low melting point eutectic with austenite at temperatures between 1150 and 1225°C depending on the base alloy composition. The solubilities determined by various investigators are given in Table 2-16.

Table 2-16 Solubility of Boron in Austenite

Austenite Matrix	Max. Solubility (wt)ppm	Eutectic Temp. (°C)
Fe	260-210	1140-1174 [139]
Fe	55 (lattice solubility)	1149 [139]
Fe-20Cr-25Ni	58	1150 [138]
Fe-20Cr-25Ni-.6Mn-.6Si-.6Nb	157	1225 [138]
Ni	300	1080 [140]
Fe	210	1170 [141]
Fe	210	1149 [142]
Fe	200	1150 [143]

2.5.3 The Location of Boron in the Solid Solution

The location of boron atoms in the γ-iron lattice has been the subject of some controversy, the atomic radius of boron being intermediate between that of the interstitial elements and the substitutional transition metal alloying elements (as in Table 2-17).

Lattice spacing studies [145,146] in both α and γ iron, with and without boron suggest that boron atoms form a substitutional solid solution while thermal expansion data by

Goldhoff and Spretnak [146] within the γ-iron region between 900 and 1200°C showed a pronounced discontinuity, suggesting a possible change of lattice position of the boron atoms from substitutional to interstitial with increasing temperature. On the other hand, internal friction investigations indicate B to form an interstitial solid solution in α-Fe [147]. Hayashi [148] concluded that boron can occupy both interstitial and substitutional sites in α-iron, and substitutional boron atoms may interact with/or become stabilized by other interstitial atoms such as carbon. Diffusion investigations indicate that the activation energy for boron diffusion in α-iron is of the order expected for substitutional solid solution [149] and is appropriate for interstitial solubility in the case of B in γ-iron [150]. Table 2.18 summarizes the above observations.

Table 2-17 Atomic Radii (Å) of Alloying Elements in Steel [144]

Element	N	C	B	Ni	Fe	Mn	Cr	Mo	Ti	Nb
Radius	.71	.77	.97	1.25	1.26	1.18	1.28	1.40	1.47	1.47

Table 2.18 Boron Sites in Different Alloys

Alloy	Boron Site	Test Method
Fe-13Ni-9B(at) (splat quenched)	0.6% in interstitial 3.6% in substitutional	Lattice parameter measurement by X-ray [151]
γ-iron	Interstitial	Diffusion activation energy [152]
α-iron	Interstitial	Internal friction [145]
α-iron, γ-iron	Substitutional	Lattice parameter [145]
Fe-0.005B(wt)	Substitutional	Lattice parameter [146]
γ-Fe-B	Substitutional-interstitial as temp. increased from 900 to 1200°C	Thermal expansion [146]
Fe-B	Substitutional B-interstitial C pair	Internal friction and strain age behaviour [153]

The simultaneous presence of carbon impurities as competitive-interstitial, or of silicon as competitive-substitutional, could also have a profound influence on boron positioning. The atomic character of the boron solution can apparently be interstitial, substitutional, or both depending on the heat treatment and the alloy's composition [138].

2.5.4 Precipitation from Supersaturated Solution-Types of Boron Compounds

There exist a large number of transition metal borides and borocarbides. Their crystallographic and thermodynamic characteristics have been extensively investigated [154]. The precipitating phase in very low carbon Fe-Cr-Ni alloys is the tetragonal boride $(Fe,Cr)_2B$ and the partial substitution of iron and chromium by other metallic alloying elements such as Ni, Mn etc has been confirmed. Carbon can replace boron to a considerable extent in M_2B compounds, but the possibility of nitrogen substitution does not appear to be documented [154].

An FCC borocarbide $M_{23}(B,C)_6$ was found in carbon-containing stainless steel. The metallic component of this compound is rich in chromium, but can be replaced by Fe, Mn, Mo, and other elements leading to lattice parameter changes as seen in Table 2.19.

Table 2.19 Lattice Parameters of $M_{23}B_6$ Type Borides

Compounds	$Fe_{23}C_6$	$(Fe,Mn)_{23}B_6$	$Cr_{23}B_6$	$Cr_{23}(C_{3/4},B_{1/4})$
Lattice Parameter(Å)	10.7	10.6	10.84	10.71

Boron additions have no substantial effect on the volume fraction or nature of the $M_{23}C_6$ and MC carbides. However, the presence of boron in steel can lead in certain cases to quite marked changes in precipitation kinetics and particle distributions. This effect can be attributed to boron vacancy interaction and the energy of precipitate formation.

Table 2.20 Types of Borides Resulting From Different Processes

Alloy System	Type of Boride	Process
Fe-B	Ni_3B and Fe_3B	In splat-quenched [151]
20Cr-15Ni steel	$Cr_1Fe_1Ni_{0.1}B$ (Cr_2B a=14.71, b=7.41, c=4.25)	[138]
Low carbon steel (55 wt ppm B)	$Fe_{23}(B,C)_6$ (FCC, a=10.6A)	g.b. p.p having parallel cube-cube orientation relationship with one of the neighbouring grains [155]
70Fe-18Cr-2Mo-Si-9B	Fe_3B(a=5.43,b=4.45,c=6.66) FeCrB(a=4.22,b=7.32,c=1.457) M_3B_2	Rapid quenched [155]

In austenitic steel, it has been shown that during slow solidification boron can segregate to the NbC particles of the interdendritic eutectic regions around the eutectic or be precipitated in the NbC particles in these regions. It seems clear, therefore, that boron can substitute for carbon in NbC and that the extent of this substitution increases with a decreasing rate of solidification. Segregation of boron to NbC during the conventional solution treatment of Nb-bearing stainless steel is not anticipated [156].

2.5.5 Boron Segregation and the Determination of Segregation

It had been known that the addition of small amounts of boron may alter the properties of various alloys through the segregation of boron to the grain boundaries. In doing so, grain boundary cohesion will be increased and grain boundary energy reduced. The amount of boron necessary to form a monolayer at a grain boundary has been calculated by making the following assumptions:

1) boron has very little solubility in γ or γ'' phases;

2) the grains are a stacked structure of dodecatetrahedrons;

3) the inter-atomic spacing of atoms at the grain boundary is approximately 0.35nm.

A plot of grain size vs the calculated boron concentration necessary to form a monolayer at grain boundaries is shown in Fig.2.36 [157].

With the development of techniques to directly measure grain boundary segregation of boron, a further understanding of its behaviour has been achieved. The techniques to examine the grain boundary segregation require both high spatial resolution and elemental sensitivity. In 1966, Bean et al [158] applied an autoradiographic method to observe the distribution of boron atoms in intermetallic compounds. The year after, Hughes and Rogers [160] developed the technique further and showed that there was a possibility of detecting the segregation of boron to the grain boundaries in steel containing less than 1 ppm boron. The binding energy of boron/grain boundary in γ-iron has been estimated to be 9.6 ± 1.0 kcal/mol using this method [159]. Ueno investigated the segregation

behaviour of boron in the austenite region [161] by means of autoradiography and found that:

1) Boron atoms migrate to austenite grain boundaries during cooling.

2) The time-temperature-segregation characteristics of Boron are of a C-curve nature (from 600 to 1000°C, with a nose at 700°C).

3) The effect of boron on bainitic transformation depends predominantly on the distribution of boron at austenite grain boundaries. The rate of bainitic transformation is most retarded when boron atoms are segregated homogeneously along the boundaries, but the retarding effect decreases as the degree of boron precipitation increases.

4) The loss of effect of boron on hardenability due to the addition of nitrogen is caused by a decrease in effective boron concentration during quenching.

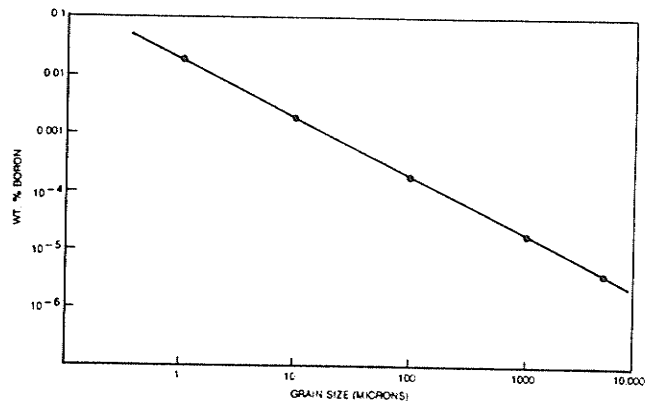

Fig.2.36 Grain size vs calculated wt% of boron needed to form a monolayer of boron at the grain boundaries [157].

Secondary Ion Mass Spectroscopy (SIMS) has been gaining wide application in detection of boron segregation at the grain boundaries since 1971. It has a mass sensitivity of the order of 10^{-10} to 10^{-12} grams and gives a resolution of 1-5μm. Maitrepierre et al employed this technique combined with TEM to examine the influence of boron on the decomposition of austenite in low carbon steels [162]. It was found that the grain boundary segregation of boron was cooling rate dependent and a boron free zone existed on both sides of γ-grain boundaries. These phenomena was attributed to a vacancy-aided boron diffusion. Both boron segregation and $Fe_{23}(B,C)_6$ could inhibit the nucleation of ferrite on γ-grain boundaries.

Boron segregation to the grain boundaries has been also examined by Scanning Auger Microprobe (SAM) on a hydrogen embrittled AISI 1520 steel. It appears that localized boron (either boron segregation to prior austenite grain boundaries or the formation of very small borocarbide clusters or precipitates) is deleterious in the sense of enhancing intergranular hydrogen embrittlement in the absence of any other solute enhancing element except carbon [163].

Combined TEM/SIMS/Autoradiography has revealed [164] that increasing the austenitizing temperature increases the apparent intensity of boron segregation to the austenite grain boundaries during subsequent cooling. This has been explained as follows:

1) The coarser grain size gives a smaller grain boundary area, thus a greater concentration of boron per unit grain boundary for a given amount of boron in

solution.

2) In steels containing strong carbide-forming elements such as vanadium, the boron is partitioned between the matrix and any undissolved carbides. A high austenitizing temperature dissolves the carbides and thus returns boron to solution in the austenite, making more boron available for segregation on the grain boundaries during cooling.

Quantitative analyses of boron segregation have been carried out using both SIMS (Ion-implanted boron in pure iron as a standard) [165] and combined TEM/FIM/atomic probe techniques [128].

2.5.6 Effect of Boron on Surface and Interface Energy

A surface topography technique has been used to measure the etched grain boundary grooves in order to determine the effect of boron concentration on the surface and grain boundary energies at various temperatures [166]. It was found that increasing the boron concentration from 0.001 to 0.006 wt%, while other constituents were kept relatively constant, reduced the ratios of γ_{gb}/γ_{sv} and γ_{gb}/γ_{tb} in all cases. The effect was greatest at 1050 and 1150°C, and least at 1250 and 950°C.

Since the grooves from which the energy ratio were derived were formed during the solution treatment, this effect is attributed to the equilibrium segregation at the solution treatment temperature and is independent of the non-equilibrium processes taking place

during cooling as discussed previously. A reduction in grain-boundary energy (increasing groove angles) by boron was also observed by Adair et al [167]. They found that increasing the temperature from 871°C to 1000°C led to a decrease in the relative interfacial energy, indicating a positive temperature coefficient of adsorption of boron in γ-iron.

Table 2.21 Reduction in Grain Boundary Energies with Increasing Boron Concentration [156,166]

Material	Temp (°C)	Change in B (ppm) concentration	Reduction in γ_{gb}	
			%	Mj/m^2
316 (0.05wt%C)	950	10 to 60	12	45
	1050	10 to 60	34	210
	1150	10 to 60	39	310
	1250	10 to 60	20	130
316 (0.12wt%C)	950	10 to 65	16	55
	1050	10 to 65	29	100
	1150	10 to 65	29	200
	1250	10 to 65	25	150
Ni	900	0 to 100	35	360
	1000	0 to 100	50	420

In the iron and nickel alloys it has been found that the saturation concentration of free surface and grain boundary concentrations expressed in atoms/m^2 were approximately equal [156]. Thus, when a grain boundary fractures, the newly formed surface will have only half its equilibrium concentration of boron and thus $\gamma_{FS} > \gamma_{sv}$ (where γ_{sv} is the free surface energy). When the cracks are formed or extended in order to produce the new surface, an amount of energy must be supplied by the release of stored elastic energy which is at least equal to $2\gamma_{FS}-\gamma_{GB}$ (γ_{FS} is the surface energy of the newly formed fracture surface). If the reduction of γ_{FS} due to the increase in boron content is equal to only half the reduction in γ_{sv}, then $2\gamma_{FS}-\gamma_{GB}$ will be reduced when an increase in the grain boundary segregation of boron occurs [156]. According to the measurement shown in Table 2.21, it appears that boron segregation at the grain boundaries of iron, nickel and 316 S.S. would weaken the grain boundaries.

2.6 Interaction of Sulphur with Other Elements

2.6.1 Effect of Sulphur Segregation and Precipitation of Sulphide

Similar to boron, sulphur has been found to affect the material's properties by forming sulphide or segregating to grain boundaries. A few examples are given here to illustrate sulphur's influence. An abnormal grain boundary hardening trend was found by Westbrook [168] in Ni-S system: the grain boundary hardness decreased rapidly when quenching temperatures were above 600°C and became equal to the grain interior or bulk hardness at ~850°C. As the quenching rate increased from air cooling → oil quenching → water quenching → ice water quenching, the grain boundary hardness increased. These

observations suggest that a vacancy assisted non-equilibrium segregation model controls this hardening process. Tensile tests on Ni-10 ppm S by Thompson [169] showed an increased yield strength and fracture ductility with increased cooling rate from the recrystallization temperature. Increased ductility was correlated with decreasing intergranular fracture and was independent of yield strength. Films of a grain boundary phase which appeared to be Ni_3S_2 were observed in TEM foils and Auger spectroscopy showed that the boundaries were enriched in sulphur. Intergranular embrittlement of a cast Ni-base alloy (84Ni-12Al-4TA, 60 at ppm S) was found after aging at 700°C for 24 hrs. The AES study suggests that the mechanism of age embrittlement in this alloy is related to the formation of a continuous film of sulphide at the grain boundaries [170].

Saindrenan and Larere observed [171] dynamic S segregation to the surface of Ni-270 (99.8% Ni-0.5 wt ppm S) and the effects of segregation of this type within the grain boundaries at temperatures where equilibrium segregation is kinetically impossible. It is suggested that this dynamic sulphur segregation is the result of two mechanisms:

(1) A mechanism corresponding to diffusion of sulphur accelerated by a flux of vacancies in supersaturation. This mechanism may be enhanced during annealing at 450°C following a quench from 1150°C.

(2) The second mechanism is associated with the primary recrystallization and is explained by a dragging of the impurities by the grain boundaries. This phenomenon was observed on cold-worked samples after annealing at 450°C.

2.6.2 Interaction of Alloying and Tramp Elements

Segregation of other elements such as phosphorous, carbon and niobium has been observed in the past and has caused changes to the alloy's properties. Carbon and niobium segregation to grain boundaries made the materials more susceptible to HAZ microfissuring during welding. Phosphorus was found to segregate to grain boundaries and the concentration decreased with increasing austenitizing temperature from 900 to 1100°C for 1hr when a subsequent water quench was used [172,173]. The adhesion of various elements to the grain boundary can be evaluated by the binding energy. The binding energies of tramp elements with the grain boundary are given in Table 2.22.

Table 2.22 Impurity-grain boundary binding energy

P in Fe	-47 KJ/mol [172,174] E_b = -32000 - 17T (J/mol) [150,158]
B in Fe	-97 KJ/mol
C in Fe	-30 KJ/mol
S in Fe	-1.5 eV [101]

The adhesion can also be compared in interfacial activity [156], which is the initial steep slope of the interfacial energy versus bulk concentration curve. Solutes with a very low solid solubility usually have a very high interfacial activity. For example, $IA_{B\text{-}Ni}$, $IA_{B\text{-}Fe}$ = 10^4 mJ/m^{2}at while $IA_{Fe\text{-}P}$ = $10^{2.7}$ mJ/m^{2}at.

In commercial alloys, the segregation of solute atoms can not be considered independently due the interaction of various alloying elements. For example, segregation of carbon atoms can displace phosphorus atoms at grain boundaries in iron [175] and a site competition effect has been also observed in iron containing 40 wt ppm S and 10, 40 and 100 wt ppm C. It has been also found that there is a positive correlation between sulphur and carbon concentrations at a given intergranular surface which is attributed to the effect of grain boundary structure on the number of available sites for impurity segregation. The average sulphur concentration, however, decreases with increasing average carbon concentration at the intergranular surface [176]. The influence of various alloying elements on the segregation of phosphorous has been studied and can be summarized as follows [150,154,158]:

(1) Ni, Cr, Mn and V: These do not affect the segregation of P

(2) B: the intergranular phosphorus concentration is about 50% lower in the boron-containing alloy ($<$ 15wtppm) than in the boron-free samples. The segregation of B and P may be described by an equilibrium of mutual displacement.

(3) Mn: the segregation level of P is increased at higher temperature by enhancing the diffusivity of P. No enrichment of Mn at the grain boundaries has been observed.

(4) C: Carbon alloying was found to slightly decrease P segregation. C segregates to the austenite grain boundaries, not only during quenching, but also in equilibrium in austenite. The effect of carbon on P segregation may be described by means of a segregation equilibrium of mutual displacement.

2.7 Scope and Nature of the Present Investigation

As discussed in the previous section, no comprehensive and systematic study has been carried out to examine the effect of heat treatment on the microstructure and microfissuring of cast Alloy 718. The objective of this study was to understand how the following microstructural aspects affect the HAZ microfissuring: 1) The volume fraction of low melting phases (Laves and M(C,N) phases), 2) Grain boundary precipitation, 3) Grain boundary segregation and 4) Material hardness. Various microstructures were obtained by the following heat treatments:

1. Homogenize as-cast alloy at temperatures of 1037, 1066, 1093 and 1163°C to attain microstructures with different amounts of secondary phases. This is the main focus of the present investigation.
2. Double solution treat (at 927°C/1 hour + 927°C/1 hour) specimens homogenized at 1037, 1066, 1093 and 1163°C to obtain material with various microstructures in solution heat treated conditions.
3. Age (760°C/5 hours + 650°C/1 hour) specimens homogenized at 1037, 1066, 1093 and 1163°C to obtain material with different microstructures at aged condition.

The microstructure was analyzed by analytical scanning electron microscopy (SEM) and analytical transmission electron microscopy (TEM). Segregation of various elements was studied by SIMS and grain boundary orientation by the electron back scatter diffraction (EBSD) technique. Quantitative analysis of secondary phases was carried out using an

optical image analyzer. Specimens after various heat treatments were electron beam welded using a voltage of 44KV and a beam current of 79mA at a welding speed of 152cm/min. The selection of welding parameters, which gave the maximum amount of Heat Affected Zone (HAZ) microfissures, was based on the results of our previous investigation. The microstructure of both the FZ and HAZ were examined using both SEM and TEM. The weldability of the material in various heat treated conditions was evaluated by measuring Total Crack Length (TCL) around the weldment cross section.

In the next chapters, the experiment procedures and the technique used to examine the relevant characteristics of the material will be described.

CHAPTER THREE

EXPERIMENTAL PROCEDURES

Specially cast blocks of Inconel 718 were obtained for these studies. The as-received material as well as variously heat treated material were microstructurally characterized and welded by EB welding technique. The microstructures of the heat affected zone (HAZ), fusion zone (FZ) and microfissuring tendency of the welded material were also evaluated. In this chapter, the details of these techniques will be briefly described.

3.1 Material

Cast Alloy 718 was supplied by Precision Cast Corporation, Portland, Oregon. The material was specially prepared by investment casting technique into 1.6 cm x 8 cm x 20 cm blocks. The chemical composition and mechanical properties of the as-received material are given in Tables 3-1 and 3-2, respectively.

Table 3-1 Chemical Composition of Alloy 718 (wt%)

Ni	Cr	Fe	Co	Mo	Nb	Si	Mn
52.97	18.61	Bal.	0.09	3.06	5.01	0.16	0.03
Ti	Al	B	S	C	P	Mg	Cu
0.81	0.43	0.003	0.005	0.07	0.009	<0.001	0.02

Zr<0.005 and Hf<0.005

Table 3-2 Mechanical Properties of Cast Alloy 718

Ultimate strength: 1075MPa
Yield strength (0.2% offset): 903MPa
Elongation on 4D: 10%
Hardness: 36 Rc

3.2 Heat Treatment

For the preliminary evaluation of microstructure and weldability, various heat treatments were selected with the homogenization temperature ranging from 1037 to 1163°C, and solutioning and ageing temperatures as specified in Table 3-3.

Table 3-3 Heat Treatment Parameters

Homogenization : 1037°C/1hr 1067°C/1hr 1093°C/1hr 1163°C/1hr
Homogenization and Solution : 1037°C/1hr + 927°C/1hr + 927°C/1hr 1067°C/1hr + 927°C/1hr + 927°C/1hr 1093°C/1hr + 927°C/1hr + 927°C/1hr 1163°C/1hr + 927°C/1hr + 927°C/1hr
Homogenization and Ageing: 1037°C/1hr + 760°C/5hr + 650°C/1hr 1067°C/1hr + 760°C/5hr + 650°C/1hr 1093°C/1hr + 760°C/5hr + 650°C/1hr 1163°C/1hr + 760°C/5hr + 650°C/1hr
Homogenization, Solution and Ageing 1037°C/1hr + 927°C/1hr + 927°C/1hr + 760°C/5hr F.C.* to 650°C/1hr 1067°C/1hr + 927°C/1hr + 927°C/1hr + 760°C/5hr F.C. to 650°C/1hr 1093°C/1hr + 927°C/1hr + 927°C/1hr + 760°C/5hr F.C. to 650°C/1hr 1163°C/1hr + 927°C/1hr + 927°C/1hr + 760°C/5hr F.C. to 650°C/1hr

*F.C.-Furnace cool at a rate of 55°C/hr

For grain boundary segregation analysis and subsequent HAZ microfissuring evaluation, the material was initially heat treated to 1250°C at a controlled heating rate of 1°C/min from 1000°C, held for 30 mins and then water quenched. By using slow heating, constitutional liquation was prevented. Using this homogenization treatment, the majority of the secondary phases went into solution and a 'clean' microstructure was obtained for evaluation. The material was then subjected to a series of heat treatments at temperatures and cooling rates given in Table 3-4. The cooling rates were determined by an implanted thermocouple and the average cooling rates from heat treatment temperature to 500°C were measured.

Table 3-4 Heat Treatment Temperature, Holding Time and Cooling Methods

Temp.(°C)	950	1037	1163	1240
Time (min.)	136	96	45	23
Cooling Methods	Air Cool* & Water Quench#	Air Cool & Water Quench	Air Cool & Water Quench	Air Cool & Water Quench

* Air Cool ≈20°C/sec

\# Water Quench ≈ 400°C/sec

The holding time was chosen to give the same boron diffusion distance, d=1 mm, at various heat treatment temperatures as calculated using the diffusion equation.

$$d=\sqrt{2Dt} \qquad <56>$$

where $D=2x10^{-7}exp(-0.91\ Ev/Kt)$ (m^2/s) [128], k=Boltzmann's constant and T=temperature (K).

Additional heat treatments as detailed in Table 3-5 were carried out to examine the effect of the hardness of the material on HAZ microfissuring.

Table 3-5 Heat Treatment Parameters Used to Examine the Effect of Hardness

1163°C/1hr
1163°C/1hr + 760°C/5hr F.C. to 650°C/1hr (Age)
1163°C/1hr + 927°C/1hr + 927°C/1hr (Solution Treat)
1163°C/1hr + 760°C/200hrs (Overage)
1163°C/1hr + 927°C/1hr + 927°C/1hr (Solution Treat) + 760°C/200hrs (Overage)

3.3 Sample Preparation

3.3.1 Metallographic Examination

Samples for metallographic examination (optical and SEM) were sectioned from blocks heat treated to various conditions described in 3.2, and mechanically polished through

abrasive SiC paper to a final 1 μm diamond slurry. All specimens were etched either chemically in Kalling's #II reagent or in 10% oxalic acid electrolytically at 3-5 V for 30 to 60 seconds using a stainless steel beaker as the cathode.

3.3.2 Weldability Evaluation

Specimens for evaluation of weldability were sectioned perpendicular to the welding direction at 1 cm intervals. Five sections were examined for each heat treatment condition, each being metallographically prepared using the technique described in 3.3.1.

3.3.3 Carbon Extraction Replicas

The replication technique was used to prepare specimens for TEM examination of the precipitates in the FZ and HAZ. A carbon film was deposited onto a bulk specimen. The carbon deposition was carried out under vacuum of about $2x10^{-5}$ torr using an Edwards Auto 306 Vacuum Coater. The carbon film on the sample was then scored into 3mm x 3mm squares and electrolytically etched in 10% HCl/methanol solution at 20-30 V until separated from the substrate. The carbon films were floated in distilled water and then gathered on 200 mesh copper grid for examination in a TEM.

3.3.4 Thin Foil Microscopy

Specimens for TEM evaluation were sliced with a slow speed diamond saw. After mechanical grinding down to about 120μm thickness, 3mm discs were mechanically punched from the specimens. A Gatan Disc Grinder 623 was used to further thin the

discs to about 80 μm and then a dimple with thickness around 10 to 20 μm was made using a Gaton 656 Dimple Grinder in the centre of the disc. Discs thus prepared were then ion milled by a Gatan-Dual Ion-Mill at 600 V and 1mA, using a starting angle of 15° and a finishing angle of 10°.

3.3.5 Specimens for SIMS Analysis

Heat treated cubes (1cm x 1cm x 1cm) as described in Table 3-4 were cut in half, and the cut surfaces were polished using standard metallographic techniques and lightly etched electrolytically in 10% oxalic acid to reveal the grain boundaries. Microhardness indentations were used to mark the grain boundaries in the etched condition and the specimens were then repolished using a diamond paste to remove the etched layer.

3.3.6 Specimen Preparation for EBSD Analysis

Grain boundary orientations in various specimens were measured using an Electron Back-Scattered Diffraction (EBSD) technique. Since this technique is relatively sensitive to surface deformation, specimens were mechanically polished with 6 μm diamond paste and then electrolytically polished using 20% H_2SO_4 in methanol at 25 V and 2-4 A for 20 seconds using a stainless steel beaker as the cathode.

3.4 Instrumentation

3.4.1 Optical Microscopy

Two optical microscopes were employed in this study: 1) Olympus-Vanox T for

microstructural examination at intermediate magnifications (50~1000X), 2) Vickers Fifty-Five microscope for observing and recording the overall weldment at low magnifications (5~15X).

3.4.2 Scanning Electron Microscopy (SEM)

The microstructures of the base material, HAZ and fusion zones were examined using a JEOL 840 SEM using the secondary electron image mode on the etched surface. Semi-quantitative composition analyses were carried out using Energy Dispersive Spectrometry (EDS) with either beryllium window (7.6μm) or Norvar window (0.3μm). HAZ microfissures were measured on the SEM at a magnification of 550X.

3.4.3 Transmission Electron Microscopy (TEM)

High resolution microstructural analysis of the base metal and weldments was performed using a JEOL 2000 FX TEM/STEM equipped with a Tracor Northern model TN 5400 EDS detector/spectrometer (beryllium window). Selected Area Diffraction (SAD) and EDS semi-quantitative chemical analysis were used to characterize various observed phases according to their crystal structure and chemical composition. Carbon extraction replicas were used to study the nature of second phase particles extracted from the fusion zone and HAZ. The grain boundary precipitates were examined by thin film electron microscopy technique.

3.4.4 Image Analysis

Volume fraction of various microstructural constituents were measured using a Leitz Image Analyzer with more than 2000 points being counted for each heat treatment condition. The standard deviation was calculated using the following formula:

$$p=p\pm z\sqrt{\frac{p(1-p)}{n}} \qquad <57>$$

where p is the volume fraction obtained, n is the number of points counted and z=1.96 for 95% confidence level. Table 3-6 lists the standard deviation at various volume fractions and numbers of points counted.

Table 3-6 Standard Deviation of the Measurement [177]

Volume Fraction	Standard Deviation at 95% Confidence Level	
	2000 points	4000 points
0.1	0.0130	0.0093
0.05	0.0095	0.0067
0.02	0.0061	0.0043
0.01	0.0044	0.0030
0.005	0.0031	0.0020
0.001	0.0014	0.0009

3.4.5 Hardness Testing

An effort was made to correlate the HAZ microfissuring with the material's bulk hardness after various heat treatments. The hardness was measured using a Rockwell Hardness Tester. The reported values (HR_B) are an average of five readings.

3.4.6 Gleeble Simulation

The Gleeble tester, a computer-controlled high temperature thermomechanical simulation device, was used to produce a large HAZ area in several variously heat treated specimens for microstructural evaluation. Laboratory scale specimens (3cm long and 1cm diameter) were resistance heated between water-cooled copper jaws by pulsed (120Hz) alternating current. A thermocouple was percussion welded to the midpoint of the specimen surface, providing the feedback signal for control of the thermal cycle. All specimens were subjected to a thermal cycle as illustrated in Fig.3.1. The thermal cycle produced during electron beam welding is also included in this figure for comparison. Gleeble simulation tests were conducted at CANMET, Ottawa, using a Gleeble 1500.

3.4.7 Differential Scanning Calorimetry (DSC)

A NETZSCH DSC 404 was used to detect dissolution/liquation temperatures of various phases during heating and the alloy's solidification path during cooling. The heating and cooling rates used in this study were 20°C/min. Reaction temperatures were determined by finding the temperature at which the DSC curve deviated from the local baseline. The determination was somewhat subjective when two reactions overlapped. Reaction

temperatures were determined from the heating curves. Tests were carried out by Netzch in Germany to the above requirements and the data was supplied to the author for analysis.

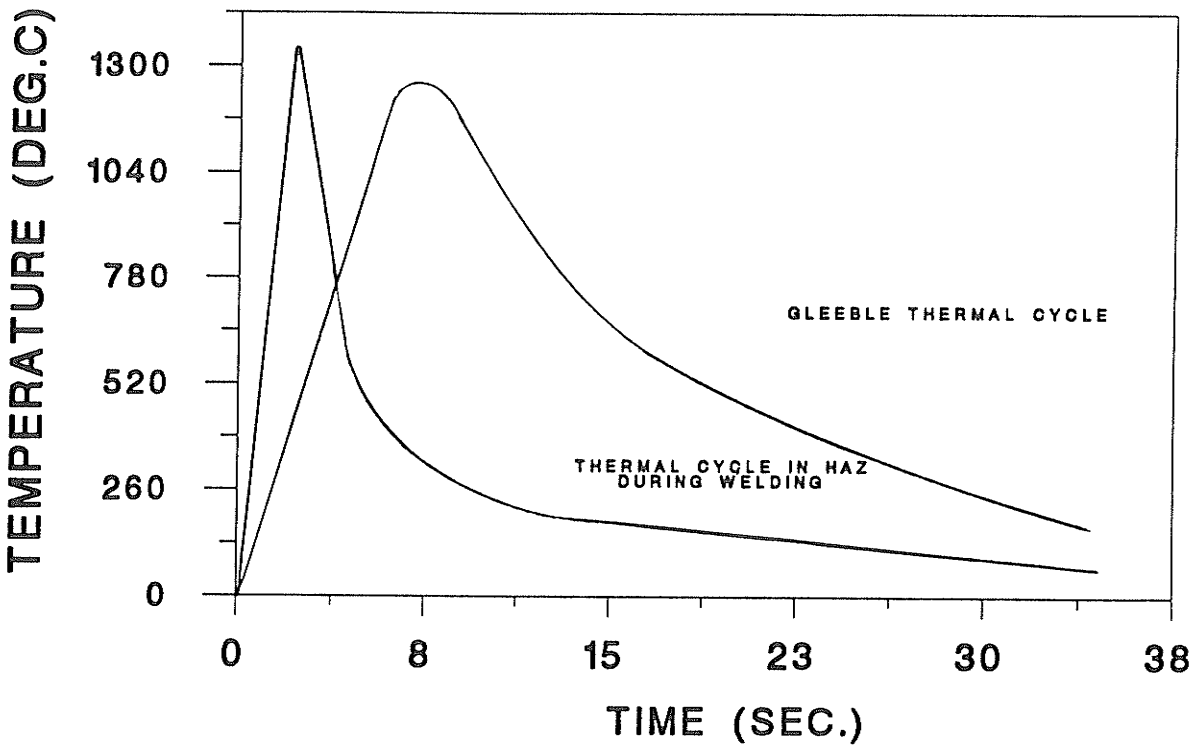

Fig.3.1 Comparison of thermal cycles during gleeble test and electron beam welding.

3.4.8 Secondary Ion Mass Spectrometry (SIMS)

The principle of SIMS can be described as the energetic ion bombardment of the surface of a material which causes atoms to be ejected by the sputtering process. A fraction of sputtered species are ejected either as positive or negative ions and the mass of this fraction can be analyzed in a mass spectrometer to determine the elemental composition

of the surface. Because of the very high signal/background ratios which are peculiar to mass spectrometry, this technique is extremely sensitive and can thus detect trace quantities of elements on a surface. SIMS can provide ion images with spatial resolution of a few μm and elemental resolution to a few ppm. Primary ion beams of O_2^+, O^-, Ar^+, Xe^+ and Cs^+ are normally available on the instrument. Very electronegative elements such as H, O, S, and P are most sensitive to a cesium ion beam, while an O_2^+ ion beam is primarily used for most other elements. For boron detection, SIMS has a superior concentration resolution as compared to other techniques (Fig.3.2) and analysis can be conducted on a larger area. For these reasons, SIMS was chosen to analyze elemental segregation, especially that of boron to the grain boundaries.

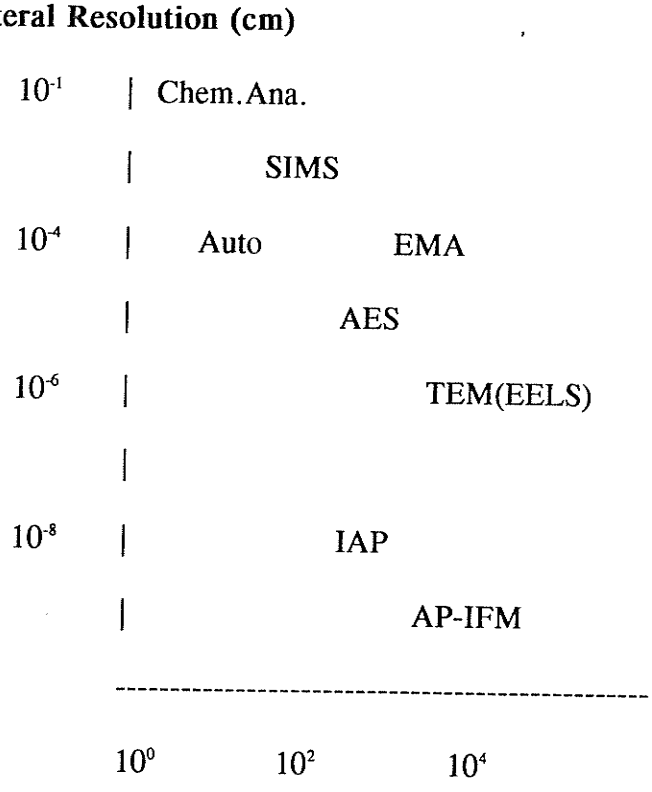

Fig.3.2 Boron Detection Limit ppm(wt) [179].

The heart of a SIMS apparatus is the combination of a primary beam source and a mass spectrometer to analyze the sputtered ions. Additionally, a preparation chamber where samples can be etched, cleaved or chemically treated, and fast entry lock are included. An atom beam (such as an inert gas) and liquid metal ion beam (such as Cs) can be used as the primary beam. A neutral primary beam is usually produced by passing a high-energy ion beam through a chamber containing high pressure inert gas. The ion component of the beam is removed using electrostatic deflection plates. When a liquid metal source is used, the liquid metal flows through a fine aperture and, under the influence of a high positive electrostatic field relative to its surroundings, forms a cone from the apex of which intense positive ion emission occurs.

The depth of SIMS analysis, which is an important consideration in segregation studies, depends primarily upon the sputtered depth during the time of analysis. It extends from 5 to 50 Å deep, depending upon the energy of primary ions, the ion production area (controlled by beam size and raster gating parameters) and ion detection sensitivities [178].

The analyses of elemental segregation at grain boundaries in this study were carried out by the author using a Cameca IMS-4f Secondary Ion Mass Spectrometer at CANMET, Ottawa. Negatively or positively charged secondary ions emitted from the surface were used to obtain mass-resolved ion images. SIMS analysis was performed using the following instrument settings:

Raster: 250-500 μm

Image Field: 250 μm

Primary Beams: O_2^+, Cs

Primary Ion Beam Current: 2.5 μA

Primary Ion Beam Voltage: 12.5 keV

E-Slit: Partially Closed

Boron segregation can be examined on both mass 42 ($^{10}B^{16}O^2$) (20% abundance) and mass 43 ($^{11}B^{16}O^2$) (80% abundance). When mass 42 was used, there was no interference from other elements as seen from Fig.3.3, while $^{27}Al^{16}O$ can produce an overlapping image with mass 43 ($^{11}B^{16}O^2$) as seen in Fig.3.4. Therefore, the $^{10}B^{16}O_2^-$ signal on mass 42 was recorded to prevent the interference of $^{27}Al^{16}O^-$ with $^{11}B^{16}O_2^-$. Other elements such as C, S, P, Al, Mo and Nb were also analyzed by collecting specific secondary ions as listed in Table 3-7.

Table 3-7 Primary and Secondary Ions Used for Detecting Different Elements

Elements	Primary Ion	Secondary Ion
S	C_s	S^-
P	C_s	P^-
B	O_2^+	$^{10}B^{16}O_2^-$
C	O_2^+	C^-
Nb	O_2^+	Nb^+, NbO^-
Mo	O_2^+	Mo^-
Al	O_2^+	$^{27}Al^{16}O^-$

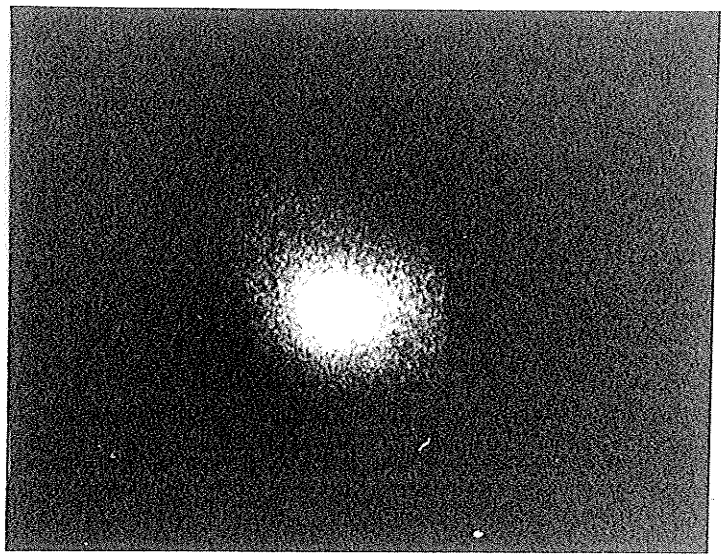

Fig.3.3 Image of mass 42 ($^{10}B^{16}O^{-}_{2}$).

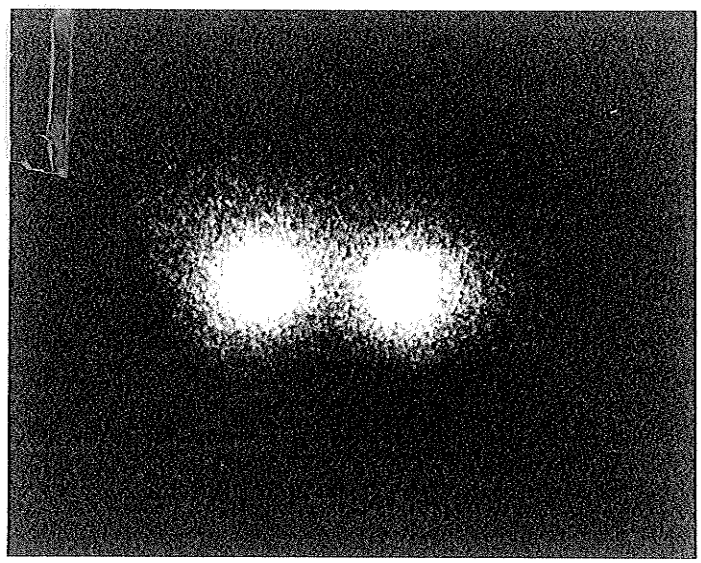

Fig.3.4 Image of mass 43 ($^{27}Al^{16}O^{-}$ and $^{11}B^{16}O^{-}_{2}$).

3.4.9 Electron Back-Scatter Diffraction (EBSD)

There are numerous methods that can be used to detect the grain boundary orientation [180]: optical, x-ray, neutron, TEM-based and SEM-based techniques. EBSD technique used in the present study is one of the SEM-based methods.

Electron back-scatter diffraction patterns are generated by the interaction of a primary electron beam with a steeply tilted specimen. In order to view the diffraction pattern, two preliminary but essential steps are needed in addition to the usual procedures used when operating an SEM for conventional topographical examination. The first requirement is that the angle between the incident beam and the specimen surface be small, 10°-30° in order to minimize the amount of signal which is absorbed and to maximize the diffraction proportion. The second requirement is related to specimen preparation. The beam/specimen interaction depth is approximately 10nm and this layer must be relatively strain free and clean to obtain the patterns. The diffraction patterns are essentially Kikuchi patterns. They are formed in the SEM when a stationary probe is focused on the specimen. Initially, the incident beams scattered elastically through large angles within the specimen so that electrons diverge from a point source just below the specimen surface and impinge upon crystal planes in all directions. The subsequent elastic scattering of the divergent electrons by the crystal planes forms an array of Kikuchi cones whenever the Bragg condition is satisfied. Inelastic scattering events also occur and these contribute to a diffuse background. There are two diffraction cones for each set of crystal planes, one from diffraction from the upper side and one from diffraction from

the lower side of the planes. The intensities of the cones are determined by structure factor considerations and dynamical diffraction under a many-beam condition. Patterns are obtained by the intersection of the Kikuchi cones with the viewing screen.

EBSD is now accepted as being the optimum technique for the routine measurement of grain boundary misorientation and grain boundary plane orientation. Its particular advantages over selected area channelling (SAC) technique are the greatly improved resolution (100-300 nm in the best case compared to 2-3 μm) and the analysis efficiency (at least 10 times faster). Although TEM is capable of obtaining data from grains 10 nm diameter at an angular precision of 0.1, the sample preparation for TEM analysis is very tedious and only a limited number of grains can be examined. Therefore, EBSD was considered to be the most suitable technique for conducting determination of grain orientations in the present study.

The grain orientations on the polished surface of cast and wrought Alloy 718 specimens were measured by EBSD using a JEOL-840A SEM at Ontario Hydro Research Centre, Toronto. An operator carried out the analysis under instruction from the author. The SEM was equipped with an on-line electron-backscattered-diffraction pattern analysis system developed by Dingley. A typical computer-enhanced electron back scatter pattern from a FCC lattice is shown in Fig.3.5.

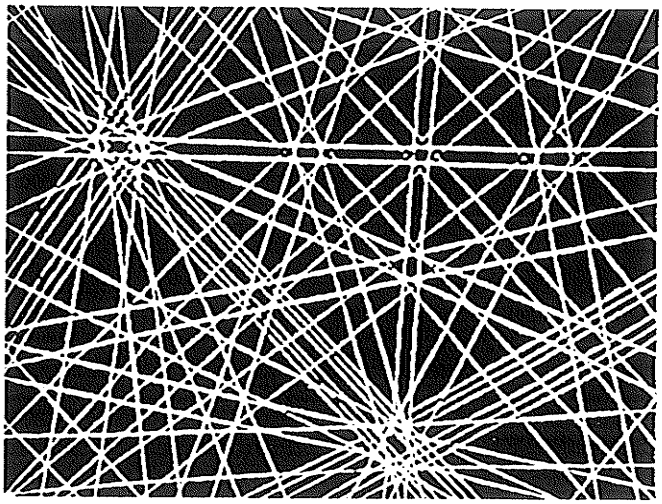

Fig. 3.5 Typical computer-enhanced EBSP from FCC structure.

A combined misorientation angle between two grains and the axis of misorientation is characterized by the reciprocal of the proportion of shared lattice sites, i.e. a 'Coincidence Site Lattice', CSL. The value of this parameter is designated Σ. The most common example is a primary twin boundary which has a Σ value equal to 3. The commonly accepted procedure for assessing boundary type is called the Brandon Criterion which will be described in the results section.

3.4.10 Welding and Microfissuring Evaluation

Bead-on-plate welding was carried out on as-received as well as heat treated plates using a Sciaky Mark VII electron beam welder at Bristol Aerospace Ltd., Winnipeg. The EB welder was used with a sharp focus (no beam oscillation) at 44KV, 79mA and 152cm/min. The plates were ground and cleaned prior to the welding operation. A

temperature profile of welding was obtained by implanting thermocouples in the HAZ and FZ (Fig.3.1).

The microfissuring tendency of specimens that were given different heat treatments was evaluated by measuring the Total Crack Length (TCL) in the HAZ. In previous work [74], a cracking index was used to characterize HAZ weld cracking behaviour. The cracking index was defined as

$$C.I.=\Sigma\frac{l_1+l_2+l_3+l_4+l_5+\cdots}{area\ of\ HAZ} \qquad <58>$$

where l_1, l_2, and l_3 are individual crack length measurements.

The cracking index normalizes the HAZ cracking relative to varying heat inputs. In the present case, since the welding parameters were kept constant, the area of the HAZ is, therefore, constant. Hence, the cracking index can be substituted by the TCL_i value which is the sum of the individual crack lengths measured over a constant area of HAZ in various samples. In order to statistically increase the reliability of the TCL_i values, five measurements were made on different sections for each heat treatment and the sum of those values was used as the TCL in this investigation. Specifically,

$$TCL=\sum[\sum(l_1+l_2+l_3+etc.)]=\sum(TCL_1+TCL_2+TCL_3+etc.) \qquad <59>$$

CHAPTER FOUR

RESULTS

In this chapter, the results of the microstructural examination of the base metal, HAZ and FZ and HAZ microfissuring will be described. The effect of heat treatment on microstructure and HAZ microfissuring tendency are also compared.

4.1 Microstructural Examination of Base Material

4.1.1 Microstructure of As-Received Material

The microstructure of as-cast Alloy 718 was initially evaluated on the optical microscope. As shown in the optical micrograph (Fig.4.1), a heavy dendritic structure was present in the as-received cast Alloy 718, with dark interdendritic areas and bright dendritic areas. Some precipitates were found in the interdenditic area. The cast alloy 718 was also observed to have very coarse grain size, ranging from 3 to 10mm.

The composition of both dendritic and interdendritic areas were analyzed using SEM/EDS and the results are shown in Table 4-1. Note that Nb is strongly partitioned to the interdendritic areas, while Cr and Fe are depleted in the interdendritic area. Si, Ti and Mo are slightly enriched in the interdendritic areas and Ni does not show any partitioning.

Table 4-1 Chemical Composition of

Dendritic and Interdenditic Areas (wt%)

	Interdendritic Area			Dendritic Area		
	Ave.	Max.	Min.	Ave.	Max.	Min.
Al	0.41	0.54	0.13	0.56	0.73	0.44
Si	0.43	0.86	0.27	0.27	0.37	0.15
Ti	1.38	1.85	1.10	0.48	0.60	0.38
Cr	15.04	18.56	8.41	20.1	20.27	19.78
Fe	13.95	17.35	7.36	20.8	21.55	19.65
Ni	51.47	54.55	48.39	52.3	52.96	52.05
Nb	13.88	24.86	7.41	2.7	3.76	2.07
Mo	3.34	4.60	2.64	2.88	4.08	2.54

The secondary phases observed in the interdendritic area were examined in SEM. There are five types of precipitates present in the cast structure and all of these particles have distinct morphologies, i.e. needle-like, eutectic, cubic, irregular and disk-shaped. It has been reported [5,25] that phases commonly present in Alloy 718 are needle-like δ-Ni_3Nb, island like A_2B Laves phase, cubic TiN nitrides, discrete MC carbides and disk-shaped γ"(Ni_3Nb) + spheroidal γ'(Ni_3Al). The chemical composition of various constituents was

measured semi-quantitatively by EDS on an as-etched surface and a certain deviation would be expected due to the preferential etching of chemicals to different phases. The chemical compositions included in the following tables are from the average of ten measurements and the variation is within $\pm 5\%$. Phases were tentatively identified by their unique characteristic morphologies and confirmed by their chemical compositions.

The needle-like δ-Ni_3Nb in the cast alloy 718 is shown in Fig.4.2. The EDS analysis was performed on this phase using the electron beam in a spot mode. Due to the resolution limitations of EDS/SEM, about 2μm laterally and 5 μm in depth, the composition of δ-Ni_3Nb phase given in Table 4-2 is not considered to be very accurate. EDS/TEM was used to more precisely determine the composition of δ phase in thin foil. The results (Table 4.3) show that δ phase can be expressed as $(Ni,Cr,Si,Fe)_{0.70}(Mo,Nb)_{0.3}$. The difference between EDS/SEM and EDS/TEM can be observed by comparing the results in Table 4-2 and Table 4-3. The composition determined by EDS/SEM is a combination of δ phase and the matrix, therefore, higher values of Ni, Fe, and Cr were obtained in EDS/SEM than in EDS/TEM.

Using the Norvar plastic window, recently added to the SEM, light elements such as C and B can be detected. Carbon was not found in the cubic-shaped particles as seen in Fig.4.4. A strong nitrogen peak (Fig.4.5a) was observed on EDS spectrum of Ti-rich M(N), however, the software was not able to quantify the amount of nitrogen. The precipitate is thus identified as a nitride, enriched in Ti with other element partitioning

on M position in M(N). Both carbon and nitrogen peaks were observed on the EDS spectrum (Fig.4.5b) of irregular-shaped particles (Fig.4.4), which can thus be identified as M(C,N) carbonitrides. The chemical composition determined using the Norvar window are also included in Table 4-2.

The observed lamellar eutectic phase (Fig.4.2) was found from EDS analysis (Fig.4.3b) to have a chemical composition of A_2B, where A represents Fe, Cr, Si and Ni, and B represents Nb, Mo and Ti. It is therefore confirmed to be a eutectic Laves phase.

Disk shaped γ" phases were found in the vicinity of γ/Laves constituent in some as-received material as illustrated in Fig.4.6 which is not the common case in this material. The chemical composition measurement was also conducted using both EDS/SEM and EDS/TEM. The composition obtained from SEM has larger amounts of Ni, Fe and Cr in γ" phase than that determined by TEM. A stoichiometry of γ" phase can be deduced to be $(Ni,Cr,Fe)_{0.75}(Mo,Nb)_{0.25}$ from the EDS/TEM measurements.

In summary, the as-cast alloy is found to consist of a γ-matrix, needle-like δ-Ni_3Nb (Fig.4.2), cubic Ti-rich M(N) (Fig.4.4), lamellar Laves phase (Fig.4.2) and irregular-shaped Nb-rich M(C,N) (Fig.4.4). Occasionally particles of γ" phase (Fig.4.6) are also present. The compositions of the various phases determined by EDS/SEM are summarized in Table 4-2.

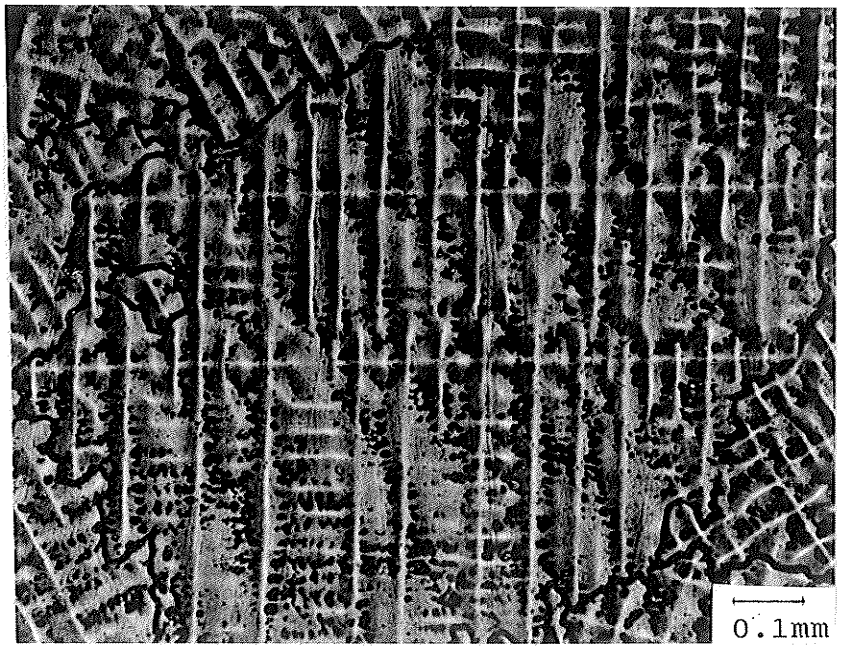

Fig. 4.1 Optical micrograph of cast Alloy 718 at as-cast condition, heavy dendritic structure was observed.

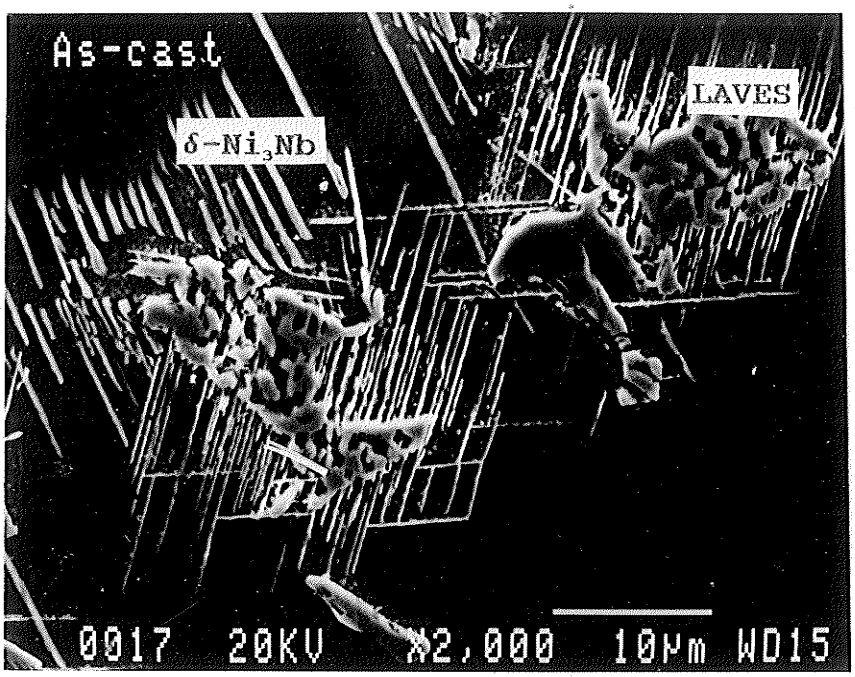

Fig.4.2 Microstructure of δ-Ni_3Nb phase and Laves phase in the as-cast material.

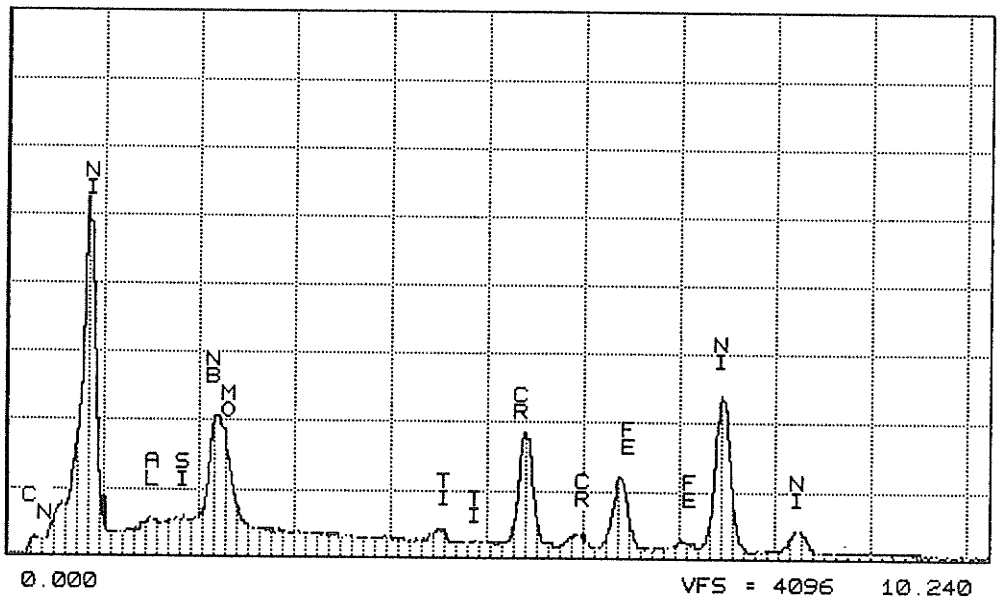

(a)

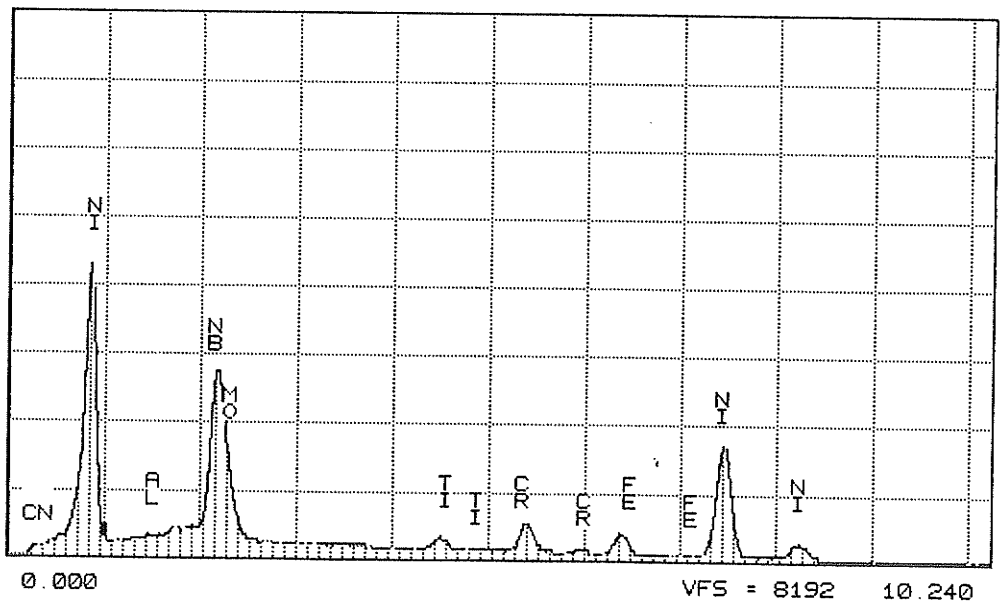

(b)

Fig.4.3 EDS spectra of δ-Ni_3Nb phase (a) and Laves phase (b).

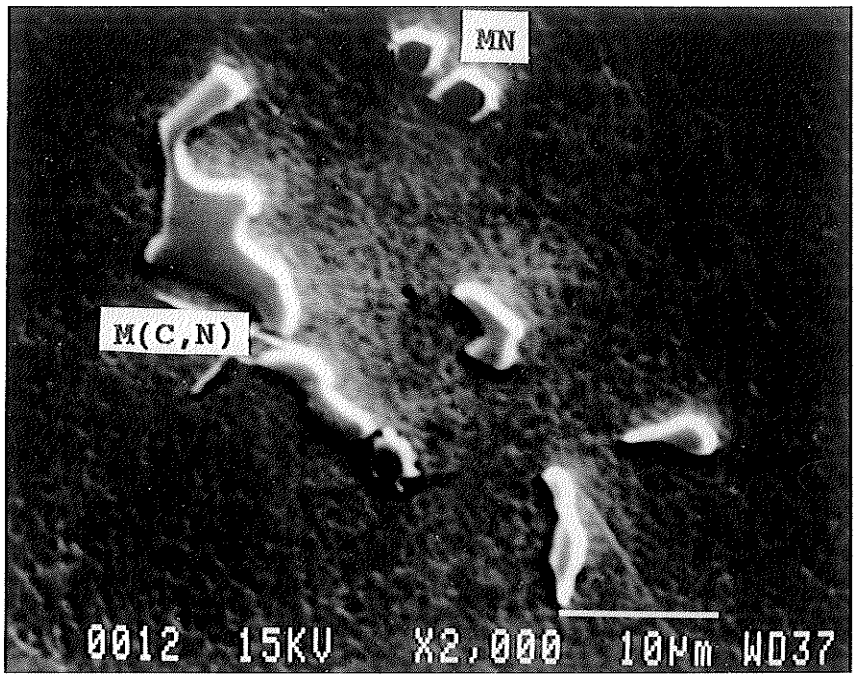

Fig.4.4 Cubic shaped MC and Irregular shaped M(C,N) in the as-cast condition.

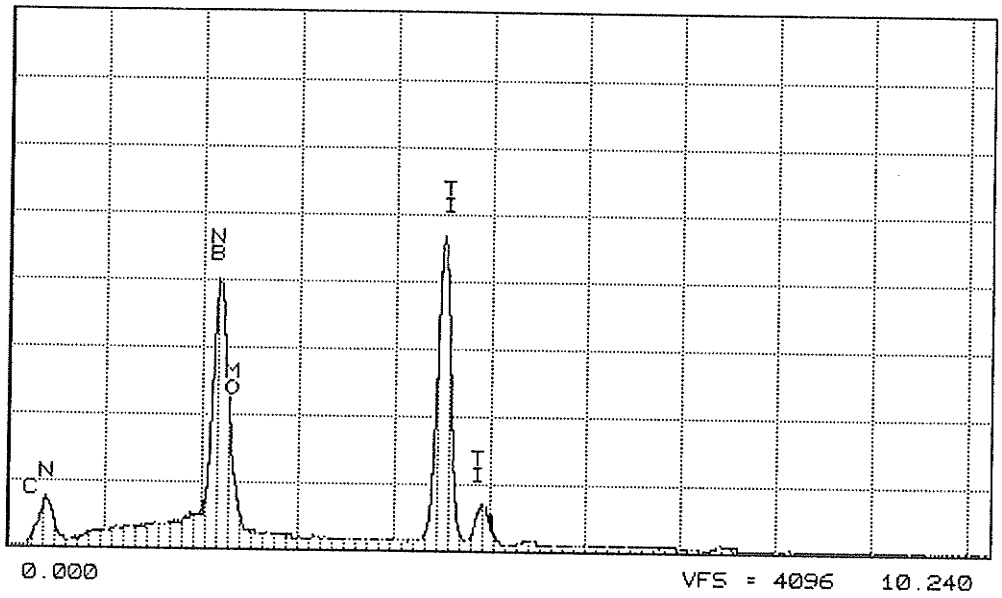

(a)

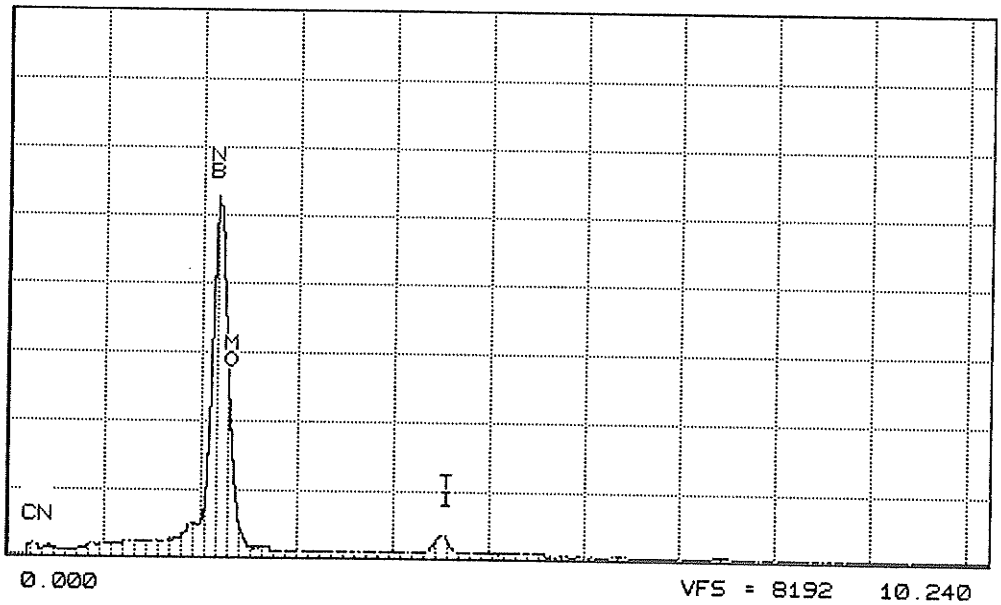

(b)

Fig.4.5 EDS spectra of MN nitride (a) and M(C,N) carbonitride (b).

Fig.4.6 γ"-Ni_3Nb in the as-cast Alloy 718

TABLE 4-2 Chemical Composition of Different Phases

Determined by SEM/EDS

	δ-Ni_3Nb	γ''	Laves		M(C,N)		MN
	wt%	wt%	at%	wt%	wt% (incl.C)	wt%	wt% (incl.C)
Al	0.64	0.58	1.24	0.53	0	0	
Si	0.47	0.49	2.12	0.95	0	0	0
Ti	1.31	1.19	1.12	0.85	2.9	7.99	0
Cr	16.27	16.19	19.15	15.86	0.78	0.89	0.94
Fe	14.72	14.66	14.43	12.84	0.75	0.56	0.65
Ni	52.0	52.22	42.08	39.36	1.86	1.13	1.42
Nb	10.13	10.28	14.20	21.02	69.88	86.46	35.14
Mo	4.50	4.38	5.03	7.69	1.18	2.97	1.58
C					22.64		0

Table 4-3 Chemical Composition Determined by EDS/TEM

	δ-Ni_3Nb		γ"-Ni_3Nb	
	wt%	at%	wt%	at%
Al	0	0	0	0
Si	0.18	0.45	0	0
Ti	0	0	2.37	3.25
Cr	11.73	15.51	2.81	3.56
Fe	11.08	13.44	1.79	2.11
Ni	35.56	40.92	62.03	69.29
Nb	23.26	16.98	20.59	14.59
Mo	18.11	12.81	10.25	7.04

4.1.2 Microstructures After Homogenization Heat Treatment

Specimens after homogenization treatments at 1037°C/1hr, 1066°C/1hr, 1093°C/1hr and 1163°C/1hr were examined in SEM and the microstructures are shown in Fig.4.7a, b, c and d. The microstructure of specimens heat treated at 1037°C/1hr (Fig.4.7a) contains three types of phases with distinct features: needle-shaped, lamellar eutectic and irregular-shaped phases. These phases were identified by EDS to be δ-Ni_3Nb, Laves

phase and M(C,N) carbonitrides. A smaller amount of δ-Ni_3Nb phase was observed in the 1037°C/1hr heat treated specimen as compared to the as-cast microstructure. As the homogenization temperature increases from 1036 to 1093°C, the amounts of needle-shaped δ-Ni_3Nb and lamellar Laves phase decrease as can be observed from Fig.4.7 a,b and c. The microstructural examination of a specimen after the 1163°C/1hr heat treatment indicated that the needle-shaped δ-Ni_3Nb had completely dissolved, as shown in Fig.4.7d, and Laves phase was hardly detectable. However, no change in the amounts of Nb(C,N) and TiN was observed. Comparing Fig.4.7a,b,c and d, it can be concluded that both δ and Laves phases decreased with increasing homogenization temperature, while the amount of M(C,N) carbonitrides remained constant.

4.1.3 Microstructures After Solution Treatment

The microstructures after homogenization and solution treatments were examined in SEM and are shown in Fig.4.8 a, b, c and d, representing specimens heat treated at 1037°C/1hr + 927°C/1hr + 927°C/1hr, 1066°C/1hr + 927°C/1hr + 927°C/1hr, 1093°C/1hr + 927°C/1hr + 927°C/1hr and 1163°C/1hr + 927°C/1hr + 927°C/1hr respectively. All the secondary phases, needle-shaped Ni_3Nb, eutectic Laves phase and irregular M(C,N) carbonitrides, found in the as-cast and homogenized conditions were also present in the homogenization and solution treated specimens. When Fig.4.7 is compared with Fig.4.8, it can be observed that in both conditions an increase in homogenization temperature causes a reduction in the amounts of δ-Ni_3Nb phase and Laves phase and the M(C,N) does not seem to be affected. An increased amount of δ was observed after solutioning,

which is more evident by comparing the microstructure of 1093°C/1hr specimen (Fig.4.7c) with that of 1093°C/1hr + 927°C/1hr + 927°C/1hr specimen (Fig.4.8c). It was also observed that most of the grain boundaries after solution treatment were covered by δ-Ni_3Nb precipitates as seen in Fig.4.9a and b.

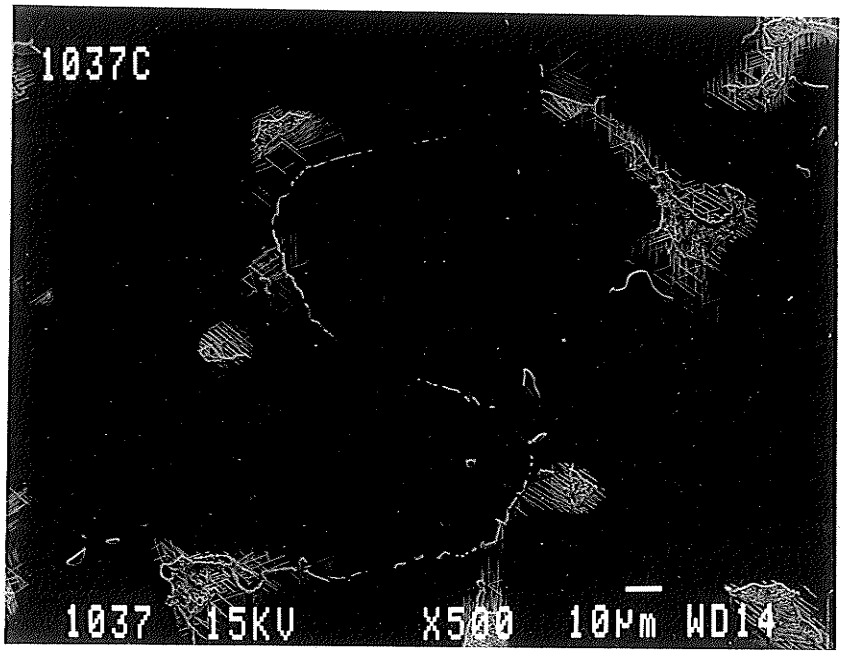
1037C
1037 15KV X500 10µm WD14

(a)

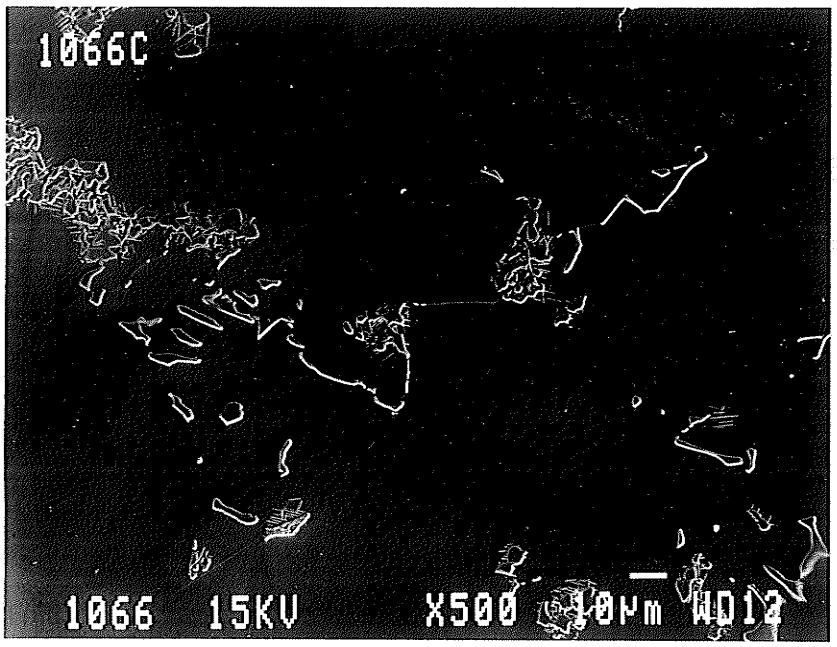
1066C
1066 15KV X500 10µm WD12

(b)

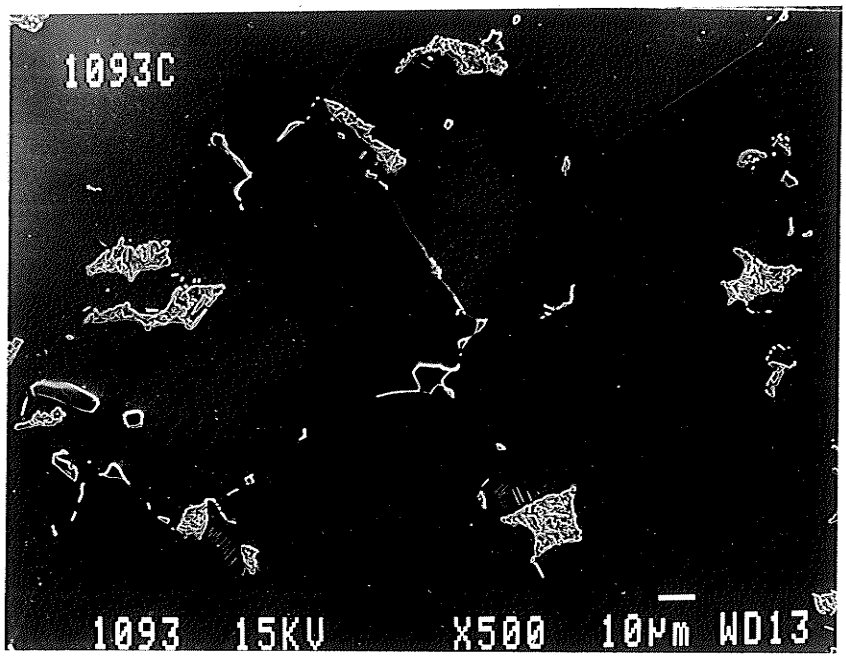

(c)

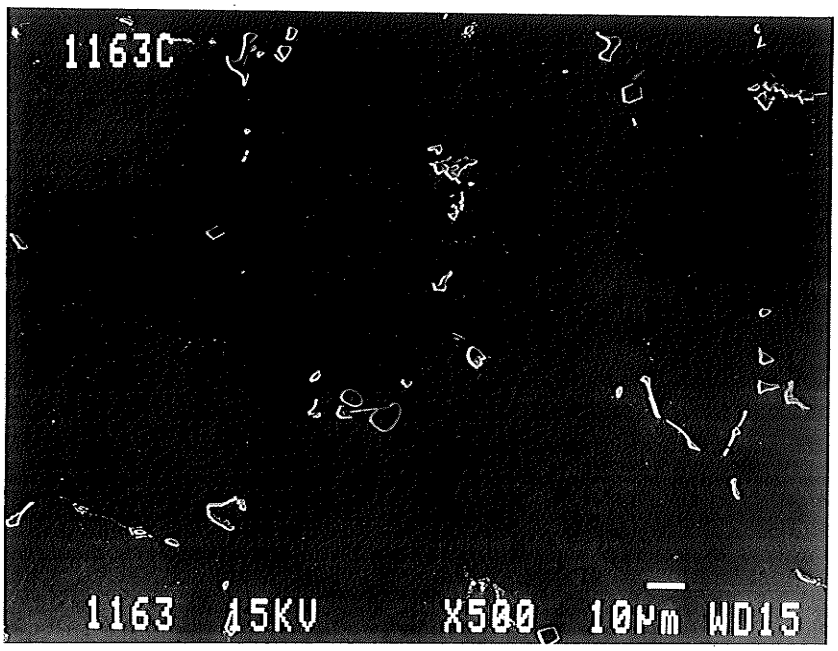

(d)

Fig.4.7 Microstructures after homogenization treatment for 1 hr at 1037°C (a), 1067°C (b), 1093°C (c) and 1163°C (d).

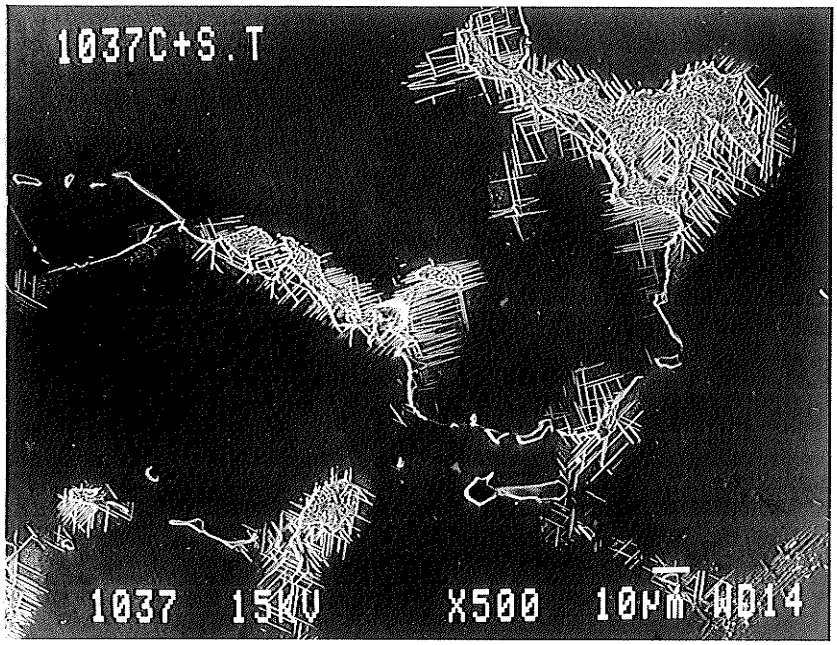
1037C+S.T
1037 15KV X500 10μm WD14

(a)

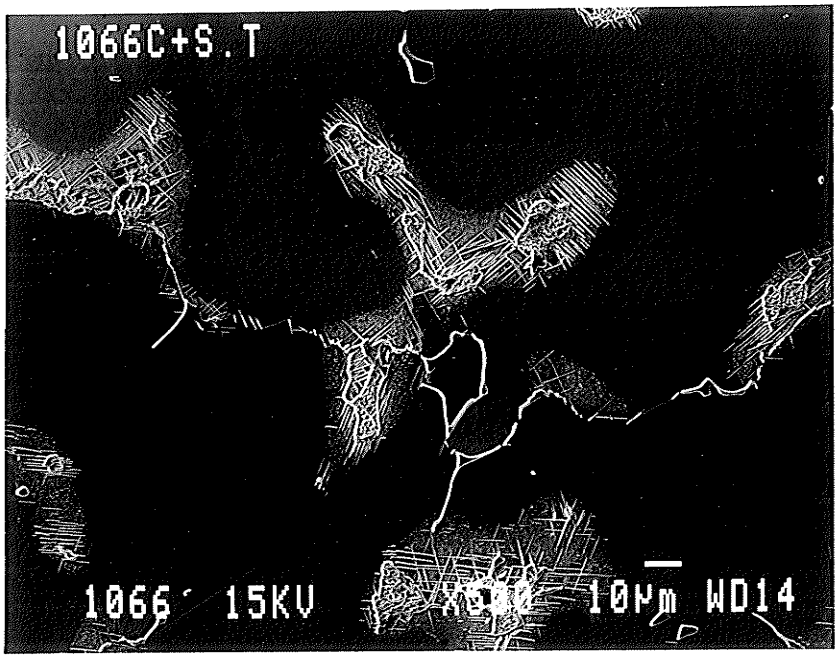
1066C+S.T
1066 15KV 10μm WD14

(b)

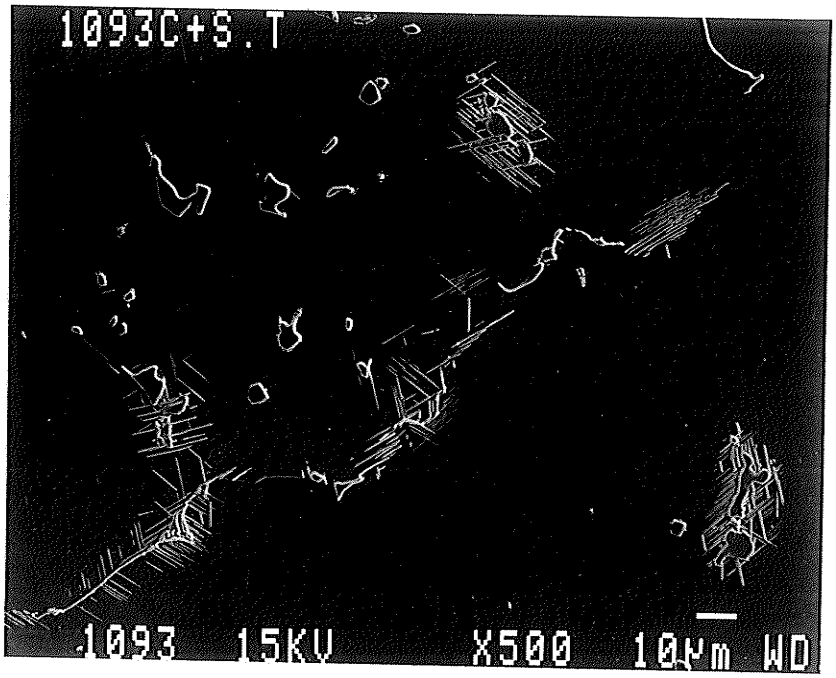

(c)

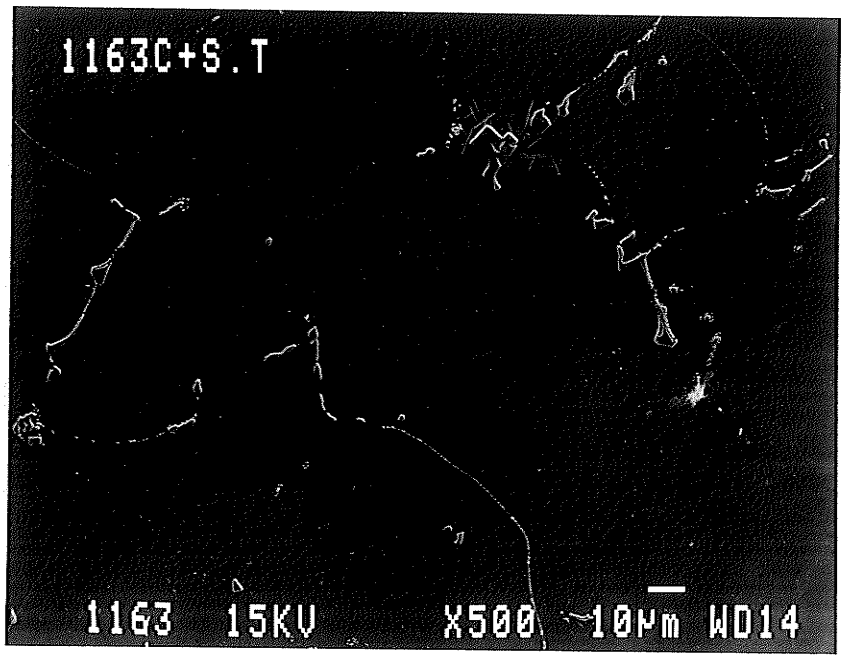

(d)

Fig.4.8 Microstructures after homogenization treatment for 1 hr at 1037°C (a), 1067°C (b), 1093°C (c) and 1163°C (d) followed by solution treatment at 927°C/1hr + 927°C/1hr.

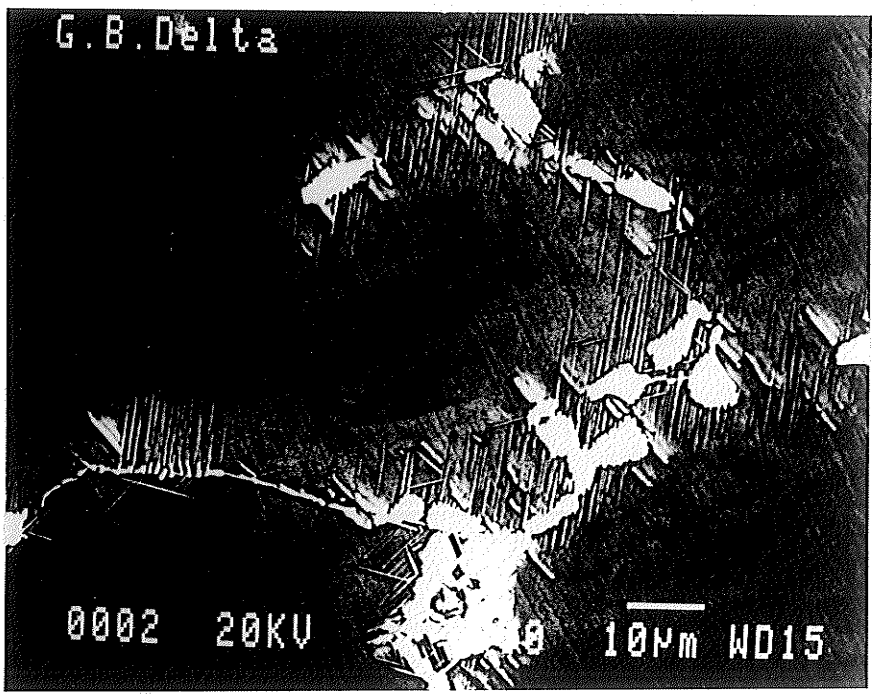

(a)

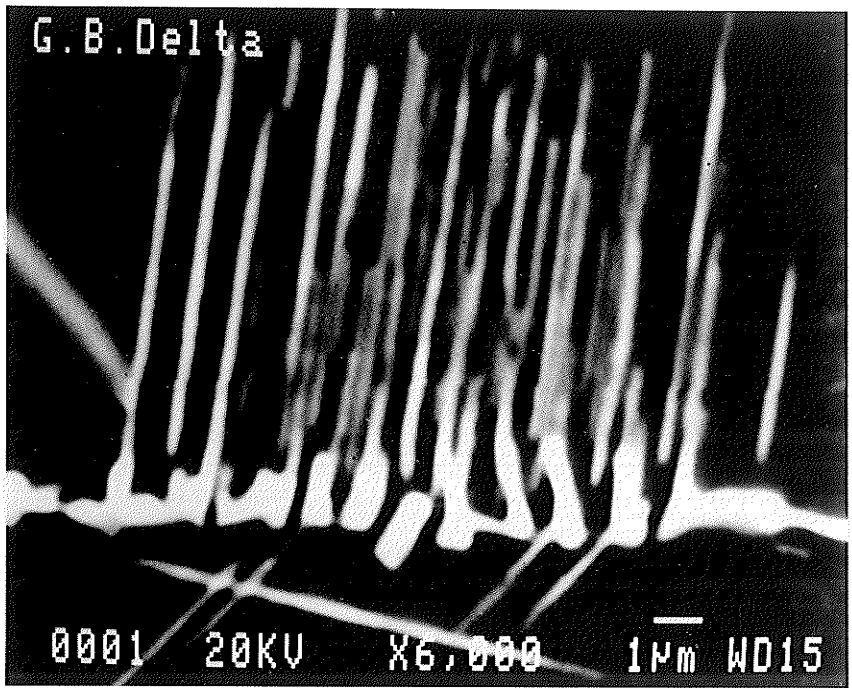

(b)

Fig.4.9 Microstructure after solution treatment showing grain boundary δ-Ni_3Nb at low magnification (a) and high magnification (b)

4.1.4 Microstructures After Ageing Treatment

The microstructures of the specimens aged at 760°C/5hrs + 650°C/1hr after being homogenized at 1037°C, 1066°C, 1093°C and 1163°C are shown in Fig 4.10 a, b, c and d. By comparing these with the microstructures shown in Fig.4.7, it is seen that there is no apparent microstructural change as observed in SEM after ageing (Fig.4.10). It is known that γ" and γ' precipitate during aging which leads to hardness changes. However, they would be too fine to be resolved in SEM. The hardness changes after various heat treatments will be given in section 4.3.

4.1.5 Microstructures After Homogenization, Solution and Ageing Treatments

The microstructures after homogenization (1037°C/1hr, 1066°C/1hr, 1093°C/1hr and 1163°C/1hr), solution (927°C/1hr + 927°C/1hr) and ageing (760°C/5hrs + 650°C/1hr) treatments are shown in Fig.4.11 a, b, c and d, respectively. Secondary phases, δ-Ni_3Nb, eutectic Laves phase and M(C,N) carbides, were observed and their volume fractions varied with the homogenization and solution treatments in the same manner as described in 4.1.3. The amount of Laves phase and δ-Ni_3Nb decreased with an increase in the homogenization temperature and more δ-Ni_3Nb precipitated during solution treatment as compared to the homogenization treated material (Fig.4.7). Ageing treatment after solution treatment results in precipitation of γ"+γ' which, however, can not be resolved in SEM. Hardness increase after ageing, which will be presented in section 4.3, indicated the precipitation of γ"+γ' phases.

4.1.6 Microstructures After Overageing Treatment

The microstructures after overageing at 760°C for 200 hours were analyzed by SEM. As shown in Fig.4.12, the main changes observed on overaging was a coarsening of $\gamma" + \gamma'$ precipitates, such that their size is sufficiently large to be resolvable in SEM.

4.2 Quantitative Analysis of Secondary Phases

The volume fractions of the various phases after homogenization, homogenization and solution, and homogenization and ageing heat treatments were measured using image analysis. The results are plotted against homogenization temperature in Fig.4.13, 4.14 and 4.15. Quantitative analyses confirmed the observations reported in 4.1. Specifically, during homogenization the δ-Ni_3Nb phase went into solution at about 1093°C (Fig.4.14) and the majority of the Laves phase was in solution at 1163°C (Fig.4.13); solution treatment enhances δ-Ni_3Nb precipitation as compared to only homogenization treatment (Fig.4.14), and ageing heat treatment slightly decreased the amount of δ-Ni_3Nb and Laves phases (Fig.4.13 and 4.14). The total amount of carbonitrides and nitrides were observed to be unaffected by the heat treatments used in this study as shown in Fig.4.15. γ' and $\gamma"$ are too fine to be measured quantitatively using image analysis technique.

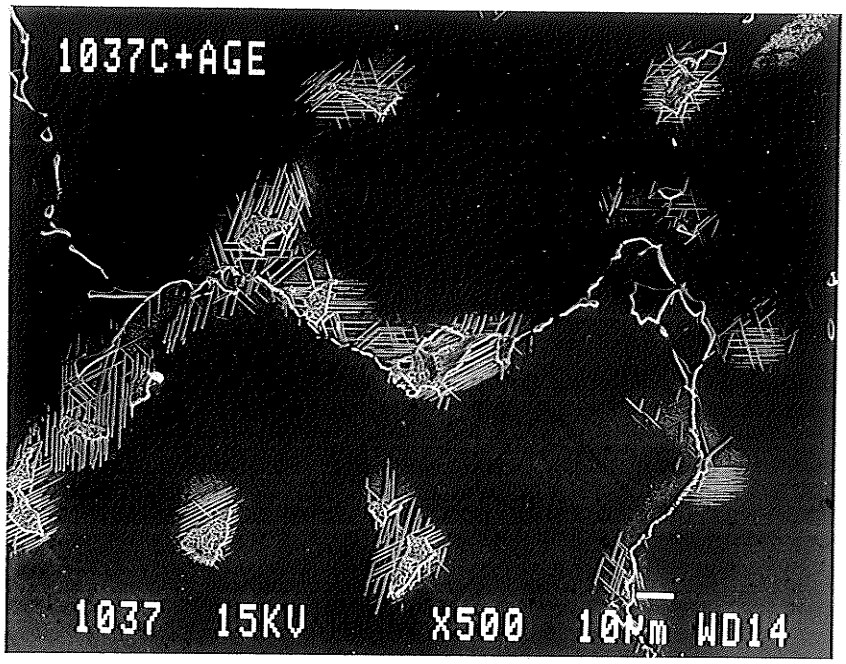
1037C+AGE
1037 15KV X500 10µm WD14

(a)

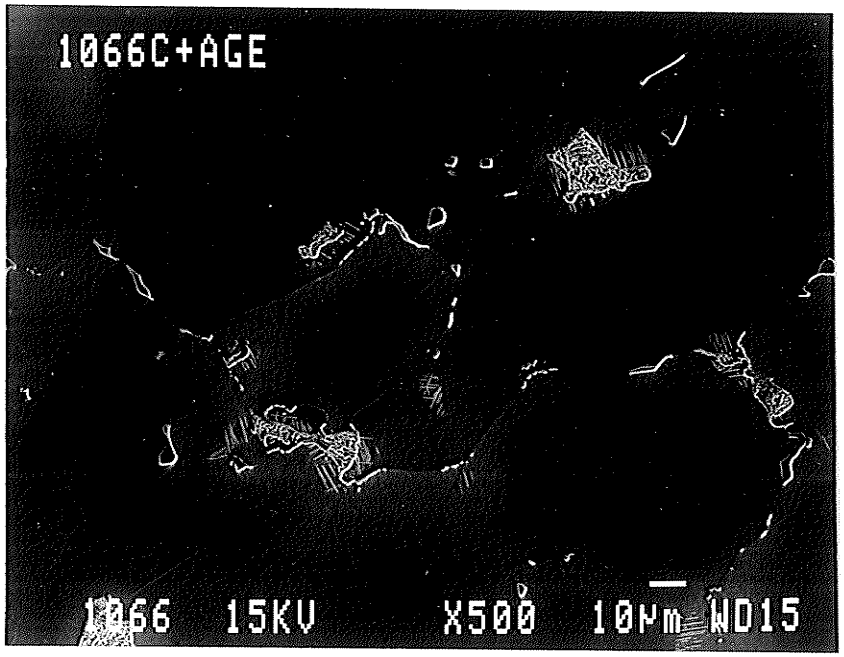
1066C+AGE
1066 15KV X500 10µm WD15

(b)

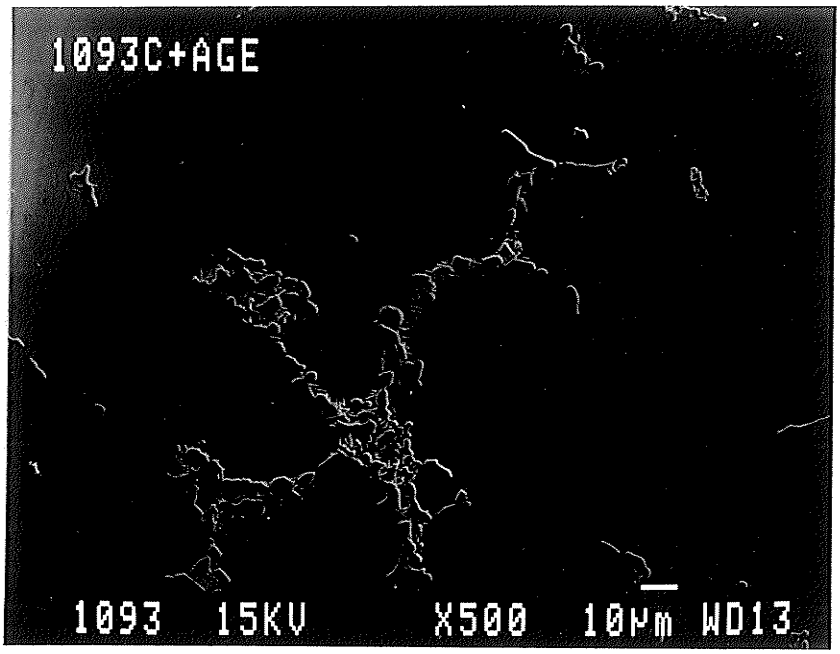

(c)

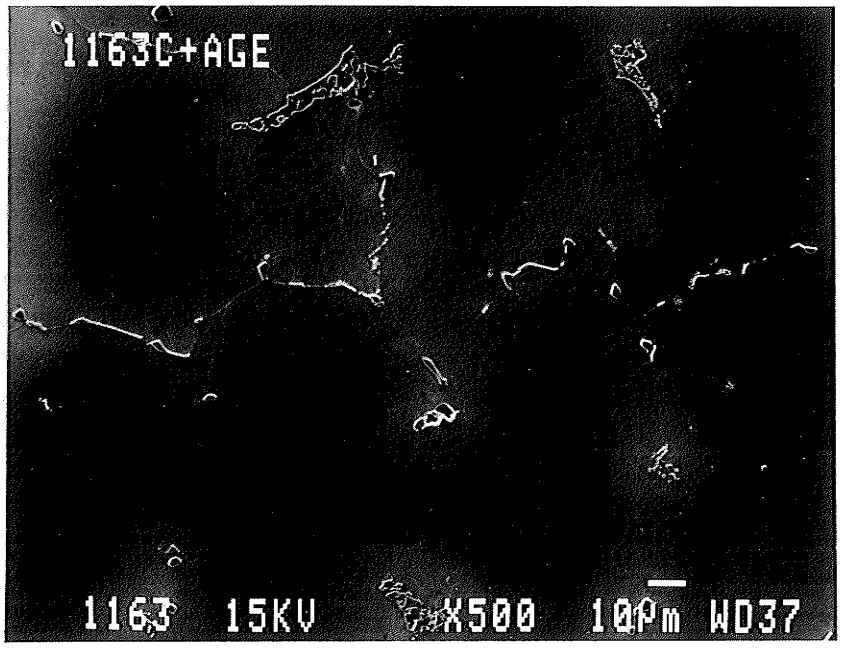

(d)

Fig.4.10 Microstructures after homogenization treatment for 1 hr at 1037°C (a), 1067°C (b), 1093°C (c) and 1163°C (d) followed by ageing at 760°C/5hrs F.C. to 650°C hold for 1hr.

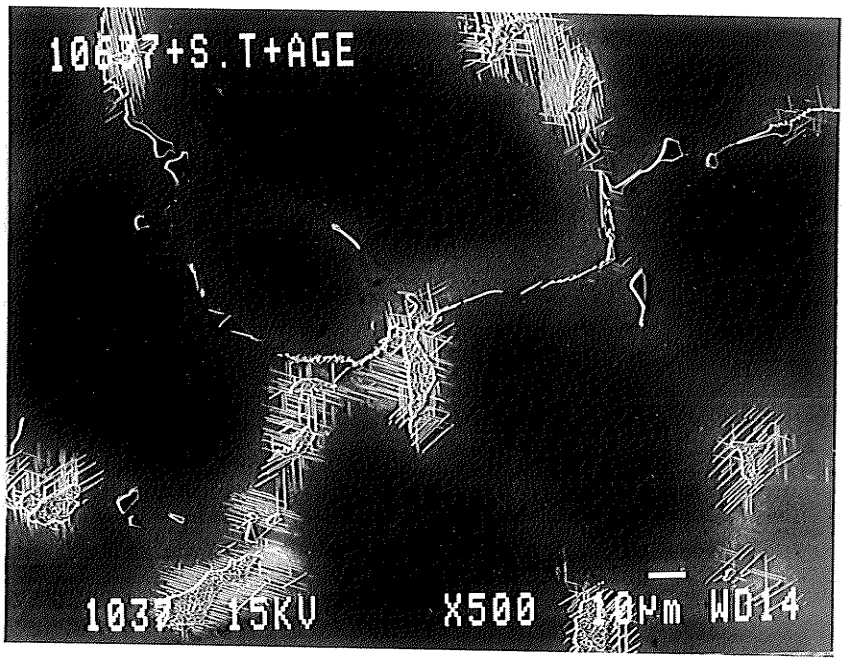
1037+S.T+AGE
1037 15KV X500 10µm WD14

(a)

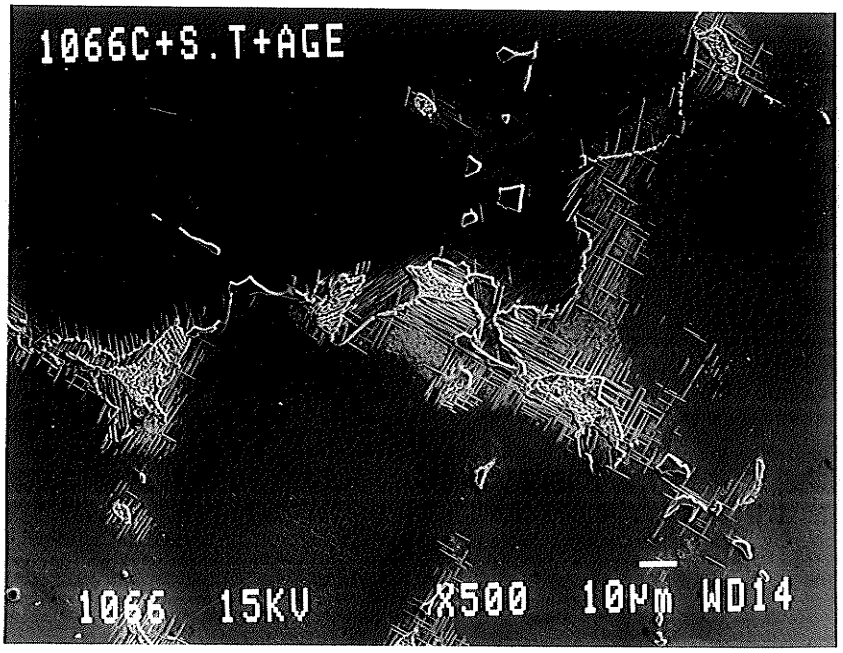
1066C+S.T+AGE
1066 15KV X500 10µm WD14

(b)

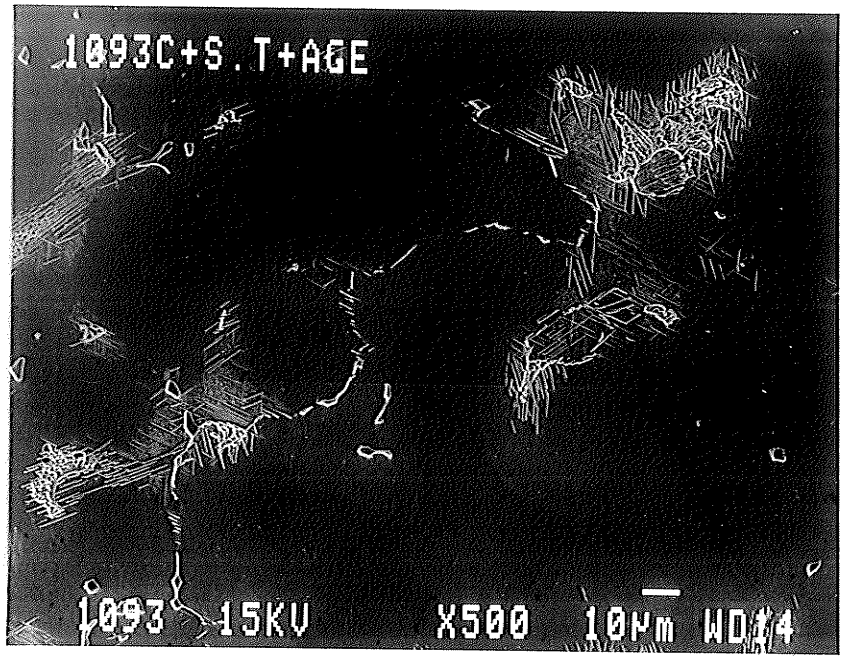

(c)

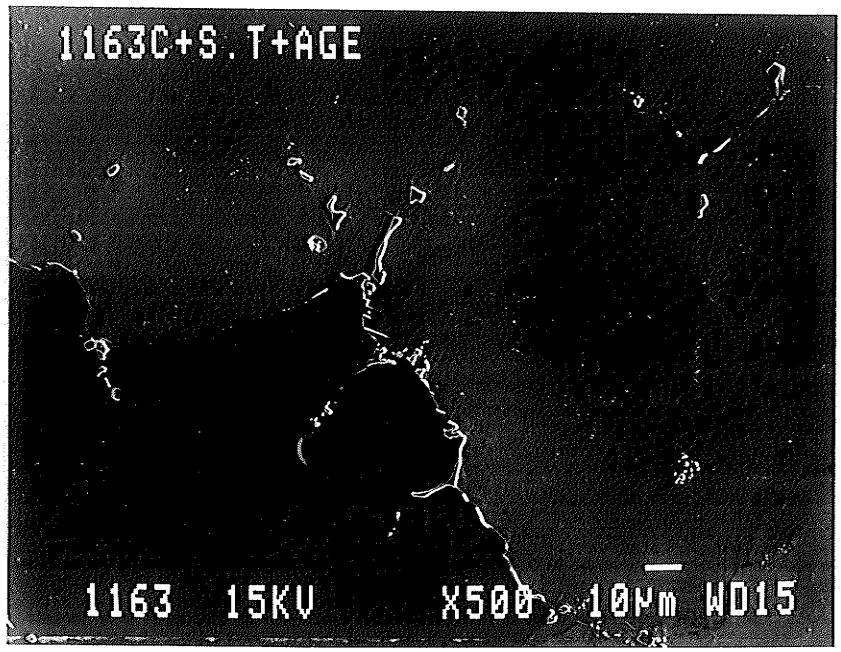

(d)

Fig.4.11 Microstructures after homogenization treatment for 1 hr at 1037°C (a), 1067°C (b), 1093°C (c) and 1163°C (d) followed by solution treatment at 927°C/1hr+927°C/1hr and ageing at 760°C/5hrs F.C. to 650°C hold for 1hr.

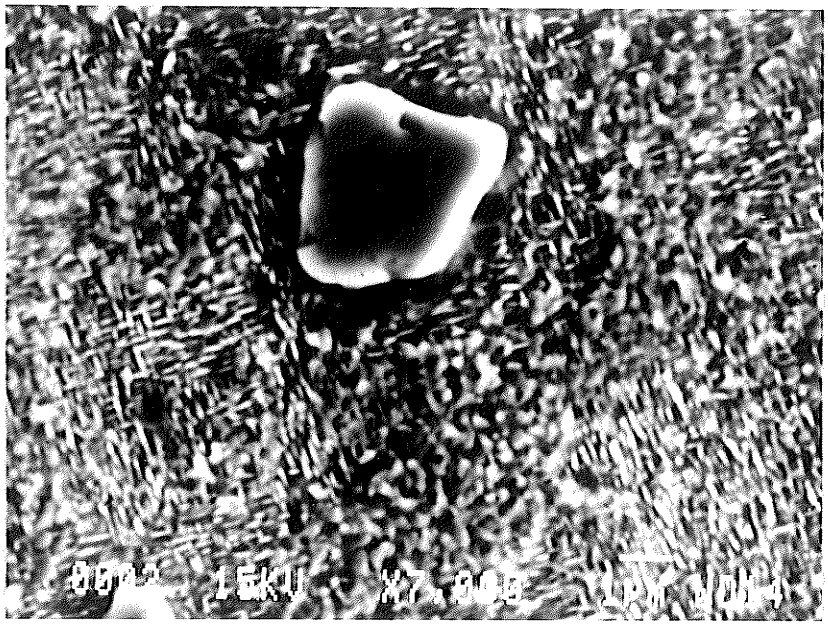

Fig.4.12 Microstructure after homogenization and overageing treatments at 1163°C/1hr + 760°C/200 hrs.

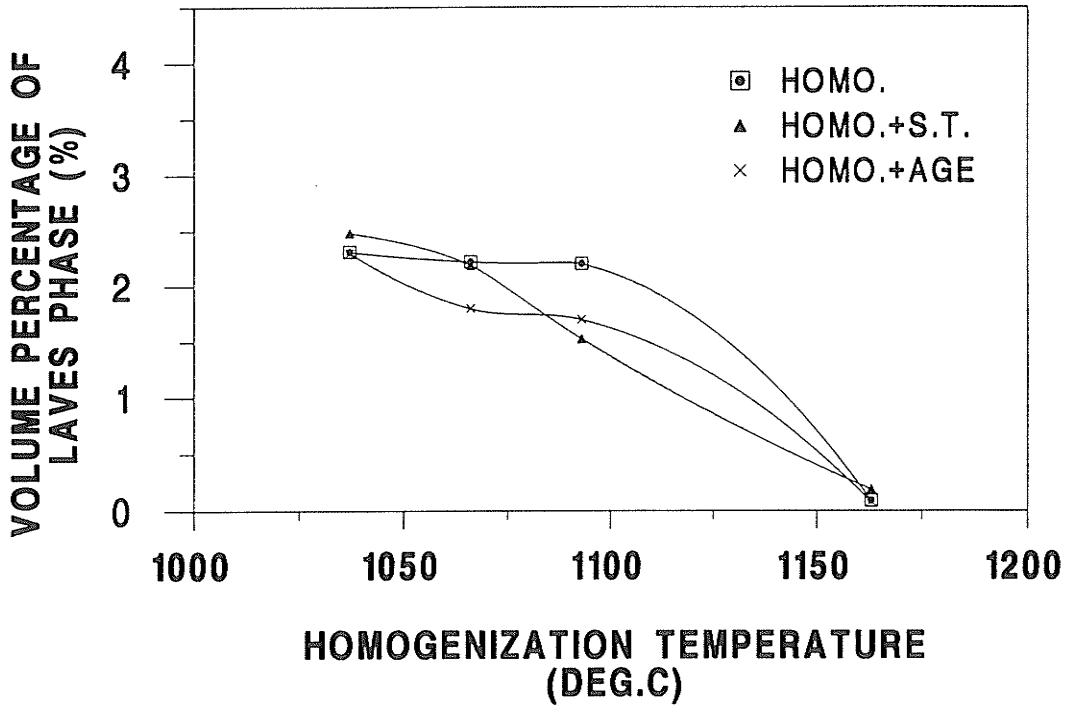

Fig.4.13 Volume fractions of Laves phase after homogenization, solution and ageing heat treatments.

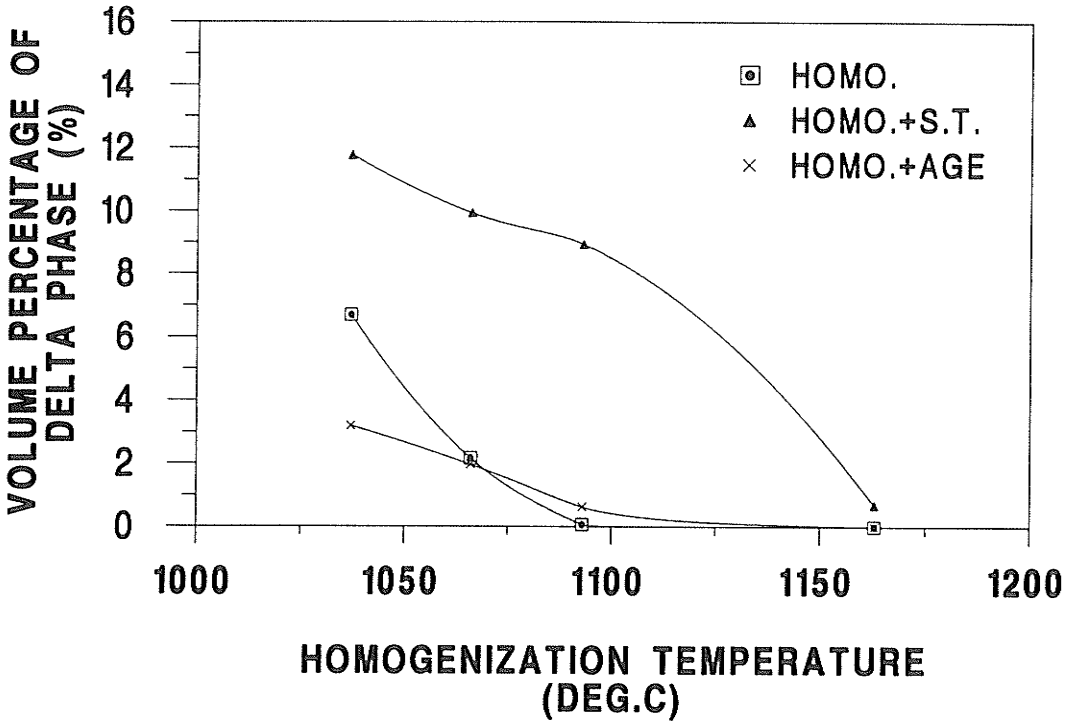

Fig.4.14 Volume fraction of δ-Ni_3Nb phase after homogenization, solution and ageing heat treatments.

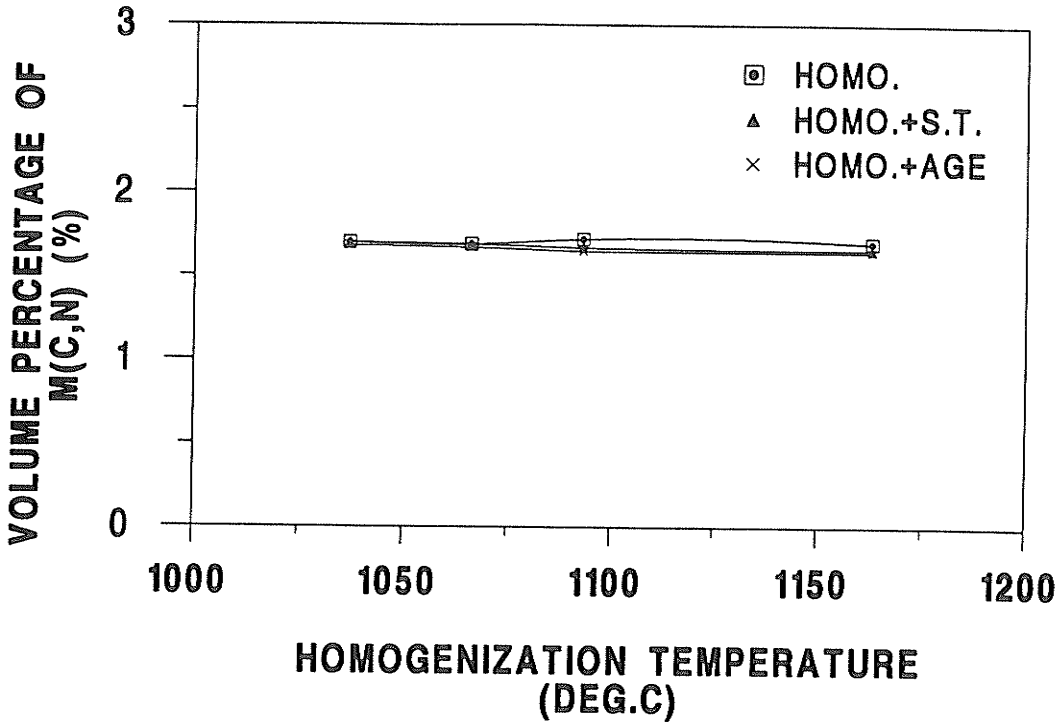

Fig.4.15 Volume fractions of M(C,N) after homogenization, solution and ageing heat treatments.

4.3 Hardness Measurement Results

Hardness measurement results (Fig.4.16) showed that the hardness values after different homogenization heat treatments (curve a in Fig.4.16) and homogenization + solution treatments (curve b in Fig.4.16) are at the same level, whereas, ageing after both homogenization (curve c in Fig.4.16) and homogenization and solution heat treatment (curve d in Fig.4.16) increases hardness which can be attributed to the precipitation of the strengthening phases $\gamma''+\gamma'$. It is also observed that an increase in the homogenization temperature from 1037 to 1163°C does not affect the hardness of all the subsequently heat treated specimens (curves a, b, c and d). Fig.4.17 illustrates the effect of different heat treatments on the hardness. Homogenization and solution treatments did not seem to change the hardness as compared to the as-received condition while ageing after homogenization and solution treatments increased the hardness value. Hardness after overageing at 760°C for 200 hours remained at the same level as observed in the standard aged condition.

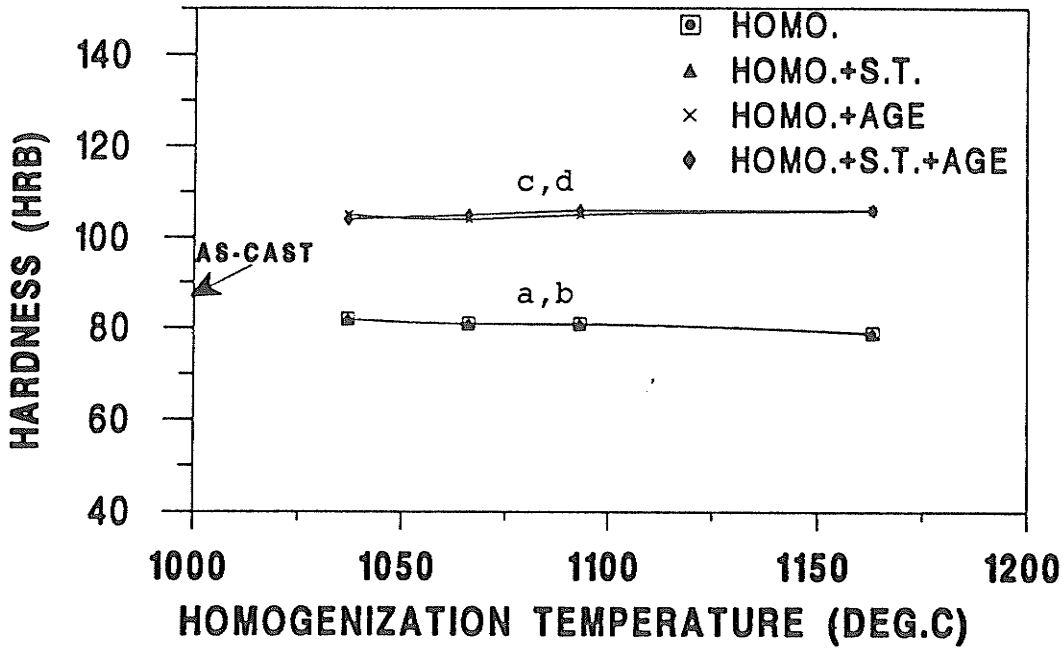

Fig.4.16 Hardness values after various heat treatment: homogenization (a), homogenization + solution (b), homogenization + ageing (c) and homogenization + solution + ageing (d).

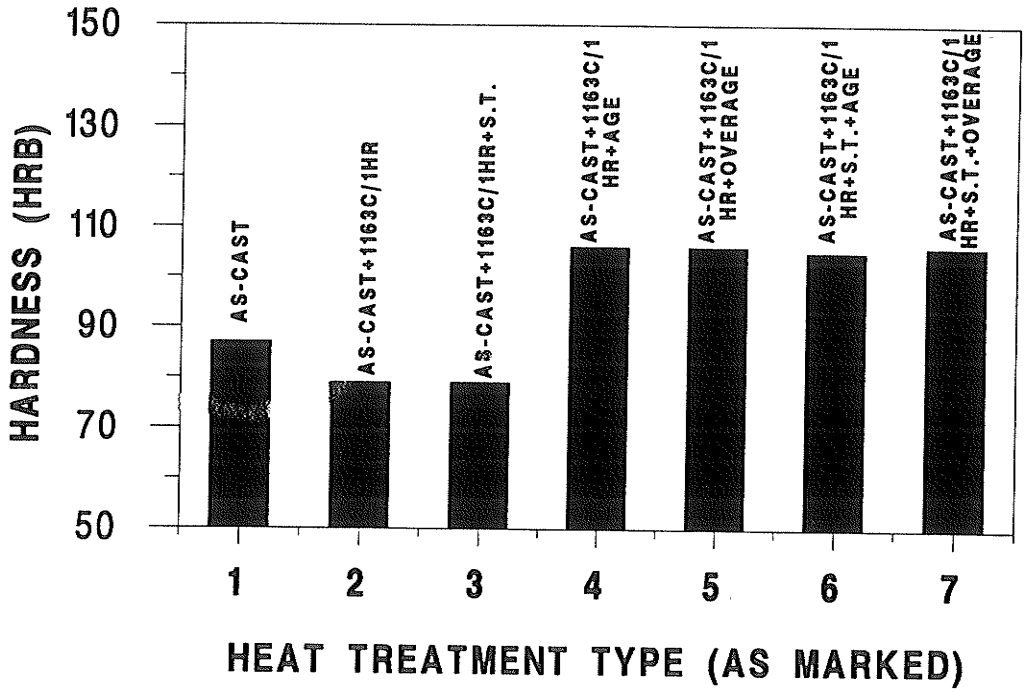

Fig.4.17 Effect of heat treatment type (homogenization, solution, ageing and overageing) on material hardness.

4.4 Microstructural and Microfissuring Evaluation of Weldments

A weld is generally divided into three regions; Fusion Zone (FZ), Heat Affected Zone (HAZ) and base material as indicated in Fig.4.18. The FZ consists of base metal that is completely melted and solidified during welding. The HAZ can be divided into the partially melted zone, the portion of the base metal located just outside the weld interface within which the extent of melting occurs from 0 to 100%, and the true HAZ which is the portion in which all microstructural changes produced by welding occur in the solid state. The EB welds produced using the welding parameters defined in this study have the shape of a nail as shown in Fig.4.19. Most of the microfissuring occurred in the HAZ and under the nail-head of the weld, as will be seen in the following section. The microstructure of the base metal has been described in the previous section and will not be dealt with here. Rather, the evaluation of microstructures of HAZ and FZ will be emphasized in this section.

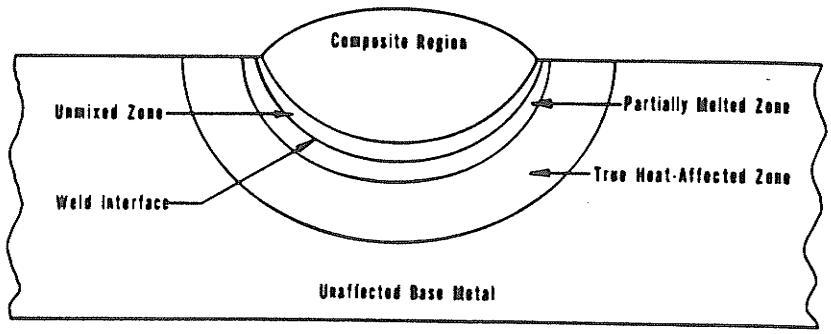

Fig.4.18 Illustration of three zones (base metal, HAZ and FZ) in an electron beam weld [30].

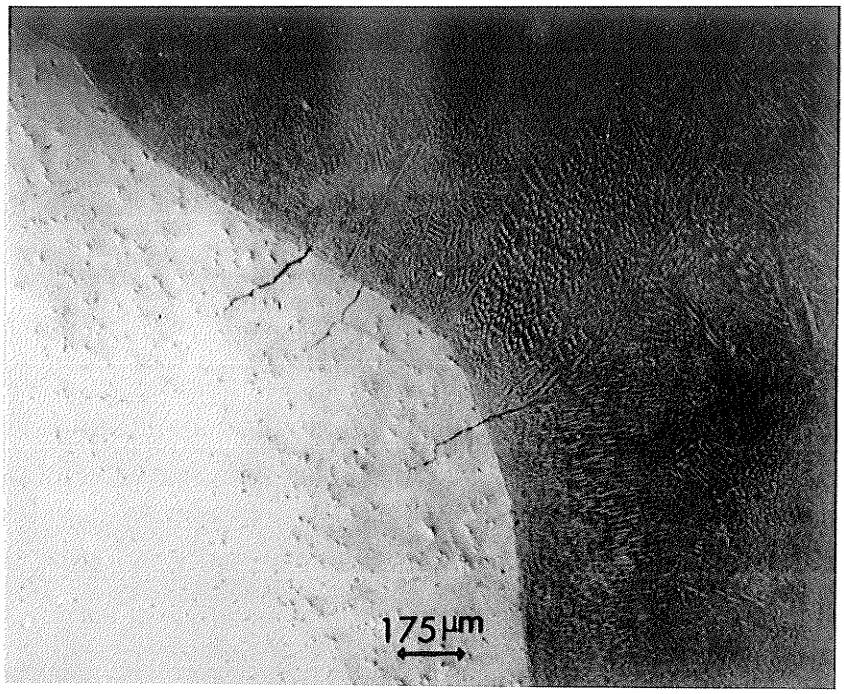

Fig.4.19 HAZ microfissures.

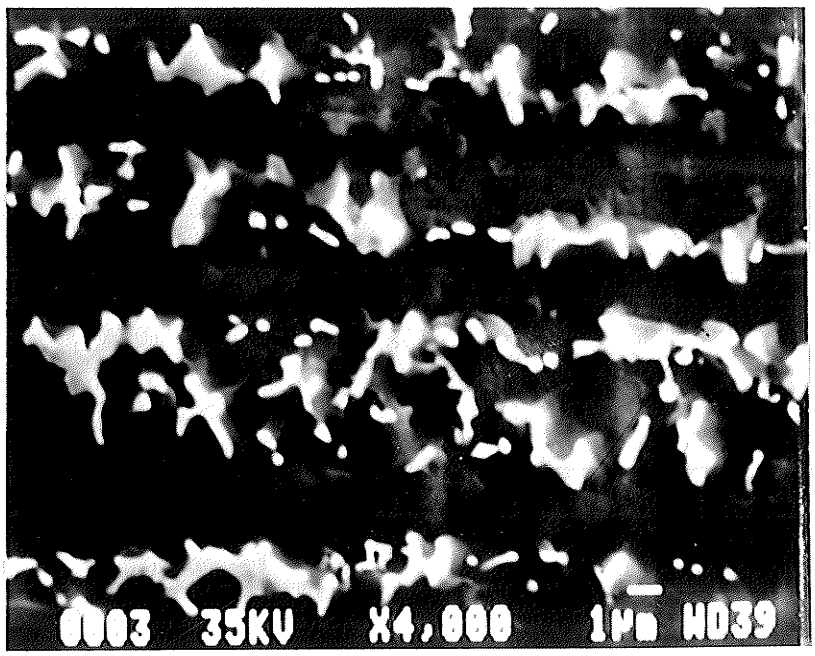

Fig.4.20 SEM micrograph of fusion zone.

4.4.1 Microstructure of Fusion Zone

The fusion zone microstructure was initially examined by SEM. A fine dendritic structure similar to the as-received parent material was observed in SEM as shown in Fig.4.20, with the secondary phases distributed in the dendrites. The details of the secondary phases in the fusion zone were too fine to be resolved by SEM.

A TEM study was conducted using carbon extraction replicas. Most of the precipitates were observed to have a feather-like morphology as shown in Fig.4.21a. The chemical composition of this type of phase was analyzed using EDS and the spectrum is given in Fig.4.21b. It is basically a Nb/Mo-rich phase with small amount of Ti. Selected Area Diffraction Pattern (SADP) technique was used to detect the crystal structure of this unknown phase, and it was found that this Nb-rich phase has a FCC structure with lattice parameter a=0.437 nm. Based on these observations and results from other investigations [77,181], this phase was identified as an MC-type carbide.

Some spherical particles were observed in the FZ as shown in Fig.4.22a. EDS was conducted (Fig.4.22b) and it was found to be a Cr-rich phase. The crystal structure of this spherical phase was analyzed by SAD and it was found to have a FCC structure with lattice parameter a=1.09nm. As both $M_{23}C_6$ and M_6C have similar lattice parameters and chemical compositions, it difficult to differentiate one from the other. Therefore, the observed phase can only be identified as $M_{23}C_6$ (or M_6C).

A few irregular shape particles were observed to be associated with MC type carbides as seen in Fig.4.23a. This phase was analyzed by both SADP and EDS chemical analysis techniques. As shown in Fig.4.23b and Table 4-5, this phase has a chemical composition of A_2B where A represents Ni,Cr,Fe and Si and B represents Nb,Mo and Ti. This phase was found to have a HCP structure with lattice parameters a=0.471nm, c=0.792nm, typical of A_2B type Laves phase.

The chemical composition of various phases observed in the fusion zone are summarized in Table 4-5. The results reported in references [77,181] are also given in this table for comparison. The compositions obtained are very similar to those reported, with differences between these results being attributed to the difference between the material and instruments used. The lattice parameters of various phases are summarized in Table 4-6 and are observed to be consistent with the values reported by other investigations [77,181].

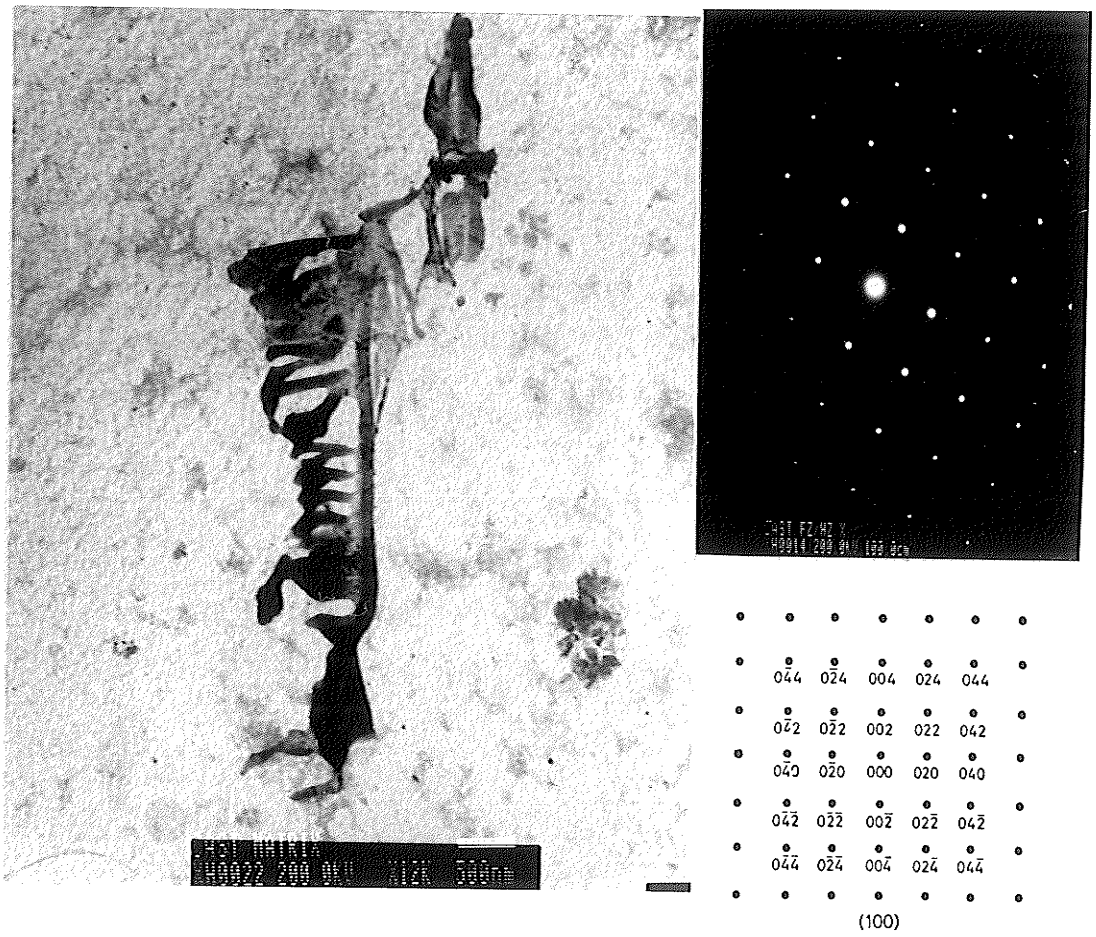

(a)

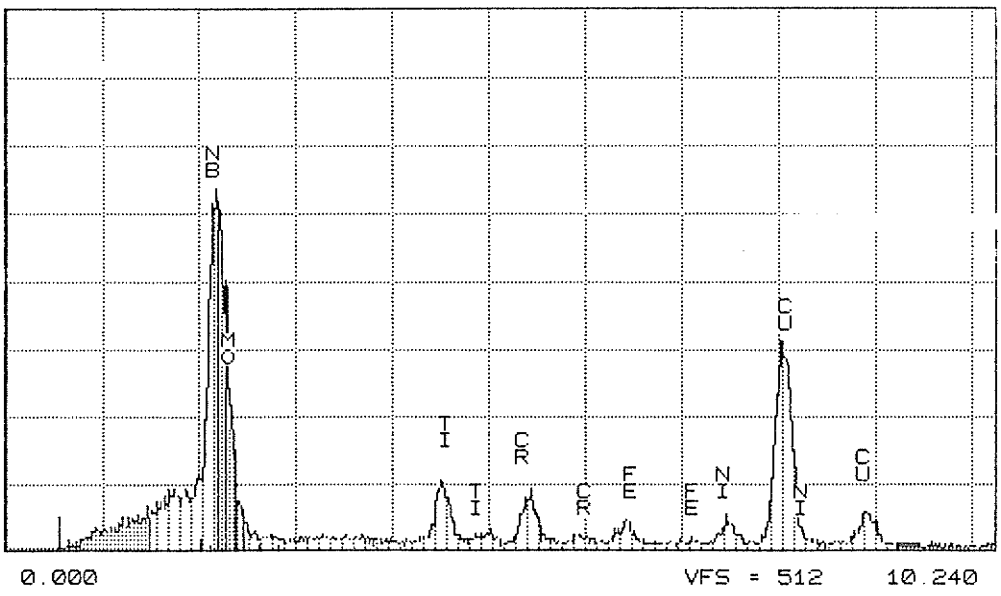

(b)

Fig.4.21 TEM micrograph (a) and EDS spectrum (b) of MC-type carbides in FZ.

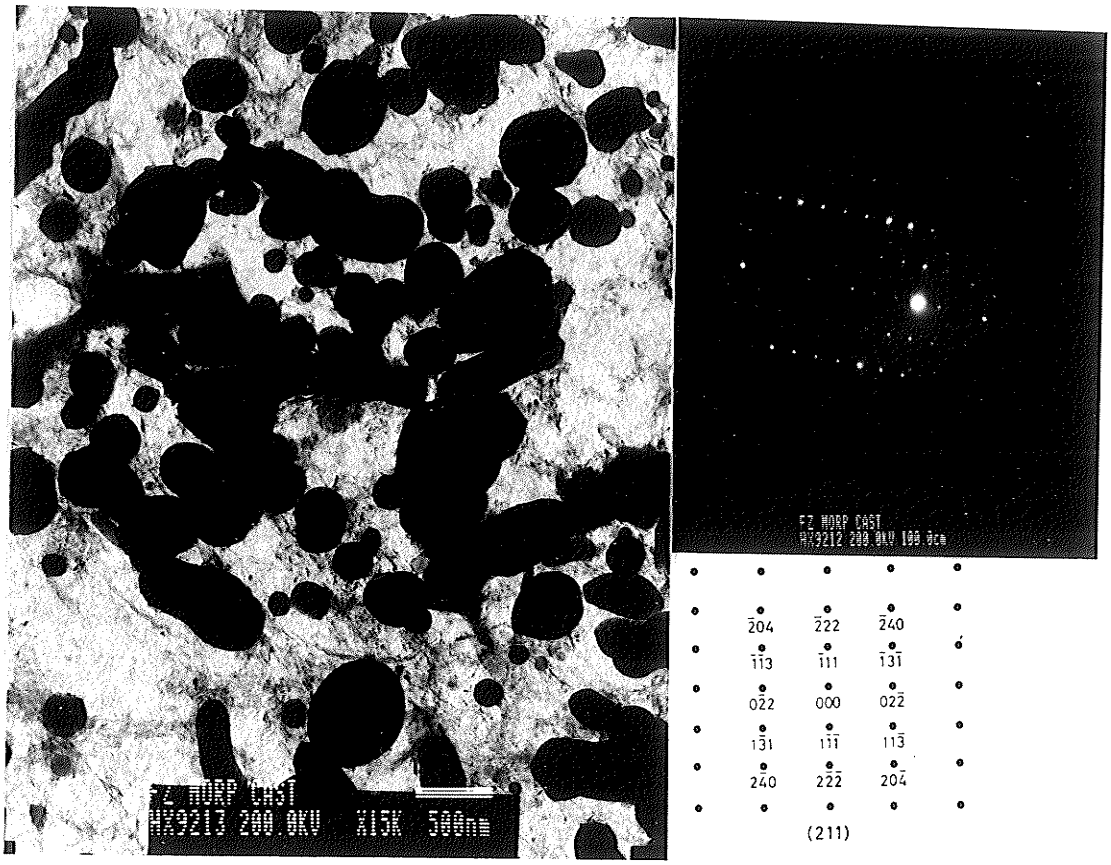

(a)

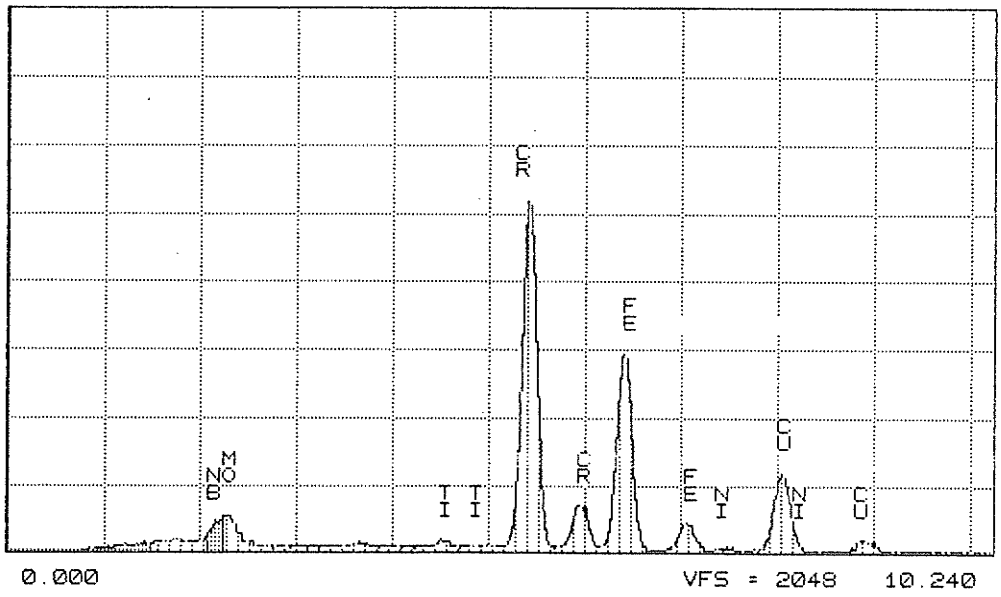

(b)

Fig.4.22 TEM micrograph (a) and EDS spectrum (b) of $M_{23}C_6$ (or M_6C) in FZ.

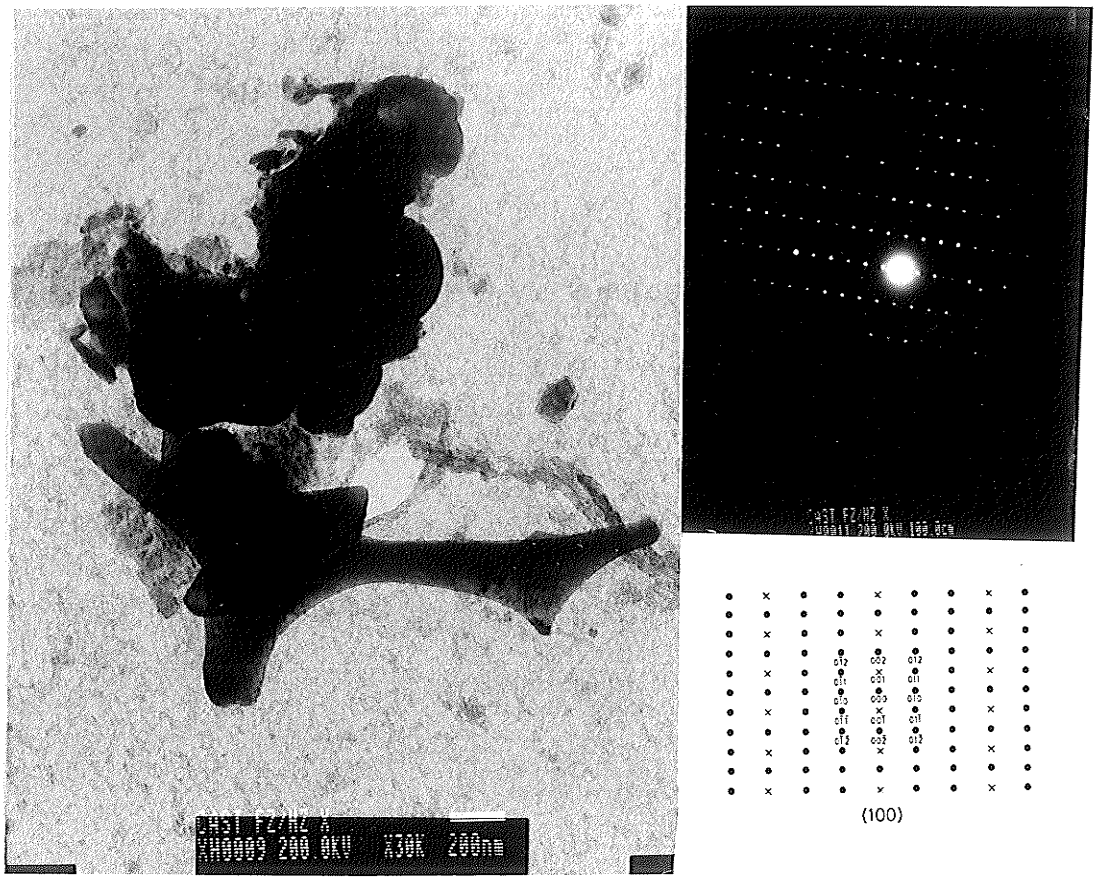

(a)

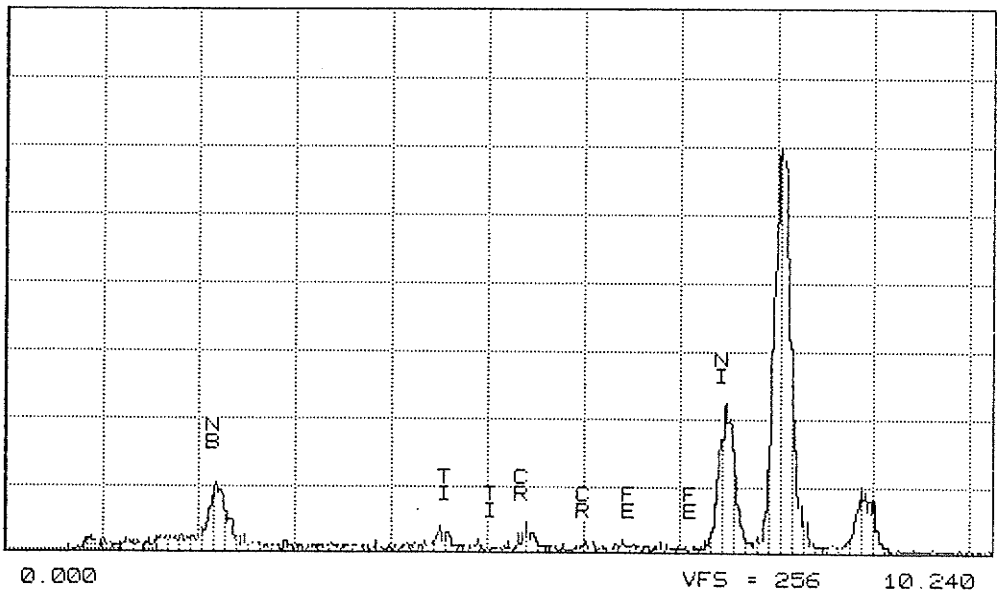

(b)

Fig.4.23 TEM micrograph (a) and EDS spectrum (b) of Laves phase in FZ.

Table 4-5 Typical Composition of Various Phases

Determined by TEM/EDS (at%)

	M(C,N)	MC [181]	Laves	Laves [77]	$M_{23}C_6$	$M_{23}C_6$ [77]
Al	2.5	-	0.5	0.1	0.5	0
Si	6.9	-	4.0	0.5	0.9	0
Ti	7.6	8.0	2.5	1.5	0.7	0
Cr	6.3	3.0	13.5	13.5	59.9	63
Fe	2.8	0.5	12.5	11.5	32.5	18
Ni	3.0	2.0	34.7	38.5	0.5	5
Nb+Mo	70.8	80.0	31.9	28.0	4.4	14

Table 4-6 Lattice Parameters of Various Phases

Phases	Lattice Parameters
M(C,N)	a=0.437nm
	a=0.443nm [181]
	a=0.442nm (NbC), a=0.424nm (TiN?) [77]
Laves	a=0.471nm, c=0.792nm
	a=0.467nm, c=0.771nm [181]
	a=0.474nm, c=0.772nm [77]
$M_{23}C_6$	a=1.09nm
	a=1.09nm (M_6C) [77]
	a=1.06nm ($M_{23}C_6$) [77]

4.4.2 Microstructures of HAZ (SEM)

The temperature gradient during the welding cycle of cast Alloy 718 can be divided into five regions:

I. Temperature exceeding the liquidus of interdendritic area.

II. Temperature above M(C,N) constitutional liquation temperature (M(C,N)/γ eutectic).

III. Temperature above Laves phase constitutional liquation temperature (Laves/γ

eutectic), and below the M(C,N) constitutional liquation temperature.

IV. Temperature below the Laves/γ eutectic temperature with no liquation reaction occurring in this region. however, temperature is high enough to cause the dissolution of δ and γ".

V. Temperature at which no microstructural changes occur and only thermal expansion is expected.

Since liquation occurs in regions I to III, the microstructural changes in these three regions are therefore examined in both weld HAZ and gleeble HAZ.

Weld HAZ

Region I: In this area, partial melting occurred during welding and the resolidified structure (Fig.4.24a) has similar features as observed in FZ (Fig.4.20). However, the precipitates have a larger size than that observed in the FZ. The majority of the resolidified constituent is eutectic phase which was identified as Laves phase by the composition. Small amounts of irregular-shape particles were also present in the HAZ and are defined as M(C,N) type carbides due to their high Nb/Mo and Ti content (Fig.4.24a). The compositions of these phases were determined using EDS/SEM and are reported in Table 4-7.

Region II: Due to the welding thermal effect, constitutional liquation of both M(C,N) and Laves phases occurred in this area and the formed liquid resolidified during the cooling cycle. Two types of phases were found in this region as shown in Fig.4.24b, one

with eutectic feature and the other with irregular shape. The lamella spacing in the observed eutectic phase is smaller than that of Laves phase formed from the casting and the irregular particles are finer than the primary carbides. These two phases were confirmed to be Laves phase and M(C,N) type carbides from their chemical composition (Table 4-7) as determined by EDS/SEM.

Region III: In this area, the temperature achieved during the welding cycle is above the Laves phase/γ eutectic temperature but below the M(C,N) carbide/γ eutectic temperature. Only constitutional liquation of Laves phase is expected to occur. Microstructural examination in SEM revealed the resolidified eutectic Laves phase as shown in Fig.4.24c and it is seen that the formed eutectic Laves phases are finer than the original ones. From the fact that original M(C,N) remained unaffected in this region (Fig.4.24c) during welding, it could be concluded that the constitutional liquation of Laves phase resulted in the formation of finer Laves in this region .

Gleeble HAZ

Region I: Partial melting occurred in the dendritic area of the original cast structure. Resolidified eutectic phase and script phase were observed in SEM as shown in Fig.4.25a,b and c. The chemical compositions of these phases were analyzed using EDS/SEM with the results given in Table 4-7. The script-shaped phase was found to be enriched in Nb/Mo and Ti and it was identified as M(C,N) carbides from its distinct composition and morphology. The eutectic phase has a composition typical of Laves phase (i.e. A_2B with Fe,Cr,Si and Ni taking the A position and Nb,Mo and Ti the B position). Therefore, this eutectic phase is concluded to be Laves phase.

Region II: In this area, both M(C,N) carbides and Laves phases could liquate constitutionally. SEM examination showed the existence of two types of particles, discrete and eutectic as shown in Fig.4.25b. EDS analysis confirmed that they are M(C,N) carbide and Laves phase from their unique chemical compositions (Table 4-7).

Region III: Similar to the region III in the weld HAZ, constitutional liquation of Laves phase occurred and the formed liquid resolidified into finer eutectic as seen in Fig.4.25c. M(C,N) carbides were unaffected during the Gleeble thermal cycle.

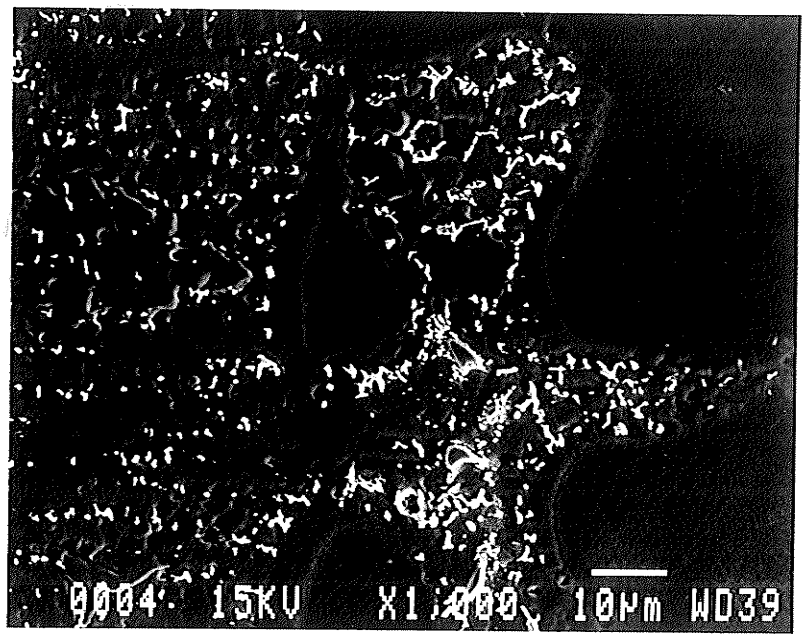

(a)

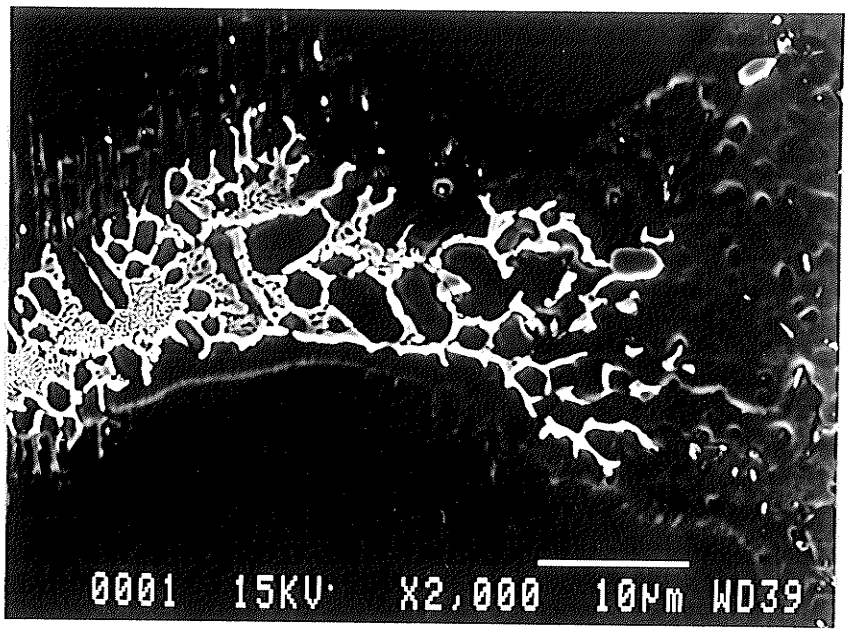

(b)

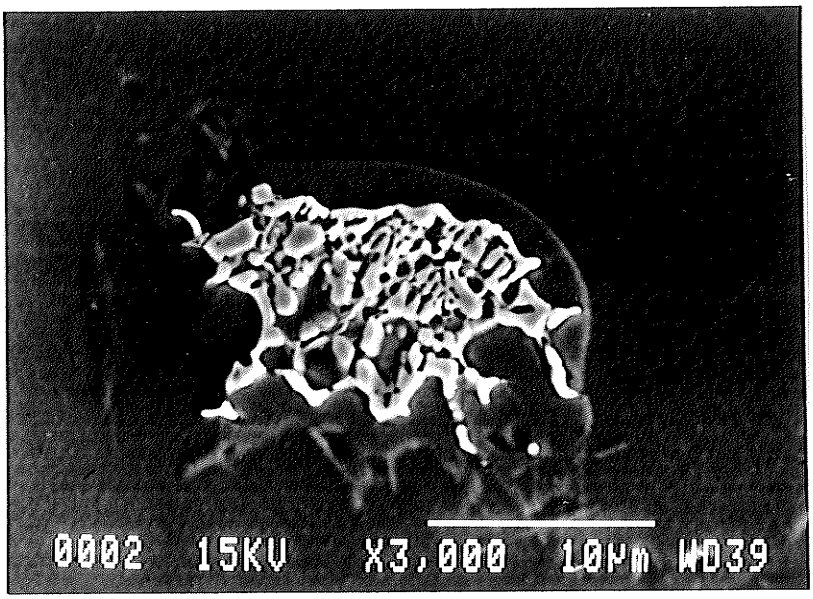

(c)

Fig.4.24 Microstructure of HAZ in Electron beam weld. (a) resolidified Laves phase and MC, (b) constitutional liquation of Laves phase and MC and (c) constitutional liquation of Laves phase.

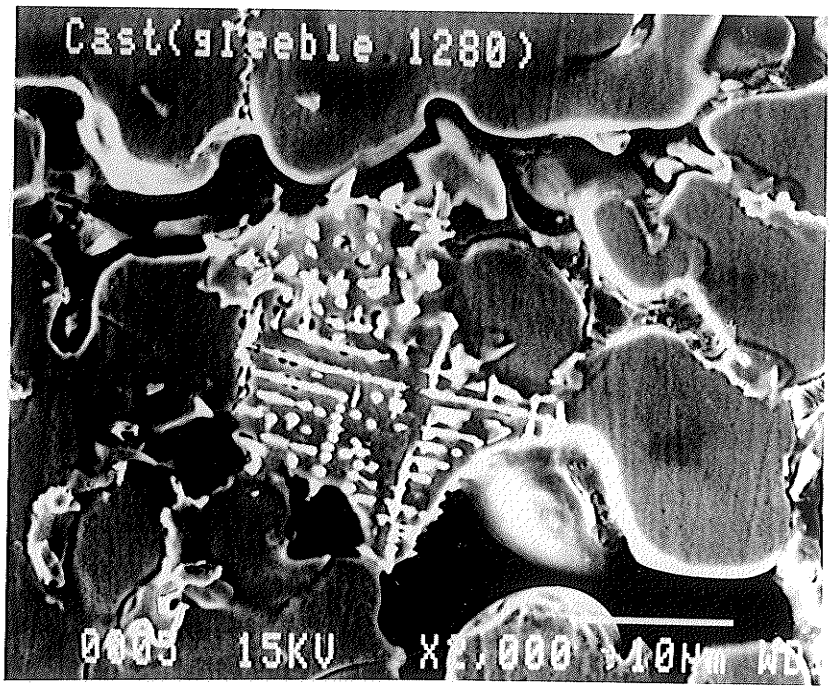

(a)

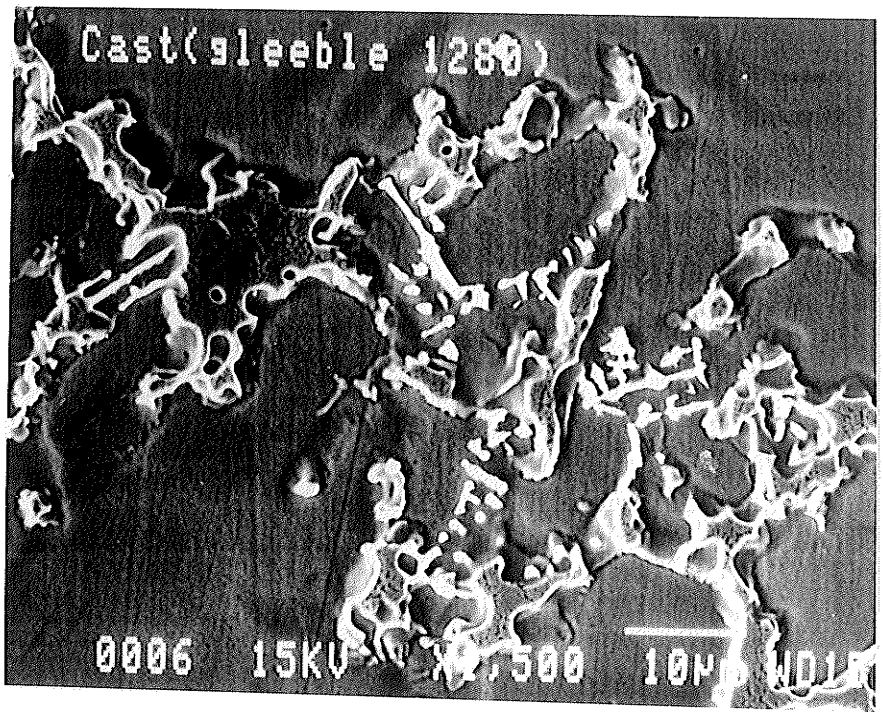

(b)

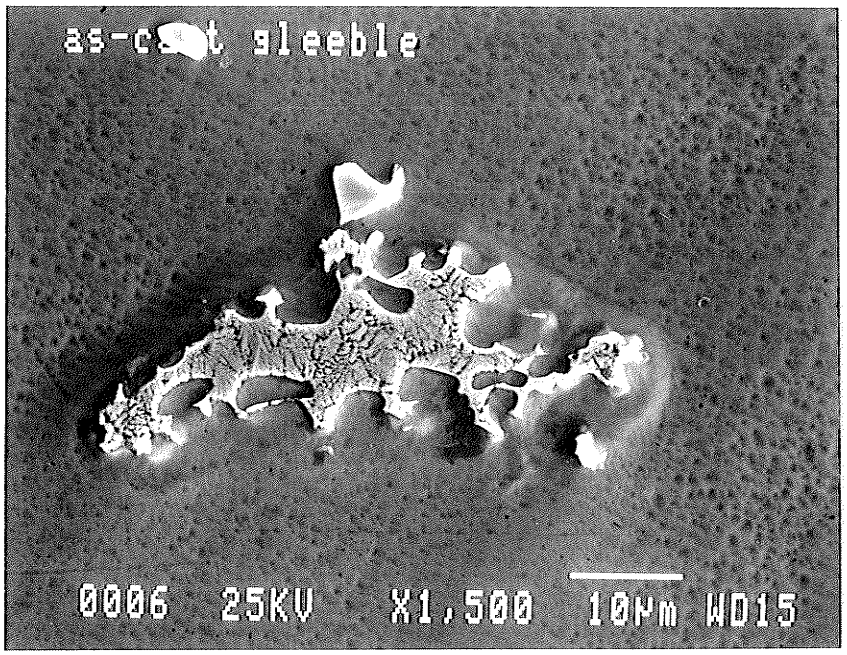

(c)

Fig.4.25 Microstructure of Gleeble simulated HAZ. (a) resolidified Laves phase and MC, (b) constitutional liquation of Laves phase and MC and (c) constitutional liquation of Laves phase.

Table 4-7 Chemical Composition of HAZ Constituents

	Laves Weld HAZ		M(C,N) Weld HAZ		Laves Gleeble HAZ		M(C,N) Gleeble HAZ	
	wt%	at%	wt%	at%	wt%	at%	wt%	at%
Al	0.24	0.57	0	0	0.25	0.58	0.08	0.27
Si	1.06	2.40	0	0	0.68	1.55	0	0
Ti	1.33	1.78	4.08	7.50	1.35	1.8	5.53	9.97
Cr	12.63	15.55	0.87	1.46	13.1	16.1	0.89	1.48
Fe	10.77	12.34	0.45	0.70	11.0	12.59	0.60	0.93
Ni	41.21	44.93	1.63	2.44	42.4	46.1	2.12	3.12
Nb	26.08	17.97	87.99	83.32	27.3	18.7	86.35	80.25
Mo	6.68	4.46	4.98	4.57	3.78	2.51	4.42	3.98

4.4.3 HAZ Microfissuring and Weldability Evaluation

4.4.3.1 HAZ Microfissuring

Electron beam bead-on plate welding produced a nail-shaped weld as shown in Fig.4.19. Most of the HAZ microfissures were observed to have occurred on grain boundaries and were oriented in a characteristic manner, i.e. perpendicular to the boundary zone (contours of the weld pool). In some cases, the HAZ crack extended into

the weld zone. The lengths of the cracks were observed to be generally about a few tenths of a millimetre. A microfissure at higher magnification (Fig.4.26) clearly illustrates the presence of constituents along both surfaces. A SEM/EDS analysis was carried out to determine the nature of these phases. Both M(C,N) and Laves phase (as marked in Fig.4.26) identified by their compositions (Table 4-8) were observed to be present on HAZ microfissures. A lamellar type of Laves phase was observed as shown in a SEM micrograph in Fig.4.26 while MC carbides have a morphology similar to that observed in the as-cast condition; i.e. irregular shape.

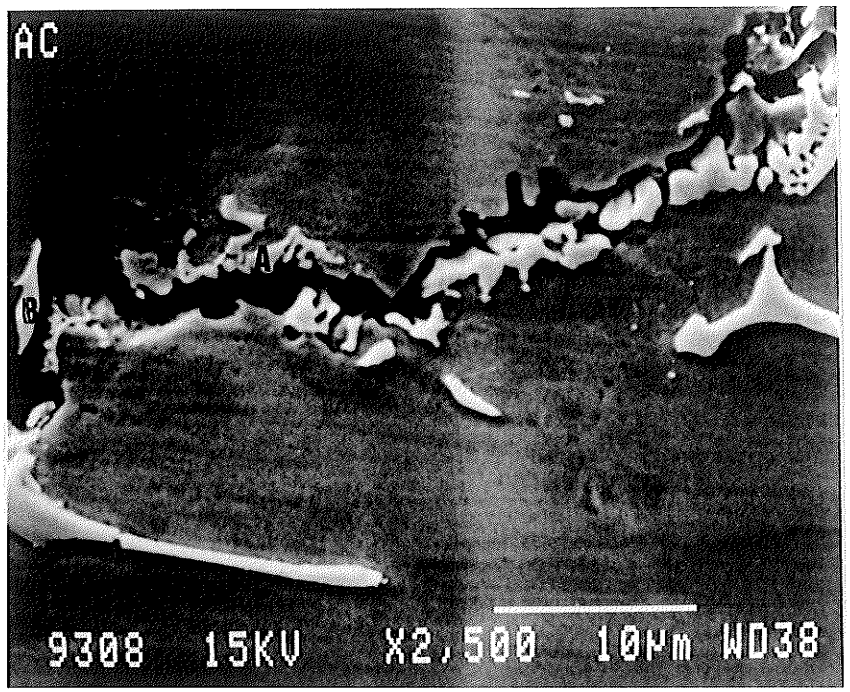

Fig.4.26 HAZ microfissure and microfissure constituents in electron beam weld (A: Laves phase and B: M(C,N)).

Table 4-8 Chemical Composition of

Constituent on Microfissure (wt% and at%)

	Laves		M(C,N)	
	wt%	at%	wt%	at%
Al	0.07	0.18	0	0
Si	0.98	2.09	0	0
Ti	0.85	1.17	6.34	11.32
Cr	13.01	16.4	1.05	1.73
Fe	11.82	13.84	0.76	1.16
Ni	36.04	40.14	2.69	3.92
Nb	30.04	21.14	85.67	78.78
Mo	7.18	4.89	3.48	3.10

4.4.3.2 HAZ Microfissuring Evaluation (TCL)

The values of TCL after various heat treatments were measured (Appendix II) and plotted against the heat treatment temperature as shown in Figures 4.27, 4.28, 4.29 and 4.30.

The effect of homogenization treatment: It is observed from Fig.4.27, curve b, that in the as-homogenized condition the total crack length decreases initially with an increase

in the homogenization temperature (1037 to 1066°C) and then increases over the range of 1066 to 1163°C.

The effect of homogenization and solution treatment: The TCL after homogenization and solution treatment was also examined and is shown in Fig.4.27, curve c. It was observed that as the homogenization temperature is increased, the TCL first decreased (from 1037°C+ST to 1066°C+ST) and then increases (from 1066°C+ST to 1163°C+ST). Similar trends were observed in TCL for specimens after homogenization and homogenization + solution treatment as shown in Fig.4.27 curve b and c.

The effect of homogenization and ageing: The TCL is seen to increase continuously as the homogenization heat treatment temperature is increased from 1037 to 1163°C (Fig.4.27 curve a). Comparing curve a, b and c in Fig.4.27, it can been seen that the TCL trend observed in curve b and c is not present in curve a.

The effect of homogenization and solution and ageing treatment: As the homogenization temperature is increased from 1037 to 1163°C prior to solutioning and ageing, the TCL increased continuously as shown in Fig.4.28. The same trend was observed in both homogenization + ageing and homogenization + solution + ageing treated specimens as seen in Fig.4.27 curve a and Fig.4.28.

The effect of heat treatment type: The effect of heat treatment type on TCL is plotted

on a bar chart in Fig.4.29. It can be seen that the homogenization heat treatment at 1163°C increased the TCL as compared to the as-cast condition while solution heat treatment after homogenization and prior to ageing reduced TCL. Ageing after both homogenization and homogenization and solutioning increased the TCL.

The effect of homogenization temperature (from 950 to 1240°C) and cooling rate (air cool and water quench): The variation in TCL with homogenization temperature in specimens that were air cooled after homogenization (Fig.4.30 curve a) showed the same trend as seen in Fig.4.27 curve b as was expected. However, the specimen that were water quenched revealed an unusual trend as seen in Fig.4.30 curve b which will be discussed in section 5.3.

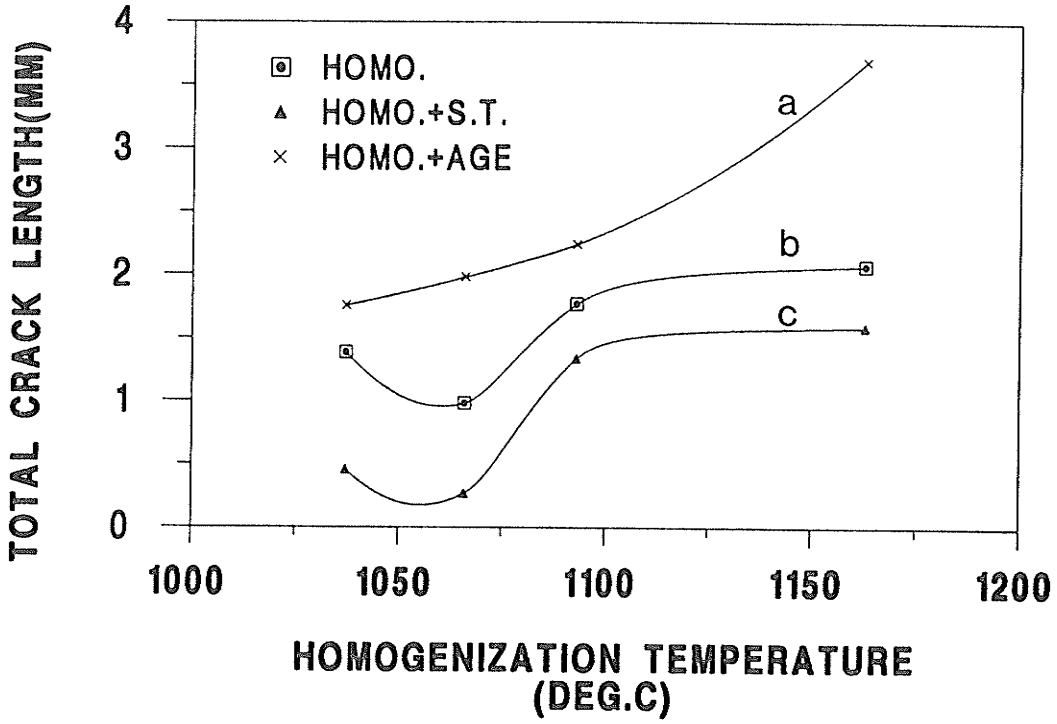

Fig.4.27 Total crack length after homogenization (b), homogenization and solution treatment and (c) homogenization and ageing treatment (a).

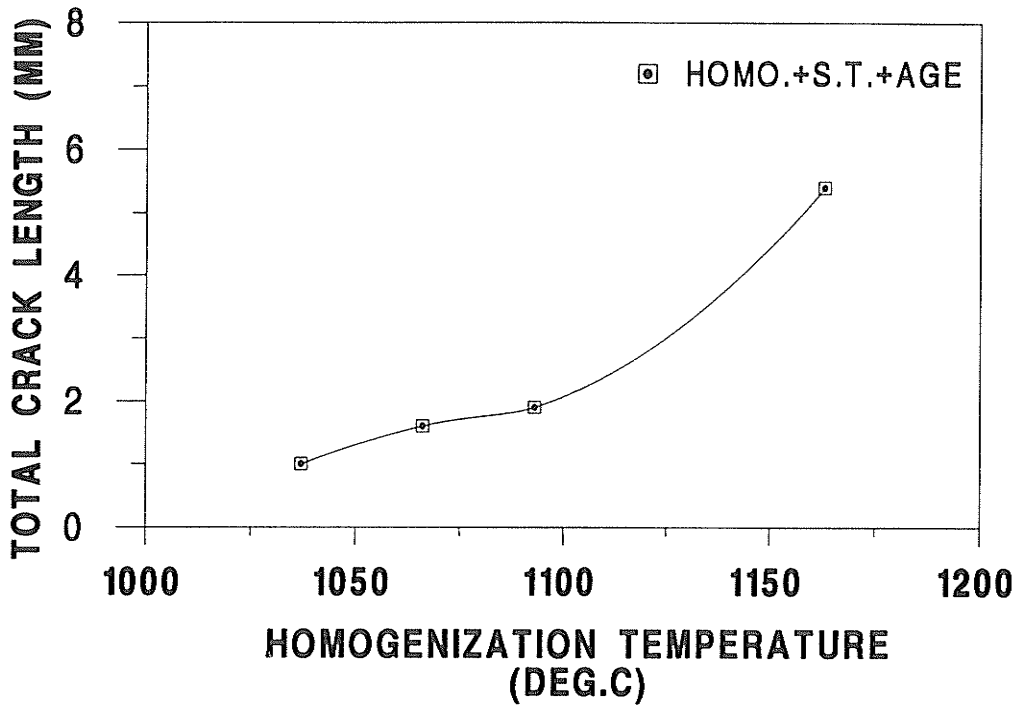

Fig.4.28 Total crack length after homogenization, solution and ageing treatments.

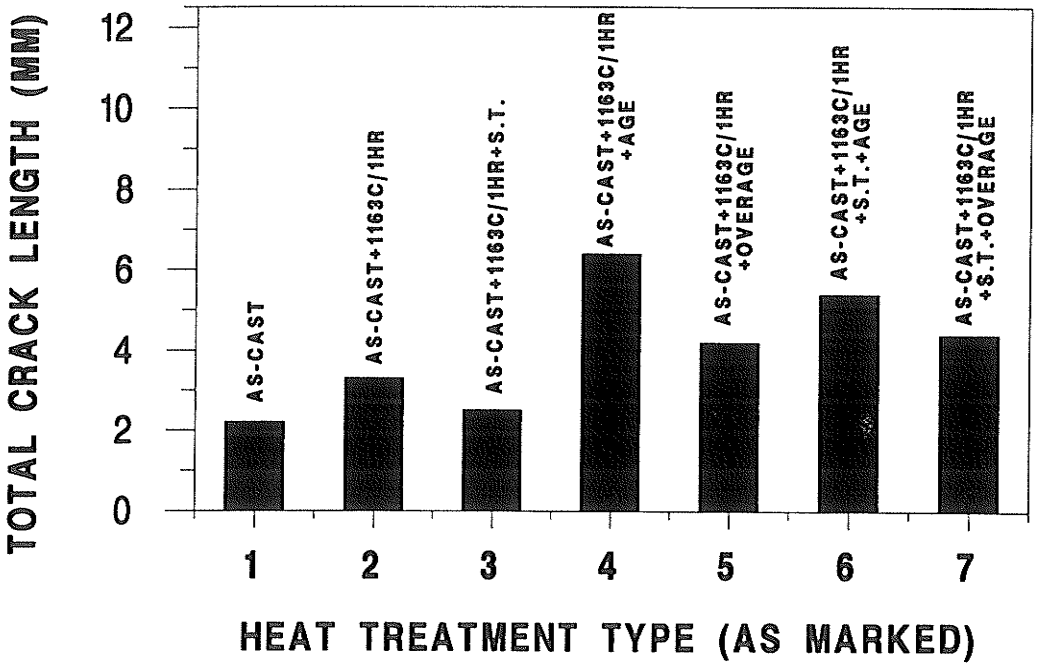

Fig.4.29 Effect of heat treatment type (homogenization, solution and ageing treatments) on total crack length.

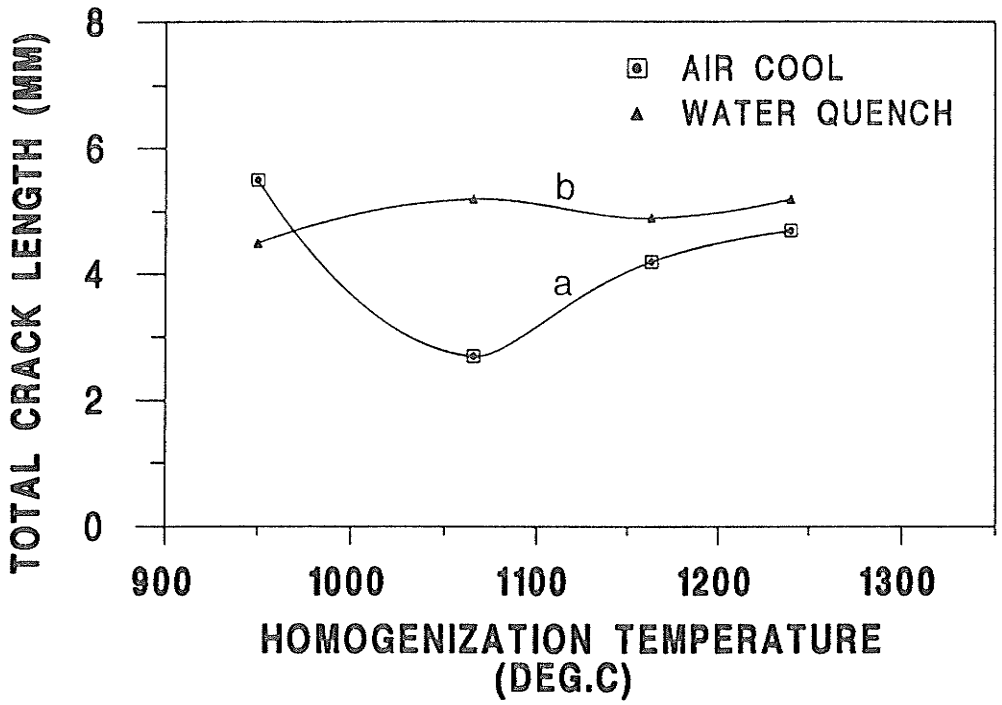

Fig.4.30 Effect of homogenization temperature and cooling rate on total crack length (a: air cool and b: water quench).

4.5 Differential Scanning Calorimetry (DSC)

Figures 4.31 and 4.32 illustrate the heating and cooling cycles of two specimens in two different heat treatment conditions (Fig.4.31 for a specimen in the as-cast condition, Fig.4.32 for specimen homogenized at 1163°C). The temperature of transformation was determined by the deviation point from the baseline. Fig.4.31 shows a typical DSC curve of as-cast Alloy 718. The heating portion shows three deviations (marked as A,B and C on the curve) from the local baseline, representing the γ/Laves phase liquation reaction at point A (1165°C), γ/MC liquation reaction at point B (1267°C) and the bulk γ matrix melting starting at point C (1310°C). On cooling, the following solidification reactions were observed: primary γ solidification at point D (starting at 1335°C) and the γ/Laves reaction at point E (1167°C). A γ/MC reaction during solidification was not detected in this study. The results are summarized in Table 4-9, along with the results of other investigators [182] for comparison.

Table 4-9 Average Reaction Temperatures (°C)

Heating/Cooling Rate	Liquidus	Solidus	Laves	MC
20°C/min.	1310	1335	1165	1267
10°C/min. [182]	1320	1362	1198	1252

It is observed in Fig.4.31 that the first transformation begins at 1165°C during heating. This reaction is understood to be the start of the melting of Laves phase. However no

such transformation was observed in specimens homogenized at 1163°C (Fig.4.32) corroborating the metallographic results which showed that most of the Laves phases had gone into solution after this heat treatment. As the temperature is increased, M(C,N) starts to melt at 1267°C (indicated as B) followed by the melting of the bulk alloy at 1310°C (indicated as C). The liquidus for this alloy is about 1310°C and solidus about 1335°C. The cooling curve for the specimen after homogenization at 1163°C shows the same features as that observed in the cooling curve for the as-cast specimen, i.e. primary γ solidification occurred at 1335°C (point D) which was followed by a γ/Laves reaction at 1167°C (point E). A γ/MC reaction during solidification was not detected in this study but has been observed by other investigators [182].

Other specimens in different heat treatment conditions were also analyzed by DSC and the temperatures at which various reactions occurred are given in Table 4-10. The difference in DSC curves between these specimens is the presence of the liquation reaction of Laves phase.

Table 4-10 Reaction Temperatures (°C) During

Heating and Cooling Measured by DSC

Heat Treatment	On Heating				On Cooling		
	δ	Laves	M(C,N)	γ	γ	M(C,N)	Laves
As-cast	no	1165	1267	1310/ 1335	1335/ 1314	*	1167
1036°C	no	1165	1267	1310/ 1335	1322/ 1310	*	1167
1036°C + 927°C/1hr + 927°C/1hr	no	1165	1267	1310/ 1335	1330/ 1312	*	1167
1163°C	no	no	1267	1310/ 1335	1332/ 1310	*	1167
1163°C + 927°C/1hr + 927°C/1hr	no	no	1267	1310/ 1335	1335/ 1314	*	1167
1163°C + 760°C/5hr F.C.to 650°C/1hr	no	no	1267	1310/ 1335	1335/ 1315	*	1167

* not detected

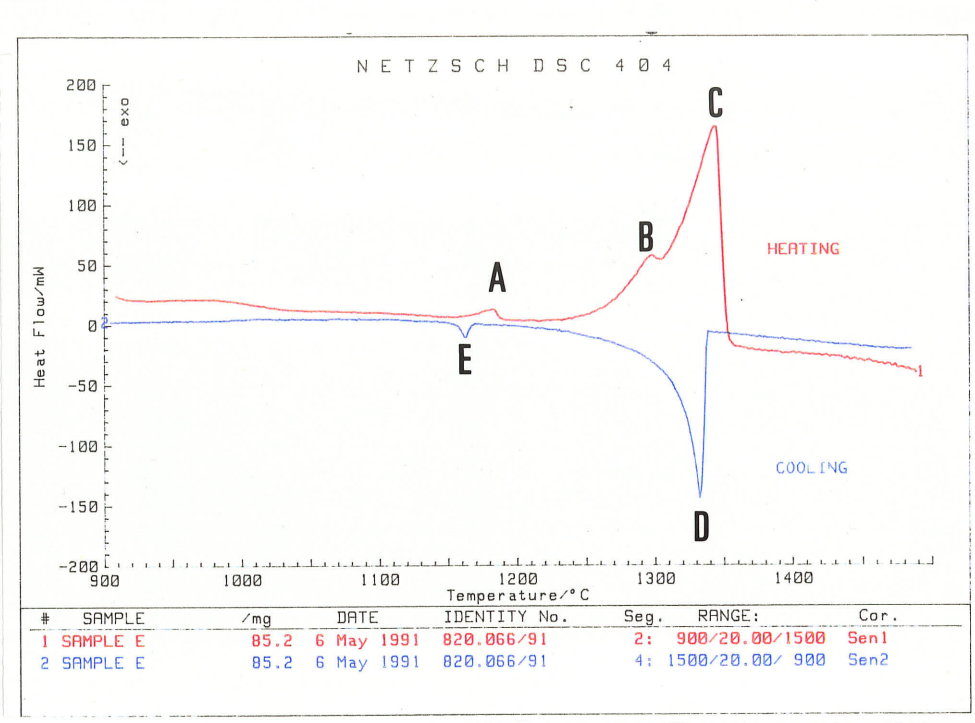

Fig. 4.31 DSC diagram of as-cast material (A: Laves phase reaction temperature, B: carbide reaction temperature, C: γ melting temperature, D: γ solidification temperature and E: Laves phase solidification temperature).

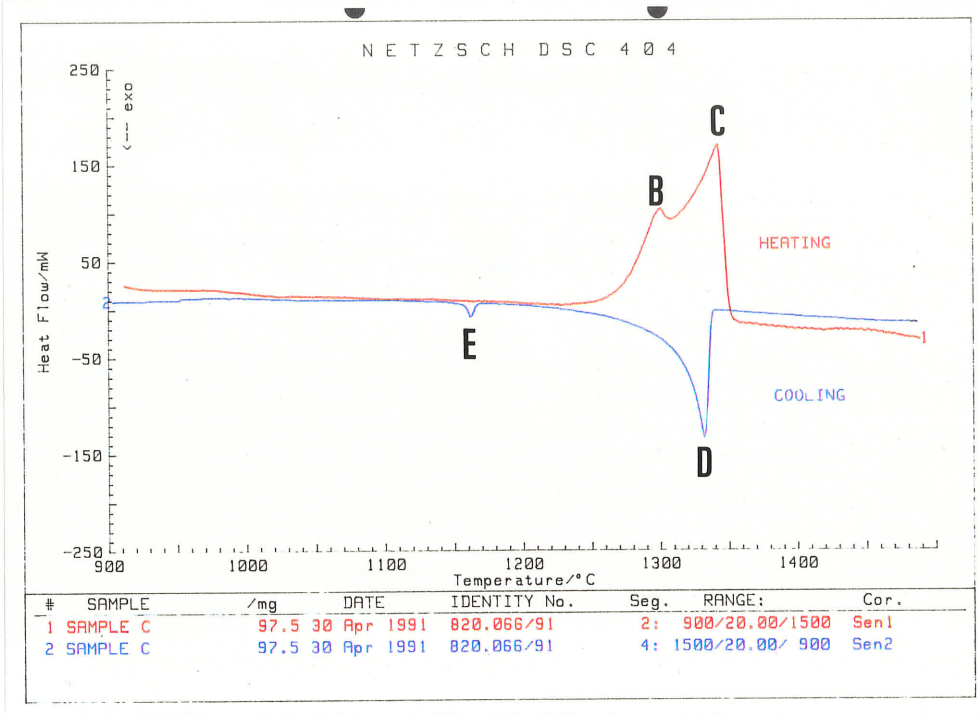

Fig. 4.32 DSC diagram of specimen homogenization treated at 1163°C/1hr (B: carbide reaction temperature, C: γ melting temperature, D: γ solidification temperature and E: Laves phase solidification temperature).

4.6 SIMS Analysis of Elemental Segregation

C, S, P, Al, Mo and Nb were analyzed using different SIMS instrument operation modes as described in Table 3-7 in the experimental procedures section. None of these elements was observed to segregate to the grain boundaries. Signals from these elements were detected from discrete particles (as in Fig.4.33 for S, Fig.4.34 for C and Fig.4.35 for P) which can be interpreted as precipitates (such as carbides) or segregation of these elements to particle-interfaces.

The boron distribution in the as-cast condition is shown in Fig.4.36 which illustrates a dendritic pattern of boron distribution in the matrix. Since the distribution coefficient of boron in Ni is much less than unity, it indicates that the interdendritic area would be enriched in boron. It was observed that after 1163°C/1hr (A.C.) heat treatment boron seems to segregate to the grain boundaries (Fig.4.37). After this initial investigation, a series of heat treatments (Table 3.4) were conducted to systematically examine the nature of boron segregation in terms of its response to heat treatment temperature and cooling rate.

4.6.1 Boron Segregation Behaviour after Air Cooling

Eight grain boundaries were analyzed in each heat treatment condition with all the boron images being recorded at the same instrument settings. Fig.4.38(a-d) shows a set of images illustrating boron distribution on the grain boundaries after heat treatment at different temperatures (950-1240°C) followed by air cooling. Comparing these four

images, it can be concluded that as the temperature increases (from 950 to 1067°C), the intensity of the boron signal decreases and then increases with temperature from 1067 to 1240°C. However, there is a slight variation in the intensity of B signal from grain boundary to grain boundary which will be discussed in the following section.

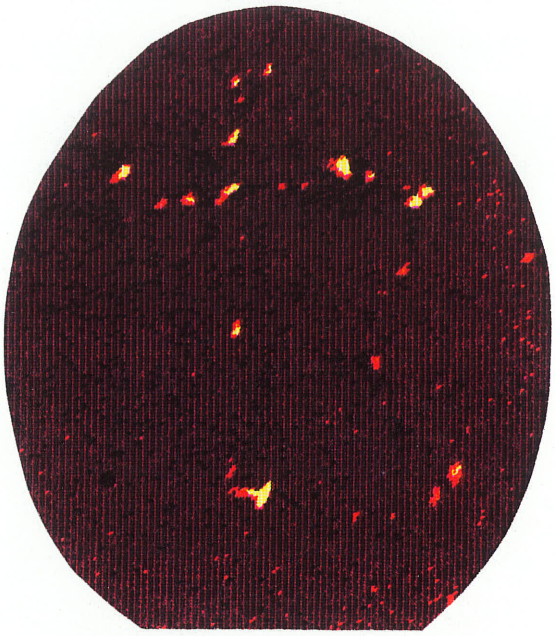

Fig.4.33 SIMS image of sulphur.

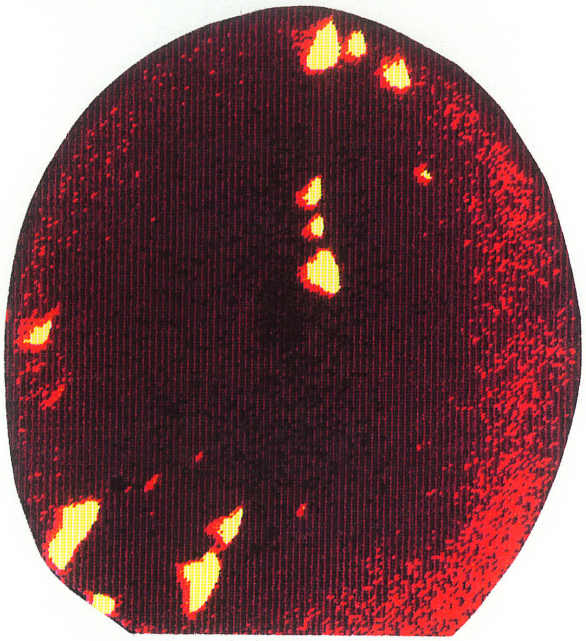

Fig.4.34 SIMS image of carbon.

Fig.4.35 SIMS image of phosphorus.

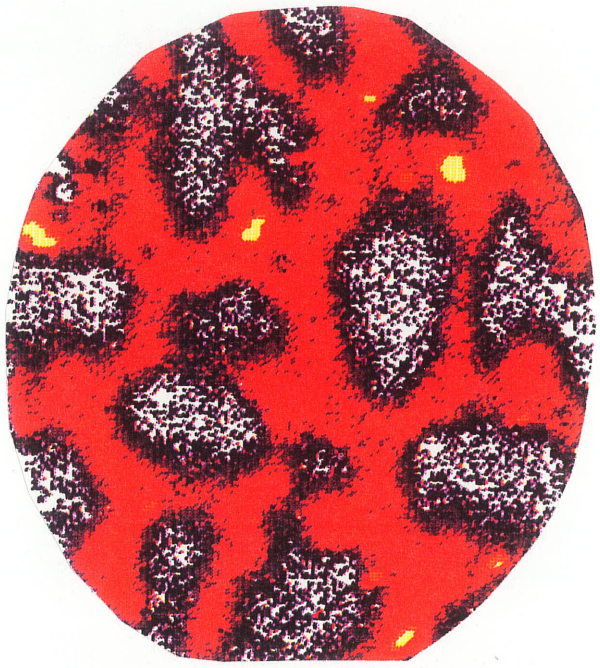

Fig.4.36 Boron distribution in the as-cast material.

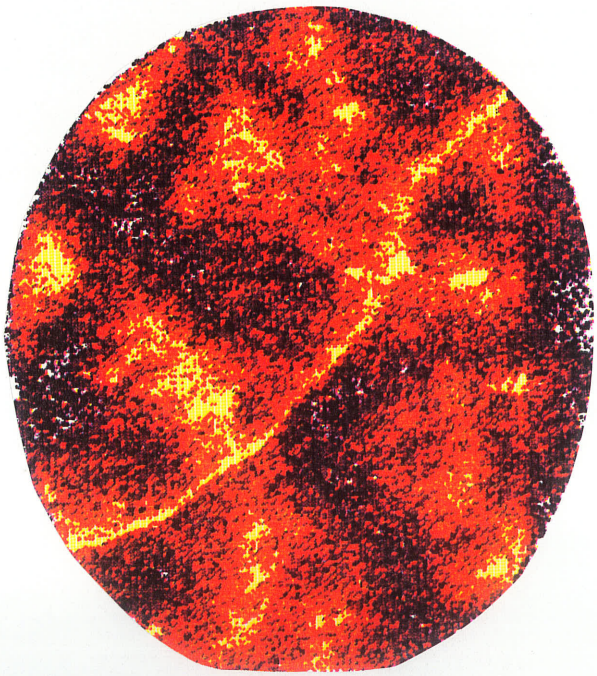

Fig.4.37 Boron grain boundary image in specimen after heat treated at 1163°C/1hr.

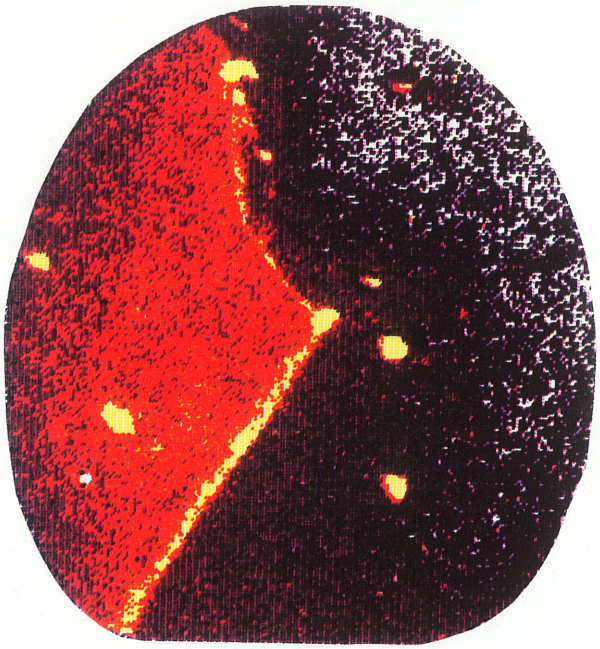

(a)

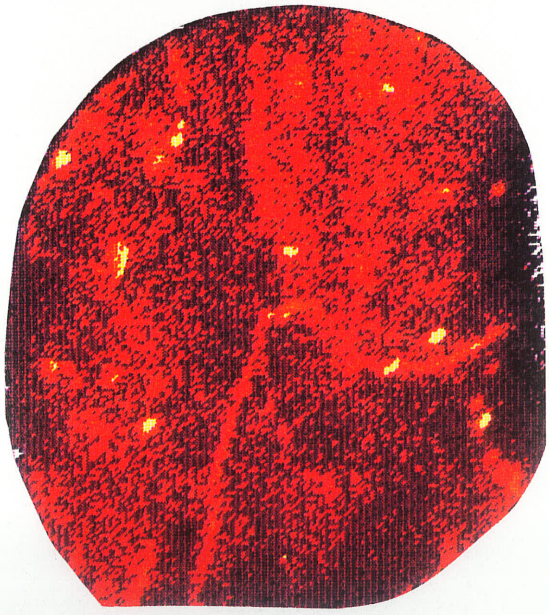

(b)

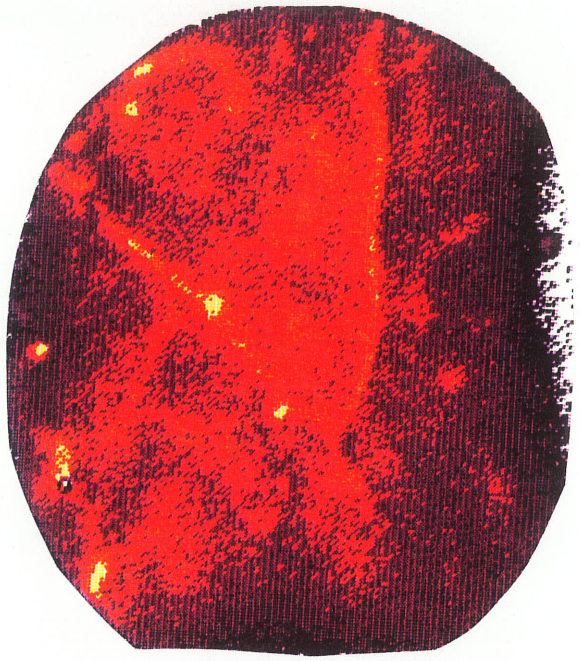

(c)

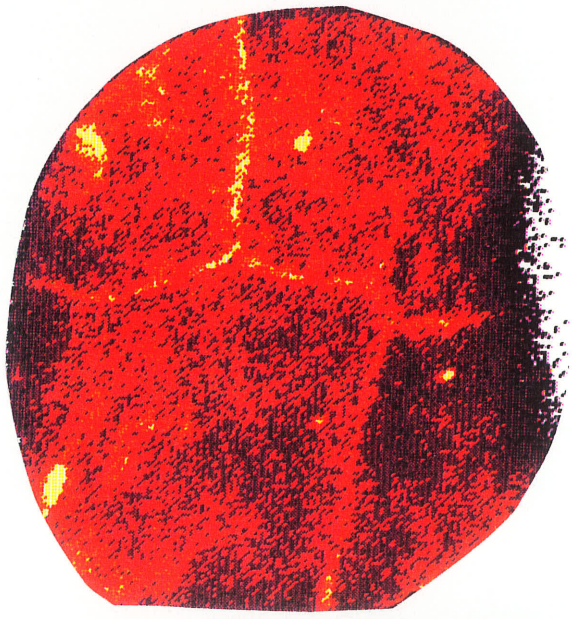

(d)

Fig.4.38 Boron images from specimens heat treated at 950°C (a), 1067°C (b), 1093°C (c) and 1240°C (d) and air cooled.

4.6.2 Boron Segregation After Water Quenching

Fig.4.39 illustrates four images representing the boron distribution at the grain boundaries after heat treatment at the above temperatures followed by rapid quenching. The boron intensity decreases continuously with temperature over the range of 950 to 1240°C. A comparison of Fig.4.38 and Fig.4.39 shows that the boron intensities are different from the specimen that was air cooled as compared to that which was water quenched from the same temperature and the difference in intensity increases as the temperature rises. This suggests that boron segregation is sensitive to cooling rate for the heat treatment temperature. Bright particles were also observed on all the specimens (Fig.4.38 and 4.39) which could be borides or segregation of boron to secondary phase/matrix interfaces.

4.6.3 Boron Segregation to HAZ Microfissures

In order to relate the observed segregation of boron at the grain boundaries to the weld HAZ microfissuring, welded specimens were also analyzed by means of SIMS in this study. A strong boron image was recorded from HAZ microfissure areas as seen in Fig.4.40, which suggests an influence of boron in the formation of microfissures.

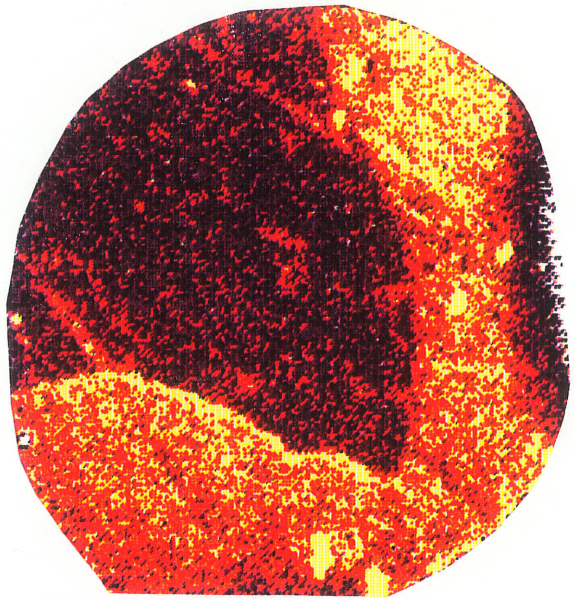

(a)

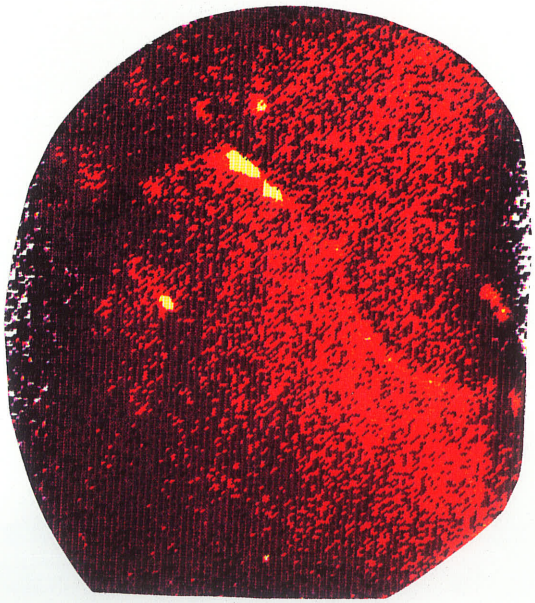

(b)

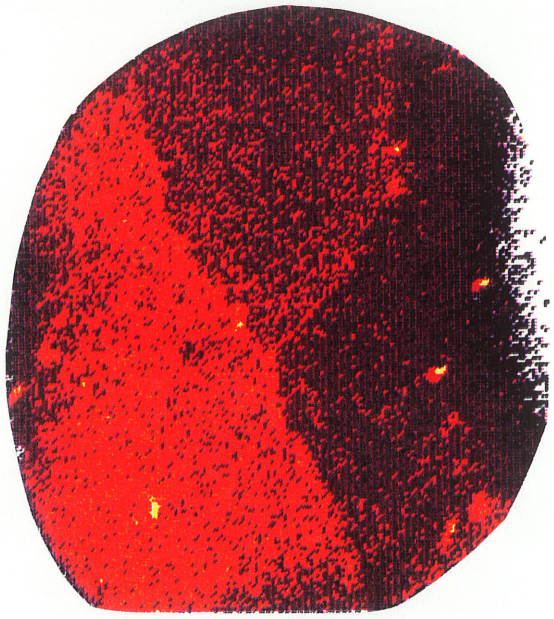

(c)

(d)

Fig.4.39 Boron images from specimens heat treated at 950°C (a), 1067°C (b), 1093°C (c) and 1240°C (d) and water quenched.

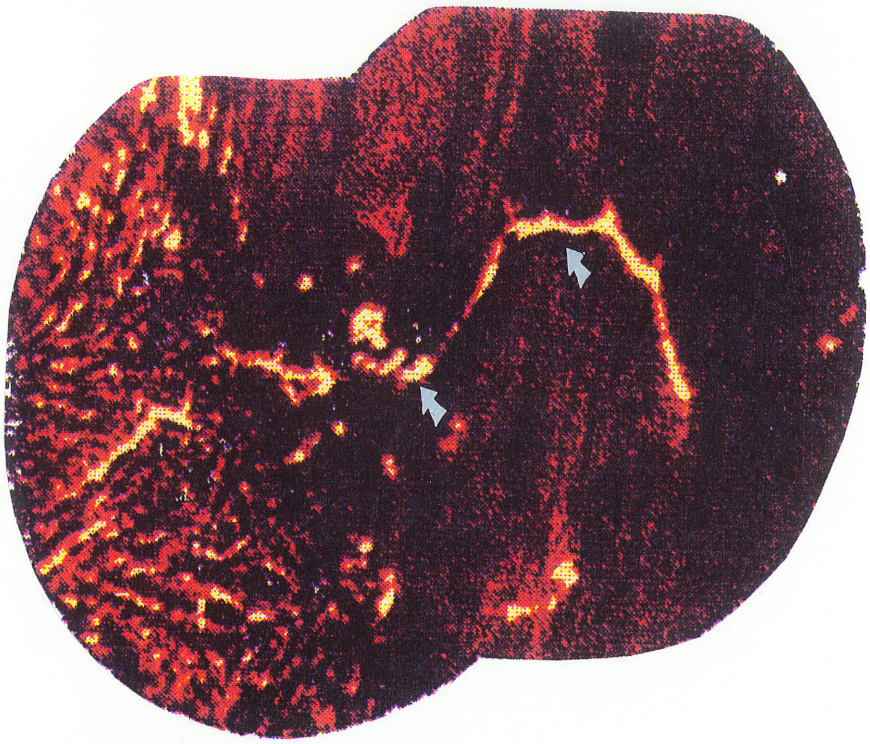

Fig.4.40 Boron image of HAZ microfissure as indicated by arrow.

4.7 Measurement of Grain Boundary Orientation

The orientation of individual grains was determined from the identification of two zone axes on the computer-enhanced electron back-scattering pattern (Kikuchi lines). The crystallographic relationships of grains were represented in rotation matrix form. Individual boundaries were classified according to the nearest Coincidence Site Lattice (CSL) relationship in the range $\Sigma=1$ to 49 using the rotation matrix method [183]. Classification was based upon minimizing the ratio of the determined angular deviation from a CSL ($\Delta\theta_d$), to that allowed on the basis of Brandon's criterion ($\Delta\theta_c$) [184] where

$$\Delta\theta_c = 15^o \Sigma^{-1/2} \qquad <60>$$

This is based on the concept that if the deviation of a pair of grains from exact coincidence can be accounted for by introducing a set of dislocations in the boundary at spacing such that their core structures do not overlap, then the grains are considered to be in coincidence. Thus a $\Sigma=3$ primary twin boundary is still considered to be in coincidence for deviation from the exact twin orientation by up to 8.66° and two grains separated by a small-angle boundary of up to 15° are considered to be in coincidence at the $\Sigma=1$ level (i.e. the same orientation).

The misorientation of grain boundaries was calculated and the results are given in Table 4-11. It is seen that more than 96% of the grain boundaries in this alloy are of a random type, which is not unexpected for cast alloys. Wrought Alloy 718 was analyzed as a reference and the result in Table 4-12 suggests that the fraction of random grain boundaries is much lower for wrought Alloy 718.

Table 4-11 Grain Boundary Mis-Orientation of Cast Alloy 718

Total grain boundaries analyzed: 55
No. of random grain boundaries: 51
No. of Σ39: 2
No. of Σ9: 1
No. of Σ3: 1
Percentage of random grain boundaries: 93%

Table 4-12 Grain Boundary Mis-Orientation of Wrought Alloy 718

Total grain boundaries analyzed: 25
No. of random grain boundaries: 17
No. of Σ27: 1
No. of Σ3: 6
No. of Σ1: 1
Percentage of random grain boundaries: 68%

CHAPTER FIVE

DISCUSSION

In this chapter, the rationale for the observed microstructure of as-cast material and the influence of subsequent heat treatments on it are first discussed. This is followed by an explanation for the microstructures observed in FZ and HAZ. The observed microfissuring behaviour of welded cast Alloy 718 is then rationalized on the basis of the microstructures of base material, HAZ and FZ.

5.1 Microstructural Examination

5.1.1 Base Metal Microstructure

The development of microstructures in castings is largely dominated by two interrelated occurrences, dendrite formation and elemental segregation. Dendritic solidification results in a repetitive microstructural morphology within the solidified grains.

It can be observed that the cast Alloy 718 possesses a heavy dendritic structure with the darker regions being the interdendritic areas (Fig.4.1), which are enriched in Nb, Ti, Si and Mo, but lower in Fe and Cr due to segregation. Partitioning of solutes with their distribution coefficient less or larger than unity occurs during solidification. Explicit determination of the distribution coefficients for various alloying elements can be carried out from SEM/EDS data in Table 4-1. From solidification theory, the initial solid to form is at the dendrite core and will have a composition of kC_0, where C_0 is the nominal concentration of that element in the alloy. The distribution coefficient, k, is not

necessarily constant during the solidification process. The initial distribution coefficients for various alloying elements have been calculated using the minimum solute concentration in the dendrites divided by the nominal concentration given in Table 3-1 and are listed in Table 5-1. Data quoted in the literature are also included.

Table 5-1 Distribution Coefficient of Various Elements in Alloy 718

Element	Nb	Si	Ti	Fe	Ni	Cr	Mo	Al
Cast 718	0.50	0.63	0.47	1.05	0.98	1.06	0.83	1.0
718 weldment[182]	0.48	0.67	0.63	1.04	1.0	1.03	0.82	1.0

It was seen that the results of the present study are very similar to those obtained by other investigators[182]. The values of the distribution coefficients are implicit indicators of the effects of individual alloying elements on the melting/solidification temperatures of the alloy. Alloying elements having distribution coefficients less than unity cause a depression of the liquidus and solidus temperature as their concentration is increased [186]. In the present study, elements such as Nb, Si, Ti, Mo along with trace elements such as S, P, C and also boron cause a decrease in the melting point. The opposite occurs for alloying elements that have distribution coefficients greater than unity.

Elemental segregation often causes the matrix solubility limit to be exceeded such that

terminal solidification constituents occur at final solidification sites. The DSC and microstructural examination conducted during this study and a survey of the literature suggest that the liquid→solid→solid transformation in Alloy 718 follows the sequence of: $L \rightarrow L+\gamma \rightarrow L+\gamma+MC \rightarrow L + \gamma + MC +$ Laves phase $\rightarrow \gamma + MC +$ Laves phase $\rightarrow \gamma + \delta + MC +$ Laves phase $\rightarrow \gamma + \delta + \gamma'' + \gamma' + MC +$ Laves phase.

Various reactions in cast Alloy 718 occur at the following temperatures, which were also listed in Table 4-9:

$L \rightarrow \gamma$ at 1330°C

$L \rightarrow \gamma + MC$ at a temperature of 1267°C (heating curve was used)

$L \rightarrow \gamma$+Laves phase at a temperature 1167°C

The microstructure of as-cast material has been analyzed by several investigators [185-189]. The phases normally found were described as discrete MC particles, eutectic Laves phase, needle like δ, disk-shaped $\gamma''(Ni_3Nb,Al)$; and spheroidal γ' (Ni_3Al, Nb). In this study, phases observed in the as-cast material were: M(C,N) carbonitrides (in some cases it originated from MN core) (Fig.4.2 and 4.3), A_2B Laves phase and δ-Ni_3Nb (Fig.4.2), and cubic-shaped Ti rich nitrides (Fig.4.3). γ'' and γ' were also observed in some areas (Fig.4.4). Phases were identified by their characteristic morphology and confirmed by EDS analysis. EDS/SEM was not able to determine the composition of γ'' and δ phases due to its limited spatial resolution. Therefore, TEM with EDS was used and results are given in Table 4-3. These results suggest the following stoichiometry of δ and γ'' phases:

δ-$(Ni,Cr,Fe)_{0.7}(Mo,Nb)_{0.3}$

γ"-$(Ni,Cr,Fe)_{0.75}(Mo,Nb)_{0.25}$

It is also noted in Table 4.2 that in this study the Laves phase does not have an exact A_2B ([Ni,Fe,Cr,Co]$_2$[Nb,Mo,Si,Ti]) stoichiometry, with A atoms accounting for about 77at% and B atoms accounting for 23at% of the phase.

The stability of various phases present in cast Alloy 718 has been examined [185] and is shown in Fig.5.1, which indicates the temperature at which they start to dissolve (e.g., Laves phase at 1160°C and δ at 1050°C). However, the actual situation is that phases start to go into solution at a temperature well below the specified temperatures and the amount of phases dissolved depends on the heat treatment temperature and the holding time. Both qualitative analysis by SEM and quantitative analysis by Image Analyzer were conducted in this study to examine the stability of various phases during various heat treatments.

The δ-Ni_3Nb volume fraction was observed to decrease with increasing homogenization temperature (Fig.4.14) and it completely dissolved after 1093°C/1hr. The amount of Laves phase showed the same trend as the δ phase (Fig.4.13), with most of the Laves phase going into solution after 1163°C/1hr. The amount of M(C,N) was observed to remain unaffected by the various heat treatments used in this study (Fig.4.15).

Solution heat treatment increased the amount of both intra- and inter-granular δ-Ni_3Nb as illustrated in Fig.4.8 and 4.9. The amount of δ-Ni_3Nb was not significantly affected by the homogenization heat treatment below 1163°C but drastically decreased after homogenization heat treatment at 1163°C before solution treatment. It was noted by other researchers [190] that grain boundaries in the interdendritic regions associated with δ precipitates showed extensive migration and the uniformly spaced δ plates grew into only one of the two adjoining grains. This was confirmed in this study. In addition to precipitating δ, solution treatment also dissolved a certain amount of Laves phase as seen in Fig.4.13. The amount of M(C,N) did not change with solution treatment. Depending on the cooling rate from the solution heat treatment temperature, γ" and γ' may precipitate during cooling. It was observed [191] that a 930°C heat treatment precipitated γ" in the Nb-rich regions of the microstructure.

It has been reported [190] that during ageing, the majority of γ" + γ' precipitated in the Nb-rich interdendritic regions and γ" + γ' have been reported to be absent in the vicinity of the dendrite core. Due to the precipitation of γ" + γ', the hardness (strength) level is increased which was measured and is shown in Fig.4.16 and 4.17. γ'+γ" precipitates were not resolved by SEM study in this investigation. Quantitative analysis showed that decreased amounts of δ and Laves phases were present after ageing, but no explanation can be given at this stage. However, a contradictory observation by Thompson found that some δ had grown at the grain boundaries by a discontinuous precipitation mechanism in cast Alloy 718 during ageing [191]. Overageing resulted in

the coarsening of $\gamma''+\gamma'$ which could be resolved by SEM. An example is shown in Fig.4.12 which is a secondary electron image of specimen aged at 760°C/5hrs + 650°C/1hr. It was also observed that $\gamma''+\gamma'$ were preferably distributed in the interdendritic area.

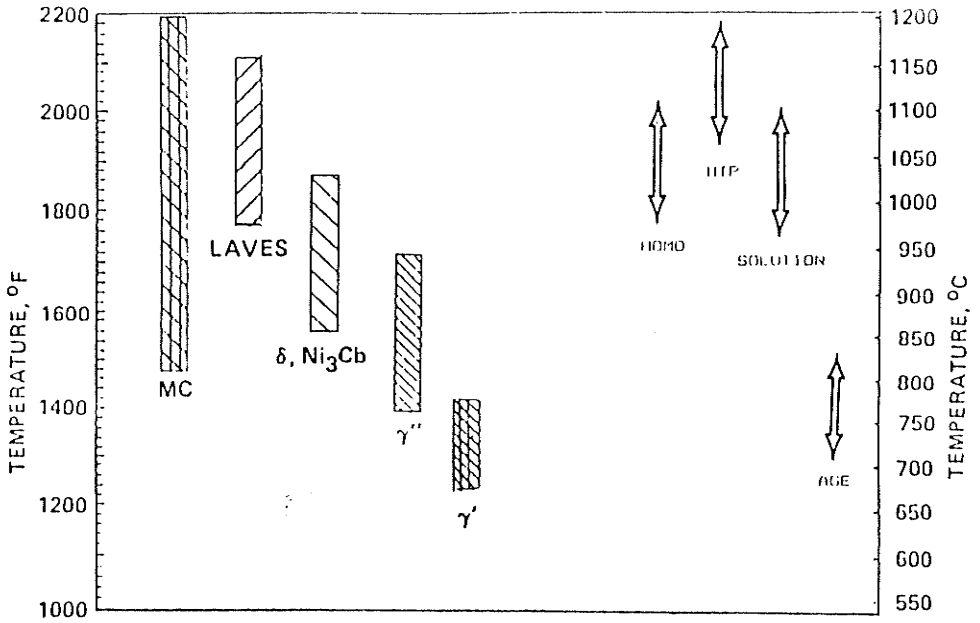

Fig.5.1 temperature-phase stability diagram for cast 718 [187]

It is worth noting that the microstructure (as-cast and heat treated) varied from heat to heat and even within one casting, which can be attributed to the difference in chemical composition and cooling rates. Therefore, a variation in the results of quantitative analysis is not unexpected.

5.1.2 Fusion Zone Microstructures

Due to the rapid solidification of the weld after welding, the constituents in the fusion zone are generally much finer than these observed in ordinary castings and can be only resolved by TEM. Some investigators have conducted TEM analysis of the fusion zone on both forged [77] and cast Alloy 718 [182 and 192]. The GTAW weld of cast Alloy 718 consists of primary γ, interdendritic eutectic-type constituents involving Laves phase and MC(NbC) carbides. It has been observed that γ/Laves phase was by far the more predominant phase. In an EB weld of wrought 718 [77], cross-linked sheets of lamellar MC carbides mixed with Laves phase precipitates were observed. In this study, several constituents were found in the EB welded fusion zone. They are dendritic M(C,N) (Fig.4.21), blocky Laves phase (Fig.4.23), and globular $M_{23}C_6$ (Fig.4.22) with the majority($>90\%$) of the precipitates being M(C,N). The lattice parameters and chemical composition of the phases are listed in Tables 4-5 and 4-6. A variation in compositions observed in this study when compared with those cited in the literature are possibly due to the different cooling rate that occurs during solidification after welding as compared to a normal casting process. The variation in chemical composition would lead to a variation in lattice parameters as well.

When the observed FZ microstructures are compared with those reported by others [77,182,192], it is found that the presence of, and the amount of precipitates, varies from one study to another, especially the presence and the amount of Laves phase. The cooling rate (or welding speed) and the composition of the material can have a major influence.

The effect of cooling rate on the occurrence and volume fraction of solidification products, especially Laves phase in this study, can be discussed using solidification theory.

The calculation of the amount of Laves phase present in the weld has been conducted by several investigators [181,182]. Their calculations were based on a cellular solidification model developed by Brody and Flemings [193] following the earlier work of Scheil [194]. The following assumptions were made for the calculations [181,182]:

(1) No solid state diffusion occurs during solidification.

(2) Distribution coefficient k remains constant during the entire solidification process.

(3) Only segregation of Nb is important for the formation of Laves phase. That is, the γ/Laves phase constituent will form when the solubility of Nb in the solidifying γ dendrites is exceeded (over 0.093 in this case).

(4) There is no effect of cell tip radius of curvature on the distribution coefficient k.

(5) Thermodynamic equilibrium is maintained at the moving solid/liquid interface.

Under these assumptions, the fraction of solid that forms at any instant f_s is related to its composition C_s by the following relationship:

$$C_S = kC_0(1-f_S)^{k-1} \qquad <61>$$

where k is the distribution constant and C_o is the nominal concentration of Nb. The fraction of the second phase (Laves phase in this case) is given by:

$$f = [C_{mass}/(kC_0)]^{\frac{1}{k-1}} \qquad <62>$$

where, C_{mass} is the solid solubility of Nb in the dendrites. As k for Nb is not constant during solidification in this study, an initial value of k=0.50 (from Table 5-1) is used for calculations, C_0=0.05 is the nominal Nb concentration and C_{mass}=0.093 is taken to be the solubility of Nb in austenite [182]. The amount of Laves phase formed during solidification is calculated to be

$$f_{Laves}=(\frac{0.093}{0.5x0.05})^{\frac{1}{0.5-1}}=0.072=7.2wt\% \qquad <63>$$

Since the density of the eutectic γ=8.76gm/cm^3 and the density of the Laves phase=8.54gm/cm^3, the volume fraction of Laves phase is calculated to be 7.0% which is about twice as much as the measured value.

When the solidification speed, R, is constant, the amount of solute carried forward ahead of the interface is proportional to the characteristic distance D/R, where D is the diffusivity of solute in the liquid, and the amount of the solute is therefore inversely proportional to the speed of solidification R. If the value of R is increased, D/R and the amount of solute carried forward is decreased which will cause the amount of secondary phase to decrease. With an increase in cooling rate, an effective distribution coefficient should be used in the above equation which is given by [195]:

$$k_E=\frac{k_0}{k_0+(1-k_0)\exp(\frac{-Rd}{D})} \qquad <64>$$

where d is the thickness of the boundary layer through which the solute must diffuse, D is the diffusion coefficient and is approximated to be 5x10^{-5}cm^2/sec [196], and R is the

solidification speed, a value of 5cm/sec being used for electron beam welding.

At very low speeds, $k_E = k_0$, but as the speed increases and the diffusion zone becomes relatively more important, k_E approaches a value of "1". The value of d is limited by the velocity of movement of the liquid parallel to the interface and depends also on the viscosity of the liquid. It varies from about 10^{-3}cm, for very vigorous stirring, to about 10^{-1}cm for natural convection [195]. The value of k_E approaches k_0 as the effectiveness of mixing is increased; that is, as the value of R is decreased, d is decreased and the diffusion coefficient D is increased. The value of k_E for solidification during electron beam welding can therefore be estimated as follows:

$$k_E = \frac{0.5}{0.5 + (1 - 0.5)\exp(-\frac{5x10^{-3}}{5x10^{-5}})} \approx 0.99 \qquad <65>$$

The fraction of Laves phase can now be calculated by using the effective coefficient k_E as follows:

$$f_{LAVES} = (\frac{0.093}{0.99x0.0501})^{\frac{1}{0.99-1}} = 1.3x10^{-25}(wt\%) \approx 0 \qquad <66>$$

It is seen from this equation that the value of Laves phase percentage is significantly different than the value (7.2%) obtained in Eq.<63>. This would explain why less Laves phases are observed in EB welds than both in the as-cast and GTAW welds. From the above calculation, it can be concluded that during fast solidification, as in EB welding, non-equilibrium phases such as Laves phase can be drastically reduced (i.e.

approaching zero) as compared to that observed in castings in which the cooling rate from solidification is relatively slow.

In this investigation the heat treatment prior to welding did not have any influence on the fusion zone microstructures.

5.1.3 Heat Affected Zone Microstructures

In general, two minor microstructural constituents have been identified in the HAZ: Laves + MC-type carbides [58,77,197]. By employing a high resolution electron microscopy technique, Vincent found that in the wrought Alloy 718 80 to 90% of the secondary phases present in the HAZ were Laves phase and MC-type carbides [77]. He found that small amounts of secondary phases such as γ", δ, M_3B_2 boride, MgO, MNP phosphide and carbosulphide were also present in the HAZ.

Laves phase and MC carbonitrides were found in both EB HAZ and Gleeble simulated HAZ in the present study (Fig.4.24 and 2.25). The microstructural changes in the HAZ observed are described as follows:

EB Weld HAZ:

I: Liquation in interdendritic area and resolidification into eutectic Laves phase and discrete M(C,N) carbonitrides.

II: Constitutional liquation of Laves phase and M(C,N) carbonitrides.

III: Isolated melted pools of γ with different composition, unaffected matrix and

resolidification of γ into eutectic Laves phase.

Gleeble HAZ:

I: Both Laves phase and M(C,N) carbonitrides partially liquated and resolidified into Laves phase/γ eutectic and script M(C,N).

II: Grain boundary liquation.

III: Isolated melted pool of Laves phase which resolidifies into eutectic Laves phase. The eutectic Laves phases in this region were surrounded by a 'cloudy zone' (Fig.4.25c), which is an indication of liquation occurring during the simulated thermal cycles. EDS/SEM analysis revealed that the cloudy zones are enriched in Nb (13-15%) relative to the surrounding matrix. The cloudy zones do not have any internal structure, suggesting that the liquid solidified epitaxially from the adjacent solid matrix.

GTAW HAZ [41]:

The cast GTAW HAZ showed the following microstructural features:

I: Extensive liquation adjacent to the weld fusion boundary.

II: Liquation at the grain boundaries.

III: Complete liquation of Laves phase, Nb-riched carbides remained unaffected.

IV: Liquation at Laves phase/γ interface.

The liquid formed in region I and II solidified into Laves phase and/or M(C,N) carbonitride depending on the cooling rate (as discussed in section 5.1.2) and the alloy's Nb and C content. It is also interesting to note that the morphology of the resolidified

constituents resulting from different processes, i.e., dendritic M(C,N) carbonitrides were formed in EBW FZ (Fig.4.21), irregular shaped M(C,N) in EBW HAZ (Fig.4.24) and script M(C,N) in Gleeble HAZ (Fig.4.25). The occurrence of different phases could be caused by the difference in cooling rates and local chemical composition. Grain boundary liquation was also observed in the EBW HAZ and Gleeble simulated HAZ (Fig.4.24 and 4.25), leaving the HAZ grain boundaries with microfissures if thermal stresses exceed a critical value, or ghost marked grain boundaries due to chemical difference between the grain boundary area and the adjacent area which was observed in GTAW HAZ [41].

5.1.4 HAZ Microfissuring

HAZ microfissuring occurs due to the inability of the grain boundary material to sustain the thermal stresses caused by the weld cycle. The mechanism of crack formation and propagation will be discussed in the following section. The formation of liquid on the grain boundaries has been attributed to partial constitutional liquation of Laves phase and M(C,N) carbonitride on grain boundaries or as a consequence of grain boundary sweeping during welding [198]. The presence of certain tramp elements on grain boundaries would further assist the wetting of the liquid. The liquid, enriched in liquidus depressant Nb, Mo, Si and possibly trace elements B, S, P and C, resolidifies into M(C,N) carbonitride and/or Laves phase on grain boundaries or on the sides of microfissures depending on when the microfissures develop (Fig.4.26).

5.2 Elemental Segregation at Grain Boundaries

In the examination of elemental segregation by means of SIMS, boron was observed to segregate to grain boundaries and the intensity of boron segregation varied with heat treatment temperature and cooling rate from the heat treatment temperature. Boron was also found as discrete particles in the SIMS micrographs. Since borides were not detected in cast Alloy 718 used in this study, the occurrence of these bright particles could be attributed to boron segregation to secondary phase/matrix interfaces which was imaged as a particle due to the limited resolution of SIMS technique.

In this section, two types of boron segregation, viz. equilibrium segregation and non-equilibrium segregation, will be discussed both qualitatively and quantitatively. The effects of heat treatment temperature, cooling method, grain size and the nature of grain boundaries will be also considered.

5.2.1 Mechanism of Equilibrium and Non-Equilibrium Segregation

Equilibrium grain boundary segregation occurs when an alloy is held at a temperature sufficiently high to allow appreciable diffusion of impurities to the grain boundaries, thus reducing the free-energy of the system [199]. The concentration of an element, C_b, caused by this type of segregation can be expressed by:

$$C_b = \frac{C_m e^{-E_b/kT}}{1 + C_m e^{-E_b/kT}} \qquad <67>$$

where E_b is the binding energy of solute atoms with grain boundaries and C_m is the

nominal concentration of the solute in the matrix. A value of 0.65 eV is used to calculated the boron equilibrium segregation concentration and the calculated values are plotted against temperature in Fig.5.2. It can be observed that as the temperature increases, the amount of segregation decreases exponentially. This is the classical equilibrium segregation behaviour as first discussed by Mclean [88].

Non-equilibrium segregation occurs during cooling from high temperatures, as proposed by Westbrook and Aust [98-101]. As described in the literature review section, this type of quench-induced segregation occurs when the binding energy, E_{vs}, (between vacancy and solute atoms) is positive and large relative to the thermal energy kT ($E_{vs} > > kT$) and the impurity atoms are mobile and diffuse either interstitially or substitutionally [103-105]. On an atomic level, the solute atoms are actually dragged by moving vacancies toward vacancy sinks such as grain boundaries.

Before calculating the non-equilibrium segregation of boron, it is important to know the binding energy between a boron atom and a vacancy in the alloy being studied. Aust and co-workers [101] have plotted the binding energy (E_{vs}) against the distribution coefficient (k) as shown in Fig.5.3. The distribution coefficient (k) of boron can be approximated to be equal to 0.0073 [200]. From this value a binding energy of $E_{vs} \approx 0.5$ eV can be estimated from Fig.5.3, which is the same value as was assumed by Williams in the development of his model [161]. Faulkner [112] calculated the binding energy to be equal to 0.57 eV using an elasticity model.

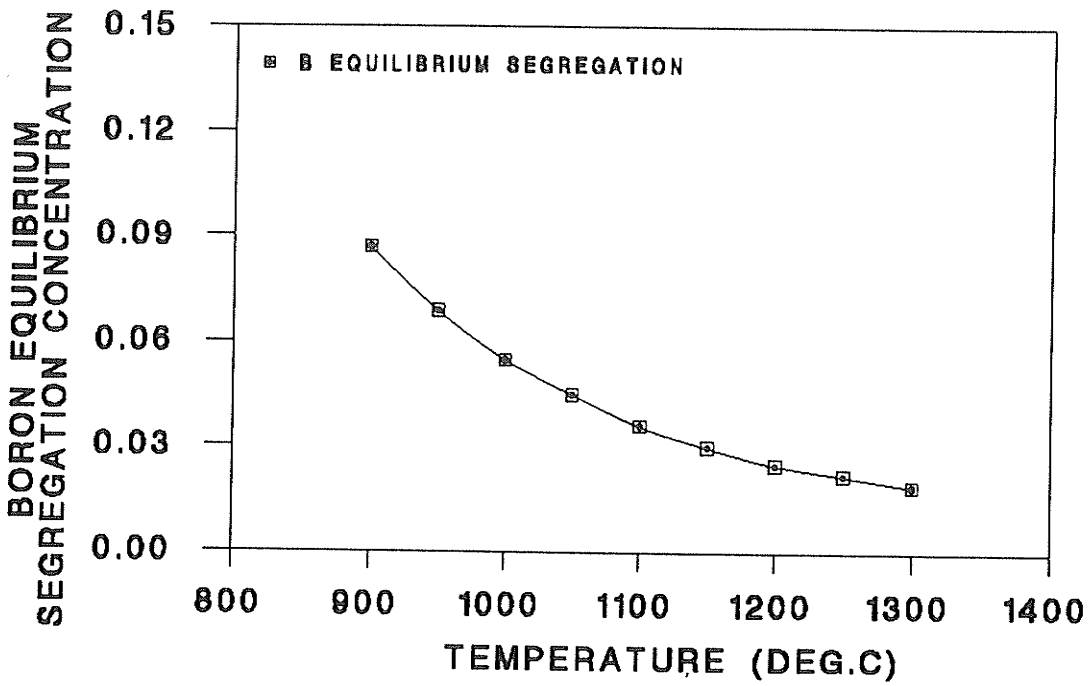

Fig.5.2 Relationship of boron equilibrium segregation concentration and heat treatment temperatures.

The values of the thermal energy kT are 0.10 eV and 0.13eV at 900 and 1250°C respectively, well below the binding energy E_{vs} for a boron vacancy complex. According to Aust [101] and Anthony [103-105], non-equilibrium segregation occurs only if $k << 1$ and $E_{vs} > kT$. Therefore, it is thermodynamically possible for B to segregate to grain boundaries or other vacancy sinks in a non-equilibrium mode when an alloy containing B is quenched from the 900-1250°C temperature range. The concentration of boron vacancy complexes formed at different temperatures is calculated and tabulated in Table 5-2.

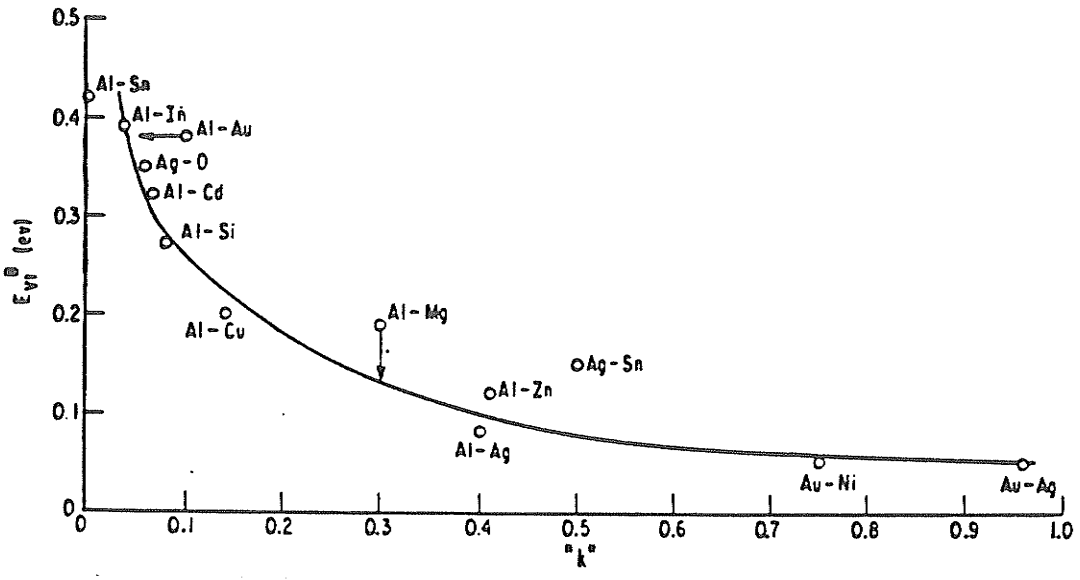

Fig.5.3 Relationship between solute distribution coefficient and solute vacancy binding energy [101].

Table 5-2 Concentrations of Vacancy and Solute-Vacancy Complex

Energy of Formation of Vacancy (E_{vf}) [101] 1.4 eV		
Binding Energy of Boron and Vacancy (E_{vs}) [101,114,128] 0.5 eV		
Boron concentration (at%)(C_s) in cast alloy 718 0.016%		
Vacancy Concentration C_v [107] $=Kexp(-E_{vf}/kT)[1-ZC_s+ZC_sexp(E_{vs}/kT)$ K=4 (geometry factor) Z=12 (co-ordination number)	950°C	$7.3x10^{-6}$
	1240°C	$1x10^{-4}$
Vacancy-Solute Complex Concentration $C_{vs}=KC_vC_s$ where $K=12exp(E_{vs}/kT)$	950°C	0.000156%
	1240°C	0.00085%

These calculations show that at 950°C there is a small portion (< 1.6ppm) of boron atoms involved in the solute-vacancy complexes. When the temperature is 1240°C, small but significant, amounts of boron-vacancy complexes (8.5ppm) are formed which contribute to non-equilibrium segregation of boron during cooling.

Faulkner [114] assumed that

1) Only diffusion of boron-vacancy complex occurs.

2) Non-equilibrium segregation occurs only between T_i (heat treatment temperature) to $T_{0.5Tm}$ (half of the melting temperature).

Based on these assumptions, he developed the following expression to determine the magnitude of non-equilibrium segregation of boron as follows:

$$\frac{C_b}{C_g} = A\exp\left[\frac{E_{VS}-E_f}{kT_i} - \frac{E_{VS}-E_f}{kT_{0.5T_m}}\right]\frac{E_{VS}}{E_f} \qquad <68>$$

where A is the correction factor and is approximated to be 3 (Appendix VI), C_b is the segregating atom concentration on the grain boundaries, C_g is the segregating atom concentration in the unsegregated regions (0.016at%), E_b is the binding energy between vacancy and impurity and is equal to 0.5eV [114], E_f is the vacancy formation energy (=1.4eV in γ stainless steel [161]) and T_m is the average of liquidus and solidus and is 1320°C for cast alloy 718.

It can be observed from this equation that non-equilibrium segregation increases with:

1) increasing temperature, i.e., the higher the heat treatment temperature, the

the solute-vacancy complex mobility and concentration (5.2.2).

2) large E_b ($>>kT$).

Other factors also increase the amount of non-equilibrium segregation. They are:

1) large difference in atomic size and electronic structure between the segregant and matrix atoms, which increases the tendency for segregation.

2) relatively fast cooling rate to exceed any likelihood of desegregation (see section 5.2.4).

3) large grain size (see section 5.2.5).

4) faster diffusion rate of solute-vacancy complexes relative to vacancies which results in solute accumulation at grain boundaries.

The calculated values of non-equilibrium segregation of boron in alloy 718 as a function of temperature are given in Fig.5.4.

5.2.2 Temperature Dependence of Boron Segregation

5.2.2.1 Equilibrium Segregation

Boron images (SIMS) taken from specimens heat treated at different temperatures and holding times are shown in Fig.4.39. Non-equilibrium segregation is not likely to occur at the cooling rate used (400°C/sec) and the boron segregation is mainly driven by the equilibrium mode during holding at heat treatment temperature. The variation in boron intensity follows the calculated trend presented in Fig.5.2. That is, the boron segregation intensity decreases with increasing heat treatment temperature.

Since the time of holding at the heat treatment temperature is long enough to allow sufficient amount of boron to diffuse a distance of 1 mm and the distance is constant for all the heat treatments, any kinetic effect of the process can be neglected in considering the overall segregation of boron in this study.

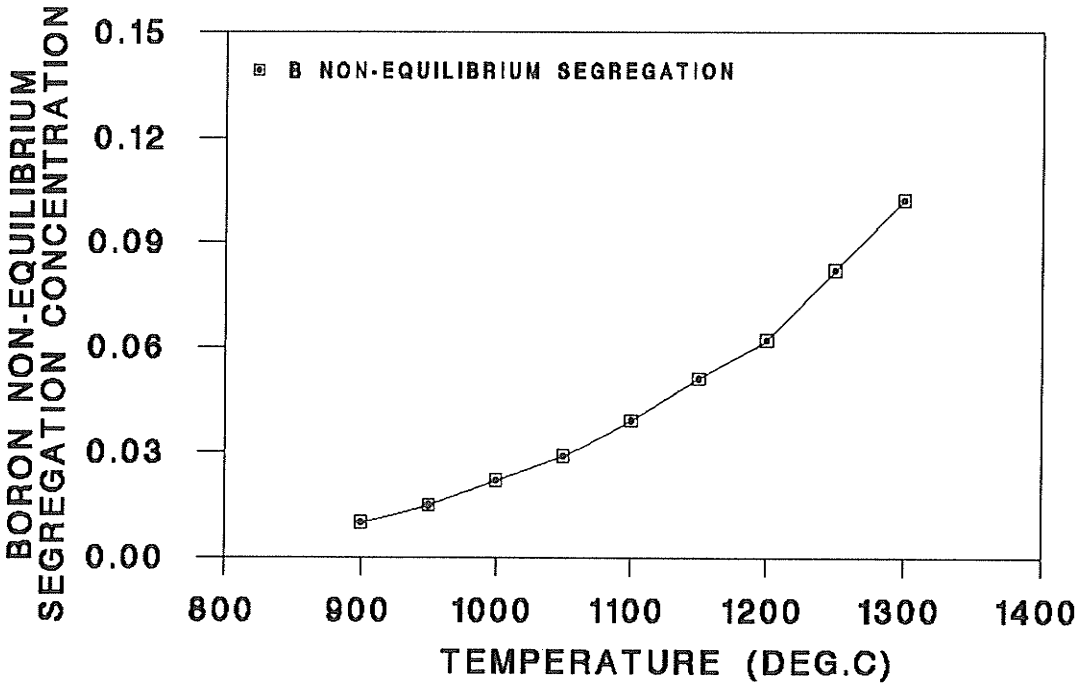

Fig.5.4 Relationship of boron non-equilibrium segregation concentration and heat treatment temperatures

5.2.2.2 Non-Equilibrium Segregation

The occurrence of only non-equilibrium segregation was not observed in this study as the samples were held at heat treating temperature for a sufficiently long period of time (Table 3.4) so that equilibrium segregation always occurred. When the specimens were air cooled, the observed segregation was a combination of both equilibrium and non-equilibrium segregation. This will be discussed in detail in the next section.

5.2.3 Effect of Heat Treatment Temperature on Overall Boron Segregation

The heat treatment temperature and subsequent cooling rate affect the grain boundary segregation in different ways, i.e., equilibrium segregation decreases as the temperature rises while non-equilibrium segregation increases with increasing temperature. Both experimental and calculated results [117,119,123] show that non-equilibrium segregation occurs during cooling and only within a certain cooling rate range. However, equilibrium segregation occurs during holding at the heat treatment temperature. Thus, every thermal treatment produces a certain amount of boron segregation, both equilibrium (curve a in Fig.5.5) and non-equilibrium (curve b in Fig.5.5), and the amount of non-equilibrium segregation depends on the cooling rate and the initial temperature of heat treatment. The overall level of boron segregation is represented by curve c in Fig.5.5. This curve exhibits a transition temperature. Below this temperature, equilibrium segregation dominates and above it non-equilibrium segregation prevails. The transition point varies with the cooling rate as will be discussed in the next section.

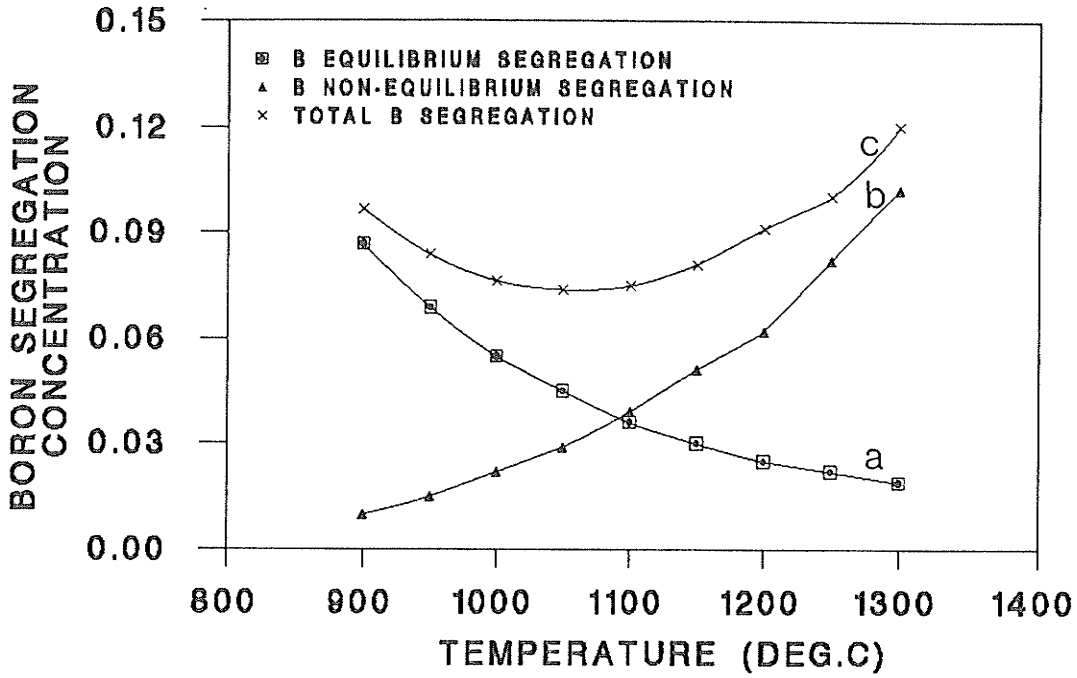

Fig.5.5 Combination of boron equilibrium and non-equilibrium segregation. (a) equilibrium segregation, (b) non-equilibrium segregation and (c) Total boron segregation.

The results in Fig.4.38a, b, c and d represent a combination of equilibrium and non-equilibrium segregation where an intermediate cooling rate (air cooling) is used. The lowest boron segregation was observed at 1067°C which is around the transition temperature at the cooling rate of 20°C/sec. On the other hand, when specimens were water quenched from the heat treatment temperature at 400°C/sec, non-equilibrium segregation is not expected to occur due to insufficient time being available for the diffusion of boron-vacancy complexes. Therefore, images in Fig.4.39 a, b, c and d represent mainly equilibrium segregation, i.e. the extent of segregation decreases with

the temperature. Reasonable agreement between the observed and predicted value of equilibrium and non-equilibrium segregation of boron is observed by comparing Fig.4.38 to Fig.5.5 and Fig.4.39 to Fig.5.2.

5.2.4 Dependence of Boron Segregation on Cooling Rates

The dependence of segregation of boron to grain boundaries on the cooling rate was first noted by Ueno and Inoue [201] in 1973 when they examined the effect of boron on hardenability of low carbon steels. Using autoradiography, they found that the time-temperature characteristics of segregation of boron had the shape of a C-curve.

In Faulkner's equation (Eq.<68>), it was assumed that only the diffusion of boron-vacancy complex occurred. However, dissociated impurities will diffuse away from the grain boundary vicinity when an impurity gradient is created by the diffusion of a boron-vacancy complex. This process is defined as desegregation. Non-equilibrium segregation is strongly dependent on the cooling rate. The degree of segregation is the highest at intermediate cooling rates for which sufficient time is available to let vacancy-solute atom pairs diffuse to the grain boundaries but not sufficient to let deposited solute atoms diffuse away from the grain boundary region.

The experimental results of Karlsson [123] showed that the extent of non-equilibrium segregation when cooling from 1075°C increases with decreasing cooling rate (from 530°C/sec to 27°C/sec) then decreases when the cooling rate drops to 0.25°C/sec. This

is consistent with the nature of boron segregation observed in this study (compare Fig.4.38 and 4.39). As a diffusion-controlled process, desegregation increases with the heat treatment temperature. This suggests that the critical cooling rate, which results in a maximum amount of non-equilibrium segregation from a certain temperature, is greater when quenching from higher temperatures. A schematic diagram is thus developed from the above discussion and is shown in Fig.5.6. It summarizes the following:

a) When cooling from the same temperature, there exists a critical cooling rate such that when the cooling rate is slower than this, desegregation occurs and when the cooling rate is faster than this there is not enough time to reach maximum non-equilibrium segregation.

b) The critical cooling rate increases with increasing heat treatment temperature.

c) At the same cooling rate, higher segregation occurs when the heat treatment temperature is higher.

d) At lower heat treatment temperatures, the variation in degree of segregation with the heat treatment temperature is less sensitive to cooling rate.

5.2.5 Effect of Grain Boundary Orientation and Grain Size on Grain Boundary Segregation

SIMS analysis in this study revealed that the intensity of the boron image obtained from the same specimen varied slightly from grain boundary to grain boundary. For equilibrium segregation, it is well known that a significant variation in concentration can occur which is related to the variation in grain boundary orientation/structure [202,203].

Therefore, grain boundary orientation measurements were carried out using the Electron Back-Scattered Diffraction (EBSD) technique. The results in Table 4-11 show that more than 93% of the grain boundaries in cast Alloy 718 are of the random type ($\Sigma \geq 49$). However, only 68% of the grain boundaries in wrought Alloy 718 were of the random type. It has been reported that the frequency of random grain boundaries increases as grain size increases [204] and since the grain size of the material used in this study is large, it is reasonable to find that most of the grain boundaries are of the random type. Therefore, the variation in the intensity of equilibrium segregation of boron caused by the nature of grain boundary is negligible. For non-equilibrium segregation, the important factor is the ability of the grain boundaries to act as a vacancy sink. Experiments have shown that most of the grain boundaries, with the exception of special boundaries such as coherent twins and others with low Σ values, can operate as highly efficient vacancy sinks [126,127]. Therefore, most of the grain boundaries (>93%) will attain the same amount of non-equilibrium segregation during cooling. The geometrical effects of grain boundaries have been discussed by Karlsson [123]. It is suggested that an apparently higher intensity of boron segregation could be caused by a comparatively larger boundary area being exposed at these boundaries, and not by any real variation in the actual amount of boron segregation.

In addition to the grain boundary orientation effect, grain size also has an impact on the non-equilibrium segregation. Faulkner's model [114] predicts that a large grain size leads to a higher segregation. This is supported by Karlsson [205] who stated that the degree

of boron segregation at the grain boundaries increases with an increase in grain size. However, Williams [161] observed reduced grain boundary segregation of boron by increasing the grain size from 50 μm to 125 μm while keeping other parameters constant. Therefore, the variation in the degree of boron segregation observed in this study could be largely attributed to the direction of grain boundaries relative to the ion beam during SIMS analysis and to the variation in grain size.

By comparing the observation on wrought Alloy 718 with cast Alloy 718, it can be concluded that the cast material has more severe segregation of boron due to both a large grain size (5mm, compared to ASTM#5), and a larger percentage of random type grain boundaries; i.e. 93% as compared to 68% in wrought Alloy 718 (Table 4-12).

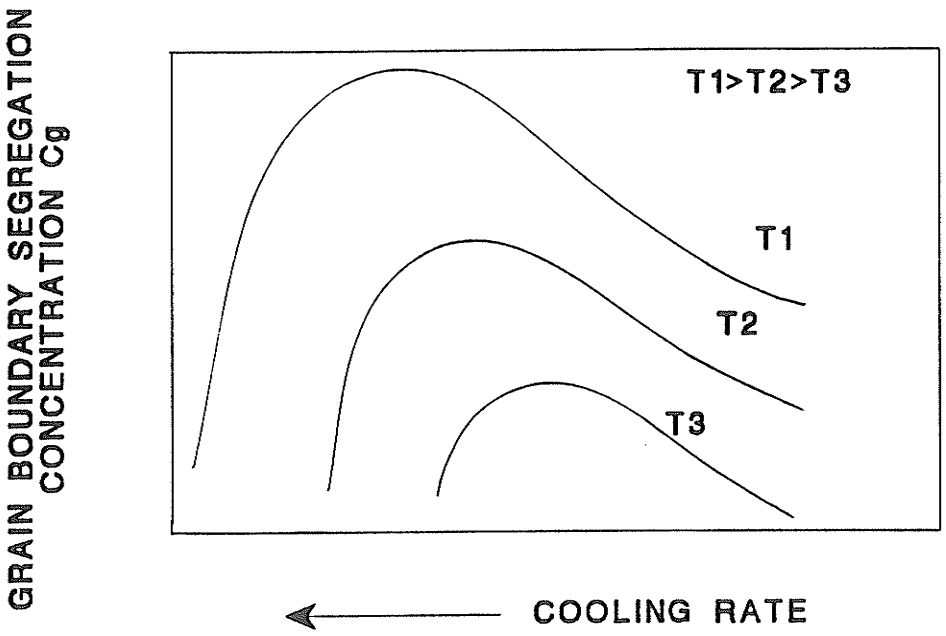

Fig. 5.6 Schematic diagram showing non-equilibrium segregation cooling rate sensitivity.

5.2.6 Effect of Other Solute Atoms on the Segregation of Boron

The presence of other trace elements such as S, P and C which have a low distribution coefficient value in cast Alloy 718 could affect the segregation rate and degree of segregation for boron and for each other in one of the following three ways:

(a) By affecting the diffusivity of elements.

(b) If one solute has a misfit with the matrix of the same sign as the other, it presumably tends to compete with the other atom in distorted regions. If the two have misfits of opposite signs and are present in about equal atomic proportions, they tend to 'pair off' in the lattice with the result that their tendency to segregate is reduced [206].

(c) If one solute atom does not have a significant misfit it may nevertheless affect the average lattice parameter sufficiently to influence the degree of segregation of other solutes.

The atomic size of solute atoms and the mismatch with the matrix (Ni base) have been calculated and are shown in Table 5-3. The P and S atoms compete with boron for substitutional sites in the matrix due to their smaller mismatch with the matrix while C occupies the interstitial positions. The mismatch of these elements in the grain boundary area can not be determined due to the complexity of the grain boundary structure. However, the existence of these elements would affect segregation behaviour of each other in one way or another.

Table 5-3 Atomic Size and Mismatch with γ-Matrix of C,S,P and B

Atom	C	B	S	P	γ-Ni
Atomic Size	.77	.79	1.02	1.16	1.25
Mismatch as Substitutional	-	0.37	0.18	0.07	-
Mismatch as Interstitial	0.48	0.52	-	-	r=0.52*

*The radius of octahedral space in FCC

5.3 HAZ Microfissuring and the Effect of Heat Treatment on TCL

5.3.1 General

In the weld HAZ, microfissures were found on solute-enriched grain boundaries adjacent to the FZ. Many cast alloys are susceptible to intergranular liquation cracking due to the formation of incipient intergranular liquid films which can open into intergranular cracks. Previous studies on cast Alloy 718 have shown that both NbC [77,58] and Laves phases [41,63] produce intergranular liquid films when subjected to the rapid thermal cycles that occur in the HAZ. It has been also theorized that the liquation process is not in itself a sufficient condition to produce severe liquation cracking, but the liquation must also be accompanied by a grain boundary wetting phenomena. One of the factors which can encourage the liquation and wetting is the interaction of elements like boron [207], sulphur [53], phosphorous [208] and carbon [53,54] within the grain boundaries.

The mechanical stresses leading to the formation of weld HAZ cracks arise from

temperature gradients, the difference in thermal expansion in different areas and the resulting plastic deformation associated with passage of the weld pool and its temperature profile [209]. Evolution of the stresses can depend significantly on the welding parameters, the degree of mechanical constraint associated with the workpiece geometry and weld fixturing, and the thermal properties of the material being welded.

The requisitions for a liquation crack to form can be summarized as:

(1) formation of liquid on grain boundary;

(2) wetting of the liquid along the grain boundary;

(3) development of thermal stresses.

The HAZ microfissuring susceptibility can be evaluated by total crack length (TCL), average crack length and maximum crack length. When no external stresses are imposed, the variation in TCL and maximum crack length have the same trend when heat treatment, grain size and weld morphology are the same [210]. The TCL used in this study to evaluate the HAZ microfissuring tendency is a sum of all the crack lengths measured on six cross sections of a weld. The standard deviation can not be obtained for the summed values of crack lengths, but standard deviation at 90% confidence level has been calculated for the average crack length measured in different specimens after various homogenization heat treatments, and is shown in Fig.5.7a. Also included in this figure is the variation in TCL with temperature for comparison (Fig.5.7b). It is seen that both TCL and average crack length vary with temperature in a similar manner.

5.3.2 Effect of Homogenization Heat Treatment on HAZ TCL

The influence of homogenization heat treatment temperature on microfissuring in Alloy 718 has been examined by several investigators. In the wrought alloy it has been shown that a higher homogenization temperature increases microfissuring [58,62,65]. In the as-cast condition the results of both Kelly [51] and Thompson [54] also suggest that the elevated temperature homogenization treatment is detrimental, with increased microfissuring occurring as the temperature is increased. Thompson and co-workers observed an approximately 9-12% increase in TCL after 1093°C/1hr treatment over the as-cast condition. Kelly found a 31% increase in TCL on varying the heat treatment from 1093°C/1hr to 1163°C/1hr + 1093°C/1hr. In the present investigation, it was observed that when the heat treatment temperature is increased the total crack length first decreased and then increased (Fig.4.27). As stated in Section 2.6, the initial objective of this study was to examine the relationship between the amount of secondary phases (Laves, M(C,N) and δ) and the total crack length in weld HAZ. It was found that the amount of Laves phase and δ decreased with the increasing temperature and the amount of M(C,N) remained constant (Fig.4.13, 4.14 and 4.15) with no correlation occurring between the volume fraction of secondary phases and the total crack length. This suggests that the amount of the low melting point Laves phase did not cause the observed variation in HAZ microfissuring with temperature.

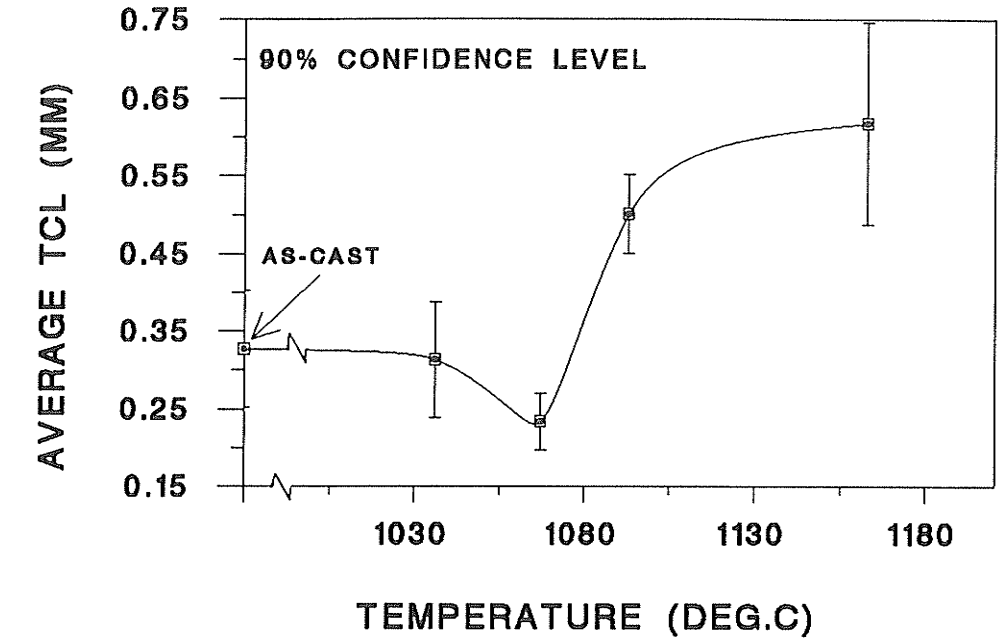

(a)

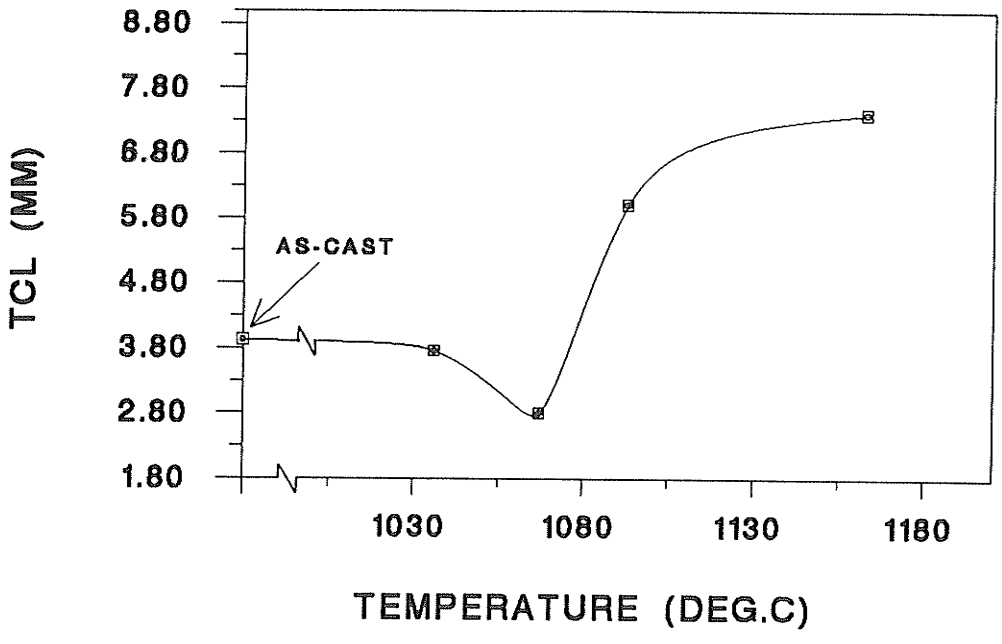

(b)

Fig.5.7 Average TCL with standard deviation (a) and TCL (b).

Many theories have been proposed to explain why high temperature homogenization results in increased cracking tendency. Kelly [51] has noted the effect of heat treatment below and in the vicinity of the Laves phase eutectic temperature. He alluded to the possibility of formation of a grain boundary film of resolidified Laves phase after homogenization at 1163°C which increases the microfissuring. Electron microscopy in the present work, however, failed to reveal any precipitate film on the grain boundaries after heat treatment at 1163°C/1hr. An example of a film-free grain boundary is shown in Fig.5.8.

Thompson proposed that non-equilibrium solute segregation occurs during welding primarily by the combination of constitutional liquation and supersolidus heating of second phase precipitates which liquate and spread along the grain boundaries [211]. He also concluded that tramp elements such as S can be released during heat treatment and can segregate to grain boundaries. Auger spectroscopic analysis showed segregation of S to free surfaces and grain boundaries [53] after a 1093°C homogenization treatment with no indication of Nb and C segregation to the grain boundaries. This can be used to explain the fact that higher homogenization temperatures lead to higher total crack length but it can not explain the variation in the values of TCL with the heat treatment temperatures observed in the present study.

The effect of boron additions on the weldability of nickel alloys has been established for some time. For example, Thompson noted the detrimental effect of boron addition on

HAZ cracking [59]. Investigation on alloy A-286 by Brooks showed that the addition of boron increased the susceptibility to HAZ cracking [212] and no constituent associated with boron was observed. Brooks believes that boron is the main element contributing to microfissuring by the decomposition of borides and changes in the liquid wetting characteristics of grain boundaries [212], though borides have not been generally observed in Alloy 718. Using hot stage SEM, Kelly [51] recently observed the liquation of grain boundaries in cast Alloy 718 containing >0.005wt% B at temperatures above 1090°C, while a low boron (0.0005wt%) alloy did not liquate at the same temperature. He also observed that grain boundary constitutional liquation by the γ/Laves phase eutectic did not occur in alloys having low boron concentration. Rather, the liquid formed during the transformation of the eutectic constituent would remain localized in interdendritic pockets. These observations suggest that the role of boron may be as a surface energy depressant for interdendritic and inter-granular eutectic-type liquids. However, the temperature dependence of boron segregation was not provided.

The existing theories of HAZ microfissuring, viz grain boundary film formation during heat treatment, sulphur segregation to grain boundaries and boride decomposition, can not explain the variation in total crack length with the heat treatment temperature shown in Fig.4.27b and 4.30a. The hardness values obtained in the study (Fig.4.16) and the amount of secondary phases (such as Laves phase, δ phase and MC carbide in Fig.4.13, 4.14 and 4.15) do not vary with the homogenization temperature in the same fashion as does the TCL in Fig.5.9. A reasonable interpretation can be provided by analyzing the

effect of heat treatment temperature on boron segregation, as determined by SIMS studies, considering the combination of equilibrium and non-equilibrium segregation concepts. When Fig.4.38, Fig.4.27b and Fig.4.30a are compared, the variation in the amount of boron segregation with temperature is observed to have the same trend as the variation in TCL. This suggests that boron segregation to grain boundaries could contribute to the tendency for microfissuring. Further analysis by SIMS carried out on welded specimens revealed strong segregation of boron on HAZ microfissures (Fig.4.40). It can be concluded from the above evidence that boron plays a significant role in HAZ microfissuring in cast Alloy 718.

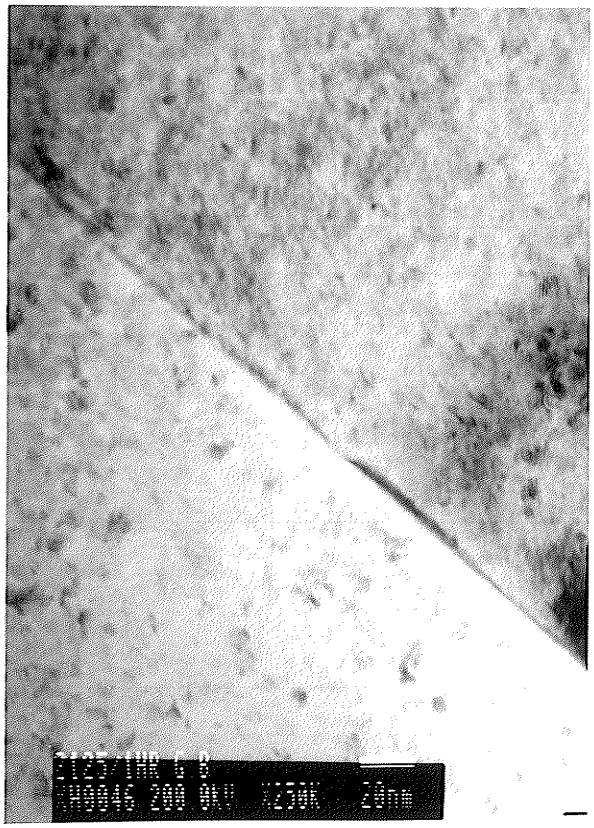

Fig.5.8 TEM micrograph revealing a 'clean' grain boundary on specimen after heat treated at 1163°C/1hr.

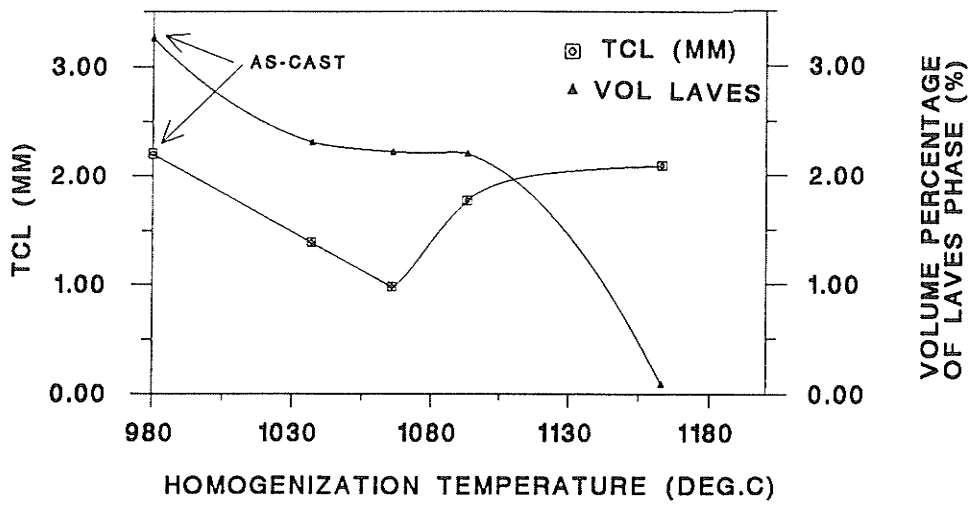

Fig.5.9 Relationship between the amount of secondary phases and TCL after homogenizing at 1037°C, 1067°C, 1093°C and 1163°C for 1 hr.

From segregation theory, rapid cooling can be shown to prevent non-equilibrium segregation of boron. To confirm this, four specimens were heat treated at temperatures in the 950 to 1240°C range and water quenched. Unexpectedly, the TCL as shown in Fig.4.30b, did not show a decrease with an increase in homogenization temperature. Instead, TCL remained nearly constant. The reason for this behaviour may be attributed to the effect of additional stresses caused by the water quench. When the homogenization temperature is increased, boron segregation is decreased which would tend to reduce the

TCL. However, there would be an increase in stress in HAZ due to quenching stress as described by $\Delta\sigma \propto C\Delta T$. Therefore, there would be an increased tendency for the HAZ microfissures to form as the combination of both quenching stresses and the thermal stresses produced during the welding cycle is increased. The influence of these two factors, reduced boron segregation and increased residual stress, may be such that they counteract each other resulting in TCL remaining nearly constant as the homogenization temperature is increased (Fig.4.30b).

The question arises as to how the boron segregation affects the HAZ microfissuring. The mechanisms by which boron and tramp elements affect HAZ microfissuring can be speculated as follows. Although the segregation of phosphorous, sulphur and other elements was not observed in this study, their existence can not be ruled out. Therefore, the following discussion will also include the possible effects of S and P.

a) During the weld heating cycle smaller particles of secondary phases such as carbides or Laves phase present on the grain boundaries totally liquate, whereas larger particles (1-2 μm) only partly liquate.

b) Due to the presence of boron and possibly sulphur and phosphorous, the wettability of the liquid formed on the grain boundaries will be increased [51,213].

c) Due to the presence of boron (and possibly S and P) in the vicinity of grain boundaries, solute segregation will occur during solidification due to the low partition coefficient k which will extend the freezing range of the liquid in

accordance with the following expression [48]:

$$\Delta T = M_L C_o \left(\frac{1-k}{k}\right) \qquad <69>$$

where C_o is solute concentration, M_L is the slope of liquidus and k is the partition coefficient (k=0.0073 for boron, 0.00028 for S and 0.145 for P [30]).

Based on the above arguments, two mechanisms for microfissuring are then possible.

Mechanism I

If HAZ microfissuring occurs when the grain boundary liquid has not solidified, then the grain boundary can be thought of as a liquid filled crack [71]. In this case, the crack growth under thermal stresses may follow the following Griffith type equation [214]:

$$\sigma = \left(\frac{8\mu\gamma}{\pi(1-\nu)c}\right)^{\frac{1}{2}} \qquad <70>$$

where σ is the crack propagation stress, μ is the shear modulus, γ is the effective fracture surface energy and $\gamma = 2\gamma_{SL} - \gamma_{GB}$, γ_{GB} is the grain boundary energy, γ_{SL} is solid/liquid interfacial energy, ν is the Poisson's ratio and c the crack length.

Mortimer [215] has suggested that for a Ni alloy, as the boron concentration increases both γ_{GB} and γ_{SV} are reduced. Table 5.4 shows his data. Due to a lack of information on γ_{SL} in Ni alloys containing boron, the γ_{SV} values have been used to illustrate the effect of boron on γ since $\gamma_{SL} = \gamma_{SV} - \gamma_{LV}$. As can also be seen in Table 5.4, a reduction in γ of 980mJ/m^2 is found at 1000°C and 440mJ/m^2 at 900°C due to a change in boron

concentration from 0 to 100ppm. Consequently, via the Griffith equation, the propagation stress will be lowered by an increase in boron concentration.

Mechanism II

If the liquid solidifies before the thermal stresses build up, then it should be possible to initiate a crack at the second phase particles (Laves phase/carbide) on the grain boundaries. The stress required to initiate a crack is then given by [216]

$$\sigma_E=\left(\frac{2G\gamma}{\pi(1-\nu)d}\right)^{1/2}\left(\frac{2c}{d}\right)^{1/2} \qquad <71>$$

where σ_E is local shear stress, 2c is particle thickness, d is slip band length, $\gamma=2\gamma_{SV}$ - γ_{GB}, G is the shear modulus and ν is Poisson's ratio.

γ can again be interpreted as has been done in the development of Mechanism I above assuming a similar segregation level of boron, especially on the surface of the crack [217]. According to this equation, when the shear component of the thermal stress exceeds σ_E, a crack will initiate at the interface. The stress, σ_E, is lowered with increasing boron (S and P) segregation, since $\sigma_E \propto \gamma^{1/2} \propto 1/B^n$ (n is a constant).

There is ample evidence in the literature that both the grain boundary [218] and solid free surface energies [219] of solid metals are lowered by solute segregation (Fig.5.10). If these two factors decrease proportionally with an increase in solute segregation, one would expect γ to follow a similar trend.

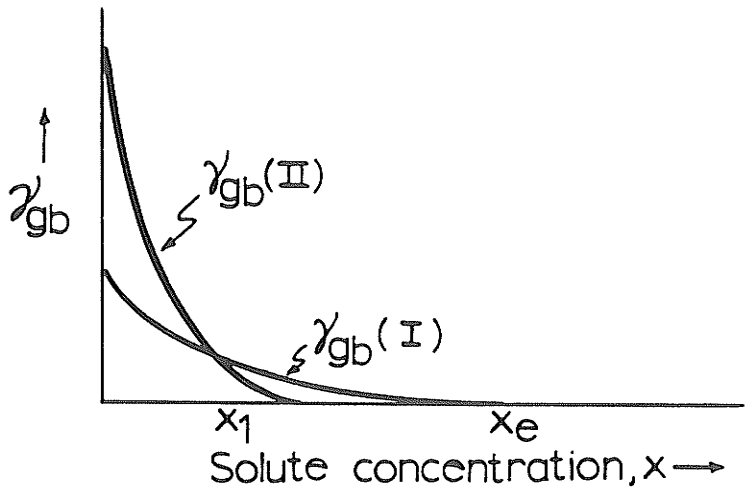

Fig.5.10 The dependence of grain boundary free energy on composition for two distinct grain boundary structures [218].

Whatever mechanism controls microfissuring, slip must not occur prior to crack initiation or crack growth, otherwise the stress concentration will be relieved. The microstructural analysis of the metallurgical evidence from the present study (Fig.4.26) show that the HAZ cracks were always associated with secondary phases at the interfaces.

In the present study, the intensity of grain boundary segregation of boron in specimen heat treated at 950°C is observed to be higher than the one treated at 1067°C. Therefore, γ is expected to be lower in a 950°C specimen as compared to a 1067°C specimen. Similarly, the value of γ is expected to be lower in a material treated at 1250°C than the one treated at 1067°C because boron segregation has a higher value. Therefore, with the

γ values being lower in specimens treated at 950°C and 1250°C than that treated at 1067°C, the value of σ_E (and σ) would also be lower in these specimens. Consequently, the TCL values should be expected to exhibit a similar behaviour as σ_E (and σ). That is to say, σ_E (or σ) $\propto \gamma^{1/2} \propto 1/B^n \propto 1/TCL^m$ (m is a constant). The increase in boron content (and possibly other solutes such as sulphur and phosphorus) at grain boundaries will also increase the value of TCL by increasing the solidification range and wetting of grain boundaries. Water quenching from the homogenization temperature as compared to air cooling would simply result in differing amounts of boron (S and P) being present on the grain boundaries and would influence the TCL values accordingly.

Table 5.4 Reduction in Grain Boundary and Surface Energy (mJ/m^2) with Increasing Boron Concentration

	Temp (°C)	Changing in Boron Conc.(ppm)	Reduction in γ_{GB}	Reduction in γ_{SV}	Reduction in $\gamma = 2\gamma_{SV} - \gamma_{GB}$
Ni Alloy	900	0→100	360	400	440
	1000	0→100	420	700	980

5.3.3 Effect of Homogenization Temperature on TCL after Homogenization and Solution Treatment

It was discussed in the previous section that TCL increases initially and then decreases as the homogenization temperature is increased (Fig.4.27b and 4.30). The same trend was

was observed in the homogenized and solution treated samples (Fig.4.27c) but in a less distinct manner. The quantitative analysis (Fig.4.14) of secondary phases showed that the increase in homogenization temperature led to a reduction in the volume fraction of both inter and intra-granular δ-Ni_3Nb. If the presence of precipitates of δ-Ni_3Nb on grain boundaries is contributing to the decrease in TCL, an increase in TCL with homogenization temperature should be expected since high temperature reduces the volume fraction of δ-Ni_3Nb. Also, as the homogenization temperature is increased, more solutes such P, S, C and B are available in the matrix for segregation during solution treatment. This again causes an increase in TCL with an increase in homogenization temperature. However, neither of the above factors can be used to explain the occurrence of a TCL dip at 1067°C. As no extensive investigation was carried out regarding elemental segregation and grain boundary microstructural changes, a conclusive explanation can not be given at the present time.

5.3.4 Effect of Homogenization Temperature on TCL After Homogenization and Ageing Treatment

An increase in TCL with homogenization temperature was also observed in specimens that were subsequently aged as shown in Fig.4.27a. This could be due to the availability of more solutes in the matrix after homogenization treatment as discussed in the previous section. As homogenization temperature increases, more solutes such as S, P, C and B are released from precipitates, interfaces and interdendritic areas. Since the equilibrium segregation concentration is proportional to the solute concentration in the matrix i.e.

$C_b \propto C_m$ (Eq. <67>), a higher grain boundary segregation concentration would occur with an increase in homogenization temperature (during the last stages of ageing at 650°C the extent of non-equilibrium segregation would be negligible). As discussed in Section 5.3.2, an increase in grain boundary segregation will assist the formation of HAZ microfissuring and cause a higher value of TCL.

5.3.5 Effect of Homogenization Temperature on TCL After Homogenization, Solution and Ageing Treatment

Various factors such as δ-Ni_3Nb precipitation and release of solute atoms as discussed in 5.3.3 and 5.3.4 could affect the TCL variation after homogenization, solution and ageing heat treatment shown in Fig.4.28. As the homogenization temperature is increased, the grain boundary elemental segregation will increase and less δ-Ni_3Nb will precipitate. Both these factors could cause the observed increase in TCL with increasing homogenization temperature. Further study needs to be carried out to confirm or exclude these possibilities and find other contributing factors that influence the microfissuring.

5.3.6 Effect of Heat Treatment Type

As shown in Fig.4.29, the type of heat treatment given affects TCL in the following way: homogenization heat treatment at 1163°C increases TCL as compared to the as-cast condition; solution heat treatment decreases TCL; ageing increases TCL and overageing reduces TCL as compared to the aged condition. As all the specimens had been

homogenized at 1163°C prior to subsequent solution and ageing, the difference in TCL was caused only by the type of heat treatment used.

Effect of Homogenization on TCL:

Homogenization at 1163°C resulted in the dissolution of δ-Ni_3Nb and Laves phase which made more Nb and other elements available for constitutional liquation during the weld heating cycle. The release of trace elements such as S, P, C and B from secondary phases, interfaces and interdendritic areas during homogenization treatment may cause increased segregation (both equilibrium and non-equilibrium). These two factors can be used to explain the increased TCL after homogenization at 1163°C as compared to the as-cast condition.

Effect of Solution Heat Treatment on TCL:

The effect of solution treatment on TCL has been reported by several investigators in wrought Alloy 718 [62,65], all showing the same trend as observed in this study; i.e. solution heat treatment improves the material's weldability. However, there is no certain explanation for this phenomenon. It was found in this study and in another investigation [220] that the presence of needle shaped δ-Ni_3Nb at the grain boundaries produced a serrated grain boundary structure (Fig.4.9) and this could help resist the propagation of HAZ cracks. Also, the precipitation of δ-Ni_3Nb may alter the grain boundary free energy and amount of segregation thus changing the grain boundary liquation temperature, solidus of the liquid and the wettability of grain boundary liquid. In addition, solution

treatment at 900 to 950°C has been considered to be an efficient way in reducing HAZ cracking by appreciably reducing the amount of 'diffusible Nb' and by restricting the intergranular liquation zone to a narrow strip at the edge of the weld pool [221]. In this way, precipitation of δ exerts a solute blocking effect and stabilizes the solutes responsible for liquation in the form of a stable intermetallic phase at high temperature. However, there is no direct evidence available either from this study or in the literature. With the techniques used in the present study, an unambiguous mechanism could not be established.

Effect of Ageing on Material's Weldability:

Higher values of TCL were obtained after ageing as shown in Fig.4.29. Ageing after both homogenization and solution treatment enhances the material's hardness by precipitating $\gamma'' + \gamma'$. As the hardness of the base material increases (Fig.4.16 and 4.17), the constraint of the weldment will increase accordingly which in turn will affect the residual stresses from the welding cycle. Besides the increase in hardness, more elemental segregation occurs at low temperatures since equilibrium segregation increases with a decrease in heat treatment temperature (Eq.<67>). An increased elemental segregation of S was observed in cast Alloy 718 after ageing by Thompson [54].

Effect of Overageing:

The overageing at 760°C for 200 hours lowered the TCL relative to that observed after ageing (760°C/5hrs + 650°C/1hr) as seen in Fig.4.29. The hardness evaluation

(Fig.4.17) did not show any changes in hardness value after overageing as compared to as-aged condition. Overageing at 760°C could result in less equilibrium segregation than at 650°C (last stage of standard ageing treatment), therefore, lower TCL should be expected.

CHAPTER FIVE

CONCLUSIONS

5.1 The microstructure of as-cast Alloy 718 studied in this investigation consisted of γ-matrix, (Nb,Mo,Ti)(C,N) carbonitrides (1.6%), δ-Ni_3Nb phase (7.9%), and eutectic $(Fe,Cr,Ni,Si)_2(Nb,Mo,Ti)$ Laves phase (3.3%).

5.2 The volume fraction of both δ-Ni_3Nb and Laves phases was found to decrease with increasing homogenization temperature while the amount of M(C,N) carbonitride did not change when the specimens were heat treated up to 1163°C. Solution treatment after homogenization enhanced the precipitation of δ-Ni_3Nb. Ageing treatment did not change the amount of Laves phase and M(C,N) while the amount of δ-Ni_3Nb was observed to decrease.

5.3 The hardness after homogenization and solution treatments was similar to that observed in the as-cast condition. Ageing increased the hardness due to the precipitation of $\gamma''+\gamma'$.

5.4 Segregation of boron to the grain boundaries of cast Alloy 718 has been observed for the first time in this study. Initial SIMS analysis showed strong segregation of boron to grain boundaries in specimens heat treated at 1163°C/1hr(A.C.) compared to those heat treated at 1037°C followed by air cooling and those heat treated at 1163°C followed by water quenching. Extensive investigations revealed the existence of two types of segregation; equilibrium and non-equilibrium segregation which occurred during heat treatments. Cooling from the heat treatment temperature at a rate of 400°C/sec. by water quenching prevented non-

equilibrium segregation of B from taking place due to insufficient time being available for diffusion of boron-vacancy complexes to occur. An intermediate cooling rate of 20°C/sec. produced by air cooling enhanced non-equilibrium segregation during cooling. As the equilibrium segregation occurred during holding at the heat treatment temperature, a combination of equilibrium and non-equilibrium segregation was observed after air cooling. The value of combined segregation of boron was observed to first decrease and then increase with the heat treatment temperature with a minimum in segregation observed in the specimen that was heat treated at 1067°C.

5.5 The precipitate particles in the fusion zone have been identified as M(C,N) type carbonitrides, $M_{23}C_6$ carbides and Laves phase. Both resolidified Laves phase and M(C,N) carbonitrides were observed in the HAZ.

5.6 On increasing the homogenization temperature from 1037 to 1163°C, TCL in HAZ decreased initially (from 1037 to 1066°C) and then increased. The variation in TCL with homogenization temperature after homogenization and solution treatment showed a similar trend. The TCL after homogenization + ageing, and homogenization + solution + ageing increased with homogenization temperature with the occurrence of a TCL dip at a temperature of about 1066°C.

5.7 The weldability of this alloy after homogenization treatment was found to be closely related to the segregation of boron to the grain boundaries. That is, the variation in HAZ TCL with pre-welding homogenization heat treatment temperature has the same trend as that of boron segregation in specimens that

were air cooled after the homogenization treatment. Strong segregation of boron was observed at HAZ microfissures.

5.8 The effect of boron segregation on the weldability can be explained by:

a) the presence of boron at grain boundaries increases the wettability of the liquid produced during welding.

b) boron lowers the solidus of the liquid that forms during welding which causes the grain boundaries to have zero-ductility when thermal stresses are increased.

5.9 A model of crack initiation and propagation based on the dependence of cracking tendency on interfacial energy influenced by the concentration of boron segregation has been suggested to account for the observed variation in TCL.

5.10 It can be concluded from this study that in order to decrease the amount of boron segregation, the following approaches can be employed if welding has to be carried out in the homogenization treated condition:

a) heat treat at higher temperatures followed by slow cooling to allow non-equilibrium desegregation to occur;

b) heat treat at transition temperature (-1067°C) followed by air cooling.

5.11 If welding is to be carried out in the solution treated condition, a pre-homogenization heat treatment at 1066°C would be beneficial. If welding is to be carried out in the aged condition, a low homogenization temperature and an intermediate solution treatment can be used to minimize the HAZ microfissuring.

REFERENCES

[1] H.L. Eiselstein, ASTM, STP369, p.68-79 (1965).

[2] E.A. Loria, J. of Metals, July, p.36 (1988).

[3] J.F. Radavich, J. of Metals, July, p.35 (1988).

[4] J.F. Barker, D.D. Krveger and D.R, Chang, Advanced High Temperature Alloys, Proc. N.J. Grant Symposium, S.M. Allen, ed., ASM, p.125 (1986).

[5] J.F. Radavich, J. of Metals, July, p.42 (1988).

[6] J.M. Oblak, D.F. Paulonis and D.S. Duvall, Met. Trans., 5A, Jan., p.143 (1974).

[7] Y. C. Fayman, Mat. Sci. and Eng., 92, p.159 (1987).

[8] F. Laves and H. Witte, Metallwirtschaft 17, p.840 (1936).

[9] M.G. Burke and M.K. Miller, CONF-910614-3. DE. 1991, 009918.

[10] W. Hume-Rothery and G.V. Raynor, The Structure of Metals and Alloys, The Institute of Metals, London, p.198 (1962).

[11] D.F. Paulonis, J.M. Oblak and D.S. Duvall, Trans. of the ASM, V.62, p.611 (1969).

[12] M. J. Donachie, Jr., in Superalloy Source Book, ed. M.J. Donachie, Jr. ASM, p.102 (1984).

[13] J.W. Brooks and P.J. Bridges, in Superalloys 1988, p.33 (1988).

[14] E. W. Ross and C. T.Sims, Superalloy II - High Temperature Materials for Aerospace and Industrial Power, ed. C.T. Sims, N.S. Stoloff and W.C. Hagel, p.97 (1987).

[15] M. Sundararaman, P. Mukhopadhyay and S. Banerjee, Met. Trans., 19A, March, p.453 (1988).

[16] R. Thamburaj. Proc. Int. Conf. on Creep, Tokyo, Japan, JSME/ASME, p.275 (1986).

[17] A.K. Koul and R. Thamburaj, Met. Trans., 16A, p.17 (1985).

[18] A.K. Koul, P. Au, N. Bellinget, R. Thamburaj, W. Wallace and J-P. Immarigeon, in Superalloy-1988, Proceedings of the Sixth International Symposium on Superalloys, p.3 (1988).

[19] J.F. Radavich and W.H. Couts, Jr., Superalloy 1984, ed. M.Gell, p.497 (1984).

[20] R. Vincent, Acta Metall., Vol.33, No.7, p.1205 (1985).

[21] D. R. Muzyka and G.N. Maniar, Metals Engineering Quarterly, ASM, Nov., p.23 (1969).

[22] A.K. Jena and M.C. Chaturvedi, J. of Mat. Sci., 19, p.3121 (1984).

[23] M.C. Chaturvedi and D. W. Chung, Metall. Trans., 12A, p.77 (1981).

[24] M.C. Chaturvedi, D.J. Lloyd and D. W. Chung, Met. Sci, 10, p.373 (1976).

[25] C.T. Sims, N.S. Stoloff and W.C. Hagel, Superalloys II, p.61 (1987).

[26] J.P. Collier, S.H. Wong and J.K.Tien, Met. Trans., 19A, July, p.1657 (1988).

[27] J.P. Stroup and L.A. Pugliese, Metal Progress, 99(2), p.96 (1968).

[28] J.M. Moyer, Superalloys 1984, ed. M. Gell, C.S. Kortovich, R. H. Bricknell, W.B. Kent and J.F. Radavich, p.443 (1984).

[29] Welding Hand Book - Welding, Cutting and Related Process, Chapter 47 (1970).

[30] K. Easterling, in Introduction of the Physical Metallurgy of Welding,

Butterworths (1985).

[31] W.F. Savage, Solidification, Segregation and Weld Imperfection, Welding in the World, 18, p.89(1980).

[32] R. Thamburaj, W. Wallace and J.A. Goldak, International Metals Reviews, Vol.28, No.1 (1983).

[33] B.F. Dyson and D.M.R. Taplin, Creep Damage Accumulation, Grain Boundaries (Conference Proceedings), ed. D.V. Edmonds, Institute for Metallurgists, Series 3(5), p.23 (1976).

[34] B.E. Payne, in The Nimonic Alloys, ed. W. Betteridg and J. Heslop, p.379 (1974).

[35] W. Yeniscavich, in Superalloy I, ed. C.T. Sims, N.S. Stoloff and W.C. Hagel (1987).

[36] J.J. Vagi, R.P. Meister and M.D. Randall, Weldment Evaluation Methods, DMIC Report, p.244 (1968).

[37] W.F. Savage and C.D. Lundin, Weld. Journal, 44, p.433s (1965).

[38] E.F. Nippes and W.F. Savage, Weld Journal, 28, p.534s (1949).

[39] D.S. Duval and W.A. Owczarsky, Welding Journal, 46, p.423s (1967).

[40] W.A. Baeslack III, S.L. West and T.J. Kelly, Scripta Met., Vol.22, No.5, p.729 (1988).

[41] W.A. Baeslack III and D. Nelson, Metallography, 19, p.371 (1986).

[42] G.A. Knorovsky, M.J. Cieslak, T.J. Headly, A.D. Romig, Jr., and W.F. Hammetter, Met. Trans., 20A, P.2149 (1989).

[43] J.C. Borland, British Welding Journal, Aug., p.508 (1960).

[44] W. F. Savage, E.F. Nippes and T.W. Miller, Welding Journal, Vol.53, Research Supplement, p.181s (1974).

[45] D.S. Duvall and W.A. Owczarski, Welding Journal, research Supplement, 46(9), p.435 (1967).

[46] J.J. Pepe and W.F. Savage, Welding Journal, 1967, Vol.46., Research Supplement, p.411 (1967).

[47] H.D. Soloman, in Treatise on Material Science and Technology, Vol.25, p.525 (1986).

[48] J.C. Borland, British Welding Journal, Nov., p.526 (1961).

[49] R.E. Pease, Welding Journal, 7, p.330s (1957).

[50] M.J. Cieslak, Welding Journal, Feb., p.49s (1991).

[51] T. Kelly, Welding Journal, Feb.,70, p.44s (1989).

[52] M.J. Lucas, Jr. and C.E. Jackson, Welding Journal, 49(2), p.46s (1970).

[53] R.G. Thompson, B. Radhakrishnan, and D.E. Mayo, J. De. Physique, C5, Supplement No.10, Tome 49, Oct., c5-471 (1988).

[54] R.G. Thompson, D.E. Mayo and B. Radhakrishnan, Met. Trans. A, Vol.22A, Feb., p.557 (1991).

[55] T.J. Morrison, C.S. Shira and L.A. Weisenbery, "Effects of Minor Elements on the Weldability of High Nickel Alloys" Proceedings of the Weld Research, N.Y. Welding Research Council, 93 (1967).

[56] R.G. Thompson, J.R. Dobbs and D.E. Mayo, Welding Journal, 65(11), 299

(1986).

[57] D.A. Canonico, Proceedings of the Weld Research, N.Y. Welding Research Council, 93, p.68 (1967).

[58] R.G. Thompson and S. Genculu, Welding Journal, 62(12) p.337 (1983).

[59] E.G. Thompson, Welding Journal, 48(2), p.70 (1969).

[60] D.S. Duvall and W.A. Owczarski, Welding Journal, 46(9), p.423 (1967).

[61] E.R. Vincent, The Microstructure of Welds in Inco 718, Dept. of Physics, University of Bristol, U.K. (1980).

[62] R.G. Thompson, Welding Journal, 66(4), p.91 (1985).

[63] B. Radhakrishnan and R.G. Thompson, Metallography, 21:453-471, p.453 (1988).

[64] R.G. Thompson, M. Koopman and B. King, Proc. Int. Symp. on the Metallurgy and Application of Superalloy 718 and 625, TMS, Pittsburgh, PA, p.53 (1991).

[65] P.J. Valdez and J.B. Steinmen, Effect of Minor Elements on the Weldability of High Nickel Alloys, NY, Welding Research Council, p.39 (1969).

[66] T.J. Kelly, Welding Journal, Nov., p.422s (1990).

[67] R.A. Mulford, Met. Trans, 14A, p.865 (1983).

[68] B. Radhakrishnan and R.G. Thompson, Met. Trans., 24A, June, p.1409 (1993).

[69] T.J. Morrison, C.S. Shira and L.A. Weisenber, The Influence of Minor Elements on Alloy 718 Weld Microfissuring. Effects of Minor Elements on the Weldability of High Nickel Alloys, New York: Welding Research Council, p.47 (1967).

[70] R.G. Thompson, J.J.Cassimus, D.E. Mayo and J.R. Dobbs, Welding Journal,

64(4), p.91 (1985).

[71] J.A. Williams, A.R.E. Singer, The Journal of the Institute of Metals, 96, p.5 (1968).

[72] J.A. Williams, A.R.E. Singer, The Journal of the Australian Institute of Metals, 11(1), p.2 (1966).

[73] B. Radhakrishnan and R.G. Thompson, Scripta Metallurgical, Vol.24, p.537 (1990).

[74] N.L. Richards, X. Huang and M.C. Chaturvedi, Material Characterization, Vol.28, p.179 (1992).

[75] N.L. Richards, R.Nakkalil and M.C. Chaturvedi, Metallurgical and Materials Transactions A, Vol.25A, Aug., p.1 (1994).

[76] C. Boucher, D. Valera, M.Dadian and H. Granjon, Hot Cracking and Recent Progress in the Weldability of Nickel Alloys Inconel 718 and Waspalloy, paper presented at the 15th Conference on Special Steels, Saint Etienne, 13-14, May, Translation by the Welding Institute, Cambridge, England (1976).

[77] R. Vincent, Acta Met., Vol.33, No.7, p.1205 (1985).

[78] R.G. Thompson, D.E. Mayo and B. Radhakrishnan, Welding Journal, Vol.22, p.557 (1990).

[79] E.R. Vincent, The Microstructure of Welds in Inco 718, Dept. of Physics, University of Bristol (1980).

[80] W.F. Savage and D.W. Dickinson, Welding Journal, Nov., p.555s (1972).

[81] J.A. Brooks, A.W. Thompson and J.C. Williams, in Physical Metallurgy of

Metal Joining, ed. R.Kossowsky, TMS-AIME, PA, p.117 (1980).

[82] J. H. Brooks and F.J. Lambert, Jr., Welding Journal, May, p.139 (1978).

[83] R.D.Thomas, Jr., Welding Journal, Dec. p.355s (1984).

[84] M.W.Richey, M.W. Doughty and C.L. White, in Prof. Conf. on Trends in Welding Research, ed. S.A.David, ASM (1986).

[85] V.P. Kujanppa, S.A. David and C.L. White, Welding Journal, Aug., p.203 (1986).

[86] E.D. Hondros and M.P. Seah, International Metals Reviews, Dec., p.262 (1977).

[87] A.H. Cottrell, "Report of a Conference on the Strength of Solids", 30, London, Physical Society, 1948.

[88] D. Mclean, "Grain Boundaries in Metals", Oxford, Clarendon Press (1957).

[89] M.P. Seah and E.D. Hondros: Proc. R. Soc., 335A, p.191 (1973).

[90] R.G. Faulkner, Acta Metall., Vol.35, No.12, p.2905 (1987).

[91] E.D. Hondros and M.P. Seah, "Physical Metallurgy", ed. R.W. Cahn & P. Hassen, North Holland (1992).

[92] W.R. Tyson, Acta Metall., 26, p.1471 (1978).

[93] M. Guttmann, Metall Trans., 5A, p.167 (1974).

[94] F.L. Carr, Trans. AIME, 197, p.998 (1953).

[95] M.P. Seah: Acta Metall., 25, p.345 (1977).

[96] P. Wynblatt and R.C. Ku, Proc. ASM Materials Science Interfacial Segregation, eds. W.C. Johnson and J.M. Blakely, ASM Metals Park, OH, p.115 (1979).

[97] M.P. Seah and E.D. Hondros, Proc. Roy. Soc., A335, p.191 (1973).

[98] J.H. Westbrook and D.L.Wood, Nature, 192, p.1280 (1961).

[99] J.H. Westbrook, Met. Rev. 9, Issue 36, p.415 (1964).

[100] J.H. Westbrook and K.T. Aust, Acta Met. Vol.11, Oct., p.1151 (1963).

[101] K.T. Aust, R.E. Hanneman, P. Niessen and J.H. Westbrook, Acta Met., Vol.16, March, p.291 (1968).

[102] R.L. Eadie and K.T. Aust, Scripta Met., Vol.4, p.641 (1970).

[103] R.E.Hanneman and T.R. Anthony, Acta Met., Vol.17, Sept, p.1133 (1969).

[104] T.R. Anthony and R.E. Hanneman, Scripta Met., 2, p.611 (1968).

[105] T.R. Anthony, Acta Met., 17, p.603 (1969).

[106] R.E. Howard and A.B. Lidiard, Phil. Mag., 12, p.1176 (1965).

[107] P. Doig and P.E. Flewitt, Acta Metall., Vol.29, p.1831 (1981).

[108] A.C. Damask and G.J. Dienes, Acta Metall., Vol.12, July, p.797 (1964).

[109] T.M. Williams, A.M. Stoneham and D.R. Harries, Metal Sci., Jan. p.14 (1976).

[110] A.C. Damask and G.H. Dienes, in Point Defects in Metals, N.Y. Gorden and Breach (1963).

[111] A. H Cottrell, An Introduction to Metallurgy, Edward Arnold, London, p.345 (1967).

[112] M.A.V. Chapman and R.G. Faulkner, Acta Metall., Vol.31, No.5, p.677 (1983).

[113] R.G. Faulkner, Material Science and Technology, June, Vol.1, p.442 (1985).

[114] R.G. Faulkner, Journal of Materials Science, 16, p.373 (1981).

[115] L. Karlsson, Acta Metall., Vol.36, No.1, p.25 (1988).

[116] T. Xu, S. Song, H. Shi, W. Gust and Z. Yuan, Acta Metall., Vol.39, No.12,

p.3119 (1991).

[117] X.L. He, Y.Y. Chu and J.J Jonas, Acta Metall., Vol.37. No.11, p.2905 (1989).

[118] T. Xu and S. Song, Acta Metall,, Vol.37, p.2499 (1989).

[119] X.L. He, Y.Y. Chu and J.J.Jonas, Acta Metall,, Vol.37, No.1, p.147 (1989).

[120] T. Xu, S. Song, Z. Yuan and Z. Yu, Journal of Materials Science, 25, p.1739 (1990).

[121] Y.Y.Chu, X.L. He, L.Tang, T. Xu and T. Ko, Proc. Int. Symp. on Grain Boundary Structure and Related Phenomena, Minakami Spa, Japan, p.25 (1985).

[122] T. Xu, J. Materials Science Letter, 7, p.241 (1988).

[123] L. Karlsson, H.Norden and H. Odelius, Acta Metall., Vol.36, No.1, p.1 (1988).

[124] C.L. Briant, Acta Metall., 31, p.257 (1983).

[125] R.W. Balluffi, Interfacial Segregation, ed. W.C. Johnson and J.M. Blakely, Am.Soc. Metals, Metals Park, Ohio (1979).

[126] R.W. Balluffi, Metall. Trans., 13A, p.2069 (1982).

[127] R.W. Balluffi, Grain Boundary Structure and Kinetics, Am. Soc. Metals, Metals Park, Ohio (1980).

[128] L. Karlsson and H. Norden, Acta Metall, Vol.36, No.1, p.13 (1988).

[129] L. Karlsson and H. Norden, Transaction of the Japan Institute of Metal, Supplement, Vo.27, p.189 (1986).

[130] L. Karlsson and H. Norden, J. De Physique, C9-N°12, Tome-45, Dec., p.391 (1984).

[131] L. Karlsson, H.-O Andren and H. Norden, Scripta Metall., Vol.16, p.297

(1982).

[132] C.P. Sullivan and M.J. Donachie, Jr., Metals Eng. Quarterly, Feb., p.36 (1967).

[133] K.J. Irvine, J. Iron Steel Inst., 186, p.54 (1957).

[134] R.A. Grange and J.B. Mitchell, Trans. ASM, 53, p.157 (1961).

[135] M.A. Burke, J. Greggi, Jr. and G.A. Whitlow, Scripta Met., Vol.18, p.91 (1984).

[136] R.F. Decker, Source Book on Materials for Elevated Temperature Application, ed. E.F. Bradley, ASM Metals Park, OH., p.279 (1979).

[137] P. Maitrepierre, J. Rofes-Vernis, and D. Thivellier, in Boron in Steel, Proceedings of the International Symposium on Boron Steel, Milwaukee, Wisconsin, Sept., p.1 (1979).

[138] H.J Goldschmidt, in Effect of Boron Additions to Austenitic Stainless Steels, J.I.S.I., 209, p.900 (1971).

[139] B.J. Thomas and G. Henry, in Boron in Steel, ed. S.K. Banerji and J.E. Morral, p.80 (1979).

[140] R.P. Elliott, Constitution of Binary Alloy, First Supplement, McGraw-Hill Book Co., NY (1965).

[141] M.E. Nicholson, Trans. Met. Soc. AIME, 200, p.185 (1954).

[142] C.C. McBride, J.W. Spretnak and R. Speiser, Trans. Amer. Soc. Metals, 46, p.499 (1954).

[143] M. Hassen, in Constitution of Binary Alloy, McGraw-Hill Book Company (1958).

[144] C.J. Smithells, Metals Reference Book, 5th ed., Butterworths, London, p.98 (1976).

[145] A.K. Shevelov, Sov. Phys. Doklady, 9, p.1254 (1958).

[146] R.M. Goldhoff and J.W. Spretnak, Trans AIME, 209, p.1278 (1957).

[147] W.R. Thomas and G.M. Leak, Nature, 176, p.29 (1955).

[148] Y. Hayashi and T. Sugeno, Acta Met., 18, p.693 (1970).

[149] P.E. Busby and C. Wells, Trans. AIME, 200, p.972 (1954).

[150] P.E. Busby, M. Warga and C. Wells, Trans. AIME, 197, p.1463 (1953).

[151] R.C. Ruhl and M. Cohen, Trans. of The Metallurgical Society of AIME, Vol.245, Feb., p.253 (1969).

[152] C.E. Birchenall, Atom Movements, ASM, Cleveland, p.116 (1951).

[153] A. Brown, J.D. Garnish and R. W. K. Honeycombe, Metal Science, Vol.8, p.317 (1974).

[154] H.J. Goldschmidt, Interstitial Alloys, Butterworths, London (1967).

[155] Y. Lin and J. Zhang, Acta Met. Sinica, Vol.23, No.4, p.346 (1987).

[156] D.A. Mortimer, Grain Boundary in Engineering Materials, Proceedings of 4th Bolton Landing Conference, ed. J.L. Walter, J.H. Westbrook and D.A. Woodford, June, (1974).

[157] T.J. Garosshen, T.D. Tillman and G.P. McCarthy, Met. Trans., 18A, Jan, p.69 (1987).

[158] C.P. Bean, R.L. Fleischer, P.W. Wartz and H.R. Hart, J. Appl. Phys., 37, p.2218 (1966).

[159] W.F. Jandeska Jr. and J.E. Morral, Metal. Trans., 3A, Nov., p.2933 (1972).

[160] J.D.H. Hughes Jr. and J.E. Rogers, J. Inst. Metals, 95, p.299 (1967).

[161] M. Ueno and T. Inoue, Transaction ISIJ, Vol.13, p.210 (1973).

[162] Ph. Maitrepierre, D. Thivellier and R. Tricot, Met. Trans., Vol.6, p.287 (1975).

[163] A. Chatterjee, J.P. Hirth, R.G. Hoagland, A. Choudhury and C.L. White, Scripta Met., Vol.21, p.79 (1987).

[164] T. M. Williams, A.M. Stoneham and D.R. Harries, Metal Science, Jan., 14 (1976).

[165] S. Hashimoto, S. Dor, K. Takahashi, M. Terasaka and M. Iwaki, Mat. Sci. and Eng., 90, p.119 (1987).

[166] D.A. Mortimer and M.G. Nicholas, Metal Science, Sept., p.326 (1976).

[167] A.M. Adair, J.W. Spretnak and R. Speiser, J. of Metals, Trans. AIME, Feb., p.353 (1955).

[168] J.H. Westbrook and S. Floreen, Canadian Met. Quart., Vol.13, No.1, p.181 (1974).

[169] A. W. Thompson, Grain Boundaries in Engineering Materials, Proceedings of 4th Bolton Landing Conference, June, ed. J.L Walter, J.H. Westbrook and D.A. Woodford, p.607 (1974).

[170] W.C. Johnson, J.E. Doherty, B.H. Kear and A. F. Giamer, Scripta Met., Vol.8, p.971 (1974).

[171] G. Saindrenan and A. Laree, Scripta Met., Vol.18, p.969 (1984).

[172] H. Erhartn and M. Paju, Scripta Met., Vol.17, p.171 (1983).

[173] M. Paju and H.J. Grabke, Materials Science and Technology, Feb., Vo.15, p.148 (1989).

[174] M. Paju and R. Moller, Scripta Met., Vol.18, p.813 (1984).

[175] H. Hansel and H.J. Grabke, Scripta Metall., 20, p.164 (1986).

[176] K.S. Shin and B.H. Tsao, Scripta Met., Vol.22, p.585 (1988).

[177] D.S. Moore and G.P. McCabe, Introduction to the Practice of Statistics, p.584 (1988).

[178] A. Joshi, in Interfacial Segregation, ed.W.C.Johnson and J.M. Blaklly, p.82 (1977)

[179] T.B. Cameron and J.E. Morral, Boron in Steel, Proceedings of the International Symposium on Boron Steel, Milwaukee, Wisconsin, Sept., p.61 (1979).

[180] D.J. Dingley and V. Randle, Journal of Materials Science, 27, p.4545 (1992).

[181] G.A. Knorovsky, M.J. Cieslak, T.J. Headley, A.D. Romig and W.F. Hammetter, Met. Trans., Vol.20A, Oct., p.2149 (1989).

[182] M.J. Cieslak, T.J. Headley, A.Knorovsky, A.D. Romig and T. Kollie, Met. Trans., Vol.21A, Feb., p.579 (1990).

[183] G.L. Bleris, J.G. Antonopoulos, T.H. Karakostas and P. Delavignette, Physics Status Solidi, 67, p.249 (1981).

[184] D.G. Brandon., Acta Metall., 14, p.1479 (1966).

[185] J.F. Radavich, Journal of Metals, July, p.42 (1988).

[186] M.C. Flemings, Solidification Processing, McGraw-Hill Book Co., NY, p.31 (1974).

[187] R.G. Carlson and J.F. Radavich, in Superalloy 718 - Metallurgy and Application, p.79 (1989).

[188] R.G. Thompson, Journal of Metal, July, p.44 (1988).

[189] H. Radhakrishnan and R.G. Thompson, Metallography, 21, p.453 (1988).

[190] G. Muralipharan, R.G. Thompson and S.D. Walck, Proceeding of the Second Conference on Frontiers of Electron Microscopy in Materials Science, May, p.277 (1989).

[191] G. Muralidharan, R.G. Thompson and S.D. Walck, Ultramicroscopy, 29, p.277 (1989).

[192] M.J. Cieslak, G.A. Knorovsky, T. J. Headley and A.D. Romig Jr., in Superalloy 718 - Metallurgy and Applications, p.59 (1989).

[193] H.D. Brody and M.C. Flemings, Trans AIME, Vol.236, p.615 (1966).

[194] E. Scheil, Z. Metalk, Vol.34, p.70 (1942).

[195] J.A. Burton, R.C. Primm and W.P. Slichter, J. Chem. Phys, 21, p.1987 (1953).

[196] J.C. Lippold and W.F. Savage, Modelling of Casting and Welding Processes, ed. H.D. Brody and P. Apelian, Metallurgical Society of AIME, p.443 (1980).

[197] T. Kelly, Advances in Welding Science and Technology, TWR'86, ASM, OH, p.623 (1986).

[198] J. Lippold, Welding Journal, 62, p.1 (1983).

[199] J.S. Armijo and H.S. Rosenhaum, J.Appl. Phys., 38, p.2064 (1967).

[200] D.A. Canonico, W.F. Savage, W.J. Werner and G.M. Goddman, in Effects of Minor Elements on the Weldability of High Nickel Alloy, p.68 (1967).

[201] M. Ueno and T. Inoue, Transaction ISIJ, Vol.13, p.210 (1973).

[202] R.W. Balluffi, in Interfacial Segregation, ed.W.C. Johnson and J.M. Blakly, ASM, Metals Park, Ohio (1979).

[203] C.L. Briant, Acta Metall., 31, p.257 (1983).

[204] T. Watanabe, Scripta Met., 21, p.427 (1987).

[205] L. Karlsson and H. Norden, Acta Metall., Vol.36, No.1, p.35 (1988).

[206] W. Jackson, H. Frohlich, N.F. Mott and E.C. Bullard, in Monographs on the Physics and Chemistry of Materials, Chap.5, p.143 (1977).

[207] T. Kelly, Int. Welding Research Conf., ASM, Gatlinburg, TN (1986).

[208] W.F. Savage, E.F. Nippes and G.M. Goodwin, Welding Journal, Aug., p.245 (1977).

[209] K. Easterling, Introduction to the Physical Metallurgy of Welding, Butterworths, London, p.1 (1983).

[210] P. Adam, in High Temperature Alloys for Gas Turbines, ed. D. Coutsouradis, Applied Science Publishers Ltd., London, p.737 (1979).

[211] R.G. Thompson, Intergranular Liquation Effect on Weldability, ASM Fall Meeting, Detroit, MI, p.57 (1990).

[212] J.A. Brooks, Welding Journal, Nov., p.517 (1974).

[213] W.F. Savage, E.F. Nippes and G.M. Goodwin, Welding Journal, Aug., p.245s (1977).

[214] A.A. Griffiths, Phil. Trans. Roy. Soc., A, 211, p.163 (1920).

[215] D.A. Mortimer, Grain Boundary in Engineering Materials, 4th Bolton Landing

Conference, ed. J.L. Walter, J.H. Westbrook and D.A.Woodford, p.647 (1974).

[216] E. Smith and J.T. Barnby, Metal Science Journal, Vol.1, p.1 (1967).

[217] B. Mostefera, Acta Metall., 39(12), p.3111 (1991).

[218] L.E. Murr, in Interfacial Phenomena in Metals and Alloys, Addison-Wesley, p.139 (1975).

[219] B.J. Keene, Inter. Met. Rev., Vol.33, No.1, p.1 (1988).

[220] K. Thamburaj, Proc. Int. Conf. on Creep, Tokyo, Japan, JSME/ASME, p.275 (1986).

[221] C. Boucher, D. Varalo, M. Dadian and H. Granjon, 15th Conf. on Special Steel, Staint Etienne, May (1976).

Appendix I

Volume Fraction of Secondary Phases

Homogenization Temp.		1037°C	1066°C	1093°C	1163°C
Laves Phase (3.26 as-cast)	Homo.	2.31	2.22	2.20	0.09
	Homo.+Sol.	2.48	2.19	1.53	0.19
	Homo.+Age	2.30	1.80	1.70	0.08
δ-Ni_3Nb (7.88 as-cast)	Homo.	6.70	2.17	0.07	0
	Homo.+Sol.	11.78	9.93	8.93	0.69
	Homo.+Age	3.19	1.97	0.63	0
M(C,N) (1.62 as-cast)	Homo.	1.7	1.69	1.72	1.70
	Homo.+Sol.	1.68	1.69	1.67	1.66
	Homo.+Age	1.68	1.67	1.65	1.65

Appendix II-1

Effect of Heat Treatment on hardness (HR_B)

As-cast = 87

Homogenization Temp.	1036°C	1067°C	1093°C	1163°C
Homo.	82	81	81	79
Homo. + Sol.	82	81	81	79
Homo. + Age	105	104	105	106
Homo. + Sol. + Age	105	104	105	106

Appendix II-2

Effect of Heat Treatment Type on Hardness (HR_B)

Heat Treatment Conditions	HR_B
As-Cast	87
Homogenize (1163°C/1hr)	79
Homogenize (1163°C/1hr) + Age	106
Homogenize (1163°C/1hr) + Overage	105
Homogenize (1163°C/1hr) + Sol	79
Homogenize (1163°C/1hr) + Sol + Age	106
Homogenize (1163°C/1hr) + Sol + Overage	105

Appendix III-1 TCL Measurements (mm)

Heat Treatment Conditions	1037°C	1066°C	1093°C	1163°C
Homo.	1.39	0.98	1.77	2.07
Homo + Sol	0.46	0.27	1.34	1.59
Homo + Age	1.76	1.98	2.24	3.69

Appendix III-2 Effect of Cooling Methods on TCL

Heat Treatment Temperature	Cooling Method	Total Crack Length (mm)
950°C	Water Quench	4.5
	Air Cool	5.5
1066°C	Water Quench	5.2
	Air Cool	2.7
1163°C	Water Quench	4.9
	Air Cool	4.26
1024°C	Water Quench	5.2
	Air Cool	4.7

Appendix III-3 Effect of Heat Treatment Type on TCL (mm)

Heat Treatment Conditions	TCL (mm)
As-Cast	2.2
Homogenize (1163°C/1hr)	3.3
Homogenize (1163°C/1hr) + Age	6.4
Homogenize (1163°C/1hr) + Overage	4.2
Homogenize (1163°C/1hr) + Sol	2.5
Homogenize (1163°C/1hr) + Sol + Age	5.4
Homogenize (1163°C/1hr) + Sol + Overage	4.4

Appendix VI Calculation of Coefficient A

According to Faulkner's equation:

$$C_b = AC_g \exp\left[\frac{E_b - E_f}{KT_i} - \frac{E_b - E_f}{KT_{\frac{1}{2}m}}\right]\frac{E_b}{E_f} \qquad <72>$$

where T_i = 1250°C = 1523K

$T_{1/2m}$ = 1320°C/2 = 1593K/2 = 796K

E_b = 0.5eV

E_f = 1.4eV

From Karlsson's quantitative measurements [24]

when C_g = 206ppm (at),

C_b = 0.17 at cooling rate of 31°C/s

and C_b = 0.07 at cooling rate of 13°C/s

A cooling rate of 20°C/s was used in this study, so C_b can be estimated as 0.109. Therefore

$$C_b = Ax206x10^{-}6\exp\left[\frac{0.5-1.4}{8.85x10^{-}5x1523} - \frac{0.5-1.4}{8.85x10^{-}5x796}\right]\frac{0.5}{1.4} = 0.109 \qquad <73>$$

$$A = \frac{0.109}{0.0324} \approx 3 \qquad <74>$$